

AD-R205 469

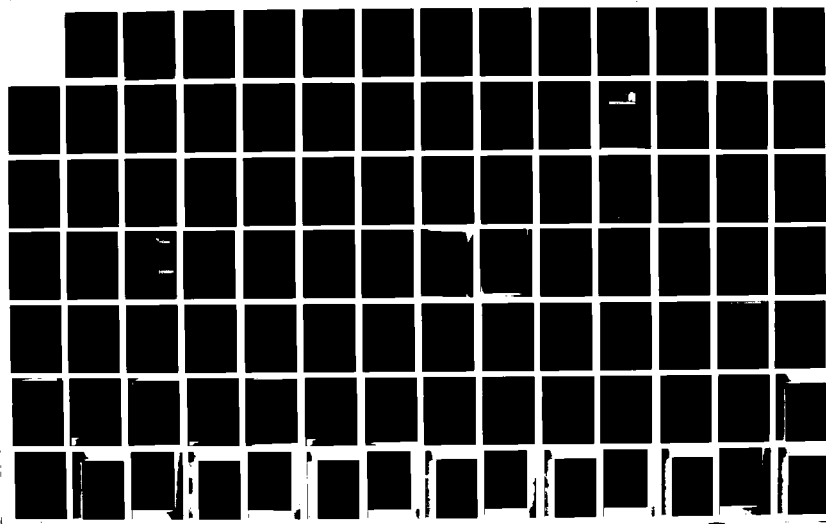
COHERENCE AND CHAOS PHENOMENA IN JOSEPHSON OSCILLATORS 1/3  
FOR SUPERCONDUCTIN (U) TECHNICAL UNIV OF DENMARK

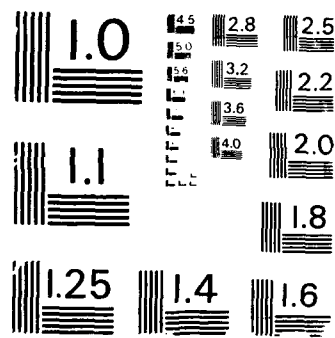
UNCLASSIFIED

LYNGBY LAB OF APPLIED MATHEMATICAL P  
P L CHRISTIANSEN ET AL 25 JAN 89

F/G 9/1

NL





COHERENCE AND CHAOS PHENOMENA  
IN JOSEPHSON OSCILLATORS  
FOR SUPERCONDUCTING ELECTRONICS

(2)

Final Technical Report

by

P.L. Christiansen, R.D Parmentier  
and O. Skovgaard

Laboratory of Applied Mathematical Physics  
The Technical University of Denmark  
Building 303, DK-2800 Lyngby  
Denmark

January 1989

United States Army  
EUROPEAN RESEARCH OFFICE OF THE U.S. ARMY  
London, England

CONTRACT NUMBER DAJA45-85-C-0042

Approved for Public Release; distribution unlimited

DTIC  
REF ID: A6210  
S  
H

Unclassified

SECURITY CLASSIFICATION OF THIS PAGE

APR 1985 469

Form Approved  
OMB No 0704-0188  
Exp Date Jun 30, 1986

REPORT DOCUMENTATION PAGE

1a REPORT SECURITY CLASSIFICATION Unclassified		1b RESTRICTIVE MARKINGS												
2a SECURITY CLASSIFICATION AUTHORITY		3. DISTRIBUTION/AVAILABILITY OF REPORT Approved for public release; distribution unlimited												
2b. DECLASSIFICATION/DOWNGRADING SCHEDULE														
4 PERFORMING ORGANIZATION REPORT NUMBER(S)		5. MONITORING ORGANIZATION REPORT NUMBER(S) R&D 4943-PH-01												
6a NAME OF PERFORMING ORGANIZATION The Technical University of Denmark	6b. OFFICE SYMBOL (if applicable)	7a. NAME OF MONITORING ORGANIZATION European Research Office USARDSG-UK												
6c. ADDRESS (City, State, and ZIP Code) Laboratory of Applied Mathematical Physics Building 303 DK-2800 Lyngby, Denmark		7b. ADDRESS (City, State, and ZIP Code) Box 65 FPO NY 09510-1500												
8a NAME OF FUNDING/SPONSORING ORGANIZATION USARDSG-UK ARO-E	8b OFFICE SYMBOL (if applicable)	9 PROCUREMENT INSTRUMENT IDENTIFICATION NUMBER DAJA45-85-C-0042												
8c. ADDRESS (City, State, and ZIP Code) Box 65 FPO NY 09510-1500		10. SOURCE OF FUNDING NUMBERS												
		PROGRAM ELEMENT NO. 61102A	PROJECT NO. IL161102BH57	TASK NO. 07	WORK UNIT ACCESSION NO.									
11. TITLE (Include Security Classification)  (U) Coherence and Chaos Phenomena in Josephson Oscillators for Superconducting Electronics														
12 PERSONAL AUTHOR(S) P.L. Christiansen, R.D. Parmentier and O. Skovgaard														
13a TYPE OF REPORT Final Technical Report	13b TIME COVERED FROM May 21, 88 TO Jan 21, 89		14 DATE OF REPORT (Year, Month, Day) 1989 January 25		15. PAGE COUNT 9									
16 SUPPLEMENTARY NOTATION														
17 COSATI CODES <table border="1"><tr><th>FIELD</th><th>GROUP</th><th>SUB-GROUP</th></tr><tr><td>20</td><td>03</td><td></td></tr><tr><td></td><td></td><td></td></tr></table>		FIELD	GROUP	SUB-GROUP	20	03					18. SUBJECT TERMS (Continue on reverse if necessary and identify by block number)  Chaos, coherence, electronics, fluxons, Josephson junctions, Melnikov method, microwaves, nonlinear dynamics, (continued p.t.o.)			
FIELD	GROUP	SUB-GROUP												
20	03													
19 ABSTRACT (Continue on reverse if necessary and identify by block number)  Work under the present contract has been dedicated to acquiring a detailed understanding of the fundamental mechanisms governing the dynamics of Josephson junction devices, with a view to employing this knowledge in the design of practical Josephson devices. Particular attention has been given to the questions of the interplay between coherence and chaos, and to determining the limits of stability of coherent states. A combination of analytical, computational, and experimental methods has been employed in order to maximize the results obtained.														
20 DISTRIBUTION/AVAILABILITY OF ABSTRACT <input checked="" type="checkbox"/> UNCLASSIFIED/UNLIMITED <input checked="" type="checkbox"/> SAME AS RPT <input checked="" type="checkbox"/> DTIC USERS			21 ABSTRACT SECURITY CLASSIFICATION Unclassified											
22a NAME OF RESPONSIBLE INDIVIDUAL Dr. Gerald R. Andersen			22b TELEPHONE (Include Area Code) 01-409 4423	22c OFFICE SYMBOL AMXSN-UK-RP										

18. continued:

oscillators, perturbation theory, phase-locking, solitons, superconductivity, thermal noise.

**COHERENCE AND CHAOS PHENOMENA  
IN JOSEPHSON OSCILLATORS  
FOR SUPERCONDUCTING ELECTRONICS**

**Final Technical Report**

**by**

**P.L. Christiansen, R.D Parmentier  
and O. Skovgaard**

**Laboratory of Applied Mathematical Physics  
The Technical University of Denmark  
Building 303, DK-2800 Lyngby  
Denmark**

**January 1989**

**United States Army  
EUROPEAN RESEARCH OFFICE OF THE U.S. ARMY  
London, England**

**CONTRACT NUMBER DAJA45-85-C-0042**

**Approved for Public Release; distribution unlimited**

**COHERENCE AND CHAOS PHENOMENA  
IN JOSEPHSON OSCILLATORS FOR  
SUPERCONDUCTING ELECTRONICS**

**Principal Investigator:** Peter L. Christiansen

**Contractor:** Laboratory of Applied Mathematical Physics  
The Technical University of Denmark  
Building 303  
DK-2800 Lyngby  
Denmark

**Contract Number:** DAJA4S-85-C-0042

**SUMMARY**

Work under the present contract has been dedicated to acquiring a detailed understanding of the fundamental mechanisms governing the dynamics of Josephson junction devices, with a view to employing this knowledge in the design of practical Josephson devices. Particular attention has been given to the questions of the interplay between coherence and chaos, and to determining the limits of stability of coherent states. A combination of analytical, computational, and experimental methods has been employed in order to maximize the results obtained.

**KEY WORDS**

Chaos, coherence, electronics, fluxons, Josephson junctions, Melnikov method, microwaves, nonlinear dynamics, oscillators, perturbation theory, phase-locking, solitons, superconductivity, thermal noise.

## TABLE OF CONTENTS

	<u>page</u>
Participating scientific personnel .....	3
Introduction .....	3
Background .....	6
Summary of most important results .....	7
Appendices .....	10



Accession For	
NTIS	<input checked="" type="checkbox"/>
DTIC	<input type="checkbox"/>
University	<input type="checkbox"/>
JSC	<input type="checkbox"/>
Other	<input type="checkbox"/>
Delivery Method	
Priority Codes	
Special and/or	
Distr	Special
A-1	

**COHERENCE AND CHAOS PHENOMENA  
IN JOSEPHSON OSCILLATORS FOR  
SUPERCONDUCTING ELECTRONICS**

**PARTICIPATING SCIENTIFIC PERSONNEL**

Michele Bartuccelli	(Ph.D. Degree, 1986)
Peter L. Christiansen	
Randy J. Flesch	
Morten Fordsmand	(M.Sc. Degree, 1985)
M. Gregory Forest	
Flemming If	(Ph.D. Degree, 1986)
Niels H. Jensen	
Sergio Pagano	(Ph.D. Degree, 1987)
Robert D. Parmentier	
Alwyn C. Scott	
Ove Skovgaard	
Mads P. Soerensen	

**INTRODUCTION**

The work performed under this contract has been described in six technical reports:

1st Periodic Report	January 1986
2nd Periodic Report	May 1986
3rd Periodic Report	December 1986
4th Periodic Report	May 1987
5th Periodic Report	November 1987
6th Periodic Report	May 1988

The results obtained under the contract have been published as follows:

**Scientific Journals**

1. F. If, P.L. Christiansen, R.D.Parmentier, O. Skovgaard, and M.P. Soerensen, "Simulation studies of radiation linewidth in circular Josephson-junction oscillators", Phys. Rev. **B32** (1985) 1512-1518.
2. M. Salerno, "A mechanical analog for the double sine-Gordon equation", Physica **17D** (1985) 227-234.
3. M. Bartuccelli, P.L. Christiansen, N.F. Pedersen, and M.P. Soerensen, "Prediction of chaos in a Josephson junction by the Melnikov-function technique", Phys. Rev. **B33** (1986) 4686-4691.

4. M. Fordsmand, P.L. Christiansen, and F. If, "Perturbation theory for radiation linewidth in circular Josephson junction oscillators", Phys. Lett. **116A** (1986) 71-72.
5. S. Pagano, M.P. Soerensen, R.D. Parmentier, P.L. Christiansen, O. Skovgaard, J. Mygind, N.F. Pedersen, and M.R. Samuels, "Switching between dynamic states in intermediate-length Josephson junctions", Phys. Rev. **B33** (1986) 174-182.
6. P.L. Christiansen, "Stability of dynamic states in Josephson junctions", Physica **23D** (1986) 68-71.
7. M. Bartuccelli, P.L. Christiansen, N.F. Pedersen, and M. Salerno, "Horseshoe chaos' in the space-independent double sine-Gordon system", Wave Motion **8** (1986) 581-594.
8. S. Pagano, N.F. Pedersen, S. Sakai, and A. Davidson, "Analytical and numerical results for a long Josephson junction with surface losses", IEEE Trans. Magnetics **MAG-23** (1987) 1114-1117.
9. S. Pagano, M. Salerno, and M.R. Samuels, "Parametric adiabatic perturbations on the sine-Gordon breather solution", Physica **26D** (1987) 396-402.
10. G. Costabile, S. Pagano, and R.D. Parmentier, "Stability of the McCumber curve for long Josephson tunnel junctions", Phys. Rev. **B36** (1987) 5225-5229.
11. M. Bartuccelli, P.L. Christiansen, V. Muto, and M.P. Soerensen, "Chaotic behaviour of a pendulum with variable length", Il Nuovo Cimento **100B** (1987) 229-249.
12. F. If, P. Berg, P.L. Christiansen, and O. Skovgaard, "Split-step spectral method for nonlinear Schroedinger equation with absorbing boundaries", J. Comp. Phys. **72** (1987) 501-503.
13. P.L. Christiansen, "Observations of real solitons", Nature **332** (1988) 12-13.
14. M. Salerno, M.R. Samuels, and H. Svensmark, "Thermal sine-Gordon system in the presence of different types of dissipation", Phys. Rev. **B38** (1988) 593-596.
15. S. Pagano, M.P. Soerensen, P.L. Christiansen, and R.D. Parmentier, "Stability of fluxon motion in long Josephson junctions at high bias", Phys. Rev. **B38** (1988) 4677-4687.
16. M.P. Soerensen, A. Davidson, N.F. Pedersen, and S. Pagano, "Crises in a driven Josephson junction studied by cell mapping", Phys. Rev. A (in press).
17. M.G. Forest, S. Pagano, R.D. Parmentier, P.L. Christiansen, M.P. Soerensen, and S.-P. Sheu, "Numerical evidence for global bifurcations leading to switching phenomena in long Josephson junctions", Wave Motion (in press).
18. M. Salerno and M.R. Samuels, "Internal oscillation frequencies and anharmonic effects for the double sine-Gordon kink", submitted to Phys. Rev. B.
19. M. Salerno, M.R. Samuels, G. Filatrella, S. Pagano, and R.D. Parmentier, "A simple map describing phase-locking of fluxon oscillations in long Josephson tunnel junctions", submitted to Phys. Lett. A.

20. M.G. Forest, "Correlations between chaos in the perturbed sine-Gordon equation and finite modal equations", preprint.

5

*The above scientific papers are included as appendices to the present report.*

Books

21. P.L. Christiansen, "Recent work on Josephson tunnel junctions within MIDIT", in **Structure, Coherence and Chaos in Dynamical Systems**, P.L. Christiansen and R.D. Parmentier, eds. (Manchester University Press, Manchester, 1988), pp. 93-112.

Conference Proceedings

22. P.L. Christiansen, "Stability of dynamic states in Josephson junctions", Workshop on Spatio-Temporal Coherence and Chaos in Physical Systems, Los Alamos, NM, USA, January 1986.

23. M.P. Soerensen, "On low dimensional chaos in rf-SQUIDS", 2nd University of California Conference on Statistical Mechanisms, U.C. Davis, CA, USA, March 1986.

24. S. Pagano, "Competing modes in Josephson oscillators", Spring Meeting of the Danish Physical Society, Nyborg, Denmark, May 1986.

25. P.L. Christiansen, "Coherent excitations in some physical and biological systems", 9th Dundee Conference on the Theory of Ordinary and Partial Differential Equations, Dundee, Scotland, June/July 1986.

26. M. Bartuccelli P.L. Christiansen, V. Muto, M.P. Soerensen, and N.F. Pedersen, "Subharmonic and heteroclinic bifurcations in a pendulum with variable length", MIDIT 1986 Workshop on Structure, Coherence and Chaos in Dynamical Systems (*hereafter abbreviated "MIDIT 1986"*), Lyngby, Denmark, August 1986.

27. G. Costabile, G. Eriksen, S. Pagano, and R.D. Parmentier, "Phase locking to external radiation of intermediate-length Josephson junctions", MIDIT 1986.

28. S. Pagano, M.P. Soerensen, R.D. Parmentier, P.L. Christiansen, F. If, M. Fordsmand, O. Skovgaard, J. Mygind, N.F. Pedersen, and M.R. Samuelsen, "Stability of dynamical states in Josephson junctions", MIDIT 1986.

29. S. Pagano, S. Sakai, and N.F. Pedersen, "Perturbation and phase space methods for soliton dynamics in a Josephson junction with bias and losses", MIDIT 1986.

30. P.L. Christiansen, "Instabilities and chaos in Josephson junctions", Conference on Nonlinear Dynamics and Chaos, Thessaloniki, Greece, August 1986.

31. P.L. Christiansen, "Perturbation of integrable systems and the Melnikov method", EUROMECH 216, Integrable Systems in Nonlinear Analytical Mechanics, Leeds, England, September 1986.

32. R.D. Parmentier, "Phase locking of coherent states in Josephson junction transmission lines", 4eme Rencontre Interdisciplinaire, Solitons et Structures Coherentes, Grenoble, France, March 1987.

33. P.L. Christiansen, "Instabilities in Josephson lines", First Workshop of the EEC Josephson Project, La Brigue, France, May 1987.

6

34. M.P. Soerensen, "Stability of fluxon motion in long Josephson junctions at high bias", First Workshop of the EEC Josephson Project, La Brigue, France, May 1987.

35. P.L. Christiansen, "How stable are strongly non-linear solitons", 12th Summer School of Mathematical Physics, Ravello, Italy, August 1987.

36. P.L. Christiansen, "Stability of sine-Gordon solitons", 4th Meeting on Waves and Stability in Continuous Media, Taormina, Italy, October 1987.

37. P.L. Christiansen and N.F. Pedersen, "Nonlinear dynamics of the Josephson junction", International Conference on Singular Behaviour and Nonlinear Dynamics, Samos, Greece, August 1988.

38. S. Pagano, M.P. Soerensen, R.D. Parmentier, P.L. Christiansen, O. Skovgaard, J. Mygind, N.F. Pedersen, and M.R. Samuels, "Stability of fluxon motion in long Josephson junctions in the presence of a magnetic field", International Conference on Singular Behaviour and Nonlinear Dynamics, Samos, Greece, August 1988.

#### Ph.D. Theses

39. F. If, "Spectral algorithms and numerical solution of some nonlinear partial differential equations", Ph.D. Thesis, Laboratory of Applied Mathematical Physics, The Technical University of Denmark, Lyngby, January 1986.

40. M. Bartuccelli, "Analytical methods for prediction of chaos in periodically forced nonlinear oscillators", Ph.D. Thesis, Laboratory of Applied Mathematical Physics, The Technical University of Denmark, Lyngby, March 1986.

41. S. Pagano, "Nonlinear dynamics in long Josephson junctions", Ph.D. Thesis, Laboratory of Applied Mathematical Physics, The Technical University of Denmark, Lyngby, September 1987.

#### BACKGROUND

The strong potential of Josephson tunnel junction devices in high-performance electronic applications has been recognized for a number of years. In a few areas, notably those involving applications of dc SQUIDs, this potential has been amply realized: measurements of extremely weak magnetic fields, with sensitivities approaching the fundamental quantum limit, have now become routine using these devices. Another area where Josephson devices show considerable promise is the realization of circuit elements — oscillators, mixers, amplifiers — for high-sensitivity, low-noise microwave or millimeter-wave receivers. Notable practical progress has also been achieved in this area: Josephson SIS mixers have been installed and function routinely in the high-sensitivity receivers employed in several radio-astronomical observatories throughout the world. However, in this area, we are still fairly far from realizing the full potential of the Josephson approach.

Our work under the present contract, as well as that performed in the context of our previous ERO contract (no. DAJA37-82-C-0057, 1982-1985), has been dedicated to acquiring a detailed understanding of the fundamental mechanisms governing the dynamics of Josephson junction devices, with a view to employing this knowledge in the design of practical Josephson devices. Work under the first contract was devoted to understanding the basic mechanisms of fluxon (flux quantum, or soliton) propagation in Josephson junctions. The practical consequence of this work, very briefly summarized, was that we were able to construct a "catalog" of the basic fluxon dynamic configurations responsible for various, experimentally observed phenomena. Under the present contract we have extended this study to the understanding of the more subtle question of the complicated interaction between coherence (i.e. regular, steady fluxon propagation) and chaos. Chaos in dynamical systems has, in recent years, become an active field of independent study, with an impressive array of theoretical and computational results. From the practical point of view, on the other hand, in particular for electronic applications, chaos represents "noise", and hence is a phenomenon that one wishes to avoid. Consequently, in this context, one studies chaos with the objective of "designing around it". A second, closely related, question is the analysis of the stability of coherent states. Often (but not always) a loss of stability signals the onset of chaos. But even when a stability boundary indicates a transition from one coherent state to another, understanding of this fact constitutes essential knowledge for the device designer.

The most significant results that we have obtained under the present contract are summarized briefly in the following section; they are described in more detail in the papers enclosed as appendices. As in the work under the previous contract, we have herein attempted to combine analytical, computational, and experimental work in such a way as to maximize the illumination cast on any given question.

#### SUMMARY OF MOST IMPORTANT RESULTS

The influence of small external perturbations, both periodic and random, on the coherent motion of fluxons in Josephson junctions, and hence on the linewidth of the microwave radiation emitted by such junctions, was studied in Refs. 1 and 4. The work in Ref. 1 was based essentially on numerical simulations of the sine-Gordon model of the Josephson junction, subjected to small external perturbations; that in Ref. 4 was analytical work based on the soliton perturbation theory of McLaughlin and Scott. The question is of considerable practical interest: experiments have shown that the relative linewidth of the radiation emitted from a Josephson junction oscillator, associated with resonant fluxon propagation, can be as narrow as  $10^{-7}$ ; it is just this fact that renders the device interesting for electronic applications.

Knowledge of the intrinsic, i.e., "classical", stability of coherent fluxon dynamical states is clearly of fundamental importance for the device designer. This question was addressed in Refs. 5, 6, 10, 15, and 17. Refs. 5, 6, and 10 were directed toward the question of the "birth" of coherent fluxon states, which give rise to zero-field steps in the current-voltage characteristic of the junction, from the uniform background state (the so-called McCumber state). The basic analytical procedure, in approximate form, was developed in Ref. 5. Comparison with numerical and experimental results demonstrated the essential correctness of the procedure. Ref. 10 extended the analytical procedure, giving an exact linear stability analysis of the McCumber state. Refs. 15 and 17 were dedicated to the "death" of coherent fluxon states by means of switching from the top of zero-field steps to the so-called gap state. Here, since the analysis is (at least so far) intractable, the approach was strictly numerical. In Ref. 15 a direct numerical integration of the model equation was used. In Ref. 17, instead, numerical techniques were used to establish the existence (and non-existence) of heteroclinic connections between the fixed points of the reduced ordinary differential equation associated with the model partial differential equation.

At the present time, the Melnikov-function technique is perhaps the best-developed and most reliable theoretical tool for studying the onset of chaos in dynamical systems. In particular, this technique permits analytic calculation of the conditions for the existence of Smale-horseshoe chaos in perturbed dynamical systems that are "sufficiently close", in a function-space sense, to an integrable system. A Smale horseshoe contains a countable set of unstable periodic orbits, an uncountable set of bounded nonperiodic orbits, and a dense orbit; consequently, the existence of a Smale horseshoe can be viewed as the first step toward a possible chaotic behavior. The Melnikov-function technique was applied to Josephson junction devices, and related dynamical systems, in Refs. 3, 7, and 11. Direct numerical integration of the model equation was used to check the validity of the predictions of the Melnikov approach regarding the threshold for the onset of chaos.

A topic that continues to attract research interest, even though not directly connected with the interplay between coherence and chaos, is the influence of the dissipative parameters in the sine-Gordon model of the Josephson junction on the dynamics of fluxons. Refs. 8, 9, and 14 have provided interesting new results in this connection. Ref. 14, in particular, has extended the usual "isolated" sine-Gordon model of the junction to a model in thermal equilibrium with a heat reservoir, thus incorporating in a natural way the effects of thermal fluctuations on the behavior of the system. Thermal noise is an important physical phenomenon, even at the very low temperatures at which superconductive Josephson devices work; consequently, an understanding of thermal effects is crucial for the accurate modelling of practical electronic devices.

As indicated above, Josephson fluxon oscillators show considerable promise for applications in high-frequency radio receivers. Since the power available from a

single such oscillator is somewhat low, a natural approach has been to construct arrays of oscillators, which, of course, is reasonable if the individual oscillators of the array can be made to work in synchronism. In Ref. 19, a first step has been taken toward the theoretical study of phase-locking of fluxon oscillators. The approach adopted has the attractive feature of reducing the problem of phase-locking to the study of the fixed points of a two-dimensional functional map.

Finally, new computational techniques for the study of particular aspects of Josephson junction dynamics have been developed in Refs. 16 and 20. Ref. 16 illustrates the application of the cell-to-cell mapping technique, originally developed for the study of other dynamical systems, to the rf-driven Josephson junction. This approach permits a complete mapping of the basins of attraction of the various attractors, both periodic and chaotic, of the system with an enormously reduced computational cost. In Ref. 20, study of the complicated dynamics of the sine-Gordon model, in a regime characterized by chaotic behavior, is reduced to the study of a finite set of modal equations, with the nonlinear modes chosen from considerations of spectral theory, resulting once again in a significant reduction of computational effort.

## Simulation studies of radiation linewidth in circular Josephson-junction fluxon oscillators

F. If, P. L. Christiansen, R. D. Parmentier,\* O. Skovgaard, and M. P. Soerensen

Laboratory of Applied Mathematical Physics, The Technical University of Denmark, DK-2800 Lyngby, Denmark

(Received 8 November 1984)

Detailed simulation studies of the dynamics of fluxons in long circular Josephson tunnel junctions under the influence of external microwave radiation and internal thermal noise are presented. The simulation algorithm uses a pseudospectral method well adapted to vector processors (CRAY-I-S), which gives a speed-up factor in computing time of typically 22 in comparison to conventional high-speed computers, and also provides results with a relative accuracy of less than  $10^{-8}$  thereby making possible the study of the very narrow radiation linewidth of such oscillators. Comparison of calculated linewidths with experimental results shows good agreement.

### I. INTRODUCTION

Josephson-junction fluxon oscillators continue to attract research interest both theoretically, in studies of nonlinear wave dynamics, and experimentally, where the very narrow linewidth of the emitted microwave radiation promises potentially interesting applications.<sup>1</sup> This very narrow linewidth makes the numerical study of the detailed dynamics of such oscillators very CPU time consuming. In order to overcome these difficulties we have developed a pseudospectral algorithm for solving the perturbed sine-Gordon equation which describes the oscillator. This algorithm employs a Fourier transformation of the spatial variable together with a finite-difference approximation to the time variable. The extensive use of fast Fourier transforms in the algorithm has made the implementation natural on a CRAY-I-S vector processor. The Fourier treatment of the space variable requires spatial periodicity in the model. In physical terms this means that we are studying a circular junction oscillator of the type first proposed by McLaughlin and Scott.<sup>2</sup> This device, as well as providing a convenient mathematical model because of periodic boundary conditions, has in recent years begun to attract research interest in its own right.<sup>3,4</sup>

The paper is structured as follows. In Sec. II we describe the mathematical model of the circular junction. Details of the numerical techniques employed are presented in Sec. III. In Sec. VI we study the behavior of the oscillator under the influence of a sinusoidal driving term in the bias current, which models external microwave irradiation. Section V contains calculations of the linewidth under the influence of Gaussian white noise, which models internal thermal noise in the junction. In Sec. VI we compare our results with existing experimental observations. In all of the sections we are focusing on a configuration with a single propagating fluxon, which corresponds to the first zero-field step in the current-voltage characteristic of the oscillator.

### II. MATHEMATICAL MODEL

As a model for the Josephson tunnel junction of overlap geometry we use the perturbed sine-Gordon equation,<sup>5</sup>

$$\varphi_{xx} - \varphi_{tt} - \sin\varphi = \alpha\varphi_t + \gamma + \eta(x,t). \quad (2.1)$$

Here  $\varphi$  is the quantum phase difference between the two superconducting layers in the junction. Space and time are normalized to the Josephson penetration length  $\lambda_J = (\Phi_0/2\pi j_0 L_p)^{1/2}$ , and the inverse of the plasma frequency  $\omega_p = (2\pi j_0/\Phi_0 C)^{1/2}$ , respectively, where  $\Phi_0$  is the magnetic flux quantum given by  $\Phi_0 = h/2e = 2.064 \times 10^{-15}$  Wb.  $L_p$  and  $C$  are the inductance and the capacitance per unit length of the junction. The first of the perturbation terms on the right-hand side of Eq. (2.1) represents the loss due to tunneling of normal electrons, in normalized units  $\alpha = G/\omega_p C$ , where  $G^{-1}$  is an effective normal resistance per unit length. The second term is the normalized bias current  $\gamma$  measured in units of  $j_0$  the maximum Josephson current per unit length. In this paper we include a third term  $\eta(x,t)$  representing either an externally applied sinusoidal driving term connected to the bias, or an internal thermal noise term connected to the loss. In this second case we assume a distributed Gaussian white noise with zero mean value.

The normalized length of the Josephson junction  $l = L/\lambda_J$  is assumed to be large compared with unity and the normalized width  $w = W/\lambda_J$  small compared with unity, allowing us to use a 1+1 dimensional model.<sup>6</sup> Because the aim of this investigation is to isolate the influence of the term  $\eta(x,t)$  on the solution to Eq. (2.1) we avoid phenomena connected with collision with junction boundaries by considering a long annular junction. Therefore, we demand spatial periodicity with period  $l$  in the two physical quantities, the voltage drop across the junction:

$$V = \frac{\Phi_0 \omega_p}{2\pi} \varphi_t, \quad (2.2)$$

and the current along the junction,

$$I = -j_0 \lambda_J \varphi_x, \quad (2.3)$$

i.e., boundary conditions

$$\varphi_t(0,t) = \varphi_t(l,t), \quad (2.4a)$$

$$\varphi_x(0,t) = \varphi_x(l,t). \quad (2.4b)$$

The fluxon traveling wave solution to the unperturbed version of Eq. (2.1) is given by<sup>7</sup>

$$\varphi = 2 \sin^{-1} [cn(\xi, k)] , \quad (2.5)$$

with  $\xi = (x - ut)/[k(1 - u^2)^{1/2}]$ . Here  $u$  is the velocity of the wave and  $k$  is the modulus in the Jacobian elliptic function.<sup>8</sup> Spatial periodicity requires  $1/(1 - u^2)^{1/2} = 2nkK(k)$ , where  $n$  is the winding number, i.e., the number of fluxons minus the number of antifluxons, and  $K(k)$  is the complete elliptic integral of the first kind. In Ref. 9 it is shown by Hamiltonian perturbation theory<sup>2</sup> that the steady-state fluxon velocity dependence on the loss and bias parameters is

$$u = 1/\sqrt{1 + (4\alpha'/\pi\gamma)^2} , \quad (2.6)$$

with  $\alpha' = \alpha E(k)/k$ , where  $E(k)$  is the complete elliptic integral of the second kind. For  $l \geq 8$  (assuming  $n=1$ ) Eq. (2.5) reduces to the kink for the infinite line  $\varphi = 4 \tan^{-1}(e^\xi)$  with  $\xi = (x - ut)/(1 - u^2)^{1/2}$ , and the velocity given by  $u = 1/\sqrt{1 + (4\alpha'/\pi\gamma)^2}$ . In the numerical simulations we have used  $l=8$ , 12.8, 20, and  $n=1$ .

### III. NUMERICAL TECHNIQUES

The very narrow linewidth of the radiation emitted from a Josephson-junction oscillator (less than 1 kHz at 10 GHz)<sup>10</sup> suggests that a relative numerical accuracy of at least  $10^{-7}$  is essential. We solve Eq. (2.1) numerically by using a pseudospectral method.<sup>11</sup> This method, a Fourier transform treatment in space together with a leap-frog scheme in time, has the advantage of simplicity and high-order accuracy in the approximations to the space derivatives. Expansion of the fluxon wave into truncated series of sines and cosines demands periodicity not only in  $\varphi_x$  and  $\varphi$ , but also in  $\varphi$  itself. Observing that the fluxon is a localized kink connecting two ground states separated by  $2\pi$  we introduce a new periodic function  $\varphi - 2\pi x/l$  whose Fourier representation we denote  $\Phi^p(t)$  with the superscript  $p=0, \pm 1, \dots, \pm p_{\max}$ .

Transforming Eq. (2.1) into the following set of ordinary nonlinear coupled differential equations:

$$-k_p^2 \Phi^p(t) - \Phi''_p(t) - F^p[\sin\varphi] = \alpha \Phi'_p(t) + l\gamma \delta_{p,0} + N^p(t) , \quad (3.1a)$$

$$k_p = 2\pi p/l, \quad p=0, \pm 1, \dots, \pm p_{\max} \quad (3.1b)$$

in which  $F^p$  and  $N^p$  are the Fourier components of  $\sin\varphi$  and  $\eta$ , respectively, and  $\delta_{p,0}$  denotes the Kronecker symbol, and using second-order central differences to approximate the time derivatives we get an explicit scheme for the time evolution of the Fourier components

$$\Phi_{j+1}^p = [2\Phi_j^0 - (1 - \alpha\Delta t/2)\Phi_{j-1}^0 - \Delta t^2(S_j^0 + l\gamma + N_j^0)]/(1 + \alpha\Delta t/2) , \quad (3.2a)$$

$$\Phi_{j+1}^p = [(2 - \Delta t^2 k_p^2)\Phi_j^p - (1 - \alpha\Delta t/2)\Phi_{j-1}^p - \Delta t^2(S_j^p + N_j^p)]/(1 + \alpha\Delta t/2), \quad |p| > 0 , \quad (3.2b)$$

where  $S_j^p$  equals  $F^p[\sin\varphi]$  at time  $j\Delta t$ , calculated each time step by transforming  $\Phi_{j+1}^p$  back to  $x$  space, calculat-

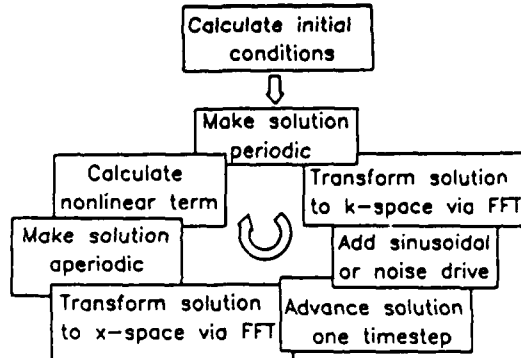


FIG. 1. Schematic diagram of numerical simulation procedure.

ing  $\sin\varphi$  and then transforming again to  $k$  space as indicated schematically in Fig. 1.

Figure 2 shows the computed  $\varphi_x$  as a function of time at an arbitrary point on the junction. This signal consists of an almost-periodic sequence of pulses. In fact, it is the deviation from perfect periodicity that gives a nonzero linewidth of the radiation. Since the deviation is small it is necessary to devise a very accurate method for determining the revolution periods  $T_n$  for the circulating fluxon. We do this by calculating  $T_n$  as the time for the mean value of the phase over  $x$  to change by  $2\pi$ . The fundamental frequency of the signal then becomes  $f_0 = 1/\langle T_n \rangle$ , where brackets denote an average value. We take the power spectrum of the signal near  $f_0$  to be the distribution of the computed values of  $1/T_n$ .

Figure 3 shows the calculated  $T_n$ 's in a computer experiment with the driving term  $\eta=0$  in Eq. (2.1). As can be seen from Fig. 3, the relative accuracy  $\Delta T/\langle T_n \rangle \lesssim 10^{-8}$ . In fact, examination of the numerical output shows that it is approximately  $7 \times 10^{-9}$ . The long transient arises from the fact that the initial conditions given by

$$\varphi(x, 0) = f(x, 0) - \sin^{-1}(\gamma) , \quad (3.3a)$$

$$\varphi(x, -\Delta t) = f(x, -\Delta t) - \sin^{-1}(\gamma) , \quad (3.3b)$$

where  $f(x, t)$  is the fluxon traveling wave solution to the unperturbed sine-Gordon equation as given by Eq. (2.5)

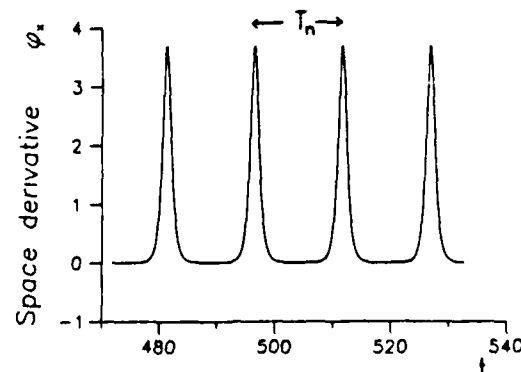


FIG. 2. Time dependence of the space derivative of the fluxon wave form, showing the  $n$ th period of revolution  $T_n$  for  $\alpha=0.01$ ,  $\gamma=0.02$ ,  $\eta=0$ , and  $l=12.8$ .

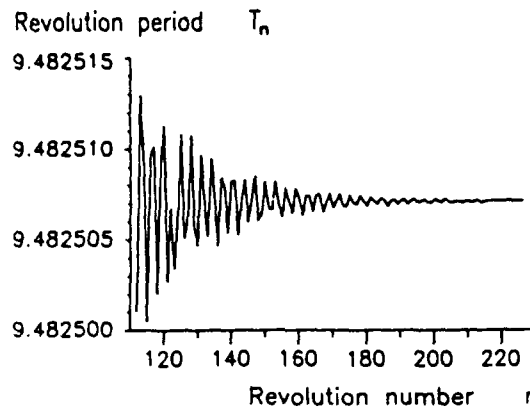


FIG. 3. Revolution period  $T_n$  as a function of revolution number  $n$  for  $\alpha=0.01$ ,  $\gamma=0.02$ ,  $\eta=0$ , and  $l=8$  showing high level of computational accuracy achieved.

and  $\sin^{-1}(\gamma)$  is the ground state, are not exactly equal to the final propagating configuration.

We note at this point that the accuracy of the results was checked by doubling  $p_{\max}$  in Eq. (3.1b), in order to ensure that no spurious Fourier modes due to the discretization in  $x$  space are produced, and halving  $\Delta t$  in Eqs. (3.2). The values used for  $p_{\max}$  ranged from 64 to 256 and those for  $\Delta t$  from 0.075 to 0.0025, depending on the parameters  $l$  and  $\gamma$ .

The computer program was implemented on an IBM 3033 in double precision (approximately 16 significant digits) and on a CRAY-1 vector processor in single precision (approximately 15 significant digits) using optimizing FORTRAN compilers. In the former case we have used the IMSL-routine FFT2C for fast Fourier transform.<sup>12</sup> In the latter case, by making full use of vectorization of the computer code and the CRAY routines for Fourier transform and vector copying CFFT2 (Ref. 13) and CCOPY (Ref. 14) we gained a speed-up factor in computing time of 22. Each long simulation requires typically  $5 \times 10^5$  time steps on a 512-point spatial lattice and uses approximately 10 min of CPU time on the CRAY-1-S as opposed to approximately 4 h on a scalar machine.

Finally, we have compared the steady-state fluxon velocity, given by  $u=l/\langle T_n \rangle$ , with the predicted value

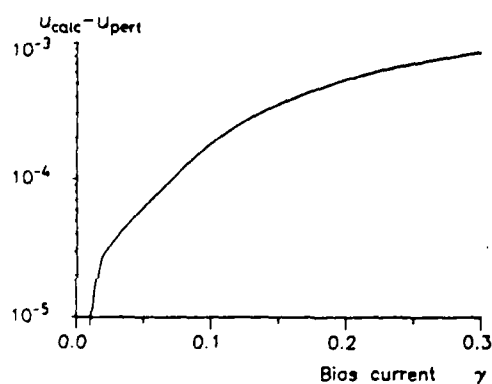


FIG. 4. Difference between average propagation velocity as computed numerically  $u_{\text{calc}}$  and calculated from perturbation theory  $u_{\text{pert}}$  from Eq. (2.6) as a function of the bias for  $\alpha=0.01$ ,  $\eta=0$ , and  $l=8$ .

from Hamiltonian perturbation theory, Eq. (2.6). The result is seen in Fig. 4. The deviation for large bias values is expected because the perturbation theory is only valid for small  $\gamma$  values.

#### IV. SINUSOIDAL DRIVING TERM

In this section we investigate the behavior of the fluxon velocity when the driving term is given by

$$\eta(x,t)=\eta(t)=\eta_0 \sin(\Omega t), \quad (4.1)$$

as a function of the driving frequency  $\Omega$ . This might be considered as a model of microwave irradiation of the junction. Using the definition of the normalized momentum

$$p(t)=-\frac{1}{l} \int_0^l \varphi_x \varphi_d dx, \quad (4.2)$$

and separating the phase into a kink part and a background part<sup>15</sup>  $\varphi(x,t)=\varphi^k(x,t)+\varphi^m(t)$ , and assuming that the length of the junction is large, allowing expressions for the infinite junction to be used, we get the following equation for the momentum  $p^k$  of the kink,

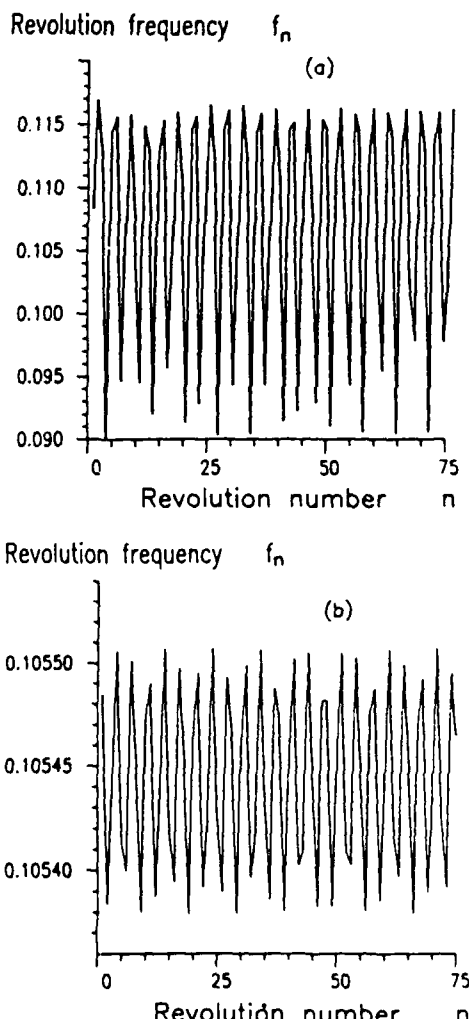


FIG. 5. Revolution frequency  $f_n$  as a function of revolution number  $n$  for sinusoidal drive,  $\eta(t)=\eta_0 \sin(\Omega t)$ , with  $\alpha=0.01$ ,  $\gamma=0.02$ ,  $\Omega=0.86$ ,  $\eta_0=0.01$ , and  $l=8$ . (a) Numerical simulation. (b) Kink model.

$$\frac{dp^k}{dt} + \alpha p^k = \frac{\pi}{4} \left[ \gamma + \eta_0 \sin(\Omega t) + \alpha \frac{d\varphi^k}{dt} + \frac{d^2\varphi^k}{dt^2} \right]. \quad (4.3)$$

Thus, the background motion becomes an effective driving term for the kink part. From Eq. (2.1) we derive the linearized equation for  $\hat{\varphi}^k = \varphi^k + \sin^{-1}(\gamma)$ , assuming that  $\hat{\varphi}^k \ll 1$ ,

$$\frac{d^2\hat{\varphi}^k}{dt^2} + \alpha \frac{d\hat{\varphi}^k}{dt} + (1 - \gamma^2)^{1/2} \hat{\varphi}^k = -\eta_0 \sin(\Omega t). \quad (4.4)$$

Combining Eqs. (4.3) and (4.4) we obtain for the kink momentum

$$p^k(t) = \frac{\pi}{4} \left[ \frac{\gamma}{\alpha} + \frac{\eta_0}{(\alpha^2 + \Omega^2)^{1/2}} \sin(\Omega t - \theta_1) - \frac{\eta_0 \Omega}{\{[(1 - \gamma^2)^{1/2} - \Omega^2]^2 + \alpha^2 \Omega^2\}^{1/2}} \cos(\Omega t - \theta_2) \right], \quad (4.5a)$$

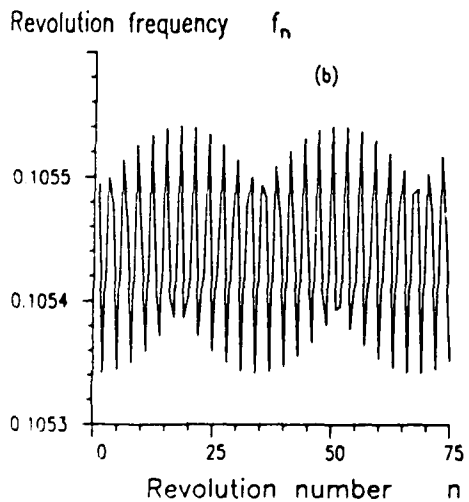
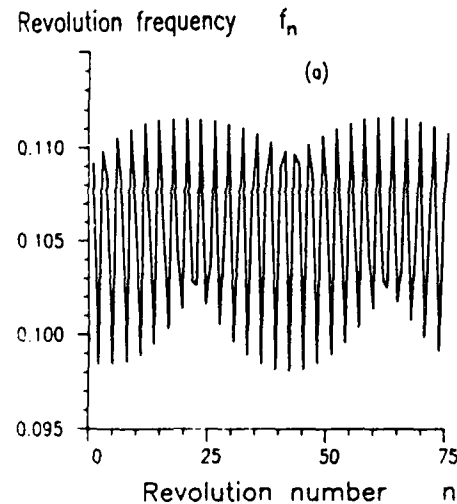


FIG. 6. Revolution frequency  $f_n$  as a function of revolution number  $n$  for sinusoidal drive,  $\eta(t) = \eta_0 \sin(\Omega t)$ , with  $\alpha = 0.01$ ,  $\gamma = 0.02$ ,  $\Omega = 0.89$ ,  $\eta_0 = 0.01$ , and  $l = 8$ . (a) Numerical simulation. (b) Kink model.

$$\theta_1 = \tan^{-1}(\Omega/\alpha) \quad \text{and} \quad (4.5b)$$

$$\theta_2 = \tan^{-1}[\alpha\Omega/((1 - \gamma^2)^{1/2} - \Omega^2)].$$

The instantaneous kink velocity is then calculated from  $p^k = u/(1 - u^2)^{1/2}$ . In order to compare this approximate theoretical description with the numerical result we calculate the  $n$ th period  $T_n$  according to the formula

$$\int_{t_{n-1}}^{t_n+T_n} u dt = l,$$

$$\text{with} \quad (4.6)$$

$$u = p^k / [1 + (p^k)^2]^{1/2}.$$

Figures 5–7 show a comparison of the results from this linearized model and from numerical simulations of Eq. (2.1) with  $\Omega = 0.86$ ,  $0.89$ , and  $1.10$ , respectively. In all cases it is seen that the kink model is able to reproduce the fluctuations in the revolution frequency  $f_n = 1/T_n$  in great detail.

As a measure of the amplitude of the frequency fluc-

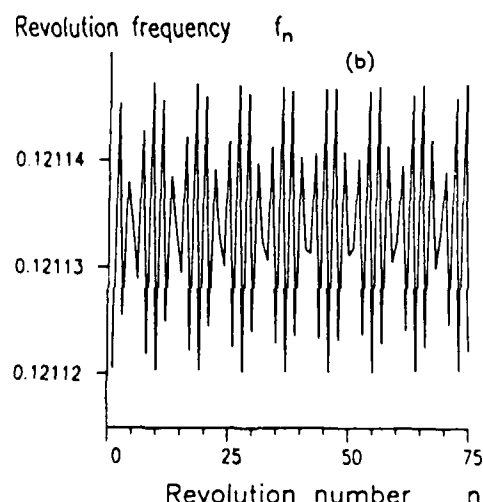
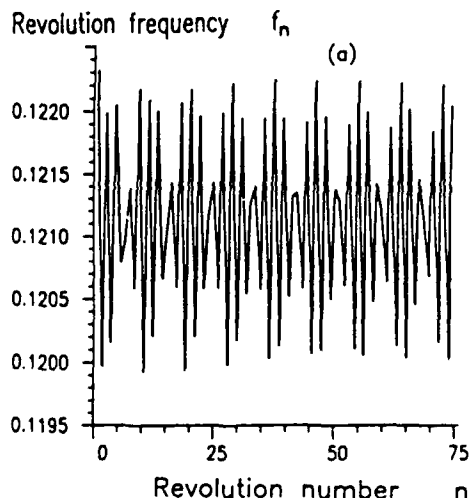


FIG. 7. Revolution frequency  $f_n$  as a function of revolution number  $n$  for sinusoidal drive,  $\eta(t) = \eta_0 \sin(\Omega t)$ , with  $\alpha = 0.01$ ,  $\gamma = 0.05$ ,  $\Omega = 1.10$ ,  $\eta_0 = 0.01$ , and  $l = 8$ . (a) Numerical simulation. (b) Kink model.

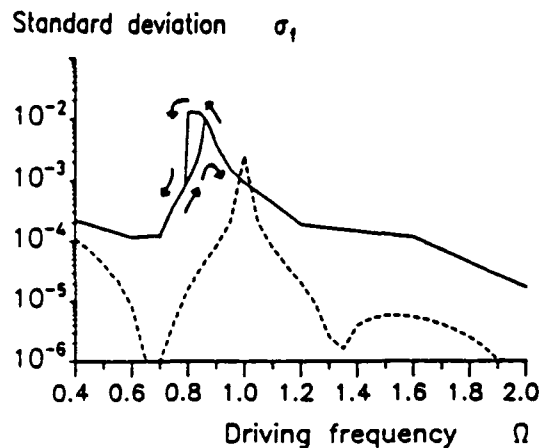


FIG. 8. Standard deviation of revolution frequency  $\sigma_f$  as a function of driving frequency  $\Omega$ . Solid curve, numerical simulation; dashed curve, kink model; parameters,  $\alpha=0.01$ ,  $\gamma=0.02$ ,  $\eta_0=0.01$ , and  $l=8$ .

tuation, which is essentially the linewidth of the oscillator, we have calculated the standard deviation of the revolution frequency  $\sigma_f = [\langle (f_n - \langle f_n \rangle)^2 \rangle]^{1/2}$  for values of the cyclic driving frequency  $\Omega$  between 0.4 and 2.0.

The full curve in Fig. 8 shows the results from the numerical simulation and the dashed curve those from the kink model. The kink model predicts a resonance just below the plasma frequency  $\Omega=1$ , whereas the numerical simulation yields this peak at a somewhat lower frequency. Moreover, the numerical results exhibit a hysteresis not seen in those of the kink model and a difference in scale. The discrepancy in resonance frequency and hysteresis behavior is attributable to the fact that we have used a linearized kink model. Presumably, the use of a higher-order expansion in Eq. (4.4) would yield a behavior analogous to that of a soft nonlinear spring<sup>16</sup> thus reducing these discrepancies. It is not clear, however, to what extent the difference in scale would be resolved by such a refinement.

## V. GAUSSIAN WHITE NOISE

The term  $\eta(x,t)$  in Eq. (2.1) is here considered to be Gaussian white noise with zero mean  $\langle \eta(x,t) \rangle = 0$  and autocorrelation function

$$R_\eta(\zeta, \tau) = \langle \eta(x,t) \eta(x+\zeta, t+\tau) \rangle = \sigma_\eta^2 \delta(\zeta) \delta(\tau). \quad (5.1)$$

The variance of the noise  $\sigma_\eta^2$  is connected with the loss  $\alpha$  and the absolute temperature  $T$  through<sup>17</sup>

$$\sigma_\eta^2 = 4\pi\alpha kT / \Phi_0 j_0 \lambda_J, \quad (5.2)$$

where  $k$  is the Boltzmann constant.

In the vectorized algorithm we find it convenient to introduce the noise term in  $p$ - $t$  space,  $N^p(t)$ , as

$$N^p(t) = F^{-1} \{ \sigma_\eta \exp(i(\theta_p + \theta_\omega)) \}, \quad (5.3)$$

where  $F^{-1}$  denotes the Fourier transform from  $\omega$  to  $t$  space, and  $\theta_p$  and  $\theta_\omega$  are stochastic variables uniformly distributed between 0 and  $2\pi$ , with an upper limit in  $p$  and  $\omega$  of  $p_{\max} = 1/2\Delta x$  and  $\omega_{\max} = \pi/\Delta t$ ,  $\Delta x$  and  $\Delta t$  being the resolution in space and time, respectively. Standard

Hamiltonian perturbation theory for the fluctuations  $\Delta u$  in the fluxon velocity leads to the power spectrum for  $\Delta u$ ,<sup>18</sup>

$$S_{\Delta u}(\omega) = \frac{1}{8} \sigma_\eta^2 (1 - u_0^2)^{3/2} \frac{1}{\omega^2 + \alpha^2}, \quad (5.4)$$

with the average velocity  $u_0$  given by Eq. (2.6). By a Fourier transform of Eq. (5.4) we obtain the autocorrelation function for  $\Delta u$  as an exponential

$$R_{\Delta u}(\tau) = \frac{\sigma_\eta^2 (1 - u_0^2)^{3/2}}{16\alpha} e^{-\alpha|\tau|}. \quad (5.5)$$

Thus  $\Delta u(t)$  is a normal process with zero mean and standard deviation<sup>18</sup>

$$\sigma_{\Delta u} = \frac{\sigma_\eta (1 - u_0^2)^{3/4}}{4\alpha^{1/2}}. \quad (5.6)$$

Defining the period of a fluxon revolution according to Eq. (4.6) we calculate the average frequency fluctuation as the average of the instantaneous frequency fluctuation  $\Delta u/l$  over one average period of revolution

$$\Delta f = \frac{1}{\langle T \rangle} \int_{t_0}^{t_0 + \langle T \rangle} \Delta u / l dt. \quad (5.7)$$

From Eq. (5.7) it follows that  $\Delta f$  has a normal distribution with zero mean and the standard deviation,<sup>19</sup>

$$\sigma_{\Delta f} = \frac{1}{l} \sigma_{\Delta u} \left[ \frac{2u_0}{\alpha l} \left[ 1 - u_0 \frac{1 - \exp(-\alpha l/u_0)}{\alpha l} \right] \right]^{1/2}. \quad (5.8)$$

A numerical simulation with  $\sigma_\eta = 8.8 \times 10^{-4}$  is seen in Fig. 9 showing a typical frequency distribution of  $\Delta f$  about the fundamental frequency  $f_0 = u_0/l$ . The connection between the standard deviation and the half-power linewidth is

$$\Delta f_{1/2} = \sqrt{8 \ln 2} \sigma_{\Delta f} \quad (5.9)$$

when  $\Delta f$  is normal distributed.

Figures 10 and 11 show a comparison of the standard deviation predicted by this model Eq. (5.8) and the results

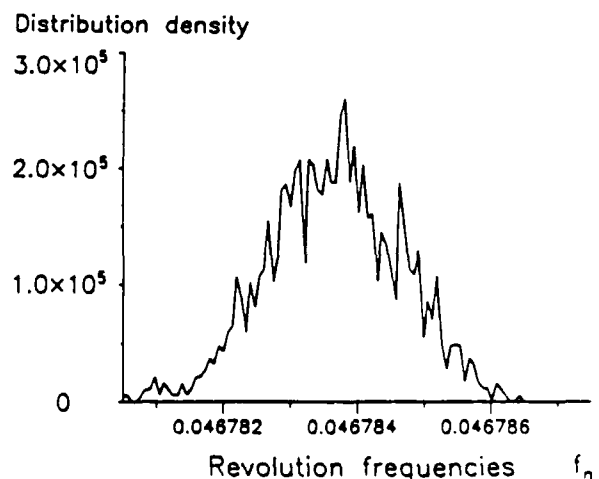


FIG. 9. Distribution of revolution frequency  $f_n$ . Numerical simulation with Gaussian noise drive:  $\alpha=0.01$ ,  $\gamma=0.034$ ,  $\sigma_\eta=8.8 \times 10^{-4}$ , and  $l=20$ .

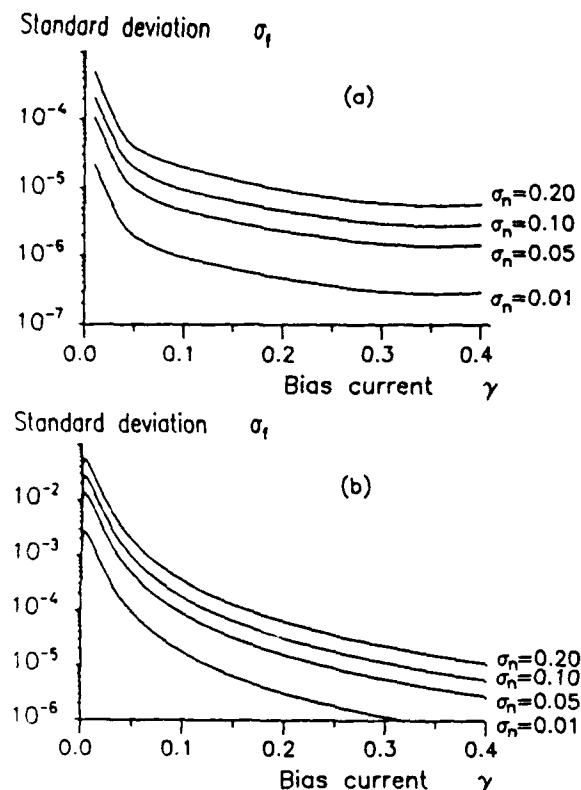


FIG. 10. Standard deviation of revolution frequency  $\sigma_f$  for white Gaussian noise drive as a function of bias current  $\gamma$ , for  $\alpha=0.01$ ,  $l=8$ , and  $\sigma_n=0.01, 0.05, 0.10$ , and  $0.20$ . (a) Numerical simulation. (b) Hamiltonian perturbation theory.

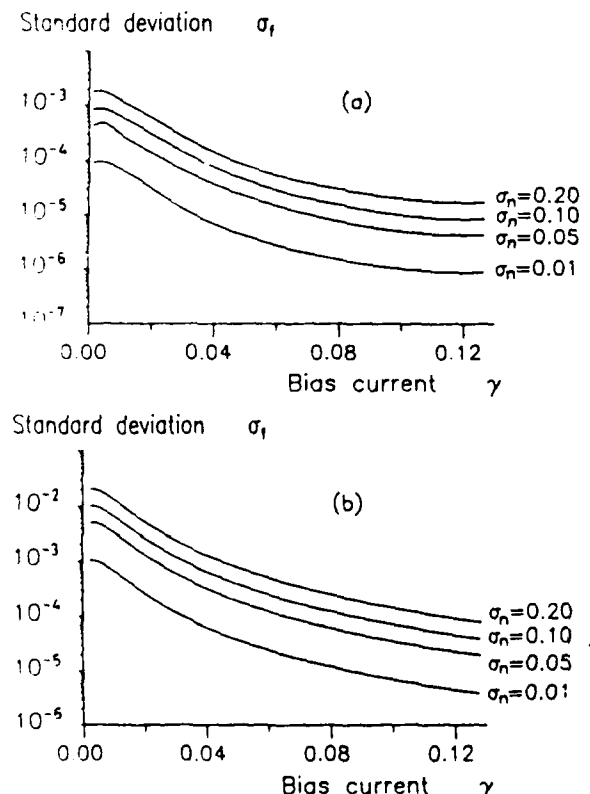


FIG. 11. Standard deviation of the revolution frequency  $\sigma_f$  for white Gaussian noise drive as a function of bias current  $\gamma$ , for  $\alpha=0.01$ ,  $l=20$ , and  $\sigma_n=0.01, 0.05, 0.10$ , and  $0.20$ . (a) Numerical simulation. (b) Hamiltonian perturbation theory.

from the numerical simulations for the lengths  $l=8$  and  $l=20$ , respectively. As can be seen, the model is able to predict the right qualitative dependence on the length, the noise amplitude, and the bias, but the model predicts an overall standard deviation that is about a factor of 10 too large. The reason for this discrepancy is at present not known.

In closing, we note that for  $\gamma$  values near 0.3 it was found necessary to augment the time resolution (by reducing  $\Delta t$ ) to avoid spurious peaks in Fig. 10(a). The existence of such spurious peaks might be an indicator of the onset of chaotic behavior at nearby points in parameter space. In fact, parameter values  $\gamma=0.3$  with  $\alpha=0.01$  lead to chaotic creation of fluxon-antifluxon pairs in the study reported by Eilbeck *et al.*<sup>20</sup>

## VI. COMPARISON WITH EXPERIMENTS

The rapidly decreasing linewidth with increasing bias shown in Figs. 10 and 11 is in qualitative agreement with the experimental observations of Fig. 1 in Ref. 10.

To compare quantitatively the calculated results with these experiments we use in Eq. (5.2) data reported by Scott *et al.*<sup>5</sup> For the junction No. N25L, assuming a temperature of 4 K, Eq. (5.2) gives  $\sigma_f=0.0052$ . Noting from Fig. 9(a) that  $\sigma_f$  scales linearly with  $\sigma_n$ , we calculate from Eq. (5.9) a normalized half-power linewidth  $\Delta f_{1/2}=5.5 \times 10^{-7}$  at  $\gamma=0.2$ . Taking as the normalized resonance frequency  $f_0=u_0/l \approx 0.125$  we calculate a relative linewidth  $\Delta f_{1/2}/f_0=4.4 \times 10^{-6}$ . The physical resonance frequency for junction No. N25L was 2.3 GHz.<sup>5</sup> This yields a physical linewidth of 10 kHz. Comparing with the experimental results shown in Fig. 1 of Ref. 10 and noting that  $\gamma=0.2$  corresponds to a bias point near the bottom of the zero-field step, we find excellent agreement. The same calculations for junction No. N53C,<sup>5</sup> again for  $T=4$  K and  $\gamma=0.2$ , yield  $\Delta f_{1/2}/f_0=2.3 \times 10^{-6}$ . The physical resonance frequency for junction No. N53C was 8.3 GHz, which leads to a physical linewidth of 18 kHz, once again in excellent agreement with experimental results.

## VII. CONCLUSIONS

Computational studies of the linewidth of the radiation emitted by Josephson junctions require extremely high resolution. For this reason we developed a pseudospectral method for solving the nonlinear dynamical equation describing a circular Josephson junction oscillator. Because the algorithm makes heavy use of fast Fourier transforms it was implemented on a CRAY-I vector processor. Driving terms corresponding to physically realistic situations, i.e., sinusoidal microwave irradiation and internal thermal noise, were considered. In the second case the computational results were compared with experimental results reported in the literature, and excellent qualitative and quantitative agreement was found. In addition, in both cases we have compared the computational results with approximate analytic results based on perturbation theory. Here the agreement was qualitatively good, but quantitative discrepancies were found, indicating a need for further development of perturbation theory.

## ACKNOWLEDGMENTS

It is our pleasure to thank Alwyn C. Scott for proposing this work and for his continued interest in it. We acknowledge Niels F. Pedersen for helpful discussions on modeling of thermal noise in Josephson junctions and Mogens Samuelsen for pointing out the significance of

Ref. 15 in the context of the present work. The financial support of the Danish Council for Scientific and Industrial Research and by the European Research Office of the United States Army (through Contract No. DAJA-37-82-C-0057) is gratefully acknowledged. R.D.P. thanks the Technical University of Denmark for providing support for part of the period during which this work was performed.

<sup>1</sup>Permanent address: Dipartimento di Fisica, Università di Salerno, 84100 Salerno, Italy.

<sup>2</sup>N. F. Pedersen, in *Advances in Superconductivity, NATO Advanced Study Institute Series, B100*, edited by B. Deaver and J. Ruvalds (Plenum, New York, 1982), p. 149.

<sup>3</sup>D. W. McLaughlin and A. C. Scott, *Phys. Rev. A* **18**, 1652 (1978).

<sup>4</sup>A. Davidson and N. F. Pedersen, *Appl. Phys. Lett.* **44**, 465 (1984).

<sup>5</sup>B. Dueholm, A. Davidson, C. C. Tsuei, M. J. Brady, K. H. Brown, A. C. Callegari, M. M. Chen, J. H. Greiner, H. C. Jones, K. K. Kim, A. W. Kleinsasser, H. A. Notarys, G. Proto, R. H. Wang, and T. Yogi, *Proceedings of the 17th International Conference on Low-Temperature Physics, Conference LT 17*, edited by U. Eckern, A. Schmid, W. Weber, and H. Wühl (North-Holland, Amsterdam, 1984), Part I, p. 691.

<sup>6</sup>A. C. Scott, F. Y. F. Chu, and S. A. Reible, *J. Appl. Phys.* **47**, 3272 (1976).

<sup>7</sup>J. C. Eilbeck, P. S. Lomdahl, O. H. Olsen, and M. R. Samuelson, *J. Appl. Phys.* (to be published).

<sup>8</sup>R. D. Parmentier, in *Solitons in Action*, edited by K. Lonngren and A. C. Scott (Academic, New York, 1978), p. 173.

<sup>9</sup>P. F. Byrd and M. D. Friedman, *Handbook of Elliptic Integrals for Engineers and Physicists* (Springer, Berlin, 1954).

<sup>10</sup>F. If., M. P. Soerensen, and P. L. Christiansen, *Phys. Lett.* **100A**, 68 (1984).

<sup>11</sup>E. Joergensen, V. P. Koshelets, R. Monaco, J. Mygind, M. R. Samuelsen, and M. Salerno, *Phys. Rev. Lett.* **49**, 1093 (1982).

<sup>12</sup>D. Gottlieb and S. A. Orszag, *Numerical Analysis of Spectral Methods* (Society for Industrial and Applied Mathematics, Philadelphia, 1977).

<sup>13</sup>IMSL, Inc. (Houston, Texas) *International Mathematical and Statistical Library* (9th Ed.) routine FFT2C, 1982 (unpublished).

<sup>14</sup>CRAY-I Computer Systems, *Library Reference Manual SR0014* (Cray Research, Mendota Heights, 1982), pp. 4-49; see also CRAY Computer Systems Technical Note, Complex Fast Fourier Transform Binary Radix Subroutine (CFFT2) SN0203 (Cray Research, Mendota Heights, 1983).

<sup>15</sup>CRAY-I Computer Systems, *Library Reference Manual SR0014* (Cray Research, Mendota Heights, 1982), pp. 4-9.

<sup>16</sup>O. A. Levring, M. R. Samuelsen, and O. H. Olsen, *Physica* **11D**, 349 (1984).

<sup>17</sup>A. H. Nayfeh and D. T. Mook, *Nonlinear Oscillations* (Wiley, New York, 1979), p. 161.

<sup>18</sup>M. Büttiker and R. Landauer, *Phys. Rev. A* **23**, 1397 (1981).

<sup>19</sup>A. Papoulis, *Probability, Random Variables, and Stochastic Processes* (McGraw-Hill, New York, 1965), p. 519.

<sup>20</sup>A. Papoulis, *Probability, Random Variables, and Stochastic Processes* (Ref. 18), p. 324.

<sup>21</sup>J. C. Eilbeck, P. S. Lomdahl, and A. C. Newell, *Phys. Lett.* **87A**, 1 (1981).

## A MECHANICAL ANALOG FOR THE DOUBLE SINE-GORDON EQUATION

Mario SALERNO†

*Center for Nonlinear Studies, Los Alamos National Laboratory, Los Alamos, NM 87545, USA*

Received 21 January 1985

A mechanical analog for the double sine-Gordon equation is proposed and used to analyze solitary solutions for arbitrary parameter values. The extension of this analog to other equations of the multiple sine-Gordon class is also considered.

### 1. Introduction

The sine-Gordon equation (SGE) has received much attention during the past years in connection with a remarkable variety of problems of physical interest [1]. In condensed matter physics the SGE has been used to model one dimensional chains of atoms on a periodic substrate potential. In this context, however, while the regular structure of such chains makes it natural to consider periodic potentials, there is no obvious reason for restricting these to single sinusoids. This fact has led to an increasing interest in constructing modified sine-Gordon equations with periodic but not sinusoidal potentials [2]. One way of doing this is by including in the substrate potential Fourier components higher than the sine-Gordon one, this leading to the so called "multiple sine-Gordon" equations [3]:

$$\phi_{xx} - \phi_{yy} + \sum_{i=1}^N \frac{\lambda_i}{i} \sin(\phi/i) = 0. \quad (1)$$

Among these equations a relevant role is played by the double sine-Gordon equation (DSGE) ( $N = 2$  in eq. (1)):

$$\phi_{xx} - \phi_{yy} + \lambda_1 \sin \phi + \frac{\lambda_2}{2} \sin(\phi/2) = 0, \quad (2)$$

†Dipartimento di Fisica Teorica e sue Metodologie per le Scienze Applicate, Università di Salerno, 84100 Salerno, Italy.

which just represents the first step toward a model for linear chains of atoms on generic substrate periodic potentials. Eq. (2) is also connected with several interesting physical phenomena, such as spin dynamics in the B phase of superfluid  $^3\text{He}$  [4], propagation of resonant ultrashort optical pulses through degenerate media [5], nonlinear excitations in a compressible chain of  $xy$  dipoles under conditions of piezoelectric coupling [6], ferromagnetic chains [7], organic conductors [8, 9], etc.

Since the DSGE is not integrable (the only integrable equation of family (1) is the SGE), it has been investigated numerically by several authors for particular values of parameters  $\lambda_1, \lambda_2$  [9, 10]. Depending on these values, different typical solitary wave solutions were found. A complete numerical investigation of the dynamical properties of eq. (2) with  $\lambda_1, \lambda_2$  varying in the range  $(-\infty, +\infty)$  is, however, still lacking [11]. Furthermore, in spite of their physical relevance, very little exists in the literature on equations of type (1) for  $N > 2$ .

In the present paper we propose a mechanical analog for the DSGE which easily extends to all the equations of type (1). The first mechanical analog for a soliton equation was given by Scott in 1969 for the SGE [12]. More recently, Cirillo et al. have constructed a more sophisticated SGE analog, and used it to solve practical problems in the Josephson effect area [13]. The mechanical analog

proposed here is a natural extension of Cirillo's one to the case of eqs. (1). The aim of this paper is to give a simple and unified picture of some of the properties of equations of type (1), by visualizing them on this mechanical analog. The paper is organized as follows: we describe the details of the mechanical analog for the DSGE, and indicate how dynamical equations arise. Next we consider solitary wave solutions of (2) both in terms of the mechanical analog and by direct integration of the equation. A brief discussion on the extension of the model to equations of type (1), and perspectives of future studies will be given in the conclusions.

## 2. Experiment, model

The generic section of the mechanical transmission line for the DSGE is shown in fig. 1. It consists of the following elements: an aluminium disk A, a piece of solid rubber rod B, two pendula respectively of length  $l_1, l_2$  and mass  $m_1, m_2$ , and a gearing mechanism C to provide coupling between the two pendula. The aluminium disk and

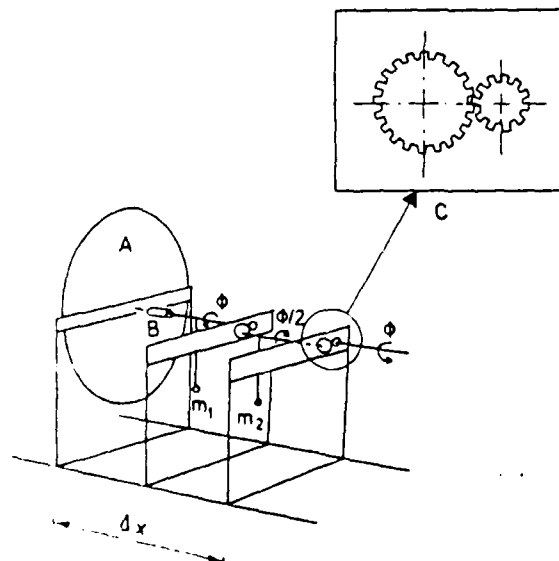


Fig. 1. A section of the mechanical line for the double sine-Gordon equation.

the two pendula are rigidly fixed to the axis of the transmission line. The rubber rod B provides the elastic coupling between the sections while the mechanism C is realized with a gear of ratio  $\frac{1}{2}$  and connected to the transmission line as in fig. 1. A practical realization of a segment of the line is shown in fig. 2. By assuming the dissipative effects on the line proportional to  $\phi_{i,i}$ , we have for the  $i$ th section the following difference differential equation:

$$\begin{aligned} I\phi_{i,i} + \alpha\phi_{i,i} &= k(\phi_{i+1} - 2\phi_i + \phi_{i-1}) \\ &- m_1 g l_1 \sin(\phi_i + \theta) \\ &- m_2 g l_2 \sin(\phi_i/2 + \psi). \end{aligned} \quad (3)$$

Here  $I$  denotes the moment of inertia,  $\alpha$  the damping constant,  $k$  the torque constant of the rubber rod, and  $m_1 g l_1, m_2 g l_2$  the gravitational restoring torques of the pendula per section of the line,  $\theta$  and  $\psi$  are initial phase angles of the two pendula with respect to the vertical line, fixed when the gear wheels are assembled into the gearing mechanism C. (Since the two pendula are rigidly connected through the gearing mechanism C, the introduction of two phase angles appears redundant; however, it will be useful for later developments. Furthermore, we assume the mechanical line to have infinite length, so that we will not be concerned at the present with boundary conditions).

Taking the  $i$ th section to be of length  $\Delta x$ , eq. (3) is written as

$$\begin{aligned} (I/g)\phi_{i,i} - k(\Delta x^2/g)(\phi_{i+1} - 2\phi_i + \phi_{i-1})/\Delta x^2 \\ = -(\alpha/g)\phi_{i,i} - m_1 l_1 \sin(\phi_i + \theta) \\ - m_2 l_2 \sin(\phi_i/2 + \psi). \end{aligned} \quad (4)$$

When  $\alpha = 0$  (lossless case) eq. (4) may be obtained from the hamiltonian of the collection of pendula,

$$\begin{aligned} H = \sum_i \left\{ \frac{1}{2} \left[ (I/g)\phi_{i,i}^2 + (k\Delta x^2/g) \frac{(\phi_{i+1} - \phi_i)^2}{\Delta x} \right] \right. \\ \left. + v(\phi_i) \right\} \end{aligned} \quad (5)$$

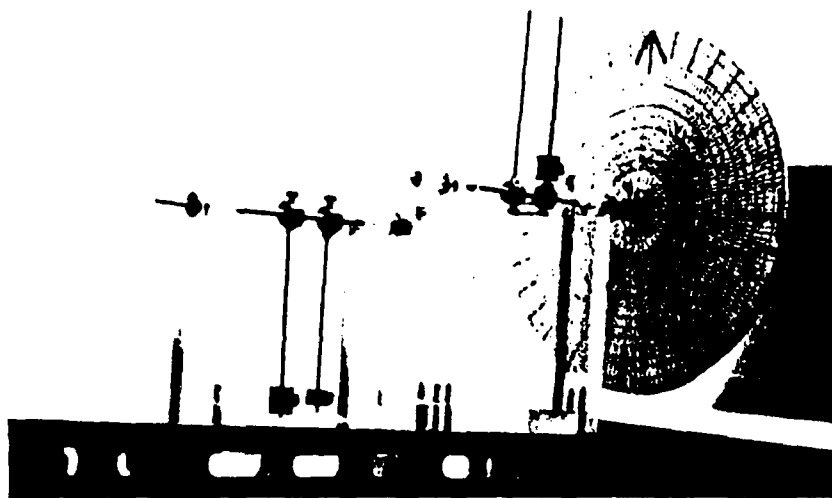


Fig. 2. A practical realization of a segment of the DSGE-line.

in the external potential

$$\begin{aligned} \epsilon(\phi_1) = & -[m_1 l_1 \cos(\phi_1 + \theta) \\ & + m_2 l_2 \cos(\phi_1/2 + \psi)]. \end{aligned} \quad (6)$$

Measuring distances in units of  $(k/g)^{1/2} \Delta x$  and time in units of  $(I/g)^{1/2}$ , eq. (4) reduces, in the limit  $\Delta x \rightarrow 0$ , to

$$\begin{aligned} \dot{\phi}_1 - \dot{\phi}_{11} = & -\gamma\phi_1 - \lambda_1 \sin\phi_1 - \lambda_2 \sin(\phi_1/2) \\ & - \lambda_3 \cos\phi_1 - \lambda_4 \cos(\phi_1/2), \end{aligned} \quad (7)$$

where  $\gamma = \alpha/g$  and

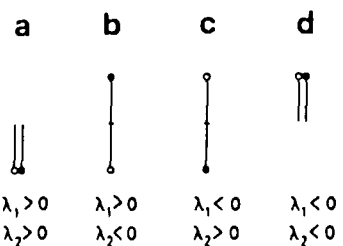
$$\begin{aligned} \lambda_1 &= m_1 l_1 \cos\theta, \quad \lambda_2 = m_2 l_2 \cos\psi, \\ \lambda_3 &= (m_1^2 l_1^2 - \lambda_1^2)^{1/2}, \quad \lambda_4 = (m_2^2 l_2^2 - \lambda_2^2)^{1/2}. \end{aligned} \quad (8)$$

When  $\alpha = 0$  and  $\theta = 0 \pmod{\pi}$ ,  $\psi = 0 \pmod{\pi}$ , eq. (7) is recognized as the DSGE with  $|\lambda_1| = m_1 l_1$ ,  $|\lambda_2| = m_2 l_2$ . From eqs. (7)–(8) it is seen that a definite choice of the initial phase angles  $\theta, \psi$  of the pendula fixes the relative signs of  $\lambda_1$  and  $\lambda_2$ . This fixes the zero points of the mechanical line (i.e., the points from which to measure angles) for any particular combination of the signs of  $\lambda_1, \lambda_2$  in eq. (2) as follows. For  $\lambda_1 > 0, \lambda_2 > 0$  we have

$\theta = 0, \psi = 0$  in eq. (8), and a zero point line as shown in fig. 3a. (The white pendulum denotes the one with mass  $m_1$ , while the black denotes the one with mass  $m_2$ .)

In similar way it is seen that the cases  $\lambda_1 > 0, \lambda_2 < 0$ ;  $\lambda_1 < 0, \lambda_2 > 0$ ;  $\lambda_1 < 0, \lambda_2 < 0$ ; in eq. (2) are respectively obtained by letting  $\theta = 0, \psi = \pi$ ;  $\theta = \pi, \psi = 0$ ;  $\theta = \pi, \psi = \pi$  in eqs. (7), (8), this corresponding on the mechanical line to having fixed the zero points respectively as in figs. 3b, 3c, 3d.

It is worth noting, however, that the model presented (i.e., eq. (7)) is more general than the DSGE, having the possibility of freely fixing the initial relative phase angles  $(\theta - \psi)$  of the pendula by properly assembling the gear mechanism C.

Fig. 3. Zero point lines for different values of  $\lambda_1, \lambda_2$ .

### 3. Behavior of the potential energy and solutions of DSGE

Being in general possible to think of the motion of a kink of eq. (2) as the motion of a classical particle in a reversed potential  $-v(\phi)$

$$v(\phi) = \lambda_1 \cos \phi + \lambda_2 \cos(\phi/2) \quad (9)$$

it is useful to consider how the potential energy of the pendula varies as  $\lambda_1, \lambda_2 \geq 0$ . Let us start by analyzing first the cases  $\lambda_1 > 0, \lambda_2 > 0$  and  $\lambda_1 < 0, \lambda_2 > 0$ . For  $\lambda_1 > 0, \lambda_2 > 0$  one knows from the previous discussion that the zero point line is with both pendula down as in fig. 3a. This corresponds to an absolute minimum of the potential energy. Starting from  $\phi = 0$  and letting the white pendulum move by  $2\pi$ , one reaches the configuration in fig. 3b. It is easily verified that this is a stable equilibrium configuration if the ratio of the gravitational torques of the black and white pendula is  $< 4$ , i.e. if  $\lambda_2 < 4\lambda_1$ ; otherwise it is unstable. For  $\lambda_2 < 4\lambda_1$  in fact, the potential energy is found to have absolute minima at  $\phi = 0 \pmod{4\pi}$ , relative minima at  $\phi = 2\pi \pmod{4\pi}$  and absolute maxima at  $\phi = \pm\delta \pmod{4\pi}$  where  $\delta = 2\cos^{-1}(\lambda_2/4\lambda_1) + 2\pi$ ; while for  $\lambda_2 \geq 4\lambda_1$  the relative minima at  $\phi = 2\pi \pmod{4\pi}$  become absolute maxima (see fig. 4). A qualitatively different behavior is obtained when  $\lambda_1 < 0, \lambda_2 > 0$ . In this case, the zero

point line is fixed as in fig. 3c. This is a stable equilibrium position ( $\pmod{4\pi}$ ) if  $\lambda_2 \geq 4|\lambda_1|$  and unstable if  $\lambda_2 < 4|\lambda_1|$ . In this last case, however, two stable equilibrium positions are found at  $\phi = \pm\delta \pmod{4\pi}$  where  $\delta = 2\cos^{-1}(\lambda_2/4|\lambda_1|)$ . The potential energy for  $\lambda_2 \geq 4|\lambda_1|$  is found to have absolute minima at  $\phi = 0 \pmod{4\pi}$  and absolute maxima at  $\phi = 2\pi \pmod{4\pi}$ ; while for  $\lambda_2 < 4|\lambda_1|$  it has absolute minima at  $\phi = \pm\delta \pmod{4\pi}$ , absolute maxima at  $\phi = 2\pi \pmod{4\pi}$  and relative maxima at  $\phi = 0 \pmod{4\pi}$ .

The corresponding behavior of the potential energy for negative values of  $\lambda_2$  is obtained from the previous case ( $\lambda_2 > 0$ ) by letting  $\phi \rightarrow \phi \pm 2\pi$  in eq. (6). Fig. 4 summarizes the different typical behavior of the potential of the pendula as  $\lambda_1, \lambda_2 \in (-\infty, +\infty)$ . The lines  $\lambda_2 = \pm 4\lambda_1$  separate regions of the  $\lambda_1-\lambda_2$  plane in which the configurations of fig. 3b and 3c are stable or unstable according to the previous discussion. Of these eight regions, however, only four are physically significant since the other four are obtained simply by shifting the potential energy. We therefore will focus in the following only on regions A, B, C, D of fig. 4 (case  $\lambda_2 > 0$ ). From the behavior of the potential energy in these regions it is evident that  $4\pi$ -kink solutions of the DSGE are possible only for parameter values of  $\lambda_1, \lambda_2$  corresponding to regions A, B, C, of fig. 4. These solutions are easily seen on the analog. A  $4\pi$ -kink solution of eq. (2) corresponding to  $\lambda_1, \lambda_2 > 0$  is shown in fig. 5. We see that while the white pendulum moves around by  $4\pi$ , the black one accomplishes a  $2\pi$  turn, giving rise to a topologically stable  $4\pi$  jump. The difference between kinks of regions A and B can be seen on the analog as a more rapid variation of the gravitational torques around  $\phi = 0$ . For  $\lambda_1 < 0, \lambda_2 > 0$  with  $\lambda_2 \geq 4|\lambda_1|$   $4\pi$  jumps are still possible (see fig. 6), but in this case the starting and final configurations are the ones shown in fig. 3c. Again it is evident from the mechanical analog that these are topologically stable solutions. In spite of the different shape  $4\pi$ -kink solutions assume on the mechanical line (see figs. 5, 6) for parameter values characterizing regions A, B, C of fig. 4, it is worth

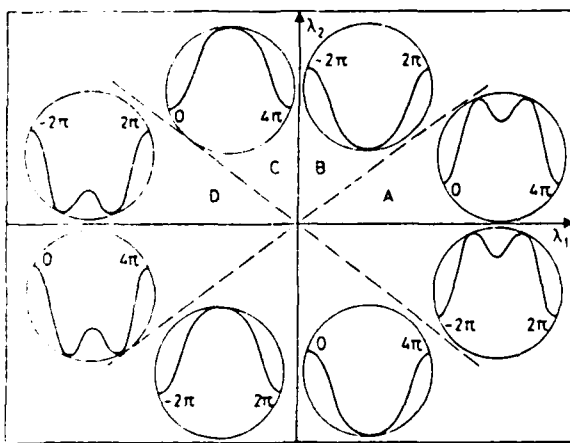


Fig. 4. Different behaviours of the potential of the pendula as  $\lambda_1, \lambda_2$  are varied in the range  $(-\infty, +\infty)$

$$\lambda_1 > 0, \lambda_2 > 0$$

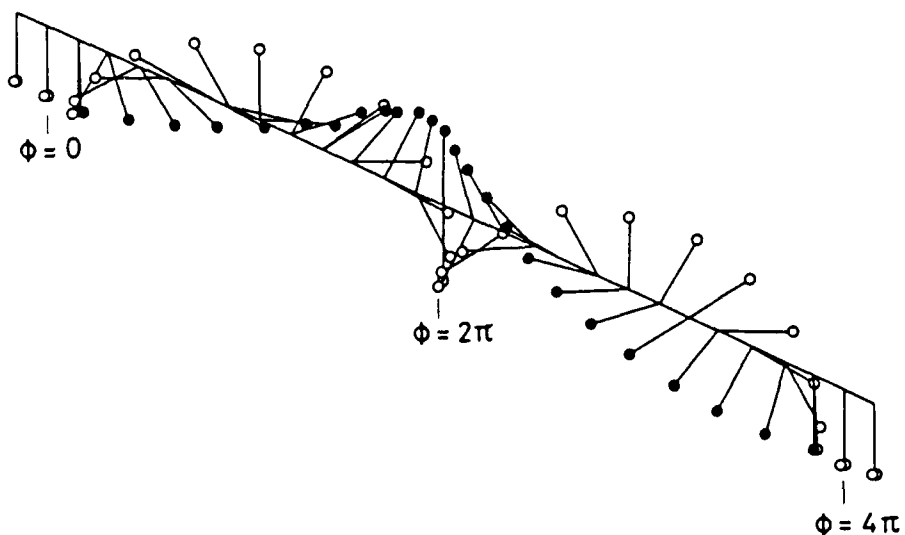


Fig. 5. A  $4\pi$ -kink of the DSGE on the mechanical line for  $\lambda_1 > 0, \lambda_2 > 0$ .

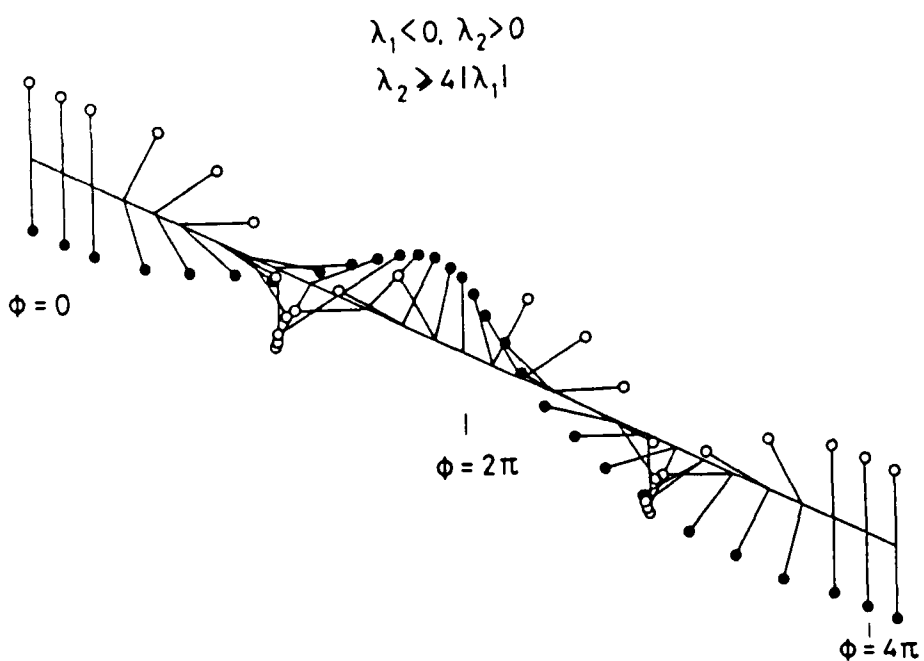


Fig. 6. A  $4\pi$ -kink of the DSGE on the mechanical line for  $\lambda_1 < 0, \lambda_2 > 0, \lambda_2 \geq 4|\lambda_1|$ .

noting that the change of the gravitational torques of the pendula in configurations of fig. 5 and fig. 6 is the same. In region D of fig. 4, two different types of kinks are possible: a small  $2\delta$ -jump and a big  $4\pi-2\delta$  one with  $\delta < \pi$ . The first type corresponds on the analog to a transition between the two stable equilibrium configurations at  $\phi = \pm \delta$  in which the black pendula pass under the line (see fig. 7), while the second type corresponds to the transition  $\delta \rightarrow 4\pi-\delta$  in which the black pendulum pass over the line (see fig. 8). Of these mechanical analog solutions one can easily find the corresponding analytical ones. To this end we look for

$$\begin{aligned}\lambda_1 &< 0, \lambda_2 > 0 \\ \lambda_2 &< 4|\lambda_1|\end{aligned}$$

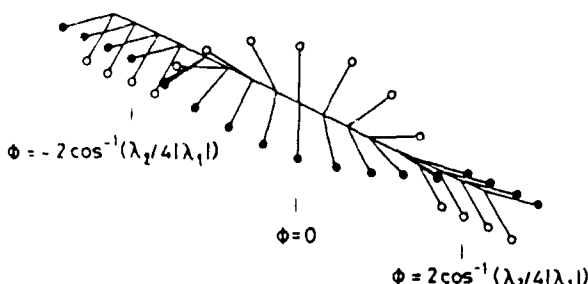


Fig. 7. A  $2\delta$ -kink,  $\delta = 2 \cos^{-1}(\lambda_2/4|\lambda_1|)$ ;  $\lambda_1 < 0, \lambda_2 > 0$ ;  $\lambda_2 < 4|\lambda_1|$

solitary wave solutions of eq. (2), i.e. solutions of the form

$$\phi(x, t) = \phi(\xi), \quad (10)$$

with  $\xi = (x - vt)/\sqrt{1 - v^2}$ ,  $v \in (-1, 1)$  and  $\phi$  satisfying the boundary conditions  $\lim_{\xi \rightarrow \pm\infty} \phi(\xi) = \phi_{\pm}$  ( $\phi_{\pm}$  are constants). By inserting ansatz (10) in eq. (2) and multiplying both sides by  $d\phi/d\xi$  we obtain (after one integration in  $\xi$ )

$$\frac{1}{2} \left( \frac{d\phi}{d\xi} \right)^2 + U(\phi) = E, \quad (11)$$

where  $U(\phi) \equiv \lambda_1 \cos \phi + \lambda_2 \cos(\phi/2)$ , and  $E$  is a constant of integration. From eq. (11) one gets

$$\xi - \xi_0 = \int_{\phi_c}^{\phi} d\phi / \{ 2(E - \lambda_1 \cos \phi - \lambda_2 \cos(\phi/2)) \}^{1/2}, \quad (12)$$

which gives  $\xi$  as a function of  $\phi$ , i.e. eq. (12) actually determines the inverse function. It is interesting to note that eq. (12) is exactly solvable in terms of elliptic functions, just as the ordinary SGE. Furthermore, for specific values of  $E$  and  $\phi_c$ , it is possible to invert (12) in terms of elementary functions. To see this it is suitable to effect the

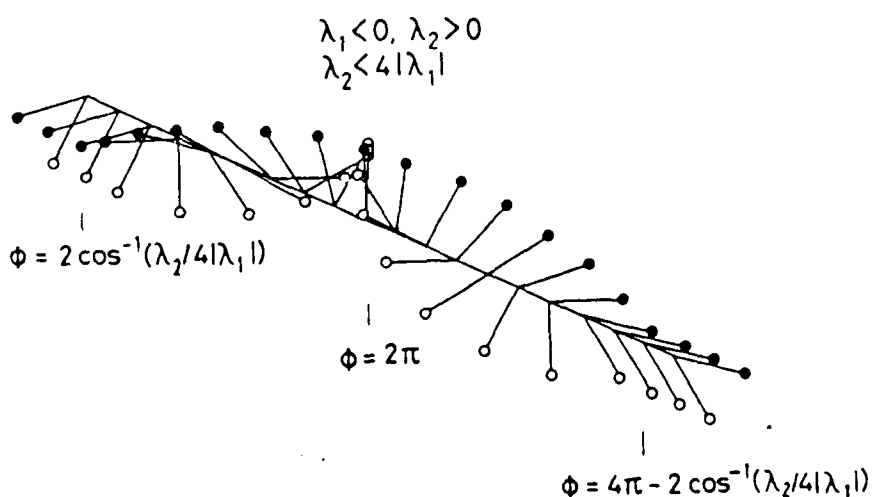


Fig. 8. A  $4\pi-2\delta$  kink for the same parameter values as in fig. 6.

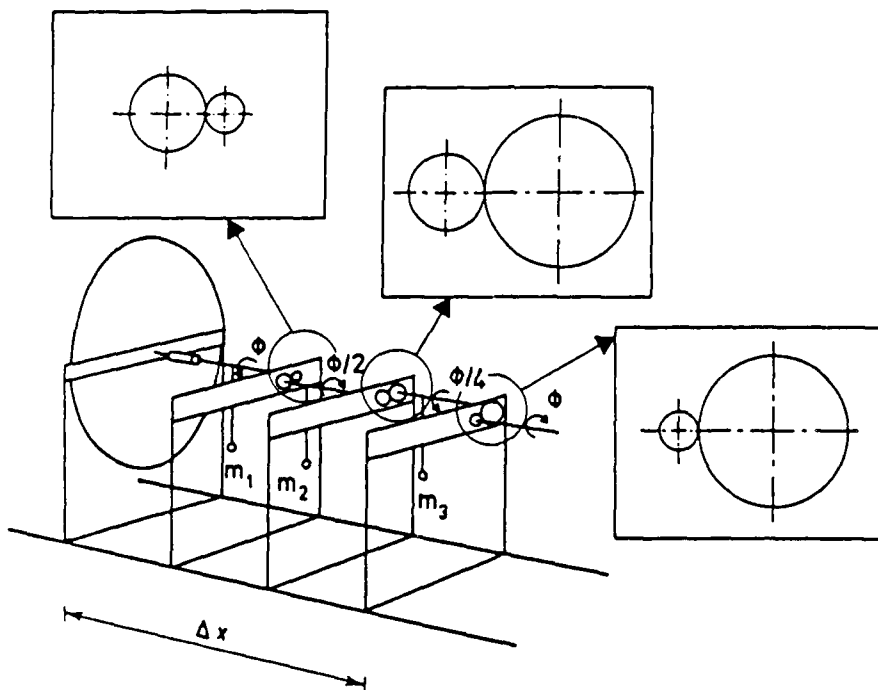


Fig. 9. A mechanical analog for the triple sine-Gordon equation [ $N = 3$  in eq. (1)] (for graphical convenience gears have been drawn as circles)

change of variable  $\phi = 2 \tan^{-1} t$  in eq. (12). The integral in (12) then becomes

$$4 \int_1^t dt / \sqrt{(\alpha t^4 + \beta t^2 + \gamma)}, \quad (13)$$

with  $\alpha = 2(E - \lambda_1 + \lambda_2)$ ,  $\beta = -2(E + \lambda_1)$ ,  $\gamma = 2(E - \lambda_1 - \lambda_2)$ , which is easily evaluated in terms of elliptic integrals of the first type (see ref. 14). By choosing  $\phi_- = 0$ ,  $\phi_+ = 4\pi$ ,  $\phi_c = (\phi_+ + \phi_-)/2$  and the constant  $E$  (energy) equal to  $-\lambda_1 - \lambda_2$  one finds from eq. (12) that

$$\begin{aligned} \phi = 4 \tan^{-1} & \left\{ (1 + 4|\lambda_1|/\lambda_2)^{1/2} \right. \\ & \times \sinh \left( \pm (|\lambda_1| + \lambda_2/4)(\xi - \xi_0) \right) + 2\pi \end{aligned} \quad (14)$$

(where the assumption  $\lambda_2 > 0$ ,  $|\lambda_1|/\lambda_2 > -\frac{1}{4}$  were made). Eq. (14) represents a  $4\pi$ -kink solution of eq. (2) for parameter values  $\lambda_1, \lambda_2$  such that  $\lambda_2 > 0$ ,  $|\lambda_1|/\lambda_2 > -\frac{1}{4}$  which correspond the mechanical analog solutions shown in figs. 5-6. Similarly

the choice  $E = (\lambda_2^2 - 4|\lambda_1|\lambda_2^2 - |\lambda_1|^2)/4|\lambda_1|$  and  $\phi_{\pm} = \pm 2 \cos^{-1}(\lambda_2/4|\lambda_1|)$  in eqs. 12-13 leads to the function

$$\begin{aligned} \phi = 4 \tan^{-1} & \left\{ \sqrt{(4|\lambda_1| - |\lambda_2|)/(4|\lambda_1| + |\lambda_2|)} \right. \\ & \times \tanh \left( \pm \rho (\xi - \xi_0) \right), \end{aligned} \quad (15)$$

while the choice  $E = (\lambda_2^2 - 2|\lambda_1|\lambda_2^2 - |\lambda_1|^2)/4|\lambda_1|$  and  $\phi_{\pm} = \pm 2 \cos^{-1}(\lambda_2/4|\lambda_1|) \pm 2\pi$  gives

$$\begin{aligned} \phi = 4 \tan^{-1} & \left\{ \sqrt{(4|\lambda_1| + |\lambda_2|)/(4|\lambda_1| - |\lambda_2|)} \right. \\ & \times \tanh \left( \pm \rho (\xi - \xi_0) \right), \end{aligned} \quad (16)$$

with  $\rho = ((16|\lambda_1|^2 - |\lambda_2|^2)/64\lambda_1)^{1/2}$ . As it is easily verified, eq. (15) represents a  $2\delta$ -kink corresponding on the mechanical line to fig. 7, while eq. (16) is the  $4\pi-2\delta$  kink of fig. 8. Thus for parameter values characterizing regions A, B, C, of fig. 4 an analytical solution of the DSGE is given by (14), while in region D two analytical solutions exist

(respectively given by eqs. (15)–(16)), all in agreement with our previous discussion. Furthermore it is not difficult to verify that (14)–(15)–(16) are stable and have finite energy (as indicated by the mechanical model). Solutions similar to these were also derived by other authors for lightly modified versions of eq. (2) (see ref. 9 and 15). We remark finally that it appears evident both from the mechanical model and by direct computations that the corresponding solutions of (14), (15), (16) for negative values of  $\lambda_2$ , are simply obtained from the previous case ( $\lambda_2 > 0$ ) by adding  $\pm 2\pi$ .

#### 4. Conclusion

In this paper a simple mechanical analog for the DSGE was presented and used to analyze solitary wave solutions for arbitrary parameter values. The way in which the analog is constructed makes it a tool to investigate a large number of equations of type (1). Indeed, by changing gear ratio's, and by including more gearing mechanisms (see fig. 9), one easily gets models for these equations. A concrete use of the analog to investigate inelastic scattering between the various kinds of kink solutions of these systems will be the matter of later works.

#### Acknowledgements

It is a pleasure to me to thank Professors S. DeFilippo, R.D. Parmentier, P. Sodano for helpful comments, and Dr. M. Cirillo for suggestions about the concrete realization of the analog.

This work was partially supported by the European Research Office of the United States

Army (Contract No. DAJA-37-82-C-0057) while the author was visiting the Laboratory of Applied Mathematics of the Technical University of Denmark, Lyngby.

#### References

- [1] For a variety of recent reviews see, for example, Solitons in Condensed Matter Physics, A.R. Bishop and T. Schneider, eds. (Springer, Berlin, 1978); Physics in one dimension, J. Bernasconi and T. Schneider, eds. (Springer, Berlin, 1981).
- [2] M. Remoissenet, and M. Peyrard, *J. Phys. C* 14 (1981) 1481. M. Peyrard and M. Remoissenet, *Phys. Rev. B* 26 (1982) 2886. M. Peyrard and D.K. Campbell, *Physica* 9D (1983) 33.
- [3] R.K. Bullough and P.J. Caudrey, in: Nonlinear Evolution Equations solvable by the Inverse Spectral Transform, F. Calogero, ed. (Pitman, London, 1978), p. 180.
- [4] K. Maki and P. Kumar, *Phys. Rev. B* 14 (1976) 118, 3290.
- [5] R.K. Dodd, R.K. Bullough and S. Duckworth, *J. Phys. A* 8 (1975) 164.
- [6] M. Remoissenet, *J. Phys. C* 14 (1981) 1335.
- [7] K.M. Leung, *Phys. Rev. B* 27 (1983) 2877; see also R. Pandit, C. Tannous and J.A. Krumhansl, *Phys. Rev. B* 28 (1983) 289.
- [8] M.J. Rice, in: Solitons and Condensed Matter Physics, A.R. Bishop and T. Schneider, eds. (Springer, Berlin, 1978), p. 246.
- [9] R.K. Bullough, P.J. Caudrey and M.H. Gibbs, in: Solitons, Springer Series in Topics in Current Physics, vol. 17, R.K. Bullough and P.J. Caudrey, eds. (Springer, Berlin, 1980), p. 107 and references therein.
- [10] O.H. Olsen and M.R. Samuelsen, *Phys. Lett.* 80 A (1980) 209; *Physica Scripta* 25 (1982) 882.
- [11] Work in progress by D.K. Campbell, M. Peyrard and P. Sodano, to appear (private communication).
- [12] A.C. Scott, *Am. J. Phys.* 37 (1969) 52.
- [13] M. Cirillo, R.D. Parmentier and B. Savo, *Physica* 3D (1981) 565.
- [14] See for example P.F. Byrd and M. Friedman, *Handbook of Elliptic Integrals* (Springer, Berlin, 1982).
- [15] C.A. Condat, R.A. Guyer and M.D. Miller, *Phys. Rev. B* 27 (1983) 473.

## Prediction of chaos in a Josephson junction by the Melnikov-function technique

M. Bartuccelli and P. L. Christiansen

*Laboratory of Applied Mathematical Physics, The Technical University of Denmark, DK-2800 Lyngby, Denmark*

N. F. Pedersen

*Physics Laboratory I, The Technical University of Denmark, DK-2800 Lyngby, Denmark*

M. P. Soerensen

*IBM Forschungslaboratorium Zürich, Säumerstrasse 4, CH-8803 Rüschlikon, Switzerland*

(Received 9 April 1985)

The Melnikov function for prediction of Smale horseshoe chaos is applied to the rf-driven Josephson junction. Linear and quadratic damping resistors are considered. In the latter case the analytic solution including damping and dc bias is used to obtain an improved threshold curve for the onset of chaos. The prediction is compared to new computational solutions. The Melnikov technique provides a good, but slightly low, estimate of the chaos threshold.

### I. INTRODUCTION

For some years the topic of chaos in the rf-current-biased Josephson junctions has attracted much interest. The first papers in that field were probably the qualitative work by Belykh *et al.*<sup>1</sup> and the numerical work by Huberman *et al.*<sup>2</sup> Since then a number of authors have made numerical calculations,<sup>3–6</sup> electronic simulations,<sup>7–12</sup> and to a limited extent experiments on real junctions.<sup>13–16</sup> One of the things that characterizes almost all this work is the lack of analytical methods to predict the onset of chaos. This situation was recently changed by the analytical works of Genchev *et al.*<sup>17</sup> and Salam and Sastry,<sup>18</sup> who used the method of Melnikov integrals<sup>18–21</sup> to predict regions in the parameter plane where chaos occurs. Their work is in some sense an extension of the early work in Ref. 1 on the shunted-junction model, and in the same spirit equations are derived for various regions of the same qualitative behavior. Together with the work of Kautz and Monaco<sup>3</sup> it is the first step towards an analytical prediction of chaos in the rf-driven Josephson junction.

In this paper we review the results of Salam and Sastry from the point of view of Josephson-junction applications. For a detailed mathematical treatment we refer to the original mathematical literature.<sup>18–21</sup> Further, we extend the method of Melnikov functions to predict chaos in a Josephson junction with quadratic damping. This latter model—unlike the model with a linear resistor—has the advantage that analytical solutions are known in the absence of an applied rf signal, and the method of Melnikov functions requires fewer assumptions. For both models the analytical predictions are compared with numerical simulations.

The paper is organized in the following way: Section II A discusses the application of the Melnikov method to a Josephson junction with a linear damping resistor. Section II B discusses the case of a Josephson junction with a quadratic quasiparticle  $I$ - $V$  curve. This model is interest-

ing for two reasons: (i) For high temperatures quadratic damping provides better agreement with experimentally measured  $I$ - $V$  curves than linear damping. (ii) A full analytical solution to the equation with quadratic damping is known. Consequently, the Melnikov technique for the case with an applied rf signal is more accurate than the corresponding case with linear damping. Finally, Sec. III contains our summary and conclusion.

### II. THE rf-DRIVEN JOSEPHSON JUNCTION

In the following we shall consider systems of ordinary differential equations of the form

$$\frac{d\mathbf{X}}{dt} = \mathbf{h}_0(\mathbf{X}) + \epsilon \mathbf{h}_1(\mathbf{X}, t, \epsilon), \quad (1)$$

where  $\mathbf{X} = (\phi, y)$ ,  $\mathbf{h}_0 = (f_0, g_0)$ , and  $\mathbf{h}_1 = (f_1, g_1)$ .

The analytical expression for the Melnikov function for systems of type (1) is<sup>21</sup>

$$M(t_0) = \int_{-\infty}^{+\infty} \mathbf{h}_0(\mathbf{X}_h(t - t_0)) \wedge \mathbf{h}_1(\mathbf{X}_h(t - t_0), t) \times \exp \left[ - \int_0^{t-t_0} \text{tr}[D_x \mathbf{h}_0(\mathbf{X}_h(s))] ds \right] dt, \quad (2)$$

where  $\mathbf{X}_h$  denotes the homoclinic orbit. Here the wedge product is defined by  $\mathbf{X} \wedge \mathbf{Y} = X_1 Y_2 - X_2 Y_1$  and  $D_x$  denotes the partial derivative with respect to  $X$ . It is important to notice that in order to apply formula (2) it is necessary to know the so-called homoclinic orbits<sup>21</sup> for the unperturbed system ( $\epsilon = 0$ ).

The Melnikov function is proportional to  $d(t_0)$ , which is the separation between the unstable orbit  $\mathbf{X}^u(t_0, t_0)$  and the stable one  $\mathbf{X}^s(t_0, t_0)$  (see Fig. 1). If  $M(t_0)$  has a simple zero and is independent of  $\epsilon$  as in (2), then the local stable and unstable manifolds intersect transversally. The presence of such intersecting orbits implies that the Poincaré map has the so-called Smale-horseshoe chaos.<sup>21</sup> A Smale horseshoe contains a countable set of unstable periodic or-

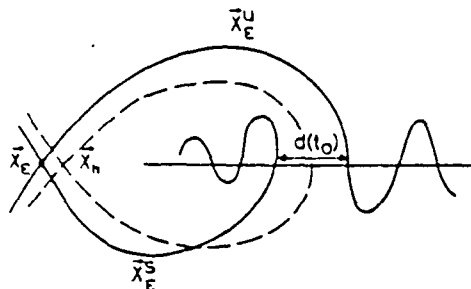


FIG. 1. Homoclinic orbit (dashed curve) and its perturbed curve (solid curve). Distance between trajectories,  $d(t_0)$ , is shown.

bits, an uncountable set of bounded nonperiodic orbits, and a dense orbit. It should be noticed that even though the Smale horseshoe is extremely complicated and contains an uncountable infinity of nonperiodic or chaotic orbits, it is not an attractor. However, it can exert a dramatic influence on the behavior of orbits which pass close to it. These orbits will display an extremely sensitive dependence upon initial conditions, and exhibit a chaotic transient before settling down to stable orbits of all periods which may constitute a strange attractor. Therefore the existence of the Smale horseshoe can be seen as the first step towards a possible chaotic behavior. Thus Melnikov's theory is expected to provide the lower boundary of the chaos threshold.

In the following we shall consider two different cases.

(i) Linear damping, which is the most commonly assumed case but for which an analytical solution to the unperturbed case (i.e., no applied rf signal) does not exist. Thus the conditions for the use of Melnikov's method are only approximately satisfied.

(ii) Quadratic damping, which in particular for high temperatures is a closer approximation to the  $I$ - $V$  curves in certain cases. This model has the important advantage that a full analytical solution in the absence of an applied rf signal is known.

#### A. The Josephson junction with linear damping

The equation for a current-driven Josephson junction may be written<sup>1-7</sup>

$$\begin{aligned}\dot{\phi} &= y, \\ \dot{y} &= -\sin\phi + \epsilon[\rho - \alpha y + \rho_1 \sin(\Omega t)].\end{aligned}\quad (3)$$

Here the overdot indicates derivative with respect to time,  $\alpha$  is the constant damping parameter,  $\rho$  is the normalized dc bias current,  $\rho_1$  is the normalized microwave current amplitude, and  $\Omega$  is the applied frequency normalized to the Josephson plasma frequency.  $\epsilon$  is a perturbative parameter that may eventually be set equal to 1, since in this case Melnikov's integral is  $\epsilon$  independent.

The unperturbed system ( $\epsilon=0$ ) is

$$\begin{aligned}\dot{\phi} &= y, \\ \dot{y} &= -\sin\phi.\end{aligned}\quad (4)$$

The heteroclinic orbits for the system [Eq. (4)] are given by

$$\begin{aligned}\phi_h(t-t_0) &= \pm 2 \tan^{-1} [\sinh(t-t_0)], \\ y_h(t-t_0) &= \pm 2 \operatorname{sech}(t-t_0).\end{aligned}\quad (5)$$

The Melnikov integral, Eq. (2), for the system (3) is

$$\begin{aligned}M(t_0) &= \int_{-\infty}^{+\infty} y_h(t-t_0)[\rho + \rho_1 \sin(\Omega t) - \alpha y_h(t-t_0)] dt \\ &= \rho \int_{-\infty}^{+\infty} y_h(t) dt + \left[ \rho_1 \int_{-\infty}^{+\infty} y_h(t) \cos(\Omega t) dt \right] \\ &\quad \times \sin(\Omega t_0) - \alpha \int_{-\infty}^{+\infty} y_h^2(t) dt.\end{aligned}\quad (6)$$

Performing the integrals of Eq. (6) with the heteroclinic orbits, Eq. (5), the following result is obtained:

$$M(t_0) = \pm 2\pi\rho - 8\alpha \pm 2\pi\rho_1 \operatorname{sech}(\pi\Omega/2) \sin(\Omega t_0). \quad (7)$$

Rearranging Eq. (7), we find a necessary condition for the intersection of the stable and unstable orbits to be<sup>17,18</sup>

$$|\pm\rho + 4\alpha/\pi| \cosh(\pi\Omega/2) \leq \rho_1. \quad (8)$$

According to the previous discussion, Eq. (8) is a necessary condition for the existence of a Smale horseshoe. [The sufficient condition requires the existence of simple zeros of  $M(t_0)$ .] The formula deviates<sup>22</sup> from results in Ref. 18 by the factor  $2/\Omega$ . The condition is given in terms of the four parameters of the problem:  $\rho$ ,  $\alpha$ ,  $\Omega$ , and  $\rho_1$ . Numerically chaos has been investigated<sup>2,4</sup> in the  $\Omega$ -versus- $\rho_1$  plane for fixed  $\alpha=0.2$  and  $\rho=0$ . Comparing in Fig. 2 the theory [Eq. (8)] and the simulations<sup>2,4</sup> for  $\alpha=0.2$ , we find that Eq. (8) predicts too low a threshold for chaos. Kautz and Monaco<sup>3</sup> speculate that intersections between stable and unstable manifolds exist everywhere above the line given by Eq. (8), but that the resulting chaotic orbit is unstable with respect to the zero-voltage state and thus not observed. The discrepancy may be illustrated by considering the case of small  $\Omega$ . For  $\Omega < \alpha$  the impedance of the capacitor is very large and the circuit may be considered almost as if it were at dc. For  $\rho=0$  the system is then well behaved at least up to  $\rho_1=1$  (shown as the dashed line in Fig. 2). The trajectory in the

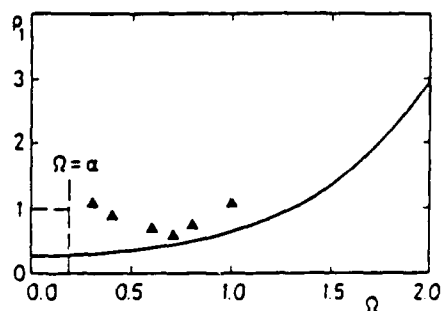


FIG. 2. Linear damping: threshold for chaos in parameter plane for  $\rho=0$ ,  $\alpha=0.2$ . Solid curve: Eq. (8). Triangles: numerical results from Ref. 4.

phase plane is an ellipse centered at the equilibrium point  $(0,0)$ . The voltage amplitude is approximately proportional to  $\rho_1\Omega/(1+\alpha^2\Omega^2)^{1/2}$ , which tends to zero as  $\Omega \rightarrow 0$ . For  $\Omega = \alpha$ , the impedance of the capacitor is the same as that of the resistor, and the capacitor can no longer be neglected.

For  $\alpha \neq 0$  very few systematic investigations exist, because the parameter space is four dimensional; however, Refs. 3, 5, and 6 contain numerical results, which can be compared with results obtained here. The structure of Eq. (8) is interesting and may be qualitatively understood from the following simple arguments. The lowest threshold of the applied rf current depends on the separation of the dc bias current from the quantity  $\rho_c = 4\alpha/\pi$ . From other investigations<sup>1</sup> it is known that  $\rho_c$  is the lowest bias current where rotating pendulum solutions exist; for this particular value of the bias current the trajectories for rotating and oscillating solutions of the pendulum equation get close to each other in the phase plane. Thus, for bias currents close to  $\rho_c$  a very small perturbation may shift the system from one orbit to the other, i.e., the threshold for the applied rf current is lowest.

We may summarize the findings for the case of the linear resistor by saying that numerically  $\rho$  should be within a band of magnitude  $\Delta\rho$  given by

$$\Delta\rho = \rho_1 \operatorname{sech}(\pi\Omega/2) \quad (9)$$

centered at  $\rho_c$  in order to obtain horseshoe chaos. Figure 3 shows this band in the  $\alpha$ -versus- $\rho$  plane.  $\rho_c = 4\alpha/\pi$  separates regions of qualitatively different behavior in the parameter plane of the unperturbed system. For  $\rho < \rho_c$  only oscillating solutions exist. For  $\rho_c < \rho < 1$  oscillating and rotating solutions exist, and for  $\rho > 1$  only rotating solutions exist. For large  $\alpha$ ,  $\rho_c$  is known to deviate from  $\rho_c = 4\alpha/\pi$  as shown in the figure. How the chaotic band develops for large  $\alpha$  is outside the scope of the present paper. Here we only notice that the chaotic band follows the linear portion of the  $\rho_c$  curve for low  $\alpha$ .

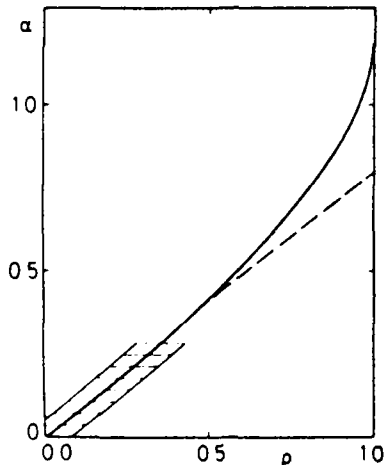


FIG. 3. Bifurcation diagram. Dashed curve:  $\rho_c = 4\alpha/\pi$ . Solid curve:  $\rho_c$  from numerical simulation. Crosshatched area: region of chaos.

### B. The Josephson junction with quadratic damping

If in the system (3) it is assumed that the resistance varies with the voltage such that  $R = \text{const}/V = (\hbar\gamma/2e)/V$ , one obtains,<sup>23</sup> with the same normalization as in the system (3),

$$\ddot{\phi} + k(\dot{\phi})^2 + \sin\phi = \rho + \rho_1 \sin(\Omega t), \quad (10)$$

where  $k = (\gamma C)^{-1}$ . Unlike the case with linear damping the exact analytical solution to Eq. (10) with  $\rho_1 = 0$  has been obtained.<sup>23</sup> Introducing  $y = \dot{\phi}$  one gets

$$\frac{dy^2}{d\phi} + 2ky^2 = 2\rho - 2\sin\phi \quad (11)$$

with the complete solution (assuming  $\rho > 0$ )

$$y^2 = \rho/k + 4/(1+4k^2)^{1/2} \cos(\phi + \beta) + C_1 \exp(-2k\phi), \quad (12)$$

where  $\tan\beta = 2k$  and  $C_1$  is an integration constant to be adjusted by the initial condition. Looking for the steady-state solution at finite voltages the transient term vanishes and Eq. (12) becomes

$$y^2 = y_0^2[\rho + \rho_0 \cos(\phi + \beta)], \quad (13)$$

where  $\rho_0 = 2k/(1+4k^2)^{1/2}$  and  $y_0 = k^{-1/2}$ . If the voltage  $\phi$  goes negative, the damping term in Eq. (10),  $k\dot{\phi}^2$ , should be replaced by  $k|\dot{\phi}|\dot{\phi}$ . However, the solution to the resulting equation for  $\phi < 0$  is obtained by a simple symmetry argument. We may note there that the parameter  $\rho_0$  has the same physical meaning as the parameter  $\rho_c$  defined for the linear resistor. Inserting  $y = \dot{\phi}$  and rearranging, we may express the solutions to Eq. (13) in terms of elliptic functions.<sup>24</sup> For  $\rho > \rho_0$  we get

$$(\phi + \beta)/2 = \operatorname{am}(u), \quad \frac{d\phi}{dt} = \dot{y} = y_0(\rho + \rho_0)^{1/2} \operatorname{dn}(u). \quad (14)$$

Here  $\operatorname{am}$  is the amplitude function and  $\operatorname{dn}$  is the Jacobian elliptic function of argument  $u = (y_0/2)(\rho + \rho_0)^{1/2}(t - t_0)$  and modulus  $m = 2/(1 + \rho/\rho_0)$ . The trajectory of the solution, Eq. (14), is shown in Fig. 4 for  $\rho = \rho_0$ , and for  $\rho$  slightly larger than  $\rho_0$ . To proceed we write Eq. (10) as the two-dimensional vector field,

$$\begin{aligned} \dot{\phi} &= y, \\ \dot{y} &= -\sin\phi - k\dot{\phi}^2 + \rho + \epsilon r_1 \sin(\Omega t). \end{aligned} \quad (15)$$

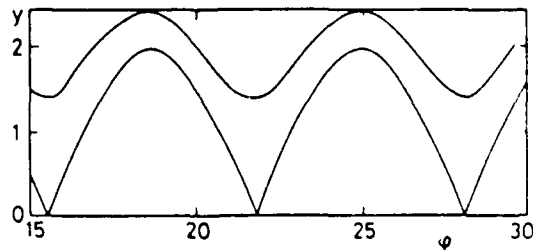


FIG. 4. Phase plane trajectories of Eq. (14) with  $k = 0.1$ . Upper curve:  $\rho = 0.2$ . Lower curve: heteroclinic orbit for  $\rho = \rho_0 = 0.196$ .

In the following we shall use the analytic solution, Eq. (14), to obtain the transverse intersections of the stable and unstable manifolds by finding the zeros of the Melnikov function. In order to do that it was noted in Sec. II that it is necessary to have a heteroclinic orbit for the unperturbed system ( $\epsilon=0$ ) connecting hyperbolic saddle points. So we must investigate the fixed points of Eq. (13) when  $\rho=\rho_0$ . The fixed points are situated on the  $\phi$  axis of the phase plane ( $\phi, y$ ). It is known<sup>19-21</sup> that the vector field  $(\dot{\phi}, \dot{y})$  should vanish at these points. This is found to be the case (i.e.,  $\dot{\phi}$  and  $\dot{y}$  are simultaneously zero) in Eq. (14) for  $\rho=\rho_0$ . Further, we shall show that the equilibrium points of the vector field  $(y, \dot{y})$  [Eq. (15) with  $\epsilon=0$ ] are of the center type at

$$(\bar{\phi}, \bar{y}) = (-\sin^{-1}(\rho) + 2n\pi, 0), \quad n = 0, \pm 1, \pm 2, \dots, \quad (16)$$

and of the saddle type at

$$(\bar{\phi}, \bar{y}) = (-\sin^{-1}(\rho) + (2n+1)\pi, 0), \quad n = 0, \pm 1, \pm 2, \dots. \quad (17)$$

We restrict the discussion to the equilibrium points in the interval

$$-\pi - \beta \leq \phi \leq \pi - \beta. \quad (18)$$

This means that we consider values of  $\rho$  such that  $\rho \leq 1$ . For  $\rho=\rho_0$  we find from Eq. (14) that  $m=1$ , and the limiting values of the elliptic functions are given by<sup>24</sup>

$$\text{dn}(u, 1) = \text{sech}(u) \quad \text{and} \quad \text{am}(u, 1) = \text{gd}(u), \quad (19)$$

where  $\text{gd}(u)$  denotes the Gudermannian function. In order to get more information on the behavior of the system about the point  $\rho=\rho_0$ , and in order to use the simple functions in Eq. (19), we rewrite Eq. (15) by adding a perturbation term  $\Delta\rho = \rho - \rho_0 = \epsilon(r - r_0)$  to obtain

$$\begin{aligned} \dot{\phi} &= y, \\ \dot{y} &= -\sin\phi - k(\dot{\phi})^2 + \rho_0 + \epsilon[r_1 \sin(\Omega t) + (r - r_0)]. \end{aligned} \quad (20)$$

For  $\epsilon=1$ , Eqs. (15) and (20) are identical. For  $\epsilon=0$  we obtain the following heteroclinic orbit by using Eq. (19):

$$[\phi_h(t), y_h(t)] = [4 \tan^{-1}[\exp(bt/2)], -\beta - \pi, b \operatorname{sech}(bt/2)], \quad (21)$$

where  $b = y_0(2\rho_0)^{1/2}$ . The Melnikov integral is then given by [Eq. (2)]

$$\begin{aligned} M(t_0) &= \int_{-\infty}^{\infty} b \operatorname{sech}[b(t-t_0)/2] [\rho - \rho_0 + \rho_1 \sin(\Omega t)] \\ &\quad \times \exp \left[ \int_0^{t-t_0} 2kb \operatorname{sech}(at'/2) dt' \right] dt. \end{aligned} \quad (22)$$

Evaluating Eq. (22), we find

$$\begin{aligned} M(t_0) &= (\rho - \rho_0) \sinh(2\pi k) / k \\ &\quad + \rho_1 b [F_1 \cos(\Omega t_0) + F_2 \sin(\Omega t_0)], \end{aligned} \quad (23)$$

where

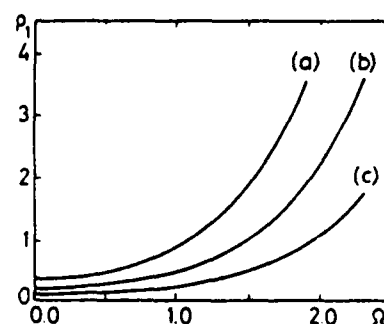


FIG. 5. Quadratic damping: Threshold for chaos in parameter plane [Eq. (24)]. (a)  $\rho=0, k=0.2$ ; (b)  $\rho=0, k=0.1$ ; and (c)  $\rho=0.1, k=0.1$ . Chaos above curves.

$$F_1 = \int_{-\infty}^{\infty} \operatorname{sech}(bt/2) \sin(\Omega t) \times \exp[4k \tan^{-1}[\sinh(bt/2)]] dt$$

and

$$F_2 = \int_{-\infty}^{\infty} \operatorname{sech}(bt/2) \cos(\Omega t) \times \exp[4k \tan^{-1}[\sinh(bt/2)]] dt.$$

It is easy to see that the integrals,  $F_1$  and  $F_2$ , are finite and not zero. It is also possible to see that transversal zeros for the Melnikov function, Eq. (23), exist. A necessary condition is

$$\rho_1 > (\rho - \rho_0) \sinh(2\pi k) / kb(F_1^2 + F_2^2)^{1/2}. \quad (24)$$

The prediction for the onset of horseshoe chaos, Eq. (24), is plotted in Fig. 5 as a function of  $\Omega$  for different values of parameters  $\rho$  and  $k$ . Note that the structure of Eq. (24) is similar to that of Eq. (8). In Eq. (24),  $\rho_0$  has the same significance as  $\rho_c = 4\alpha/\pi$  in Eq. (8), and the threshold rf current depends on the separation between  $\rho$  and  $\rho_0$ .

Alternatively, one might derive a condition for intersecting perturbed heteroclinic orbits by considering also the loss and bias terms as perturbations and use the heteroclinic orbit in Eq. (5) for insertion into the Melnikov function. The calculation proceeds in the same manner as for the linear resistor and the result is a thresh-

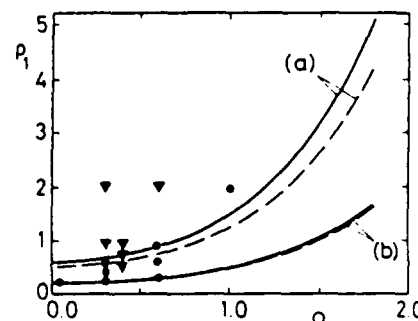


FIG. 6. Quadratic damping: Threshold for chaos in parameter plane for  $\rho=0$ . Solid curves: Eq. (25); dashed curves: Eq. (24). (a)  $k=0.3$ ; (b)  $k=0.1$ . Numerical results for  $k=0.1$ : Triangles, chaotic solutions; circles, periodic solutions.

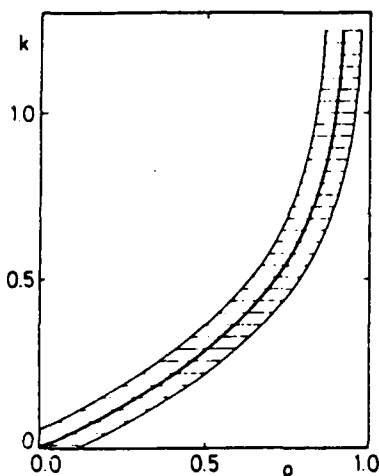


FIG. 7. Bifurcation diagram. Solid curve:  $\rho_0 = 2k(1+4k^2)^{1/2}$  as defined in Eq. (13). Crosshatched area: region of chaos.

old condition given by

$$\rho_1 \geq |\pm\rho + 2k| \cosh(\pi\Omega/2), \quad (25)$$

which is identical with Eq. (8), except that  $2k$  replaces  $4\alpha/\pi$ . For small values of the loss one should expect Eqs. (24) and (25) to give identical results. In fact, the expansion of Eq. (24) to first order in the damping constant  $k$  is identical with Eq. (25). Equation (24) may be considered a more precise condition since it is derived from the heteroclinic orbit to the unperturbed solution when both loss and bias are taken into account. Figure 6 shows a comparison between Eqs. (24) and (25) for  $k=0.3$ . A comparison between Eqs. (24) and (25) for  $k=0.1$  and some corresponding numerical simulations are also shown. We note that the Melnikov function gives too low a boundary for the onset of chaos as in Fig. 2. An equation similar to Eq. (24) cannot be derived for the case of linear damping, since the solution to the unperturbed system is not known at present.

For the case of a quadratic damping term it is possible to make a similar discussion as that in connection with

Fig. 3. Here, however, the analytic expression for the  $\rho_0$  curve is known [Eq. (13)]. For  $k \rightarrow \infty$  it approaches unity asymptotically. The band corresponding to chaos is given by

$$\Delta\rho = \rho_1 b k (F_1^2 + F_2^2)^{1/2} / \sinh(2\pi k), \quad (26)$$

which is shown crosshatched in Fig. 7.

### III. SUMMARY AND CONCLUSION

Chaos in the rf-driven Josephson junction was investigated analytically by means of the Melnikov-function technique. With a linear damping resistor only an approximate solution for the unperturbed phase plane trajectory could be used in the Melnikov integral. For the case of a quadratic damping term the analytic solution to the unperturbed case has been used, and an improved threshold curve for the onset of chaos has been obtained. For both cases, however, the Melnikov prediction gives a threshold somewhat lower than that found by direct computation. That is because the Smale horseshoe, whose existence in the Poincaré map is predicted by Melnikov's theory, is not an attractor; indeed the set of points asymptotic to it will have zero measure. Thus the existence of Smale horseshoe does not imply that typical trajectories will be asymptotically chaotic. In fact, in some cases we have transient chaos followed by asymptotically periodic motions. However, it may happen that some of the orbits constitute a strange attractor. Therefore the "presence" of the Smale horseshoe is the starting point over which a system can undertake some of the possible routes to chaos. Apparently the method seems to fail for low applied frequencies. Although the Melnikov technique seems to give a good estimate of the chaos threshold, further work is needed to obtain a detailed analytical criterion.

### ACKNOWLEDGMENTS

The financial support of the European Research Office of the United States Army (through Contract No. DAJA-37-82-C-0057) and the Consiglio Nazionale delle Ricerche (Italy) for one of the authors (M.B.) is gratefully acknowledged.

- 
- <sup>1</sup>V. N. Belykh, N. F. Pedersen, and O. H. Soerensen, Phys. Rev. B 16, 4853 (1977); 16, 4860 (1977).  
<sup>2</sup>B. A. Huberman, J. P. Crutchfield, and N. H. Packard, Appl. Phys. Lett. 37, 750 (1980).  
<sup>3</sup>R. L. Kautz and R. Monaco, J. Appl. Phys. 57, 875 (1985).  
<sup>4</sup>N. F. Pedersen and A. Davidson, Appl. Phys. Lett. 39, 830 (1981).  
<sup>5</sup>R. L. Kautz, IEEE Trans. Magn. MAG-19, 465 (1983).  
<sup>6</sup>Kazuo Sakai and Y. Yamaguchi, Phys. Rev. B 30, 1219 (1984).  
<sup>7</sup>I. Goldhirsch, Y. Imry, G. Wasserman, and E. Ben-Jacob, Phys. Rev. B 29, 1218 (1984).  
<sup>8</sup>D. D'Ippolitieri, M. R. Beasley, B. A. Huberman, and A. Libchaber, Phys. Rev. B 26, 3483 (1982).  
<sup>9</sup>M. Cirillo and N. F. Pedersen, Phys. Lett. 90A, 150 (1982).  
<sup>10</sup>H. Seifert, Phys. Lett. 98A, 213 (1983).  
<sup>11</sup>Da-Ren He, W. J. Yeh, and Y. K. Kao, Phys. Rev. B 30, 172 (1984).  
<sup>12</sup>V. K. Kornev and V. K. Semenov, IEEE Trans. Magn. MAG-19, 633 (1983).  
<sup>13</sup>V. N. Gubankov, K. I. Konstantinyan, V. P. Koshelets, and G. A. Ovsyannikov, IEEE Trans. Magn. MAG-19, 637 (1983).  
<sup>14</sup>R. F. Miracky and J. Clarke, Appl. Phys. Lett. 43, 508 (1983).  
<sup>15</sup>D. C. Cronemeyer, C. C. Chi, A. Davidson, and N. F. Pedersen, Phys. Rev. B 31, 2667 (1985).  
<sup>16</sup>M. Octavio, Phys. Rev. B 29, 1231 (1984); M. Octavio and C. Readi Nasser, *ibid.* 30, 1586 (1984).  
<sup>17</sup>Z. G. Genchev, Z. G. Ivanov, and B. N. Todorov, IEEE Trans. Circuits Syst. CAS-30, 633 (1983).  
<sup>18</sup>F. M. A. Salam and S. S. Sastry, *Chaos in Nonlinear Systems*,

- cal Systems*, edited by J. Chandra (Society For Industrial and Applied Mathematics, Philadelphia, 1984), p. 43.
- <sup>19</sup>V. K. Melnikov, Trans. Moscow Math. Soc. 12, 1 (1963).
- <sup>20</sup>V. I. Arnold, Sov. Math. Dokl. 5, 581 (1964).
- <sup>21</sup>J. Guckenheimer and P. J. Holmes, *Nonlinear Oscillation, Dynamical System, and Bifurcation of Vector Fields*, Vol. 42 of *Applied Mathematical Sciences* (Springer-Verlag, Berlin, 1983).
- <sup>22</sup>The authors have informed us that this error will be corrected in a later version [IEEE Trans. Circuits Syst. (to be published)].
- <sup>23</sup>N. F. Pedersen and K. Saermark, Physica 69, 572 (1973).
- <sup>24</sup>P. F. Byrd and M. D. Friedman, *Handbook of Elliptic Integrals for Engineers and Scientists* (Springer-Verlag, New York, 1971).

## PERTURBATION THEORY FOR RADIATION LINewidth IN CIRCULAR JOSEPHSON-JUNCTION OSCILLATORS

M. FORDSMAND, P.L. CHRISTIANSEN and F. IF

*Laboratory of Applied Mathematical Physics, The Technical University of Denmark, DK-2800 Lyngby, Denmark*

Received 16 January 1986; revised manuscript received 24 March 1986; accepted for publication 26 March 1986

The linewidth of the radiation from the Josephson ring oscillator under the influence of an external field is predicted by a new perturbation analysis which is an improvement of an earlier kink model. The linewidth is due to background oscillations rather than kink velocity fluctuations.

The Josephson-junction fluxon oscillator produces microwave radiation of very narrow linewidth. Recently, this property which is important for potential applications has been demonstrated experimentally [1] and by computational solution of the perturbed sine-Gordon equation using a pseudo Fourier spectral algorithm implemented on a CRAY-1-S vector processor [2].

In the latter reference a discrepancy between the computational results and the predictions of the kink model was found. In the present note<sup>#1</sup> an improved perturbation analysis is presented.

The circular Josephson tunnel junction of overlap geometry is modelled by the normalized perturbed sine-Gordon equation [3]

$$\phi_{xx} - \phi_{tt} - \sin \phi = \alpha \phi_t + \gamma + \eta_0 \sin \Omega t, \quad (1)$$

with periodic boundary conditions

$$\phi_x(0, t) = \phi_x(l, t), \quad \phi_t(0, t) = \phi_t(l, t), \quad (2)$$

where the  $\alpha$  term represents quasi-particle loss across the barrier, the  $\gamma$  term is the dc-bias current, and sinusoidal driving term models microwave irradiation (with amplitude  $\eta_0$  and frequency  $\Omega$ ) of the junction. The circumference of the circular transmission line, normalized to the Josephson length, is denoted  $l$ .

In ref. [2] eqs. (1), (2) were solved numerically

and the standard deviation in the frequency of electromagnetic radiation from the oscillator defined as  $\sigma_f = (\langle (f_n - \langle f_n \rangle)^2 \rangle)^{1/2}$  where  $f_n$  is the inverse of the  $n$ th fluxon revolution time,  $T_n$ , and brackets,  $\langle \rangle$ , denote the average over the revolutions, was computed in the single fluxon case (solid curve in fig. 1). Furthermore a kink model in ref. [2] based on the separation of the phase,  $\phi(x, t)$ , into a localized kink part and a background part,  $\phi(x, t) = \phi^k(x, t) + \phi^\infty(t)$ , and using momentum of the kink lead to the results shown as the dashed-dotted curve in fig. 1. The difference in scale between these computed and kink-model results motivated the present investigation.

As in ref. [2] we let  $\phi^k(x, t) = 2\pi H(x - x^k(t))$  where  $H$  is the unit step function and  $x^k(t)$  is the position of the kink at time  $t$  we get the differential equation for the background,  $\phi^\infty(t)$ ,

$$-\phi_{tt}^\infty - \sin \phi^\infty = \alpha \phi_t^\infty + \gamma + \eta_0 \sin \Omega t. \quad (3)$$

In ref. [2] the revolution time of the fluxon was defined by  $\langle \phi(x, t + T_n) - \phi(x, t) \rangle = 2\pi$  where brackets now denote a spatial average over the junction. Introducing the separation,  $\phi(x, t) = \phi^k(x, t) + \phi^\infty(t)$ , and  $\phi^k(x, t) = 2\pi H(x - x^k(t))$  into this definition, we obtain instead

$$\frac{2\pi}{l} \int_l^{l+T_n} u^k(t) dt + \phi^\infty(t + T_n) - \phi^\infty(t) = 2\pi, \quad (4)$$

<sup>#1</sup> Based on a master's thesis by one of the authors (M.F.).

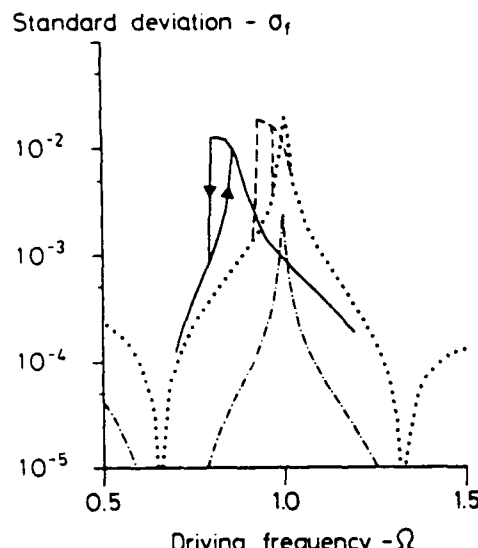


Fig. 1 Standard deviation of electromagnetic radiation versus driving frequency  $\Omega$ . Parameters  $\alpha = 0.01$ ,  $\gamma = 0.02$ ,  $\eta_0 = 0.01$ , and  $I = 8$ . Solid curve: Computational solution of eqs. (1), (2) [2]. Dashed-dotted curve: Kink model result from [2]. Dotted curve: New perturbative result using linearized version of eq. (3). Dashed curve: New perturbative result using the full eq. (1). Dotted and dashed curves overlap away from resonance region.

where the kink velocity  $u^k = dx^k/dt$ . In the kink model used in ref. [2] the background terms in (4),  $\phi^k(t + T_n) - \phi^k(t)$ , were neglected. However, numerical determination of the periodic solution of eq. (3) shows that the background part in (4) yields the dominant contribution to the fluctuation of the fluxon revolution frequency  $f_n$ . The fluctuations of  $u^k(t)$  around the power balance velocity [4],  $\bar{u}^k = [1 + (4\alpha/\gamma\pi)^2]^{-1/2}$ , turn out to be negligible. Linearizing eq. (3) around the ground state,  $\sin^{-1}\gamma$ , we obtain the dotted curve in fig. 1 exhibiting much better quantitative agreement with computer determination of the maximal value of the standard deviation than the kink model used

in ref. [2]. However, the maximum is shifted in frequency and hysteresis is missing. By solving the full nonlinear equation (3) numerically we obtain the dashed curve in fig. 1. As expected the resonance frequency is now closer to the value found in the computer experiment and a similar hysteresis phenomenon is observed. The perturbation theory predicts minima at  $\Omega = 0.65$  and  $\Omega = 0.35$  in fig. 1. At these frequencies the background frequency is a multiple of the revolution frequency of the kink. Computational data have not been obtained at these frequencies.

We conclude that the background oscillation provides the main contribution to the linewidth of the microwave radiation from the oscillator. Quantitative agreement between the prediction of non-linear perturbation theory and the computational results for the standard deviation (including the hysteresis) is found. However, the maximum standard deviation in the present perturbation theory occurs at a slightly higher frequency than in the numerical computation.

The financial support of the Danish Council of Scientific and Industrial Research and of the European Research Office of the United States Army (through contract No. DAJA-45-85-C-0042) is acknowledged.

## References

- [1] E. Joergensen, V.P. Koshelets, R. Monaco, J. Mygind, M.R. Samuelsen and M. Salerno, Phys. Rev. Lett. 49 (1982) 1093.
- [2] F. If, P.L. Christiansen, R.D. Parmentier, O. Skovgaard, and M.P. Soerensen, Phys. Rev. B 32 (1985) 1512.
- [3] A.C. Scott, F.Y.F. Chu and S. Reible, J. Appl. Phys. 47 (1976) 3272.
- [4] D.W. McLaughlin and A.C. Scott, Phys. Rev. A 18 (1978) 1652.

# PHYSICAL REVIEW B

## CONDENSED MATTER

---

Volume 33

Third Series

Number 1

---

1 JANUARY 1986

### Switching between dynamic states in intermediate-length Josephson junctions

S. Pagano, M. P. Sørensen, R. D. Parmentier, P. L. Christiansen, and O. Skovgaard  
Laboratory of Applied Mathematical Physics, The Technical University of Denmark, DK-2800 Lyngby, Denmark

J. Mygind, N. F. Pedersen, and M. R. Samuelsen  
Physics Laboratory I, The Technical University of Denmark, DK-2800 Lyngby, Denmark

174-182

Published by

THE AMERICAN PHYSICAL SOCIETY

through the  
AMERICAN INSTITUTE OF PHYSICS

## Switching between dynamic states in intermediate-length Josephson junctions

S. Pagano,\* M. P. Soerensen, R. D. Parmentier,\* P. L. Christiansen, and O. Skovgaard

*Laboratory of Applied Mathematical Physics, The Technical University of Denmark, DK-2800 Lyngby, Denmark*

J. Mygind, N. F. Pedersen, and M. R. Samuelsen

*Physics Laboratory I, The Technical University of Denmark, DK-2800 Lyngby, Denmark*

(Received 15 July 1985)

The appearance of zero-field steps (ZFS's) in the current-voltage characteristics of intermediate-length overlap-geometry Josephson tunnel junctions described by a perturbed sine-Gordon equation (PSGE) is associated with the growth of parametrically excited instabilities of the McCumber background curve (MCB). A linear stability analysis of a McCumber solution of the PSGE in the asymptotic linear region of the MCB and in the absence of magnetic field yields a Hill's equation which predicts how the number, locations, and widths of the instability regions depend on the junction parameters. A numerical integration of the PSGE in terms of truncated series of time-dependent Fourier spatial modes verifies that the parametrically excited instabilities of the MCB evolve into the fluxon oscillations characteristic of the ZFS's. An approximate analysis of the Fourier mode equations in the presence of a small magnetic field yields a field-dependent Hill's equation which predicts that the major effect of such a field is to reduce the widths of the instability regions. Experimental measurements on Nb-Nb<sub>x</sub>O<sub>y</sub>-Pb junctions of intermediate length, performed at different operating temperatures in order to vary the junction parameters and for various magnetic field values, verify the physical existence of switching from the MCB to the ZFS's. Good qualitative, and in many cases quantitative, agreement between analytic, numerical, and experimental results is obtained.

### I. INTRODUCTION

The appearance of zero-field steps (ZFS's) in the current-voltage ( $I-V$ ) characteristics of long Josephson junctions results from fluxons propagating along the junction. This observation was first noted in a pioneering paper by Fulton and Dynes<sup>1</sup> in 1973. In the same paper Fulton and Dynes reported on experiments with a mechanical analog of a long, lightly damped junction consisting of a chain of elastically coupled plane pendula. In the regime of high mean voltage (angular velocity) they found a near-uniform rotation of the pendula, but with decreasing voltage they observed that this uniform mode of operation becomes unstable against spatial fluctuations, resulting in the creation of propagating fluxons or, alternatively, a switch to the zero-voltage state. In physical terms the near-uniform rotation corresponds to a junction which is biased on the McCumber curve.

In the present paper we report on analytic, numerical, and experimental results which elucidate in more detail the instability of the McCumber curve. The analytic work is based on a stability analysis of the perturbed sine-Gordon equation which describes the dynamics of the Josephson junction. In the case of zero magnetic field this equation is linearized around a solution which corresponds to a uniform rotation of the pendula in the mechanical analog. The result is a Hill's equation. The instability regions of this equation determine the instability intervals along the McCumber curve, the number of which gives the number of ZFS's that can be reached

from the McCumber curve.

In the numerical work we use a method based on a simple extension of the multimode theory developed by En-puku *et al.*<sup>2</sup> which amounts to a consistent expansion of solutions of the perturbed sine-Gordon equation in truncated series of time-dependent Fourier spatial components. The time evolution of the Fourier coefficients is determined by direct numerical integration. The zero-order Fourier coefficient corresponds to a near-uniform rotation which acts as a parametric driving force in the system. In the instability interval corresponding to the position of the  $n$ th zero-field step the zero-order Fourier coefficient excites predominantly the  $n$ th Fourier mode and gives rise to a spatial variation in the phase along the junction which evolves into the corresponding fluxon oscillation.

The effect of magnetic field is handled in an approximate way by means of a simplification of the multimode equations. After some manipulation, the problem is again reduced to a Hill's equation which now contains the magnetic field as a parameter.

The experimental samples studied are niobium-oxide-lead junctions of overlap geometry. Experimental parameter values are adjusted by varying the sample temperature in a controlled way.

Comparison of the analytic, numerical, and experimental results yields an agreement that is at least qualitative and in many cases also quantitative. We have also observed some experimental phenomena, however, that are not contained in the model results.

## II. MATHEMATICAL MODEL AND STABILITY ANALYSIS

The mathematical model of the overlap Josephson junction is, in normalized form, the perturbed sine-Gordon equation<sup>3</sup>

$$\phi_{xx} - \phi_{tt} - \sin\phi = \alpha\phi_t - \beta\phi_{xxt} - \gamma, \quad (1a)$$

$$\phi_x(0,t) = \phi_x(l,t) = \eta. \quad (1b)$$

Here,  $\phi(x,t)$  is the usual Josephson phase variable,  $x$  is distance along the junction, normalized to the Josephson penetration length  $\lambda_j$ , and  $t$  is time, normalized to the inverse of the Josephson plasma angular frequency  $\omega_0$ . The model contains five parameters:  $\alpha$ ,  $\beta$ ,  $\gamma$ ,  $l$ , and  $\eta$ . The term in  $\alpha$  represents shunt loss due to quasiparticles crossing the junction, the term in  $\beta$  represents dissipation due to the surface resistance of the superconducting films,  $\gamma$  is the uniform bias current normalized to the maximum zero-voltage Josephson current,  $\eta$  represents the normalized external magnetic field, and the normalized length of the junction is denoted by  $l$ .

We first consider the case of homogeneous boundary conditions, i.e.,  $\eta=0$  in Eq. (1b). If  $\alpha=\beta=\gamma=0$  the McCumber solution of Eqs. (1) is exactly<sup>4</sup>

$$\phi = \phi_0(t) = 2 \operatorname{am}[t/k; k], \quad (2)$$

where  $\operatorname{am}$  is the Jacobian elliptic amplitude function<sup>5</sup> of modulus  $k$ . For nonzero  $\alpha$ ,  $\beta$ , and  $\gamma$ , we assume that Eq. (2) solves Eqs. (1) in the power-balance approximation.<sup>4</sup> This yields the following expressions for the McCumber branch of the  $I$ - $V$  characteristic of the junction:

$$\gamma = \frac{4\alpha E(k)}{\pi k}, \quad (3a)$$

$$V = \langle \phi_t \rangle = \frac{\pi}{k K(k)}, \quad (3b)$$

where  $K(k)$  and  $E(k)$  are, respectively, the complete elliptic integrals of first and second kinds.<sup>5</sup>

Following Burkov and Lissic,<sup>6</sup> we now express solutions of Eqs. (1) in the vicinity of the McCumber solution as

$$\phi(x,t) = \phi_0(t) + \tilde{\phi}(x,t), \quad (4)$$

where  $\phi_0$  is given by Eq. (2) together with the conditions of Eqs. (3), and  $\tilde{\phi}$  is a small perturbation of the form

$$\tilde{\phi}(x,t) = y(t) \exp(ibx) \quad (5)$$

with  $b$  constant. Inserting Eqs. (5) and (4) into Eqs. (1), we obtain an ordinary differential equation for  $y(t)$ :

$$\ddot{y} + (\alpha + \beta b^2)\dot{y} + [b^2 + \cos(\phi_0(t))]\cdot y = 0, \quad (6a)$$

where

$$b = n\pi/l, \quad n = 0, 1, 2, \dots \quad (6b)$$

and overdots denote derivatives with respect to  $t$ .

Equation (6a) is a damped Hill's equation;<sup>7</sup> it may have unstable solutions in certain regions of its parameter space. In such regions a small initial disturbance will lead to a large response in the solution, giving rise to the onset of a solution with spatial structure, in contrast to the

McCumber solution. As will be seen in Sec. VI, such solutions evolve into the fluxon oscillations characteristic of ZFS's.

In the limit of small  $k$ , we may approximate Eq. (2) as<sup>5</sup>

$$\phi_0(t) = \omega t + \frac{1}{\omega^2} \sin(\omega t), \quad (7)$$

with

$$\omega \equiv \langle \phi_t \rangle = \frac{\pi}{k K(k)}. \quad (8)$$

This approximation is valid for the asymptotic linear portion of the McCumber curve, i.e., for  $\omega \geq 3$ . The insertion of Eq. (7) into Eq. (6a) yields, after a simple calculation,

$$\ddot{y} + (\alpha + \beta b^2)\dot{y} + \left[ b^2 - J_1(\omega^{-2}) + \sum_{m=1}^{\infty} a_m \cos(m\omega t) \right] y = 0, \quad (9)$$

where

$$a_m = - \begin{cases} 2m\omega^2 J_m(\omega^{-2}), & m \text{ odd} \\ 2J'_m(\omega^{-2}), & m \text{ even} \end{cases} \quad (10)$$

and  $J_m$  is the Bessel function of first kind and  $m$ th order, and  $J'_m$  denotes its derivative with respect to the argument.

Using the fact that the argument of all the Bessel functions in Eq. (9) is  $1/\omega^2$  and that by assumption  $\omega \geq 3$ , we may approximate the Bessel functions as<sup>8</sup>

$$J_m(x) = \frac{x^m}{2^m m!} - \frac{x^{m+2}}{4 \times 2^m [(m+1)!]} \quad (11)$$

Using this approximation, Eq. (9) may be rewritten as

$$\ddot{y} + 2\epsilon\mu\dot{y} + \left[ \delta + \sum_{m=1}^{\infty} \epsilon^m d_m \cos(m\tau) \right] y = 0, \quad (12)$$

where  $\tau = \omega t$ ,  $\epsilon = 1/\omega^2$ ,  $\mu = (\omega/2)(\alpha + \beta b^2)$ ,

$$\delta = \left[ \frac{1}{\omega^2} \right] \left[ b^2 - \frac{\omega^{-2}}{2} - \frac{\omega^{-6}}{16} \right],$$

and overdots now denote derivatives with respect to  $\tau$ . The first few expansion coefficients are

$$d_1 = 1 - \frac{\omega^{-4}}{8}, \quad d_2 = \frac{1}{2} - \frac{\omega^{-4}}{12}, \quad d_3 = \frac{1}{8} - \frac{\omega^{-4}}{128}, \quad (13)$$

etc.

Following Nayfeh and Mook<sup>7</sup> we calculate the stability boundaries of Eq. (12) by means of a Lindstedt-Poincaré perturbation expansion in the parameter  $\epsilon$ . Retaining terms up to second order, this calculation yields

$$b^2 = \left[ \frac{\omega}{2} \right]^2 + \frac{1}{2\omega^2} \left[ 1 - \frac{1}{8\omega^4} \right] \pm \frac{1}{2} \left[ \left[ 1 - \frac{1}{8\omega^4} \right]^2 - \omega^2(\alpha + \beta b^2) \right]^{1/2} - \frac{1}{8\omega^2} \left[ 1 - \frac{1}{8\omega^4} \right]. \quad (14)$$

with  $b$  given by Eq. (6b). For given values of  $\alpha$ ,  $\beta$ ,  $l$ , and  $n$ , Eq. (14) gives two values for  $\omega$ , say  $\omega_+$  and  $\omega_-$ , which are the stability boundaries of Eq. (12), provided that the argument of the square root in Eq. (14) is positive. If this argument is negative, no instability region exists for the given parameter values. Using Eqs. (3) the voltage-stability boundaries  $\omega_+$  and  $\omega_-$  can be translated into the corresponding current values, say  $\gamma_+$  and  $\gamma_-$ .

### III. MULTIMODE THEORY

The linear-stability analysis presented in the preceding section provides estimates of the stability boundaries of the McCumber curve, but it cannot furnish the time evolution of an unstable solution. In order to follow the evolution of such an unstable solution, we consider a simple extension of the multimode theory developed by Enpuku *et al.*<sup>2</sup> The basic idea is to approximate solutions of Eqs. (1) in terms of a finite number of Fourier spatial modes whose amplitudes are unknown functions of time. This can be done with a reasonably small number of modes if two conditions are satisfied: (i) the spatial extent of a single fluxon is a sizable fraction of the length of the junction, and (ii)  $\phi$  in Eqs. (1) can be expressed in terms of periodic, continuous, and smooth functions of  $x$ . Condition (i) will be satisfied if we limit attention to intermediate-length junctions, i.e., those having  $1 \leq l \leq 5$ . Condition (ii) can easily be satisfied in the following way: We first define a new function  $\phi'$  in the double  $x$  interval  $[-l, l]$  as

$$\phi'(x, t) = \begin{cases} \phi(x, t), & 0 \leq x \leq l \\ \phi(-x, t), & -l \leq x \leq 0 \end{cases} \quad (15)$$

By construction  $\phi'$  is an even, continuous, periodic function of period  $2l$ ; however, from Eq. (1b), its spatial derivative is discontinuous at  $x=0$  and  $x=\pm l$  for  $\eta \neq 0$ . Therefore, we split  $\phi'$  into two parts, the first of which is an explicit function that satisfies Eq. (1b) and the second of which is now a smooth, even function, which, accordingly, may be reasonably approximated by a finite sum of low-order Fourier modes:

$$\phi'(x, t) = \eta |x| + \sum_{j=0}^N \theta_j(t) \cos \left[ \frac{j\pi x}{l} \right]. \quad (16)$$

Inserting Eq. (16) into Eqs. (1), we get, using the ortho-

gonality properties of the cosine function together with the fact that  $\phi'$  is even,

$$\ddot{\theta}_0 + \alpha \dot{\theta}_0 - \gamma - \frac{1}{l} \int_{x=0}^l \sin \left[ \eta x + \sum_{j=0}^N \theta_j \cos \left( \frac{j\pi x}{l} \right) \right] dx, \quad (17a)$$

$$\begin{aligned} \ddot{\theta}_m + (\alpha + \beta \omega_m^2) \dot{\theta}_m + \omega_m^2 \theta_m \\ = -\frac{2}{l} \int_{x=0}^l \sin \left[ \eta x + \sum_{j=0}^N \theta_j \cos \left( \frac{j\pi x}{l} \right) \right] \\ \times \cos \left[ \frac{m\pi x}{l} \right] dx, \quad m = 1, 2, \dots, N \end{aligned} \quad (17b)$$

with

$$\omega_m = m\pi/l. \quad (17c)$$

This system was integrated numerically using the standard predictor-corrector routine DGEAR;<sup>9</sup> the spatial integrals were evaluated by means of the fast-Fourier-transform routine FFTSC (Ref. 9) using  $N$  function samples over the interval  $[0, l]$  (corresponding to  $2N$  samples over one spatial period of  $\phi'$ ). The accuracy of the temporal integration was checked by varying the local error limit in DGEAR, and the influence of mode truncation by varying  $N$ .

### IV. APPROXIMATE ANALYSIS OF MAGNETIC FIELD EFFECTS

The multimode theory presented in the preceding section is valid for any value of the magnetic field  $\eta$ . Here we present an approximate treatment of this theory, valid for sufficiently small  $\eta$ , which reduces the problem of determining the effects of magnetic field to a simple analytic result similar to that presented in Sec. II. The approximation is based on assuming that the amplitudes of the spatial modes in Eqs. (17) are small, i.e.,

$$\sum_{j=1}^N |\phi_j(t)| \ll 1. \quad (18)$$

Using this approximation we can calculate explicitly the integrals in Eqs. (17), obtaining

$$\ddot{\theta}_0 + \alpha \dot{\theta}_0 - \gamma = - \left[ c_{0,0} - \sum_{j=1}^N b_{j,0} \theta_j \right] \sin \theta_0 - \left[ b_{0,0} - \sum_{j=1}^N c_{j,0} \theta_j \right] \cos \theta_0, \quad (19a)$$

$$\ddot{\theta}_m + (\alpha + \omega_m^2 \beta) \dot{\theta}_m + \omega_m^2 \theta_m = -2 \left[ c_{0,m} - \sum_{j=1}^N b_{j,m} \theta_j \right] \sin \theta_0 - 2 \left[ b_{0,m} - \sum_{j=1}^N c_{j,m} \theta_j \right] \cos \theta_0, \quad (19b)$$

with  $m = 1, 2, 3, \dots, N$ . Here,

$$b_{j,m} = \frac{1}{l} [1 - (-1)^{j+m} \cos(\eta l)] \left[ \frac{1}{\eta l + \pi j + \pi m} + \frac{1}{\eta l + \pi j - \pi m} + \frac{1}{\eta l - \pi j + \pi m} + \frac{1}{\eta l - \pi j - \pi m} \right], \quad (20a)$$

$$c_{j,m} = \frac{1}{l} [(-1)^{j+m} \sin(\eta l)] \left[ \frac{1}{\eta l + \pi j + \pi m} + \frac{1}{\eta l + \pi j - \pi m} + \frac{1}{\eta l - \pi j + \pi m} + \frac{1}{\eta l - \pi j - \pi m} \right]. \quad (20b)$$

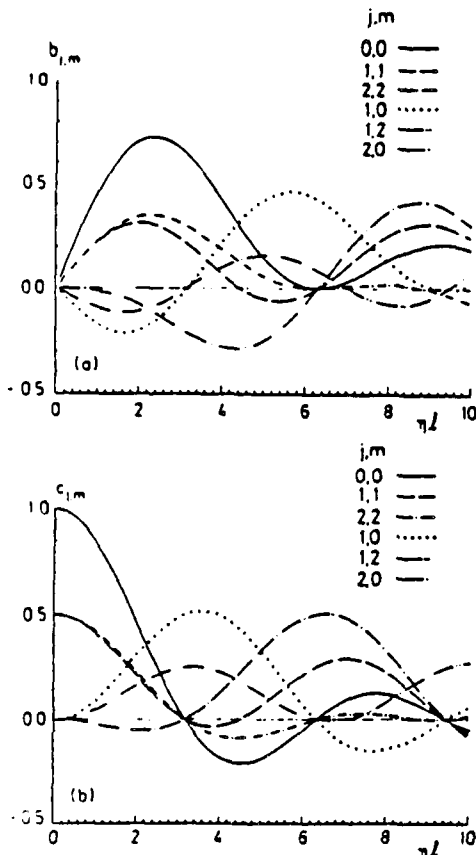


FIG. 1. Coefficients (a)  $b_{j,m}$  and (b)  $c_{j,m}$  of Eqs. (20). Note that  $b_{j,m} = b_{m,j}$  and  $c_{j,m} = c_{m,j}$ .

In Fig. 1 we show the values of  $b_{j,m}$  and  $c_{j,m}$  for  $j, m = 0, 1, 2$  and  $0 \leq \eta l \leq 10$ .

Using again the approximation (18), together with the observation from Fig. 1 that the coefficients  $b_{j,m}$  and  $c_{j,m}$

are never larger in magnitude than 1, we may further approximate Eq. (19a) as

$$\ddot{\theta}_0 + \alpha \dot{\theta}_0 - \gamma = -c_{0,0} \sin \theta_0 - b_{0,0} \cos \theta_0, \quad (21)$$

which can be cast into the form

$$\ddot{\theta}' + \alpha' \dot{\theta}' - \gamma' + \sin \theta' = 0, \quad (22a)$$

with

$$a = (c_{0,0}^2 + b_{0,0}^2)^{1/2} = \frac{\sin(\eta l/2)}{\eta l/2}, \quad (22b)$$

$$\delta = \arctan(b_{0,0}/c_{0,0}) = \eta l/2, \quad (22c)$$

$$t' = a^{1/2} t, \quad (22d)$$

$$\alpha' = a^{-1/2} \alpha, \quad (22e)$$

$$\gamma' = a^{-1} \gamma, \quad (22f)$$

$$\theta'(t) = \theta_0(t) + \delta, \quad (22g)$$

where overdots now denote derivatives with respect to  $t'$ . Equation (22a) has the same form as Eqs. (1) in the absence of spatial structure and in the absence of magnetic field, i.e., it describes a McCumber solution and consequently leads to

$$\theta_0 = 2 \operatorname{am}[\imath a^{1/2}/k; k] - \delta, \quad (23a)$$

$$\gamma = \frac{4\alpha a^{1/2} E(k)}{\pi k}, \quad (23b)$$

$$\langle \dot{\theta}_0 \rangle = \frac{\pi a^{1/2}}{k K(k)}. \quad (23c)$$

If we now assume that the solution of Eqs. (19) contains only one dominant spatial mode, say the  $m$ th (which is reasonable for a sufficiently short junction), Eqs. (19b) reduce to a single equation,

$$\ddot{\theta}_m + (\alpha + \omega_m^2 \beta) \dot{\theta}_m + \omega_m^2 \theta_m - 2(b_{m,m} \sin \theta_0 - c_{m,m} \cos \theta_0) \theta_m = -2(c_{0,m} \sin \theta_0 + b_{0,m} \cos \theta_0), \quad (24)$$

which can be written as a Hill's equation with a forcing term

$$\ddot{\theta}_m + (\alpha + \omega_m^2 \beta) \dot{\theta}_m + [\omega_m^2 + 2d \cos(\theta_0 + \psi)] \theta_m = -2\rho \sin(\theta_0 + \xi) \quad (25a)$$

by defining

$$d \equiv (c_{m,m}^2 + b_{m,m}^2)^{1/2} = \frac{1}{2} \sin \left[ \frac{\eta l}{2} \right] \left[ \frac{1}{\eta l + 2\pi m} + \frac{1}{\eta l - 2\pi m} + \frac{2}{\eta l} \right], \quad (25b)$$

$$\psi \equiv \arctan(b_{m,m}/c_{m,m}) = \frac{\eta l}{2}, \quad (25c)$$

$$\rho \equiv (c_{0,m}^2 + b_{0,m}^2)^{1/2} = \sin \left[ \frac{\eta l}{2} + \frac{\pi}{2} P_m \right] \left[ \frac{1}{\eta l - \pi m} + \frac{1}{\eta l + \pi m} \right], \quad (25d)$$

$$\xi = \arctan(b_{0,m}/c_{0,m}) = \frac{\eta l}{2} + \frac{\pi}{2} P_m, \quad (25e)$$

with  $P_m = 0, 1$  for  $m$  even, odd.

For small values of  $\eta$  it is reasonable to assume that the instability regions of Eq. (25a) are the same as those of the associated homogeneous equation.<sup>10</sup> Therefore, we restrict our attention to the homogeneous equation

$$\ddot{\theta}_m + (\alpha + \omega_m^2 \beta) \dot{\theta}_m + \left[ \omega_m^2 + 2d \cos \left[ \theta_0 + \frac{\eta l}{2} \right] \right] \theta_m = 0. \quad (26)$$

We may perform now the same procedure as used in the  $\eta=0$  case. As in that case, Eq. (26) may be cast into the form of Eq. (12), where now

$$\tau = \omega t, \quad \epsilon = 1/\omega^2, \quad \mu = (\omega/2)(\alpha + \beta\omega_m^2), \quad \delta = \omega^{-2} \left[ \omega_m^2 - 2d \left( \frac{\omega^{-2}}{2} - \frac{\omega^{-6}}{16} \right) \right]. \quad (27a)$$

The first few expansion coefficients are now given by

$$d_1 = 2d \left[ 1 + \frac{\omega^{-4}}{8} \right], \quad d_2 = 2d \left[ \frac{1}{2} - \frac{\omega^{-4}}{12} \right], \quad d_3 = 2d \left[ \frac{1}{8} - \frac{\omega^{-4}}{128} \right], \quad (27b)$$

etc. Performing the same Lindstedt-Poincaré perturbation expansion used before, we obtain the following instability boundaries to second order in  $\epsilon$ :

$$\omega_m^2 = \left( \frac{\omega}{2} \right)^2 + \frac{d}{\omega^2} \left( 1 - \frac{1}{8\omega^4} \right) - \frac{d^2}{2\omega^2} \left( 1 - \frac{1}{8\omega^4} \right)^2 \pm \left[ d^2 \left( 1 - \frac{1}{8\omega^4} \right)^2 - \frac{\omega^2}{4} (\alpha + \beta\omega_m^2)^2 \right]^{1/2}. \quad (28)$$

This expression assumes the form of Eq. (14) for  $\eta=0$ . For  $\eta \neq 0$  but small it gives the dependence of the instability boundaries on the magnetic field.

## V. EXPERIMENTAL PROCEDURE

Sample preparation and experimental technique have been described in previous publications.<sup>11</sup> Several junctions have been investigated, all Nb-Nb<sub>x</sub>O<sub>y</sub>-Pb overlap Josephson tunnel junctions of intermediate normalized length. The results reported here were obtained with a representative sample (S6-7/4), a junction of length  $L=397 \mu\text{m}$  and width  $W=17.6 \mu\text{m}$ . Geometrically, the overlap of the junction was perfect to within  $0.5 \mu\text{m}$ , the resolution of our optical microscope.

The substrate was mounted in a  $1 \times 1\text{-in.}^2$  microstrip box and thermally anchored to a copper block containing two precision Ge thermometers and a small heating element. All the  $50\text{-}\mu\text{m}$ -diam wires leading to the Josephson junction, the thermometers, and the heating element were bifilarly wound and carefully thermally anchored to the copper block.

The microstrip box was included in a vacuum can immersed in a liquid-helium glass cryostat. A low-loss (inside gold-plated) rectangular stainless-steel waveguide connected the room-temperature X-band field-effect-transistor (FET) microwave receiver to a SMA transition inside the vacuum can. The final part of the microwave system was a 20-cm-long, all-Nb, 0.085-in. SMA cable leading to a SMA-to-stripline transition in the microstrip box.

A weak coupling to the microwave system was provided by an inverted microstrip antenna placed at a fixed distance of about  $10 \mu\text{m}$  from one end of the junction. The distance to the ground plane (nonsuperconducting) could be adjusted *in situ* by means of a cryogenic differential screw.

An extremely high stability of the three external bias parameters—temperature  $T$ , current  $I_{dc}$ , and applied magnetic field  $B_{appl}$ —was essential and was verified by measuring the frequency ( $\sim 10 \text{ GHz}$ ) and linewidth ( $\sim 5 \text{ kHz}$ ) of the radiation emitted by the junction when biased

on the first ZFS. Typical frequency-tuning rates of  $\Delta\nu/\Delta T$ ,  $\Delta\nu/\Delta I_{dc}$ , and  $\Delta\nu/\Delta B_{appl}$  were  $0.1 \text{ MHz/mK}$ ,  $2 \text{ MHz}/\mu\text{A}$ , and  $0.5 \text{ MHz}/\mu\text{T}$ , respectively.

The temperature of the helium bath was regulated with a manostat to within  $\sim 1 \text{ mK}$ . A temperature stabilization better than  $10 \mu\text{K}$  at  $2.1 < T < 4.2 \text{ K}$  could be maintained for minutes by adjusting the thermal time constant of the microstrip box by regulating the exchange-gas pressure in the vacuum can. All  $50\text{-}\mu\text{m}$ -diam wires were also thermally anchored to the vacuum can.

The dc-bias current was supplied either from a sweepable constant-current generator or from a current source based on reference mercury cells. The current was fed to the junction by a long, double  $50\text{-}\mu\text{m}$ -diam wire, bifilarly wound transmission line, the hot end of which was thermostatted in order to minimize the influence of thermopowers. The dc voltage across the junction was measured using a similar transmission line. Both transmission lines were drawn inside thin-walled brass capillaries.

Input noise of either capacitive or inductive origin to the junction did not produce any observable frequency modulation or linewidth broadening of the emitted radiation. The noise of the dc amplifier used allowed us to resolve voltage-step structures less than  $100 \text{ nV}$  on a fast (10-ms response) XY recorder.

The external magnetic field was produced by a coil wound onto the vacuum can and was applied in the plane of the junction and perpendicular to its long side. The magnetic shielding of the cryostat and the wires leading to the coil was sufficient to prevent magnetic noise from interfering with the measurements. This could be checked by reading the linewidth of the emitted radiation when biased alternatively in regions of the ZFS with  $\Delta\nu/\Delta B_{appl}=0$  or  $\Delta\nu/\Delta B_{appl} \neq 0$ .

The critical-current density  $J$ , the Josephson penetration length  $\lambda_J$ , and the loss term  $\alpha$  were determined from the dc  $I-V$  characteristic (critical-current value, ZFS asymptotic voltage, and the slope of the McCumber curve at voltages corresponding to the ZFS studied) and from direct measurement of the plasma-resonance frequency.<sup>12</sup> For the junction in question (sample S6-7/4),  $J=26.2 \text{ A/cm}^2$ ,  $\lambda_J=91 \mu\text{m}$ ,  $l=L/\lambda_J=4.4$ , and  $\alpha=0.006$  at  $4.2 \text{ K}$ .

## VI. RESULTS

Figure 2 shows a portion of an  $I$ - $V$  characteristic calculated numerically from Eqs. (17) using the parameter values  $\alpha = 0.05$ ,  $\beta = 0.02$ ,  $l = 2$ , and  $\eta = 0$ . Both the McCumber background curve (MCB) and the first zero-field step (ZFS1) are evident. The inset shows in more detail the region where ZFS1 joins the McCumber curve. This region was calculated as follows: For  $\eta = 0$ , the numerical growth of an instability requires the imposition of an inhomogeneous initial condition. Accordingly, for a given  $\gamma$ , a "pure" McCumber solution was launched and allowed to stabilize for 100 normalized time units, after which a small perturbation was added. In the instability region, i.e., for  $\gamma_- \leq \gamma \leq \gamma_+$  or  $\omega_- \leq \omega \leq \omega_+$ , the perturbation grows, causing the system to switch to ZFS1. Outside of the instability region the perturbation decays, and the system relaxes back to the McCumber curve. For  $\eta \neq 0$  there is a coupling between the McCumber solution and the spatial modes through the boundary conditions, Eq. (1b); this allows the instability to develop also in the absence of an external perturbation.

Figure 3 shows the dynamics of switching in more detail. In this figure, obtained using the parameter values  $\alpha = 0.05$ ,  $\beta = 0.02$ ,  $l = 2$ ,  $\eta = 0$ , and  $\gamma = 0.16$ , a small perturbation has been added to the solution at a time prior to  $t = 500$ . Figure 3(a) shows the behavior of  $\dot{\theta}_0$  in Eqs. (17). Note from Eqs. (16) and (8) that  $\langle \dot{\theta}_0 \rangle = \langle \dot{\phi}_1 \rangle = \omega$ . For  $t \geq 500$ , we see that  $\omega \approx 3.20$ . Between  $t = 500$  and 550, a switching takes place, which, after a transient, settles into a state having  $\omega \approx 3.20$ . Figure 3(b) shows the corresponding behavior of  $\theta_1$  (the larger-amplitude oscillation) and  $\theta_2$  (the smaller-amplitude oscillation) in Eqs. (17). From this figure it is evident that the switching seen in Fig. 3(a) is associated predominantly with an exponential growth of the first-order Fourier spatial component. In a similar way, Fig. 3(c) shows the behavior of  $\theta_3$ . Comparing Figs. 3(b) and 3(c), we see that the amplitudes of the Fourier coefficients decrease rapidly with order number.

Using this numerical procedure, we find that the stability boundaries associated with ZFS1 for the parameter values used are, expressed in terms of bias current,

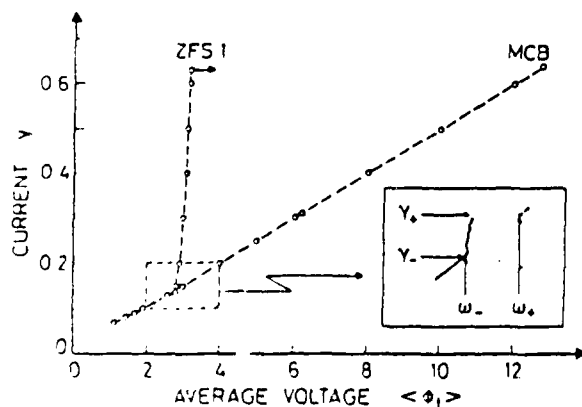


FIG. 2.  $I$ - $V$  characteristic calculation from Eqs. (17) using  $\alpha = 0.05$ ,  $\beta = 0.02$ ,  $l = 2$ , and  $\eta = 0$ , showing the McCumber background curve (MCB) and the first zero-field step (ZFS1). Inset shows detail of region where ZFS1 joins the MCB.

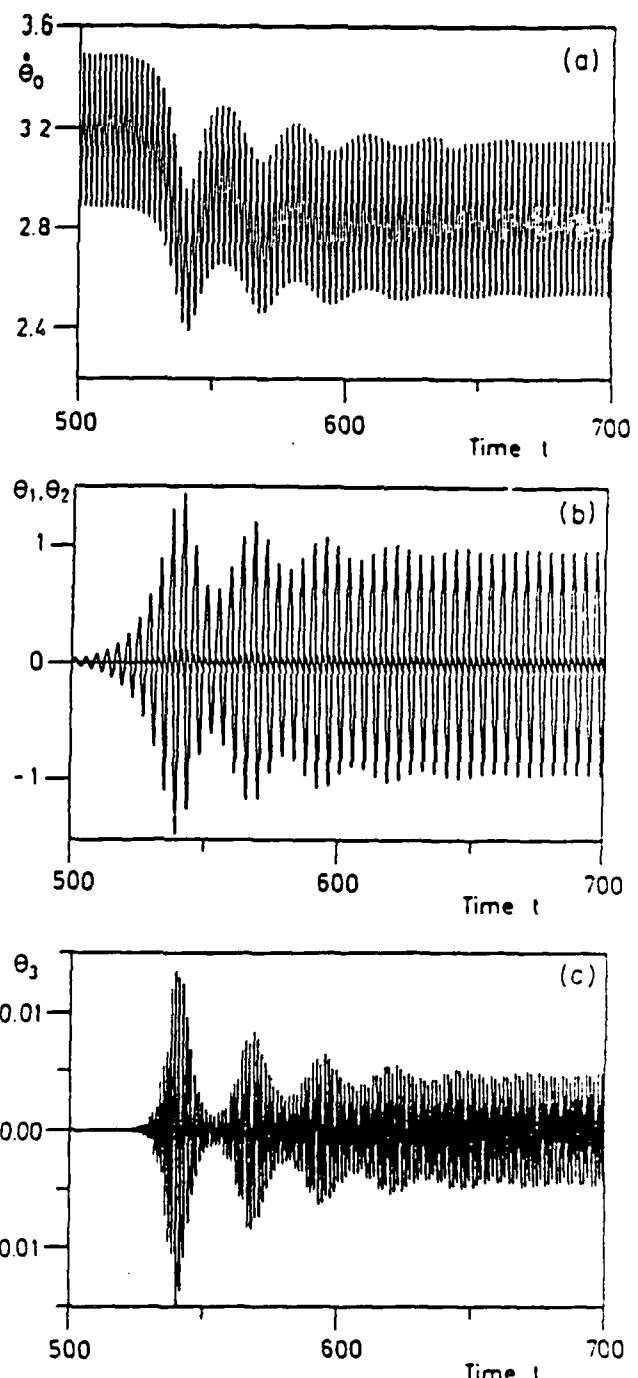


FIG. 3. Dynamics of switching from McCumber curve to ZFS1 calculated from Eqs. (17) by adding a small perturbation to the solution before  $t = 500$ , in terms of Fourier coefficients: (a)  $\dot{\theta}_0$ , (b)  $\theta_1$  (larger-amplitude oscillation) and  $\theta_2$  (smaller-amplitude oscillation), and (c)  $\theta_3$ .

$\gamma_+ = 0.1712 \pm 0.0005$  and  $\gamma_- = 0.1401 \pm 0.0001$ . Inserting the same parameter values, together with  $n = 1$  in Eq. (6b), into Eq. (14) and (3), yields  $\gamma_+ = 0.1711$  and  $\gamma_- = 0.1404$ . Considering that this instability region occurs at the very lower end of the asymptotic linear region in the McCumber curve, for which the analysis of Sec. II was developed, the agreement is more than satisfactory.

Figure 4 shows the stability boundaries, now expressed in terms of average voltage, calculated from Eq. (14) with

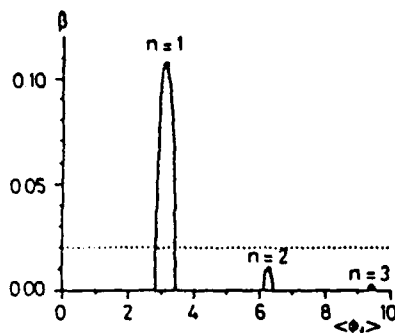


FIG. 4. Instability regions (shaded) in average voltage ( $\phi$ ) calculated from Eq. (14) for ZFS1, ZFS2, and ZFS3 for different  $\beta$ -loss values using  $\alpha=0.05$  and  $l=2$ . Dotted line corresponds to  $\beta=0.02$  used in multimode theory.

$\alpha=0.05$  and  $l=2$ , for different values of  $\beta$ . The dotted line corresponds to the value  $\beta=0.02$  used above. For these parameter values there is only one instability region in the McCumber curve; however, by lowering  $\beta$  it is possible to have as many as six such regions (the three lowest of which are shown in Fig. 4). This result helps to clarify a long-standing experimental question, i.e., what determines the number of ZFS's that may be observed in the  $I$ - $V$  characteristic of a given junction?

This situation is illustrated in more detail for ZFS1 in Fig. 5(a) and for ZFS2 in Fig. 5(b). In these figures the solid curves are calculated from Eq. (28) and translated into bias current through Eqs. (3) (this is done to facilitate comparisons with the numerical results, in which  $\gamma$  is a direct control parameter). The curves labeled 1 correspond to  $\eta=0$  and those labeled 2 to  $\eta=0.8$ . As is evi-

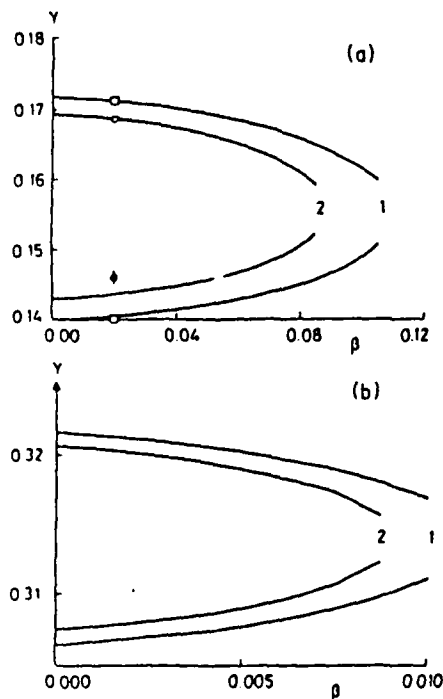


FIG. 5. Stability boundaries in current  $\gamma$  as a function of  $\beta$  loss calculated from Eq. (28) and Eqs. (3) for (a) ZFS1 and (b) ZFS2, for  $\eta=0$  (curves 1) and  $\eta=0.8$  (curves 2) using  $\alpha=0.05$  and  $l=2$ . Squares and circles in (a) are calculated from Eqs. (17) for  $\eta=0$  and 0.8, respectively.

dent from Fig. 5, the main effect of a (small) magnetic field is to reduce the width of the instability regions. The points indicated by squares and circles in Fig. 5(a) are calculated from Eqs. (17); the squares correspond to  $\eta=0$  and the circles to  $\eta=0.8$ . The error bar on the lower circle reflects the fact that for  $\eta \neq 0$  both the ZFS states and the McCumber states contain significant amounts of Fourier components, thus rendering a clear distinction between the two states somewhat difficult at the lower end of an instability region. This distinction is much sharper for the other multimode points in Fig. 5(a), and the relative error bars are contained within the dimensions of the symbols.

The dynamic state into which the system evolves after the switching shown in Fig. 3 is the fluxon oscillation state associated with ZFS1. This fact may be clearly established by comparing the results of the multimode theory, Eqs. (17), with those of the direct simulation solution of Eqs. (1) reported in Ref. 13. Figure 6 shows such a comparison. In this figure, the solid curve is the function  $\phi_1(0,t)$ , which is the voltage at the  $x=0$  end of the junction, as obtained by direct simulation. The arrival of fluxons at the junction end is clearly apparent. The dashed curve is the same function as reconstructed from Eq. (16) using  $N=3$ . The bias value used in Fig. 6 is  $\gamma=0.60$ , i.e., near the top of ZFS1. For smaller values of  $\gamma$  the agreement is even better, and the two curves are practically indistinguishable.

Figure 7(a) shows a portion of the  $I$ - $V$  characteristic of the experimental sample S6-7/4 measured at a temperature somewhat below the transition temperature of the lead counterelectrode and in zero magnetic field. The dashed arrows indicate switching from the zero-voltage current and from the first two ZFS's to the gap state. Figure 7(b) is the same characteristic with a  $10\times$  magnification of the current scale. The dotted lines in Fig. 7 indicate switching from higher-voltage to lower-voltage states. Clearly evident in Fig. 7(b) is a switching from the bottom of ZFS1 to the zero-voltage state. This may be due to a direct instability of the ZFS's toward the zero-voltage state<sup>14</sup> rather than being connected with an instability of the McCumber curve; such a mechanism is not contained in our present model.

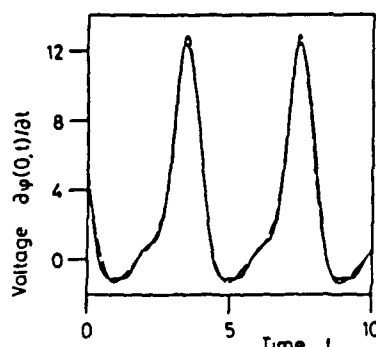


FIG. 6. Time evolution of voltage at  $x=0$  junction end as obtained by direct numerical simulation of Eqs. (1) (solid curve) and as reconstructed from Eq. (16) using  $N=3$  (dashed curve) for parameter values  $\alpha=0.05$ ,  $\beta=0.02$ ,  $l=2$ ,  $\eta=0$ , and  $\gamma=0.60$ .

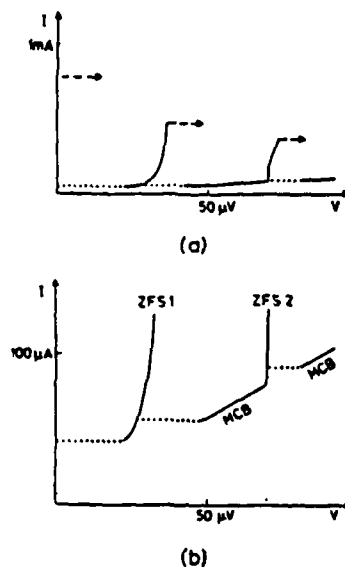


FIG. 7. (a) Detail of the  $I$ - $V$  characteristic of experimental sample S6-7/4 measured at a temperature slightly below the transition temperature of the lead counterelectrode and in zero magnetic field. Arrows indicate switching to the gap state. (b) Same characteristic with  $10\times$ -magnified current scale. Dotted lines indicate switching from higher-voltage to lower-voltage states.

The characteristics shown in Fig. 7 correspond to a normalized junction length of about  $l=3.2$  and an  $\alpha$ -loss term, estimated from the slope of the McCumber curve, of about  $\alpha=0.03$ . The experimental determination of the  $\beta$ -loss term is subject to rather large uncertainties, and so we have treated  $\beta$  as an adjustable parameter in what follows. An essential feature of the experimental procedure is that the parameter values for a given junction can be "tuned" experimentally by varying the operating temperature.

Figure 8(a) shows a comparison between the experimentally determined stability boundaries (circles) in a magnetic field associated with ZFS1 and those obtained from Eq. (28), shown as solid lines. Experimental values of voltage and magnetic field were translated into normalized terms using the formulas  $\langle\phi_1\rangle = V/\Phi_0 f_p$ , and  $\eta = 2\pi\phi_{ext}/\Phi_0 l$ , where  $V$  is the physical voltage,  $\Phi_0$  is the magnetic flux quantum,  $\phi_{ext}$  is the applied magnetic flux threading the junction, and  $f_p$  is the plasma frequency.<sup>12</sup> The experimental data were taken at a temperature for which  $\alpha=0.026$  and  $l=3.16$ , and these same parameter values were used in Eq. (28). The  $\beta$  value used in Eq. (28) was varied between 0 and 0.07; the effect of this variation is indicated by the slight thickening of the curves in Fig. 8(a). The agreement between the experimental and theoretical values for  $\omega_+$  is reasonable. The large discrepancy for the  $\omega_-$  branch may be due either to the fact that here  $\omega$  lies considerably below the lower limit of the asymptotic linear region of the McCumber curve ( $\omega \geq 3$ ), or to the fact that a switching mechanism not described by the model is involved, as mentioned above.

Figure 8(b) shows a similar comparison for ZFS2, using the same parameter values (same temperature) as in Fig. 8(a). The  $\beta$  value used in Eq. (28) was varied between 0

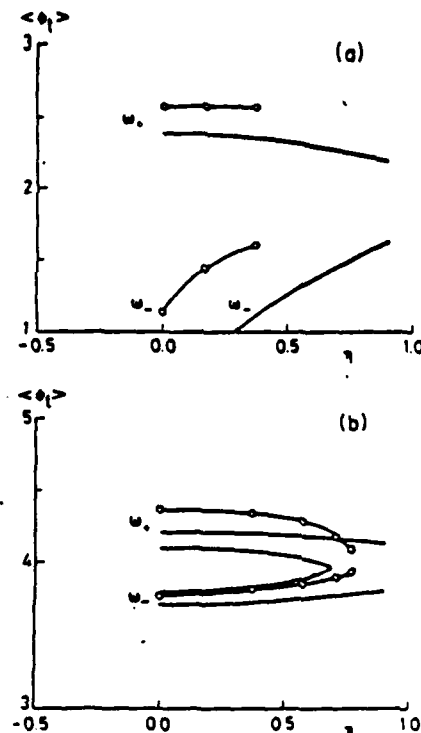


FIG. 8. Stability boundaries in average voltage  $\langle\phi_1\rangle$  as a function of magnetic field  $\eta$  measured experimentally (circles) and calculated from Eq. (28) (solid curves) for (a) ZFS1 and (b) ZFS2. Fixed parameter values:  $\alpha=0.026$  and  $l=3.16$ .  $0 \leq \beta \leq 0.07$  in (a) and  $0 \leq \beta \leq 0.05$  in (b), giving rise to the shaded regions between the solid curves.

and 0.05; the effect of this variation is indicated by the shaded regions in Fig. 8(b). The agreement obtained here for the behavior of the  $\omega_-$  branch is much better than that of Fig. 8(a). The reason for this fact may be that there is no direct switching from ZFS2 to the zero-voltage state as there is for ZFS1, as can be seen in Fig. 7(b), or that here  $\omega_- > 3$ .

Figure 9 shows a similar result for ZFS1 at a higher temperature, for which  $\alpha=0.043$  and  $l=2.56$ , and for  $\omega$

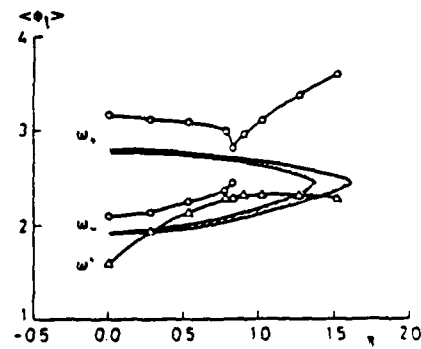


FIG. 9. Stability boundaries in average voltage  $\langle\phi_1\rangle$  as a function of magnetic field  $\eta$  measured experimentally (circles) and calculated from Eq. (28) (solid curves) for ZFS1 using fixed parameter values  $\alpha=0.043$  and  $l=2.56$ .  $\beta$  in Eq. (28) is varied in the range  $0 \leq \beta \leq 0.07$ , giving rise to the shaded regions between the solid curves. Triangles indicate experimental stability boundary  $\omega^*$  of the stable piece of the McCumber curve that appears below the bottom of ZFS1.

larger range of magnetic field. As before, circles are experimental points and solid lines are calculated from Eq. (28). Also, as before, the shaded regions between the solid curves represent the effect of varying  $\beta$  between 0 and 0.07. Two new phenomena are represented in Fig. 9. The first is that at a field value of about  $\eta=0.8$ , there is an abrupt change in the behavior of the experimental  $\omega_+$  branch. Physically, this corresponds to the disappearances of ZFS1 with increasing field and the growth of the second Fiske step (FS2) at approximately the same voltage.<sup>15</sup> The perturbation theory result derived in Sec. IV is approximately valid only for sufficiently small values of  $\eta$ ; it cannot be expected to hold for larger field values. The second new experimental phenomenon is the appearance of a stable portion of the McCumber curve below the bottom of ZFS1 at this temperature. In Fig. 9 the lower curve indicated by circles is, as before, the bottom of ZFS1, and the curve indicated by triangles is the lower stability boundary ( $\omega^*$ ) of this new piece of stable McCumber curve.

We note from Figs. 8 and 9 that the experimental stability boundaries are systematically higher than the corresponding theoretical ones. The reason for this might be that the asymptotic voltage of the ZFS's corresponds to normalized limiting velocities of the fluxons less than 1, as discussed by Scheuermann and Chi.<sup>16</sup> This would lead to a calculated value of the normalized length  $l$  larger than the real value and, correspondingly, to a shift of the theoretical voltage positions on the normalized voltage scale to lower values since, in normalized terms,  $l(\Phi_0) = 2\pi$  for ZFS1.

## VII. CONCLUSIONS

A linear-stability analysis of the perturbed sine-Gordon equation which describes the dynamics of Josephson tunnel junctions indicates that the mechanism that determines the experimental observation of ZFS's may be

described in terms of the growth of parametrically excited instabilities of the McCumber curve. This analysis gives good agreement with both numerical and experimental results in the asymptotic linear region of the McCumber curve and for sufficiently small values of the applied magnetic field. It would be useful to extend the analysis to the region of the McCumber curve below the asymptotic linear region in order to be able to study low-order steps in longer junctions.

Numerical integration of the multimode equations verifies that the parametrically excited instabilities evolve into fluxon oscillations. The multimode approach is a useful alternative to the direct numerical simulation of Eqs. (1) inasmuch as it gives reasonably reliable results at a considerably reduced computing cost. It should be remembered, however, that truncated mode expansions can be expected to give reliable results only when the dynamic states in question are reasonably smooth. Here, as elsewhere, the study of phenomena such as subharmonic generation and chaos will presumably require the use of different tools.

## ACKNOWLEDGMENTS

We are grateful to S. E. Burkov for illuminating discussions regarding the stability analysis. We gratefully acknowledge financial support from the Danish Natural Science Research Council and from the European Research Office of the United States Army through Contract No. DAJA-37-82-C-0057. One of us (S.P.) thanks the Fondazione Angelo della Riccia (Italy) for partial support for the period during which this work was performed. Another of us (R.D.P.) was supported in part by the Gruppo Nazionale della Struttura di Materia, Consiglio Nazionale delle Ricerche—CISM, Ministero della Pubblica Istruzione (GNSM/CNR-CISM/MPI) (Italy) and in part by the Thomas B. Thriges Fond (Denmark).

\*Permanent address: Dipartimento di Fisica, Università degli Studi di Salerno, I-84100 Salerno, Italy.

<sup>1</sup>T. A. Fulton and R. C. Dynes, Solid State Commun. 12, 57 (1973).

<sup>2</sup>K. Enpuku, K. Yoshida, and F. Irie, J. Appl. Phys. 52, 344 (1981).

<sup>3</sup>P. S. Lomdahl, O. H. Soerensen, and P. L. Christiansen, Phys. Rev. B 25, 5737 (1982).

<sup>4</sup>R. D. Parmentier, in *Solitons in Action*, edited by K. Lonngren and A. Scott (Academic, New York, 1978), pp. 173–199.

<sup>5</sup>P. F. Byrd and M. D. Friedman, *Handbook of Elliptic Integrals for Engineers and Physicists* (Springer, Berlin, 1954).

<sup>6</sup>S. E. Burkov and A. E. Lifsic, Wave Motion 5, 197 (1983).

<sup>7</sup>A. H. Nayfeh and D. T. Mook, *Nonlinear Oscillations* (Wiley-Interscience, New York, 1979), Chap. 5.

<sup>8</sup>M. Abramowitz and I. Stegun, *Handbook of Mathematical Functions*, 9th ed. (Dover, New York, 1970), Eq. 9.1.10.

<sup>9</sup>IMSL, Inc. (Houston, Texas), International Mathematical and Statistical Library (Edition 9), 1982 (unpublished).

<sup>10</sup>C. S. Hsu and W. H. Cheng, J. Appl. Mech. ASME 41, 371 (1974).

<sup>11</sup>B. Dueholm, O. A. Levring, J. Mygind, N. F. Pedersen, O. H. Soerensen, and M. Cirillo, Phys. Rev. Lett. 49, 1093 (1982).

<sup>12</sup>J. Bindslev Hansen, J. Mygind, S. Pagano, M. R. Samuelsen, and H. Svensmark, in *Proceedings of the International Conference on Tunneling at Low Temperatures*, Heverlee, Belgium, 25–30 August 1985 (unpublished).

<sup>13</sup>M. P. Soerensen, R. D. Parmentier, P. L. Christiansen, O. Skovgaard, B. Dueholm, E. Joergensen, V. P. Koshelets, O. A. Levring, R. Monaco, J. Mygind, N. F. Pedersen, and M. R. Samuelsen, Phys. Rev. B 30, 2640 (1984).

<sup>14</sup>N. F. Pedersen and D. Welner, Phys. Rev. B 29, 2551 (1984).

<sup>15</sup>M. Cirillo, A. M. Cucolo, S. Pace, and B. Savo, J. Low Temp. Phys. 54, 489 (1984).

<sup>16</sup>M. Scheuermann and C. C. Chi, in *Proceedings of the Third International Conference on Superconducting Quantum Devices*, West Berlin, 25–28 June 1985, Conference Digest, p. 170 (unpublished).

## STABILITY OF DYNAMIC STATES IN JOSEPHSON JUNCTIONS

Peter L. CHRISTIANSEN

*Laboratory of Applied Mathematical Physics, The Technical University of Denmark, DK-2800 Lyngby, Denmark*

Instabilities of dynamic states in linear Josephson junctions modelled by the perturbed sine-Gordon equation are investigated experimentally, computationally, and by stability theory. The narrow line-width of the electromagnetic radiation from the circular Josephson oscillator is determined computationally and by perturbation theory.

### 1. Introduction

The present paper describes recent results concerning instability of dynamic states in the linear overlap Josephson junction obtained in ref. 1 and line width of the electromagnetic radiation from the circular Josephson oscillator obtained in refs. 2-3.

In both cases the Josephson oscillator is modelled by the perturbed sine-Gordon equation [4]

$$\phi_{xx} - \phi_{tt} - \sin \phi = \alpha \phi_t - \beta \phi_{xxt} - \gamma \quad (1)$$

in normalized units. Here,  $\phi(x, t)$  is the usual Josephson phase variable,  $x$  is the distance along the junction, and  $t$  is time. The term in  $\alpha$  represents shunt loss due to quasiparticles crossing the junction, the term in  $\beta$  represents series loss due to surface resistance of the superconducting films, and  $\gamma$  is the uniform bias current. For the linear oscillator we apply inhomogeneous Neumann boundary conditions

$$\phi_x(0, t) = \phi_x(l, t) = \eta, \quad (2a)$$

where  $l$  is the length of the junction, and  $\eta$  is the external magnetic field. In the circular oscillator periodic boundary conditions

$$\begin{aligned} \phi_x(0, t) &= \phi_x(l, t), \\ \phi_x(0, t) &= \phi_x(l, t), \end{aligned} \quad (2b)$$

$l$  being the circumference of the oscillator, are used. The detailed choice of initial conditions in the numerical solutions of (1)-(2) is described in [1-2].

### 2. The linear Josephson oscillator

Fig. 1 shows a portion of an  $I-V$  characteristic obtained as the relationship between bias current,  $\gamma$ , and resulting average voltage on the junction,  $\langle \phi_x(0, t) \rangle$ , by computational integration of eqs. (1) and (2a). For intermediate-length ( $l \leq 5$ ) Josephson junction we use an extension of the multimode theory developed by Enpuku et al. [5], which amounts to an expansion of the solutions of the perturbed sine-Gordon equation in a truncated series of time-dependent Fourier spatial components. This approach provides very accurate results at a lower computational cost than direct numerical solution of the mathematical model [6]. In fig. 1 we observe an instability for  $\gamma_- < \gamma < \gamma_+$ , or  $\omega_- < \langle \phi_x \rangle < \omega_+$ . In this region the dynamic state without spatial structure,  $\phi = \phi(t)$ , which corresponds to the McCumber branch (MCB) in the  $I-V$  characteristic, becomes unstable (to small perturbations). As a result a switching occurs to a dynamic state with a spatial one-soliton structure which corresponds to the first zero-field step (ZFS 1) in the  $I-V$  characteristic. The transition which may involve creation of breather-modes [7]

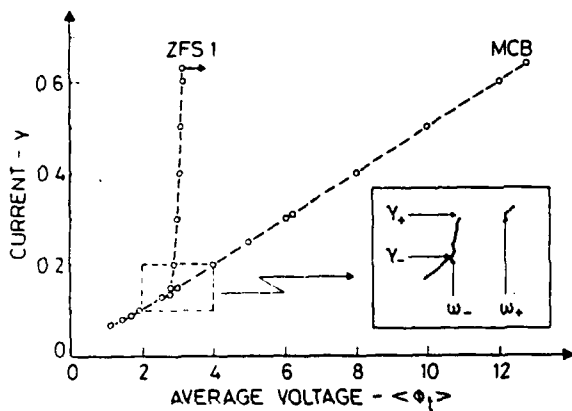


Fig. 1  $I$ - $V$  characteristic calculation from eqs. (1) and (2a) using  $\alpha = 0.05$ ,  $\beta = 0.02$ ,  $I = 2$ , and  $\eta = 0$ , showing the McCumber background curve (MCB) and the first zero-field step (ZFS 1). Inset shows in detail how ZFS 1 joins MCB.

will be an interesting object to study by means of spectral methods.

Fig. 2 illustrates the corresponding experimental findings both at the first and second zero-field steps (ZFS 1 and ZFS 2). In the two cases one and two solitons respectively are travelling back and forth on the oscillator in different configurations [8].

A stability analysis is carried out for  $\eta = 0$  using

$$\phi(x, t) = \phi_0(t) + \tilde{\phi}(x, t). \quad (3)$$

Here  $\phi_0(t)$  is the McCumber solution in the power-balance approximation [9]

$$\phi_0(t) = 2 \operatorname{am} [t/k; k], \quad (3a)$$

where  $\operatorname{am}$  is the Jacobian elliptic function of modulus  $k$ , and  $k$  satisfies

$$\gamma = 4\alpha E(k)/\pi k, \quad (3b)$$

$E(k)$  being the complete elliptic integral of second kind. The small perturbation  $\tilde{\phi}(x, t)$  is given by

$$\tilde{\phi}(x, t) = y(t) \exp(i b x) \quad (3c)$$

with  $b = n\pi/l$ ,  $n = 0, 1, 2, \dots$ . Insertion into eqs. (1) and (2a) yields the damped Hill's equation

$$\ddot{y} + (\alpha + \beta b^2) \dot{y} + \{b + \cos \phi_0(t)\} y = 0. \quad (4)$$

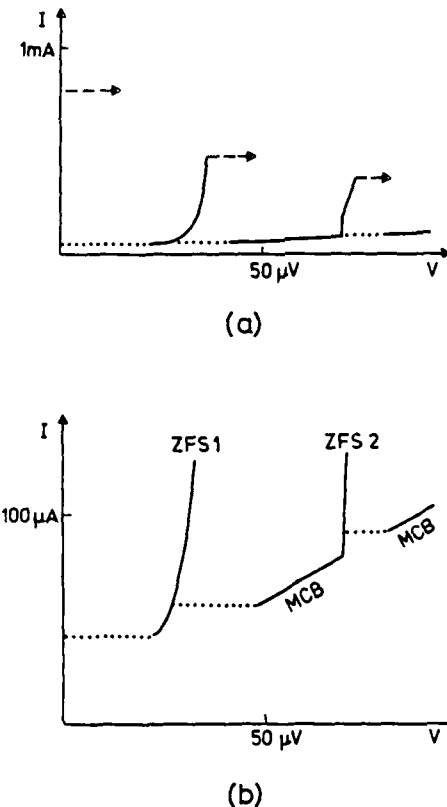


Fig. 2. (a) Detail of the  $I$ - $V$  characteristic of Nb-Nb<sub>2</sub>O<sub>5</sub>-Pb overlap junction (experimental sample S6-7/4 with  $I = 4.4$  and  $\alpha = 0.006$  at 4.2 K) measured at a temperature slightly below the transition temperature of the lead counter electrode and in zero magnetic field. Arrows indicate switching to gap state. (b) Same characteristic with  $10 \times$ -magnified current scale. Dotted lines indicate switching from higher-voltage to lower-voltage states.

where overdots denote differentiation with respect to  $t$ . For small  $k$ 's the stability boundaries for the average voltage,  $\omega_+$  and  $\omega_-$ , are determined approximately as solutions to the equations

$$\begin{aligned} b^2 &= \left(\frac{\omega}{2}\right)^2 + \frac{1}{2\omega^2} \left(1 - \frac{1}{8\omega^4}\right) \\ &\pm \frac{1}{2} \left[ \left(1 - \frac{1}{8\omega^4}\right)^2 - \omega^2(\alpha + \beta b^2) \right]^{1/2} \\ &- \frac{1}{8\omega^2} \left(1 - \frac{1}{8\omega^4}\right)^2. \end{aligned} \quad (5)$$

Fig. 3. Stability boundaries as a function of current (circles) and stability boundaries for  $\eta = 0.16$  and  $\eta = 0.17$ .

For small  $k$  the stability boundaries are given by a general complex equation. For reduced the boundary equation is given.

Fig. 3 shows the stability boundaries experimentally obtained in a magnetic field. These obtain the stability boundaries for  $\eta = 0$ . varying  $\beta$  and  $\tau$  the curves. at  $\beta$  and  $\tau$  experimentally obtainable. The be due to the theoretical values of the parameters. In Fig. 1 the results obtained in a magnetic field are compared with the theoretical results obtained in a magnetic field. The agreement between the theoretical and experimental results is good.

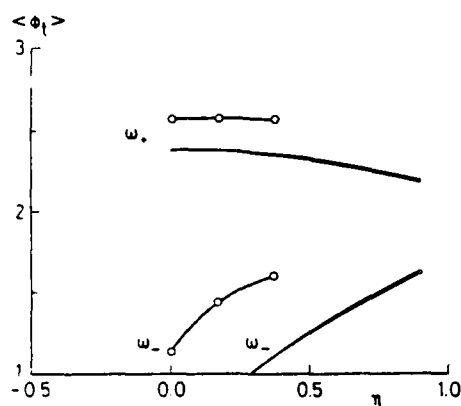


Fig. 3. Stability boundaries for ZFS 1 in average voltage  $\langle \phi_t \rangle$  as a function of magnetic field  $\eta$  measured experimentally (circles) and calculated from approximative equations for stability boundaries (solid curves). Parameter values:  $\alpha = 0.026$ ,  $I = 3.16$  and  $0 < \beta < 0.07$ .

For small values of  $\eta$  ( $\neq 0$ ) the stability boundaries have been determined approximately by a generalization of the method leading to more complex equations than (5). Parmentier [10] has reduced the damped Hill's equation (4) to a Lamé equation for which exact stability boundaries are given.

Fig. 3 shows a comparison between the experimentally determined stability boundaries (circles) in a magnetic field associated with ZFS 1 and those obtained from approximative equations for stability boundaries (eq. (5) and its generalization for  $\eta \neq 0$ ), shown as solid curves. The effect of varying  $\beta$  is indicated by the slight thickening of the curves. The instability region becomes smaller as  $\beta$  and  $\eta$  are increased. The agreement between experimental and theoretical values for  $\omega_+$  is reasonable. The discrepancy for the  $\omega_-$  branch may be due to the fact that the approximations used in the theoretical expression are poorer for low values of the average voltage.

In fig. 1 the numerical procedure predicts  $\gamma_+ = 0.1712$  and  $\gamma_- = 0.1401$ , while eq. (5) leads to  $\gamma_+ = 0.1711$  and  $\gamma_- = 0.1404$ . Thus, the agreement between the computational results and the results obtained by stability theory is very good.

### 3. The circular Josephson oscillator

So far, we have focussed on the instabilities of the dynamic states on the linear oscillator. In this section we shall demonstrate the extraordinary stability of the dynamic state in which one soliton rotates on the circular junction. Thermal noise or external microwave radiation is unable to perturb the soliton velocity much from the power-balance velocity predicted by perturbation theory [11]. As a result the electromagnetic radiation emitted by the oscillator has a very well-defined frequency. Experimentally, a line-width of less than 5 kHz at a resonance frequency of 10 GHz has been found. A relative accuracy of about  $10^{-8}$  is therefore required for computational line-width determinations. We have performed simulations of eqs. (1) and (2b) with this degree of accuracy on a CRAY-1-S vector processor. In the case of microwave radiation,  $\gamma$  in eq. (1) was replaced by

$$\gamma = \gamma_{dc} + \gamma_{ac} \sin(\Omega t), \quad (1a)$$

where  $\gamma_{dc}$  is a constant, and  $\gamma_{ac}$  and  $\Omega$  are amplitude and frequency of the microwave.

In fig. 4 the solid curve is the resulting computational determination of the line-width as the standard deviation of the electromagnetic radiation frequency,  $\sigma_f$ , versus microwave frequency,  $\Omega$ .

A perturbation theory using

$$\phi(x, t) = \phi^s(x, t) + \tilde{\phi}(t), \quad (6)$$

where  $\phi^s(x, t)$  is the travelling soliton and  $\tilde{\phi}(t)$  is a small background, leads to the ordinary differential equation for  $\tilde{\phi}(t)$

$$-\ddot{\tilde{\phi}} - \sin \tilde{\phi} = \dot{\alpha} \tilde{\phi} + \gamma_{dc} + \gamma_{ac} \sin(\Omega t) \quad (7)$$

as well as a determination of the soliton velocity  $u(t)$ . The soliton revolution time,  $T_n$  (and the corresponding frequency,  $f_n = 1/T_n$ ) has first been determined from the equation

$$\frac{2\pi}{T} \int_t^{t+T_n} u(t) dt = 2\pi, \quad (8a)$$

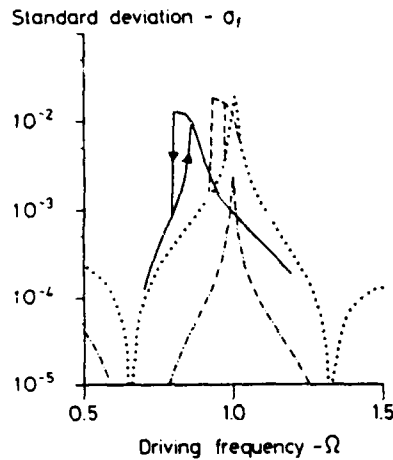


Fig. 4. Standard deviation of electromagnetic radiation frequency,  $\sigma_r$ , versus microwave frequency  $\Omega$ . Parameters in eqs. (1), (1a) and (2b):  $\alpha = 0.01$ ,  $\beta = 0$ ,  $\gamma_{dc} = 0.02$ ,  $\gamma_{ac} = 0.01$ , and  $I = 8$ . Solid curve: computational result. Dashed-dotted curve: perturbative result from eq. (8a). Dotted curve: perturbative result from eq. (8b) using linearized version of eq. (7). Dashed curve: perturbative result from eq. (8b) using full eq. (7). Dotted and dashed curves overlap away from resonance region.

which yields the dashed-dotted curve in fig. 4 in poor agreement with the solid curve. Realizing that the main contribution to the line-width stems from the background radiation,  $\tilde{\phi}(t)$ , and not from perturbations of the soliton velocity,  $u(t)$ , we replace eq. (8a) by

$$\frac{2\pi}{I} \int_t^{t+T_n} u(t) dt + \tilde{\phi}(t+T_n) - \tilde{\phi}(t) = 2\pi \quad (8b)$$

and find the dotted curve, when a linearized version of eq. (7) is used. The hysteresis phenomenon is recovered (dashed curve in fig. 4), when the full eq. (7) is used. The level of the line-width is now predicted correctly by the perturbation theory while the location of the maximum is still predicted at a slightly too high frequency.

#### 4. Conclusion

The results presented in this paper demonstrate that the Josephson junction in combination with

the sine-Gordon model is an excellent testing ground for nonlinear phenomena in the sense that computational results and theoretical predictions can be verified by comparison with experimental measurements. In this paper we have only considered soliton dynamic states and their instabilities. Chaotic phenomena also occur on the Josephson junction. To predict these theoretically, Melnikov-Arnold techniques which apply to low-dimensional systems (see e.g. [12]) must be generalized to many-dimensional systems.

#### Acknowledgements

The financial support of the Danish Council for Scientific and Industrial Research and of the European Research Office of the United States Army through contract No. DAJA-45-85-C-0042 is acknowledged.

#### References

- [1] S. Pagano, M.P. Soerensen, R.D. Parmentier, P.L. Christiansen, O. Skovgaard, N.F. Pedersen, J. Mygind and M.R. Samuels, Phys. Rev. B 33 (1986) 174.
- [2] F. If, P.L. Christiansen, R.D. Parmentier, O. Skovgaard and M.P. Soerensen, Phys. Rev. B 32 (1985) 1512.
- [3] M. Fordsmann, P.L. Christiansen and F. If, Phys. Lett. A 116 (1986) 71.
- [4] A.C. Scott, F.Y.F. Chu and S.A. Reible, J. Appl. Phys. 47 (1976) 3272.
- [5] K. Enpuku, K. Yoshida and F. Irie, J. Appl. Phys. 52 (1981) 344.
- [6] M.P. Soerensen, R.D. Parmentier, P.L. Christiansen, O. Skovgaard, B. Dueholm, E. Joergensen, V.P. Koshelets, O.A. Levring, R. Monaco, J. Mygind, N.F. Pedersen and M.R. Samuels, Phys. Rev. B 30 (1984) 2640.
- [7] D.W. McLaughlin and N. Ercolani, private communication.
- [8] P.S. Lomdahl, O.H. Soerensen and P.L. Christiansen, Phys. Rev. B 25 (1982) 5737.
- [9] R.D. Parmentier, in Solitons in Action, K. Lonngren and A.C. Scott, eds. (Academic, New York, 1978) p. 173.
- [10] R.D. Parmentier, private communication.
- [11] D.W. McLaughlin and A.C. Scott, Phys. Rev. A 18 (1978) 1652.
- [12] M. Bartuccelli, P.L. Christiansen, N.F. Pedersen and M.P. Soerensen, Phys. Rev. B 33 (1986) 4686.

## "HORSESHOE CHAOS" IN THE SPACE-INDEPENDENT DOUBLE SINE-GORDON SYSTEM

M. BARTUCCHELLI and P.L. CHRISTIANSEN

*Laboratory of Applied Mathematical Physics, The Technical University of Denmark, DK-2800 Lyngby, Denmark*

N.F. PEDERSEN

*Physics Laboratory I, The Technical University of Denmark, DK-2800 Lyngby, Denmark*

M. SALERNO

*Dipartimento di Fisica Teorica, Università di Salerno, 84100 Salerno, Italy*

Received 5 May 1986

For the driven, damped space-independent double sine-Gordon equation threshold curves for horseshoe chaos of the Smale type are derived by the Melnikov technique. Different qualitative behaviour of the solutions is found in different regions of parameter space.

### I. Introduction

During the past years a great deal of interest has been devoted to the study of the motion of simple nonlinear oscillators in the presence of dissipation and periodic forcing terms (see [1, 2], e.g., and references therein).

In particular the dynamics of a single classical particle moving in a sinusoidal potential under the influence of damping and bias was extensively studied owing to its relevance for specific physical systems such as for example Josephson junctions. Numerical tools such as Poincaré sections, Liapunov exponents, power spectra analysis, etc. [1] and analytical ones, e.g. the Melnikov-Arnold technique [1] were used to characterize the great variety of responses of the system (as a parameter is varied in the equations), ranging from multiperiodic motion to a fully chaotic one.

In view of more general applications in solid state matter, it is of interest to extend the above studies to the case in which the potential is periodic *but not* sinusoidal. A first step in this direction is to consider single particles moving in potentials which are the superposition of two sinusoidal potentials of the types  $\lambda_1(1 - \cos \phi)$  and  $\lambda_2(1 - \cos(\phi/2))$  respectively under the influence of loss and bias. This leads to the study of the following equation:

$$\phi_{tt} = -\lambda_1 \sin \phi - \frac{1}{2}\lambda_2 \sin \frac{1}{2}\phi + \epsilon[A \cos(\omega t) - \alpha \phi_t]. \quad (1)$$

When  $\epsilon = 0$ , (1) is recognized as the (space-independent) double sine-Gordon equation, which is known to play an important role in condensed matter physics [3, 4] (for a mechanical analog of it, see [5]). The  $\epsilon$ -term in (1) represents a generic structural perturbation consisting of a loss term ( $\alpha \phi_t$ ) and a time-dependent periodic bias, present in physical systems with driving forces. As a result of such perturbation,

the integrability of (1) (i.e. when  $\epsilon = 0$ ) is broken. For particular values of  $A, \alpha, \omega$ , this gives rise to the appearance of the so-called 'Smale horseshoe' [1] in the Poincaré map of (1). The aim of the present paper is to analytically investigate the dynamical behaviour of system (1). More precisely, by using the Melnikov-Arnold technique with given values of  $\lambda_1, \lambda_2$  in (1) we will determine values of the parameters  $A, \omega, \alpha$ , for which horseshoe-chaos is predicted. To this end we first briefly recall in the next section the Melnikov-Arnold technique. Then, in Section 3, we study the phase portraits of the unperturbed equation (1) ( $\epsilon = 0$ ), as  $\lambda_1, \lambda_2$  are varied in the range  $(-\infty, +\infty)$ . Finally, in Section 4, we apply the Melnikov-Arnold method to (1) and derive for different cases (corresponding to different values of  $\lambda_1, \lambda_2$ ) parameter values of  $A, \alpha, \omega$ , for which chaos is predicted. The last section contains a discussion of the main results of the paper.

## 2. Melnikov's function

We start by briefly recalling the main ideas behind Melnikov's method (a full treatment is found in [1]). We consider a system of two ordinary differential equations of the form

$$\frac{d\phi}{dt} = f_0(\phi, y) + \epsilon f_1(\phi, y, \epsilon, t), \quad \frac{dy}{dt} = g_0(\phi, y) + \epsilon g_1(\phi, y, \epsilon, t) \quad (2)$$

or, in short notation,

$$\frac{dX}{dt} = h_0(X) + \epsilon h_1(X, t, \epsilon) \quad (3)$$

where  $X = (\phi, y)$ ,  $h_0 = (f_0, g_0)$ , and  $h_1 = (f_1, g_1)$ . For system (2) the following conditions are assumed to be satisfied:

- (a) When  $\epsilon = 0$ , the system has an equilibrium point of the centre type at some point  $(\phi_0, y_0)$ , which for simplicity we assume to be simple.
- (b) The functions  $f_0(\phi, y)$  and  $g_0(\phi, y)$  are analytical in  $\phi$  and  $y$  in a sufficiently large neighbourhood of the point  $(\phi_0, y_0)$ .
- (c) The functions  $f_1(\phi, y, \epsilon, t)$  and  $g_1(\phi, y, \epsilon, t)$  are analytical in  $(\phi, y)$  in a sufficiently large neighbourhood of  $(\phi_0, y_0)$  and for all  $|\epsilon| < \epsilon_0$ . They are continuous and periodic in  $t$  with period  $2\pi$ .
- (d) For  $\epsilon = 0$ , system (2) possesses a homoclinic orbit, which we denote by

$$X(t) = (\phi(t), y(t)), \quad (4)$$

to a hyperbolic saddle point  $X_s = (\phi_s, y_s)$ . Observe that these conditions are all satisfied for our system (1). In what follows we also consider the case in which the unperturbed system has heteroclinic cycles connecting several saddle points.

With the assumptions (a)-(d) it can be shown [1] that for  $\epsilon$  small enough the saddle equilibrium point  $X_s = (\phi_s, y_s)$  gets perturbed to a saddle fix point  $X_\epsilon = (\phi_\epsilon, y_\epsilon)$  of the Poincaré map for (2).

In addition, the perturbed homoclinic orbit splits up into a stable orbit denoted by  $X_\epsilon^s(t, t_0)$  defined in the interval  $t_0 \leq t < \infty$ , and an unstable orbit  $X_\epsilon^u(t, t_0)$  defined in the interval  $-\infty < t \leq t_0$ . With  $t_0$  denoting the initial time the following results apply [6]:

$$X_\epsilon^p(t, t_0) = X(t - t_0) + \epsilon X_1^p(t, t_0) + O(\epsilon^2) \quad \begin{cases} t \in [t_0, \infty[, & p = s \\ t \in ]-\infty, t_0], & p = u \end{cases} \quad (5)$$

and

$$\frac{dX_1^p(t, t_0)}{dt} = D_x h_0[X(t - t_0)] X_1^p(t, t_0) + h_1[X(t - t_0), t] \quad (6)$$

where the index  $p$  may assume the values  $u$  (unstable orbit) and  $s$  (stable orbit), and  $D_x$  denotes the partial derivative with respect to  $x$ . Note that the initial time,  $t_0$ , appears explicitly, since solutions of the perturbed system are not invariant under arbitrary time translations ((2) is in general non-autonomous for  $\varepsilon \neq 0$ ).

To first order, the separation between  $X^u(t_0, t_0)$  and  $X^s(t_0, t_0)$  is found by taking the scalar product between  $(X^u - X^s)$  and a unit vector transverse to  $h_0(X(t_0))$ . In short notation, this separation,  $d(t_0)$ , may be expressed as

$$d(t_0) = \frac{\varepsilon h_0[X(0)] \wedge [X^u(t_0, t_0) - X^s(t_0, t_0)] + O(\varepsilon^2)}{|h_0[X(0)]|}. \quad (7)$$

Here the wedge product is defined by  $X \wedge Y = X_1 Y_2 - X_2 Y_1$ , and  $h_0 \wedge [X^u - X^s]$  is the projection of  $[X^u - X^s]$  into  $h_0$ .

The so-called Melnikov function is proportional to the distance  $d(t_0)$  between the stable and unstable manifolds in the Poincaré map at  $t_0$ , and its expression (valid on long time scale), is given by (for details, see [1])

$$M(t_0) = \int_{-\infty}^{\infty} h_0[X(t-t_0)] \wedge h_1[X(t-t_0), t] \exp \left\{ - \int_0^{t-t_0} \text{Trace } D_x h_0[X(s)] ds \right\} dt. \quad (8)$$

If  $M(t_0)$  has a simple zero independent of  $\varepsilon$ , and if  $dM/dt \neq 0$  at  $t = t_0$  is satisfied, then the local stable and unstable manifolds intersect transversely. Such transverse intersection implies infinitely many others, this giving rise (in the Poincaré map) to the appearance of a fractal invariant hyperbolic set called the Smale horseshoe [1]. A Smale horseshoe is structurally stable and contains a countable set of unstable periodic orbits, an uncountable set of bounded nonperiodic orbits, and a dense orbit.

In the following we will use the existence of a Smale horseshoe (i.e.  $M(t_0) = 0$ ,  $dM/dt \neq 0$  at  $t = t_0$ ) as a criterion of the onset of chaos.

### 3. Phase space analysis

Before applying the Melnikov method to equation (1) it is of interest to study how the phase space portraits of the unperturbed equation (here written as a first order system)

$$\dot{\phi} = y, \quad \dot{y} = -\lambda_1 \sin \phi - \frac{1}{2}\lambda_2 \sin \frac{1}{2}\phi \quad (9)$$

change when  $\lambda_1, \lambda_2$  are varied in the range  $(-\infty, +\infty)$ . To this end we first observe that (9) is a Hamiltonian system with the Hamiltonian given by

$$H(\phi, y) = \frac{1}{2}y^2 + \lambda_1(1 - \cos \phi) + \lambda_2[1 - \cos \frac{1}{2}\phi]. \quad (10)$$

Because of the periodicity of (10) we can restrict ourselves to the range of  $-2\pi \leq \phi \leq 2\pi$ . Furthermore, we note that the general case  $\lambda_1, \lambda_2 \in (-\infty, +\infty)$  in (9) can always be reduced to the case in which  $|\lambda_1| = 1$  and  $\lambda_2 \in (0, +\infty)$  by shifting  $\phi \rightarrow \phi + 2\pi$  (in order to change sign to  $\lambda_2$ ), and by rescaling time (in order to normalize  $\lambda_1$ ). Without loss of generality we shall therefore concentrate on the cylindrical phase space ( $-2\pi \leq \phi \leq 2\pi$ ) of system (9) in the cases

- (a)  $\lambda_1 = -1, \lambda_2 = \lambda$ ,
- (b)  $\lambda_1 = 1, \lambda_2 = \lambda$ .

In cases  $\lambda_1 = -1$  and  $\lambda > 0$  one easily finds that when  $0 < \lambda < 4$  the system (2) has fixed points of centre type at

$$(\phi, y) = [\pm 2 \cos^{-1}(\frac{1}{4}\lambda) + 4k\pi, 0], \quad k = 0, \pm 1, \pm 2, \dots$$

and fixed points of saddle type at

$$(\phi, y) = (2n\pi, 0), \quad n = 0, \pm 1, \pm 2, \dots$$

The level set  $H(\phi, y) = 0$  is composed of two homoclinic orbits based at

$$(\phi, y) = \left[ \pm 4 \operatorname{tg}^{-1} \left( \sqrt{\frac{4-\lambda}{\lambda}} \right), 0 \right].$$

We shall denote these two homoclinic orbits by  $(\bar{\phi}_{-1}^{\pm}, \bar{y}_{-1}^{\pm})$ . They are given by the following analytical expression (see Fig. 1(a)):

$$\begin{cases} \bar{\phi}_{-1}^{\pm}(t) = \pm 4 \operatorname{tg}^{-1} \left[ \sqrt{\frac{4-\lambda}{\lambda}} \operatorname{sech} \left( \sqrt{\frac{4-\lambda}{4}} t \right) \right], \\ \bar{y}_{-1}^{\pm}(t) = \frac{\mp 2\sqrt{\lambda}(4-\lambda) \operatorname{sech} \left[ \sqrt{\frac{4-\lambda}{4}} t \right] \left\{ \operatorname{tgh} \left[ \left( \sqrt{\frac{4-\lambda}{4}} \right) t \right] \right\}}{\lambda + (4-\lambda) \operatorname{sech}^2 \left( \sqrt{\frac{4-\lambda}{4}} t \right)}. \end{cases} \quad (11)$$

Besides, two heteroclinic orbits  $(\hat{\phi}_{-1}^{\pm}, \hat{y}_{-1}^{\pm})$  exist from  $(-2\pi, 0)$  at  $t = -\infty$  to  $(2\pi, 0)$  at  $t = +\infty$ , which have the following analytical expressions (see Fig. 1(a)):

$$\begin{cases} \hat{\phi}_{-1}^{\pm}(t) = \pm 4 \operatorname{tg}^{-1} \left[ \sqrt{\frac{\lambda}{4+\lambda}} \sinh(\sqrt{1+\frac{1}{4}\lambda} t) \right], \\ \hat{y}_{-1}^{\pm}(t) = \frac{\pm 2\sqrt{\lambda}(4+\lambda) \cosh[(\sqrt{1+\frac{1}{4}\lambda})t]}{4+\lambda + \lambda \sinh^2[(\sqrt{1+\frac{1}{4}\lambda})t]}. \end{cases} \quad (12)$$

When  $\lambda_1 = -1$  and  $\lambda_2 = \lambda \geq 4$  the system (9) has fixed points of centre type at

$$(\phi, y) = (4m\pi, 0), \quad m = 0, \pm 1, \pm 2, \dots,$$

and fixed points of saddle type at

$$(\phi, y) = [(4l+2)\pi, 0], \quad l = 0, \pm 1, \pm 2, \dots$$

Further, the level set

$$H(\phi, y) = 2\lambda$$

is composed of two heteroclinic orbits  $(\hat{\phi}_{-1}^{\pm}, \hat{y}_{-1}^{\pm})$  based at  $(\phi, y) = (\pm 2\pi, 0)$  having the same analytical expressions as in (12). We note that in this case the homoclinic orbit (11) disappears (see Fig. 1(b)).

Now we shall analyze the case when  $\lambda_1 = 1$  and  $\lambda_2 = \lambda > 0$ . One finds that for  $0 < \lambda < 4$  system (9) has fixed points of centre type at

$$(\phi, y) = (2n\pi, 0), \quad n = 0, \pm 1, \pm 2, \dots$$

and fixed points of saddle type at

$$(\phi, y) = [2\pi + 2 \cos^{-1}(-\frac{1}{4}\lambda) + 4n\pi, 0], \quad n = 0, \pm 1, \pm 2, \dots$$

The level set  $H(\phi, y) = (\lambda^2 + 8\lambda + 16)/8$  is composed of two heteroclinic orbits based at

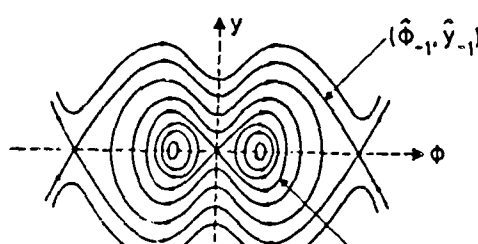
$$(\phi, y) = [2\pi \pm 2 \cos^{-1}(-\frac{1}{4}\lambda), 0].$$

We shall denote these two heteroclinic orbits by  $(\bar{\phi}_1^*, \bar{y}_1^*)$ . They are given by the following analytical expressions (see Fig. 2):

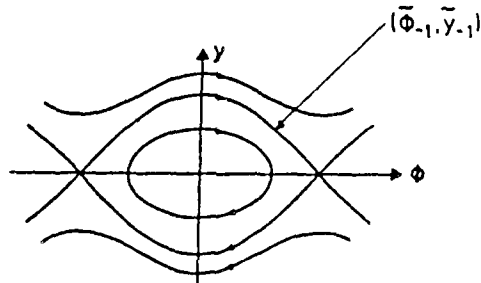
$$\begin{cases} \bar{\phi}_1^*(t) = \pm 4 \operatorname{tg}^{-1} \left[ \sqrt{\frac{4-\lambda}{4+\lambda}} \operatorname{tgh} \left( \frac{\sqrt{16-\lambda^2}}{8} t \right) \right] + 2\pi, \\ \bar{y}_1^*(t) = \frac{(16-\lambda^2) \operatorname{sech}^2 \left( \sqrt{\frac{16-\lambda^2}{64}} t \right)}{2 \left[ 4 + \lambda + (4 - \lambda) \operatorname{tgh}^2 \left( \sqrt{\frac{16-\lambda^2}{64}} t \right) \right]}. \end{cases} \quad (13)$$

Furthermore, two heteroclinic orbits exist based at

$$(\phi, y) = [\pm 2\pi \mp 2 \cos^{-1}(-\frac{1}{4}\lambda), 0]$$



(a)



(b)

Fig. 1. Phase space diagram for the Hamiltonian (10). (a) Phase space diagram when  $\lambda_1 \approx -1$ ,  $0 < \lambda < 4$ . (b) Phase space diagram when  $\lambda_1 \approx -1$ ,  $\lambda > 4$ .

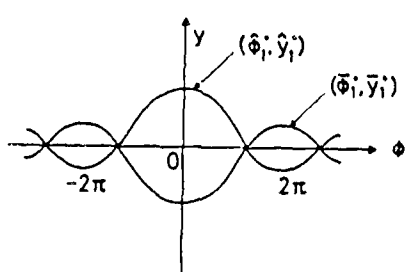


Fig. 2. Heteroclinic orbits (13) and (14).

having the following analytical expressions (see Fig. 2):

$$\begin{cases} \hat{\phi}_1^*(t) = \pm 4 \operatorname{tg}^{-1} \left[ \sqrt{\frac{4+\lambda}{4-\lambda}} \operatorname{tgh} \left( \frac{\sqrt{16-\lambda^2}}{8} t \right) \right], \\ \hat{y}_1^*(t) = \pm \frac{(16-\lambda^2) \operatorname{sech}^2 \left( \frac{\sqrt{16-\lambda^2}}{8} t \right)}{2 \left[ 4 - \lambda + (4+\lambda) \operatorname{tgh}^2 \left( \frac{\sqrt{16-\lambda^2}}{8} t \right) \right]}. \end{cases} \quad (14)$$

If  $\lambda_1 = 1$  and  $\lambda_2 = \lambda > 4$ , system (9) has fixed points of centre type at

$$(\phi, y) = (4l\pi, 0), \quad l = 0, \pm 1, \pm 2, \dots$$

and fixed points of saddle type at

$$(\phi, y) = [(4l+2)\pi, 0], \quad l = 0, \pm 1, \pm 2, \dots$$

The level set  $H(\phi, y) = 2\lambda$  is composed of two heteroclinic orbits based at  $(\phi, y) = (\pm 2\pi, 0)$  with analytical expressions given by (the phase space in this case looks like Fig. 1(b))

$$\begin{cases} \tilde{\phi}_1^*(t) = \pm 4 \operatorname{tg}^{-1} \left[ \sqrt{\frac{\lambda}{\lambda-4}} \operatorname{sinh} \left( \sqrt{\frac{\lambda-4}{4}} t \right) \right], \\ \tilde{y}_1^*(t) = \pm \frac{2\sqrt{\lambda(\lambda-4)} \cosh \left( \sqrt{\frac{\lambda-4}{4}} t \right)}{(\lambda-4) + \lambda \operatorname{sinh}^2 \left( \sqrt{\frac{\lambda-4}{4}} t \right)}. \end{cases} \quad (15)$$

#### 4. Melnikov's method for the double sine-Gordon system

In this section we shall apply Melnikov's method to system (1) in the various cases analyzed in the previous section.

We start with the case  $\lambda_1 = -1, 0 < \lambda < 4$ . Using the homoclinic orbits (11), the Melnikov function reads.

$$\begin{aligned} M^*(t_0, \lambda, A, \omega, \alpha) &= \int_{-\infty}^{+\infty} \tilde{y}_{-1}^*(t) [A \cos(\omega t + \omega t_0) - \alpha \tilde{y}_{-1}^*(t)] dt \\ &= \left\{ \mp \int_{-\infty}^{+\infty} \frac{2\sqrt{\lambda}(4-\lambda) \operatorname{sech} \left[ \sqrt{\frac{4-\lambda}{4}} t \right] \operatorname{tgh} \left[ \sqrt{\frac{4-\lambda}{4}} t \right]}{\lambda + (4-\lambda) \operatorname{sech}^2 \left( \sqrt{\frac{4-\lambda}{4}} t \right)} [A \cos(\omega t + \omega t_0)] dt \right\} \\ &\quad - \alpha \int_{-\infty}^{+\infty} \left\{ \frac{2\sqrt{\lambda}(4-\lambda) \operatorname{sech} \left[ \sqrt{\frac{4-\lambda}{4}} t \right] \operatorname{tgh} \left[ \sqrt{\frac{4-\lambda}{4}} t \right]}{\lambda + (4-\lambda) \operatorname{sech}^2 \left( \sqrt{\frac{4-\lambda}{4}} t \right)} \right\}^2 dt. \end{aligned} \quad (16)$$

Making the cosine term explicit and observing that  $\int_{-\infty}^{+\infty} y_{-1}^*(t) \cos(\omega t) dt = 0$ , because it is the integral of an odd function, we get

$$M^*(t_0, \lambda, A, \omega, \alpha) = A\bar{R}_{-1}(\lambda, \omega) \sin(\omega t_0) - \alpha\bar{F}_{-1}(\lambda), \quad (17)$$

where

$$\bar{F}_{-1}(\lambda) = \int_{-\infty}^{+\infty} \left\{ \frac{2\sqrt{\lambda}(4-\lambda) \operatorname{sech}\left[\sqrt{\frac{4-\lambda}{4}}t\right] \operatorname{tgh}\left[\sqrt{\frac{4-\lambda}{4}}t\right]}{\lambda + (4-\lambda) \operatorname{sech}^2\left(\sqrt{\frac{4-\lambda}{4}}t\right)} \right\}^2 dt$$

and

$$\bar{R}_{-1}(\lambda, \omega) = \int_{-\infty}^{+\infty} \frac{2\sqrt{\lambda}(4-\lambda) \operatorname{sech}\left[\sqrt{\frac{4-\lambda}{4}}t\right] \operatorname{tgh}\left[\sqrt{\frac{4-\lambda}{4}}t\right]}{\lambda + (4-\lambda) \operatorname{sech}^2\left(\sqrt{\frac{4-\lambda}{4}}t\right)} \sin(\omega t) dt.$$

From (17) one sees that a necessary condition for  $M^*$  to have a zero is

$$\left| \frac{\alpha\bar{F}_{-1}(\lambda)}{A\bar{R}_{-1}(\lambda, \omega)} \right| \leq 1. \quad (18)$$

If the inequality (18) is strictly satisfied for all frequencies  $\omega$ , then the Melnikov function (16) has a simple zero. When (18) becomes an equality, the zero of  $M^*$  is nontransverse and this corresponds to the so-called tangential intersection ( $dM^*/dt = 0$  at  $t = t_0$ ).

The frequencies that will correspond to this case are

$$\omega = \frac{(2k+1)\pi}{2\tilde{t}_0}, \quad k = 0, \pm 1, \pm 2, \dots \quad (19)$$

where  $\tilde{t}_0$  is the value of  $t_0$  for which (17) becomes zero.

Then, if (18) is satisfied and

$$\omega \neq \frac{(2k+1)\pi}{2\tilde{t}_0}, \quad k = 0, \pm 1, \pm 2, \dots \quad (20)$$

we have that system (9) has in its dynamics the so-called Smale horseshoe chaos.

From relation (18) we can also obtain the threshold curve for getting a Smale horseshoe in the parameter space  $(\omega, \alpha, A)$ . If we fix one of these parameters and we consider the other two as functions of each other we can obtain different threshold curves. For example, fixing  $A$  we have the following threshold curve in the  $(\omega, \alpha)$  parameter space:

$$\alpha = \frac{A\bar{R}_{-1}(\lambda, \omega)}{\bar{F}_{-1}(\lambda)}, \quad A > 0 \text{ fixed}, 0 < \lambda < 4. \quad (21)$$

This curve (see Fig. 3) represents the bifurcation diagram under which system (1) has in its dynamics a specific kind of chaos (Smale horseshoe). In Figs. 3-6 the shaded regions correspond to negative value of  $\alpha$ , and curves for  $-\alpha$  are shown. In the parameter regions below the  $\alpha$ -curve horseshoe chaos occurs.

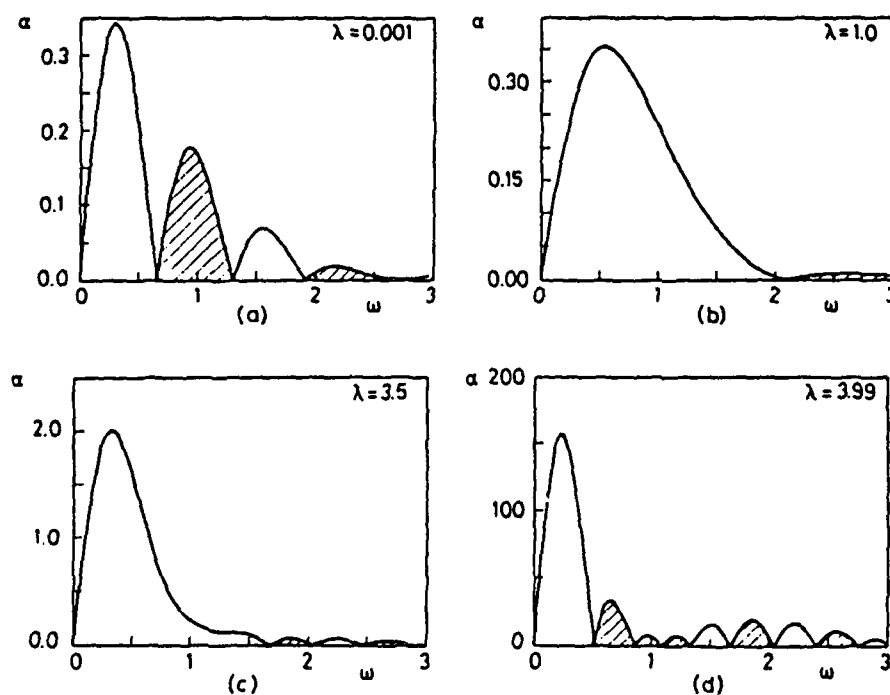


Fig. 3. Bifurcation curves for the homoclinic orbits (11) in the  $(\alpha, \omega)$  parametr space.  $A = 0.5$ ,  $\lambda_1 = -1$ . (a)  $\lambda = 0.001$ ; (b)  $\lambda = 1.0$ ; (c)  $\lambda = 3.5$ ; (d)  $\lambda = 3.99$ . Shaded regions:  $-\alpha$  is shown.

The same analysis can be carried out for the heteroclinic orbits  $(\hat{\phi}_{-1}, \hat{y}_{-1})$  in Fig. 1(a), this giving a threshold curve in the  $(\alpha, \omega)$  parameter space characterized by

$$\alpha = \frac{A \hat{R}_{-1}(\lambda, \omega)}{\hat{F}_{-1}(\lambda)}, \quad A > 0 \text{ fixed}, \quad 0 < \lambda < 4, \quad (22)$$

where

$$\hat{R}_{-1}(\lambda, \omega) = \int_{-\infty}^{+\infty} \frac{2\sqrt{\lambda}(4+\lambda) \cosh[\sqrt{1+\frac{1}{4}\lambda}t] \cos(\omega t)}{4+\lambda+\lambda \sinh^2[\sqrt{1+\frac{1}{4}\lambda}t]} dt$$

and

$$\hat{F}_{-1}(\lambda) = \int_{-\infty}^{+\infty} \left\{ \frac{2\sqrt{\lambda}(4+\lambda) \cosh[\sqrt{1+\frac{1}{4}\lambda}t]}{4+\lambda+\lambda \sinh^2[\sqrt{1+\frac{1}{4}\lambda}t]} \right\}^2 dt.$$

The threshold curve given by (22) is shown in Fig. 4 (the upper region delimited by the curve represents the chaotic region).

When  $\lambda_1 = -1$  and  $\lambda > 4$  we find that the bifurcation diagram for the orbit  $(\tilde{\phi}_{-1}, \tilde{y}_{-1})$  in Fig. 1(b) is equivalent to that of the orbit  $(\hat{\phi}_{-1}, \hat{y}_{-1})$  and therefore it is given by the same curve (22) (the only difference is that now  $\lambda > 4$ ) (see Fig. 5).

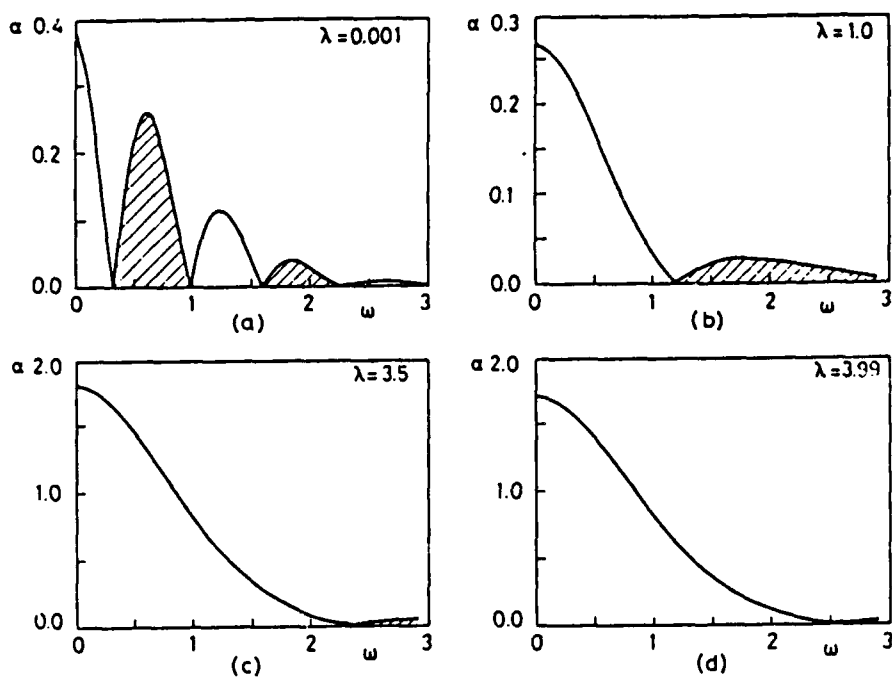


Fig. 4. Bifurcation curves for the heteroclinic orbit (12) in the  $(\alpha, \omega)$  parameter space.  $A = 0.5$ ,  $\lambda_1 = -1$ . (a)  $\lambda = 0.001$ ; (b)  $\lambda = 1.0$ ; (c)  $\lambda = 3.5$ ; (d)  $\lambda = 3.99$ . Shaded regions:  $-\alpha$  is shown.

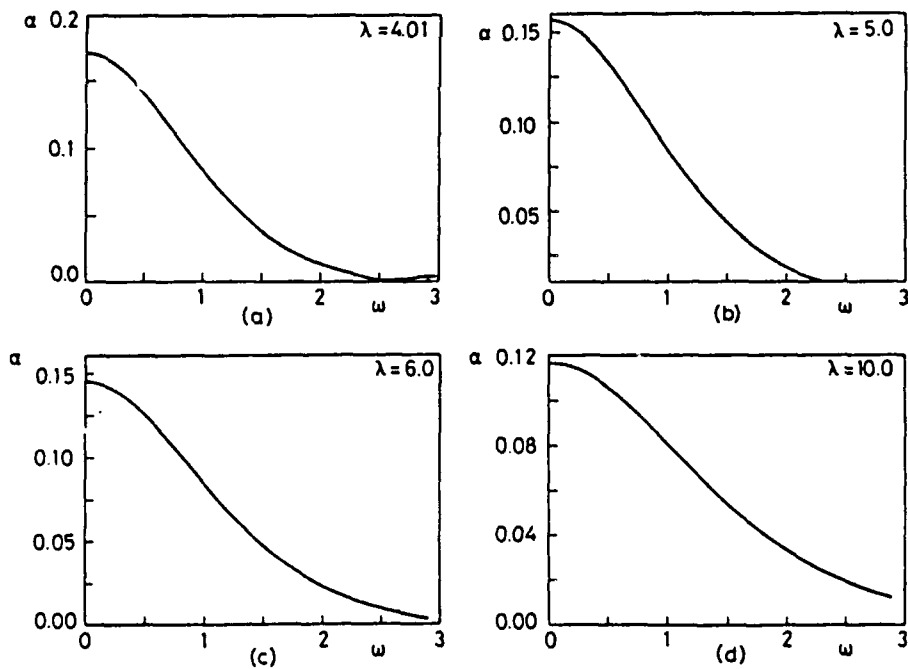


Fig. 5. Bifurcation curves for the heteroclinic orbit (12) in the  $(\alpha, \omega)$  parameter space.  $A = 0.5$ ,  $\lambda_1 = -1$ . (a)  $\lambda = 4.01$ ; (b)  $\lambda = 5.0$ ; (c)  $\lambda = 6.0$ ; (d)  $\lambda = 10.0$ . Shaded regions:  $-\alpha$  is shown.

In the case  $\lambda_1 = 1$ ,  $0 \leq \lambda < 4$ , using the heteroclinic orbit in (13) we have

$$\begin{aligned}
 M^*(t_0, \lambda, A, \omega, \alpha) &= \int_{-\infty}^{\infty} \bar{y}_1^*(t) [A \cos(\omega t + \omega_0 t) - \alpha \bar{y}_1^*(t)] dt \\
 &= \int_{-\infty}^{+\infty} \left\{ \frac{\pm(16 - \lambda^2) \operatorname{sech}^2\left(\sqrt{\frac{16 - \lambda^2}{64}} t\right)}{2 \left[ 4 + \lambda + (4 - \lambda) \operatorname{tgh}^2\left(\sqrt{\frac{16 - \lambda^2}{64}} t\right) \right]} [A \cos(\omega t)] dt \right\} \cos(\omega t_0) \\
 &\quad - \alpha \int_{-\infty}^{+\infty} \left\{ \frac{(16 - \lambda^2) \operatorname{sech}^2\left(\sqrt{\frac{16 - \lambda^2}{64}} t\right)}{2 \left[ 4 + \lambda + (4 - \lambda) \operatorname{tgh}^2\left(\sqrt{\frac{16 - \lambda^2}{64}} t\right) \right]} \right\}^2 dt
 \end{aligned} \tag{23}$$

For (23) to have a zero we must have

$$\left| \frac{\alpha \tilde{F}_1(\lambda)}{A \tilde{R}_1(\lambda, \omega)} \right| \leq 1 \tag{24}$$

where

$$\tilde{F}_1(\lambda) = \int_{-\infty}^{+\infty} \left\{ \frac{(16 - \lambda^2) \operatorname{sech}^2\left(\sqrt{\frac{16 - \lambda^2}{64}} t\right)}{2 \left[ 4 + \lambda + (4 - \lambda) \operatorname{tgh}^2\left(\sqrt{\frac{16 - \lambda^2}{64}} t\right) \right]} \right\}^2 dt$$

and

$$\tilde{R}_1(\lambda, \omega) = \int_{-\infty}^{+\infty} \frac{(16 - \lambda^2) \operatorname{sech}^2\left(\sqrt{\frac{16 - \lambda^2}{64}} t\right) \cos(\omega t)}{2 \left[ 4 + \lambda + (4 - \lambda) \operatorname{tgh}^2\left(\sqrt{\frac{16 - \lambda^2}{64}} t\right) \right]} dt.$$

In what follows we do not consider the calculations for finding the frequencies which correspond to the tangential intersection. As above they are very easily found.

The threshold curve in the  $(\alpha, \omega)$  parameter space reads

$$\alpha = \frac{A \tilde{R}_1(\lambda, \omega)}{\tilde{F}_1(\lambda)}, \quad A > 0 \text{ fixed}, \quad 0 \leq \lambda < 4. \tag{25}$$

This curve is shown in Fig. 6. In the case  $\lambda_1 = 1$  and  $0 \leq \lambda < 4$ , using the heteroclinic orbit (14), the Melnikov function becomes

$$\begin{aligned}
 M^*(t_0, \lambda, A, \omega, \alpha) &= \int_{-\infty}^{+\infty} \hat{y}^*(t) [A \cos(\omega t + \omega t_0) - \alpha \dot{y}^*(t)] dt \\
 &= \int_{-\infty}^{+\infty} \pm \left\{ \frac{(16 - \lambda^2) \operatorname{sech}^2 \left( \sqrt{\frac{16 - \lambda^2}{64}} t \right) A \cos(\omega t)}{2 \left[ 4 - \lambda + (4 + \lambda) \operatorname{tgh}^2 \left( \sqrt{\frac{16 - \lambda^2}{64}} t \right) \right]} dt \right\} \cos(\omega t_0) \\
 &\quad - \alpha \int_{-\infty}^{+\infty} \left\{ \frac{(16 - \lambda^2) \operatorname{sech}^2 \left( \sqrt{\frac{16 - \lambda^2}{64}} t \right)}{2 \left[ 4 - \lambda + (4 + \lambda) \operatorname{tgh}^2 \left( \sqrt{\frac{16 - \lambda^2}{64}} t \right) \right]} \right\}^2 dt. \tag{26}
 \end{aligned}$$

Making the same analysis as before we arrive at the following threshold curve:

$$\alpha = \frac{A \hat{R}_1(\lambda, \omega)}{\hat{F}_1(\lambda)}, \quad A > 0 \text{ fixed}, \quad 0 \leq \lambda < 4, \tag{27}$$

which we report in Fig. 7.

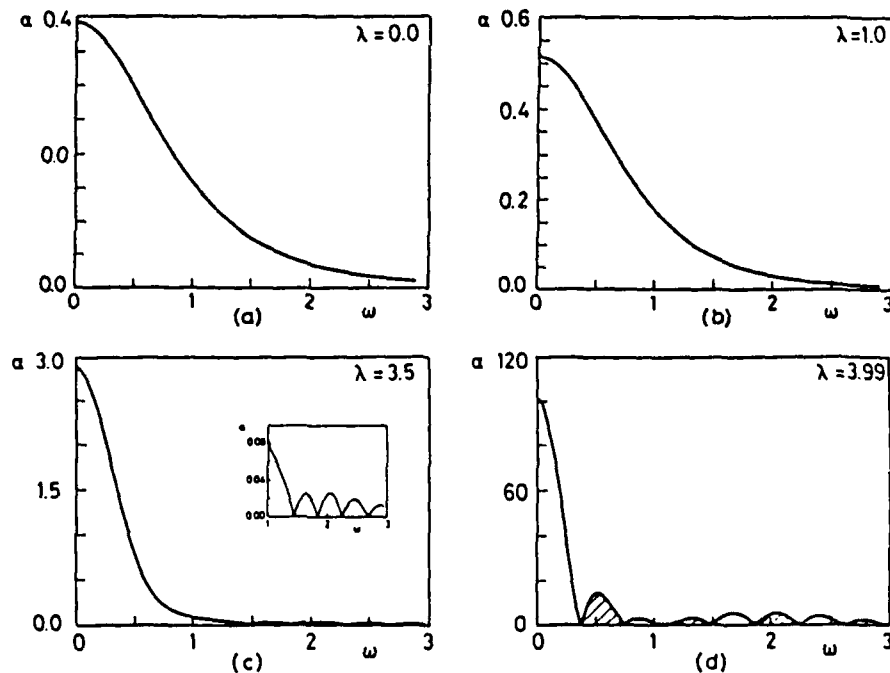


Fig. 6. Bifurcation curves for the heteroclinic orbit (13) in the  $(\alpha, \omega)$  parameter space.  $A = 0.5$ ,  $\lambda_1 = 1$ . (a)  $\lambda = 0.0$ ; (b)  $\lambda = 1.0$ ; (c)  $\lambda = 3.5$ ; (d)  $\lambda = 3.99$ . Note that when  $\lambda = 0.0$  one obtains the same bifurcation curve as that obtained for the classical pendulum. Shaded regions:  $-\alpha$  is shown.

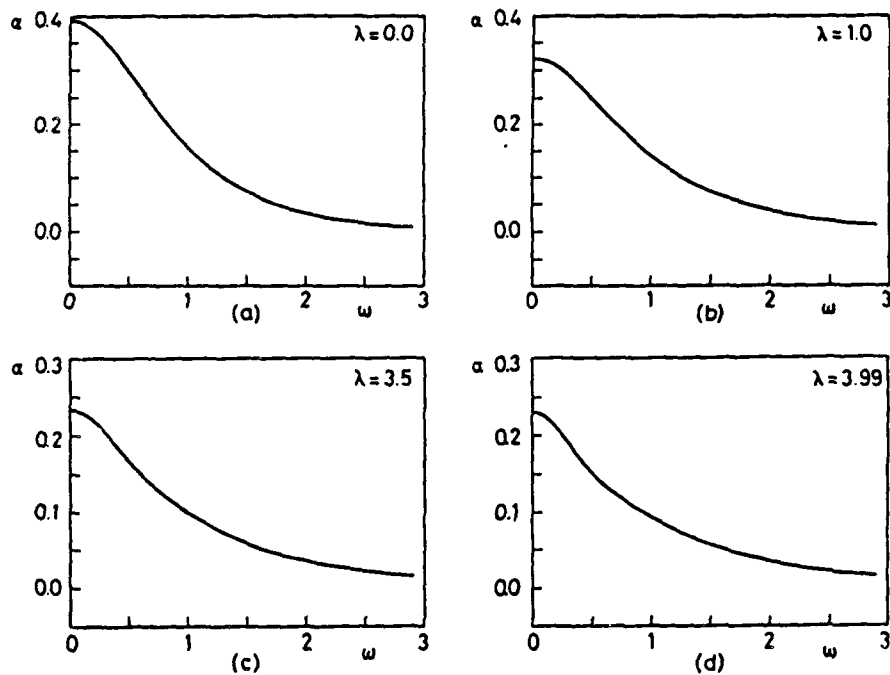


Fig. 7. Bifurcation curves for the heteroclinic orbit (14) in the  $(\alpha, \omega)$  parameter space.  $A = 0.5$ ,  $\lambda_1 = 1$ . (a)  $\lambda = 0.0$ ; (b)  $\lambda = 1.0$ ; (c)  $\lambda = 3.5$ ; (d)  $\lambda = 3.99$ . Note again that when  $\lambda = 0.0$  one obtains the same bifurcation curve as in the classical pendulum.

The last case is  $\lambda_1 = 1$ ,  $\lambda_2 > 4$ , in which we have

$$\begin{aligned}
 M^*(t_0, \lambda, A, \omega, \alpha) &= \int_{-\infty}^{+\infty} \tilde{y}_1^*(t) [A \cos(\omega t + \omega t_0) - \alpha \tilde{y}_1^*(t)] dt \\
 &= \int_{-\infty}^{+\infty} \left\{ \pm \frac{2\sqrt{\lambda}(\lambda-4) \cosh\left(\sqrt{\frac{4+\lambda}{4}}t\right) A \cos(\omega t)}{(\lambda-4) + \lambda \sinh^2\left(\sqrt{\frac{4+\lambda}{4}}t\right)} dt \right\} \cos(\omega t_0) \\
 &\quad - \alpha \int_{-\infty}^{+\infty} \left\{ \frac{2\sqrt{\lambda}(\lambda-4) \cosh\left(\sqrt{\frac{4+\lambda}{4}}t\right)}{(\lambda-4) + \lambda \sinh^2\left(\sqrt{\frac{4+\lambda}{4}}t\right)} \right\}^2 dt. \tag{28}
 \end{aligned}$$

The threshold curve

$$\alpha = \frac{A \tilde{R}_1(\lambda, \omega)}{\tilde{F}_1(\lambda)}, \quad A > 0 \text{ fixed}, \lambda > 4, \tag{29}$$

is shown in Fig. 8.

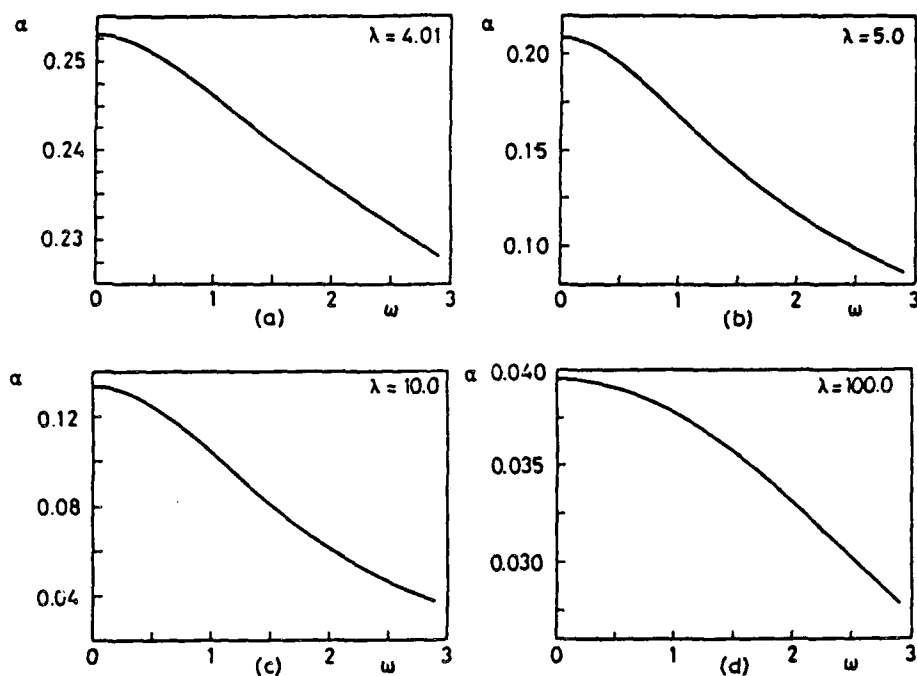


Fig. 8. Bifurcation curves for the heteroclinic orbit (15) in the  $(\alpha, \omega)$  parameter space.  $A = 0.5$ ,  $\lambda_1 = 1$ . (a)  $\lambda = 4.01$ ; (b)  $\lambda = 5.0$ ; (c)  $\lambda = 10.0$ ; (d)  $\lambda = 100.0$ . Note the reduction to the pendulum when  $\lambda \geq 5.0$ .

## 5. Discussion

In this section we discuss the results obtained in the previous section. Let us start by analyzing the case  $\lambda_1 = 1$ ,  $\lambda \geq 0$ . In this case for  $\lambda = 0$ , equation (1) reduces to the pendulum equation, and the two heteroclinic orbits, (13) and (14), reduce to the analytical expression of the pendulum separatrix. As one would have expected, we obtain in this limit ( $\lambda = 0$ ) the same bifurcation diagrams as for the simple pendulum (see Figs. 6 and 7). As  $\lambda$  goes from zero to four, the threshold curves in Figs. 6 and 7 change qualitatively and quantitatively. The turning points of these regions are the zeros of the function  $\bar{R}_1(\lambda, \omega)$  in (25). When  $\lambda = 4$ , system (9) bifurcates changing its phase portraits from Fig. 2 to a figure similar to Fig. 1(b). We see that during the bifurcation the heteroclinic orbit (13) disappears merging into the hyperbolic fixed point  $(2\pi, 0)$ . (An analysis of the linearized system (9) shows that this point is degenerate). For  $\lambda > 4$ , the bifurcation diagrams are shown in Fig. 8. When  $\lambda > 4$ , system (9) reduces to the pendulum equation, and, as expected, we see from Fig. 8 that in this limit the bifurcation diagram of (9) reduces to that of a pendulum.

Let us now consider the case  $\lambda_1 = -1$ ,  $\lambda \geq 0$ . Increasing from zero to four (excluded) we can see in the figures how the bifurcation diagrams depend on this parameter. When  $\lambda = 4$ , the system bifurcates. The phase portraits change from Fig. 1(a) to Fig. 1(b). We note that the centres  $[\pm 2 \cos^{-1}(\frac{1}{2}\lambda) + 4k\pi, 0]$ ,  $k = 0, \pm 1, \pm 2, \dots$ , disappear. This is because the fixed points  $(4n\pi, 0)$ ,  $n = 0, \pm 1, \pm 2, \dots$ , are degenerate as one can easily see from the linearization of the system at those points (we note that our system is structurally unstable). One can also see that the homoclinic orbit (11) degenerates into the fixed point  $(0, 0)$ , whereas the heteroclinic orbit (12) continuously changes its shape becoming the heteroclinic orbit

shown in Fig. 1(b). When  $\lambda > 4$ , the term  $-\frac{1}{2}\lambda \sin(\frac{1}{2}\phi)$  becomes dominant and we get again the pendulum equation. The bifurcation diagrams obtained above are also in agreement with earlier results [6-8].

We finally observe that the bifurcation diagrams in Figs. 3 and 4 do not reduce to those of a pendulum, when  $\lambda \rightarrow 0$  (note that system (9) in this limit is the antipendulum). In the limit  $\lambda = 0$ , however, the homoclinic orbit (11) and the heteroclinic orbit (12) do not exist any more, they indeed degenerate in the fixed points  $(2\pi, 0)$  and  $(0, 0)$  respectively. On the other hand, for small values of  $\lambda$  ( $\lambda \ll 1$ ) the homoclinic and heteroclinic orbits shown in Fig. 1(a) get closer to each other, and an analysis based on a first order estimate of the splitting of the corresponding stable and unstable manifolds could be too crude. This last point we plan to investigate in a future paper.

#### Acknowledgment

The financial support of the Consiglio Nazionale delle Richerche, Roma, Italy, to one of the authors (M.B.) and of the European Research office of the United States Army (through contract No. DAJA-45-85-C-0042) is acknowledged.

#### References

- [1] J. Guckenheimer and P.J. Holmes, "Nonlinear oscillations, dynamical systems, and bifurcations of vector fields", Applied Mathematical Science 42, Springer, Berlin (1983).
- [2] B.V. Chirikov, *Phys. Rep.* 52, 263-379 (1979).
- [3] A.R. Bishop, D.K. Campbell and B. Nicolaenko (eds.), *Nonlinear Problems: Present and Future*, North-Holland Mathematics Studies 61, Amsterdam (1982).
- [4] A.R. Bishop and T. Schneider (eds.), *Solitons and Condensed Matter Physics*, Springer, Berlin (1978).
- [5] M. Salerno, *Physica 17D*, 227-234 (1985).
- [6] F.M.A. Salam and S.S. Sastry, in: *Chaos in Nonlinear Dynamical Systems*, J. Chandra, ed., Society for Industrial and Applied Mathematics, Philadelphia (1984) 43-55.
- [7] M. Bartuccelli, P.L. Christiansen, N.F. Pedersen and M.P. Soerensen, *Phys. Rev. B* 33, 4686-4691 (1986).
- [8] Z.G. Genchev, Z.G. Ivanov and B.N. Todorov, *IEEE Trans. Circuits and Systems* 30, 633-636 (1983).

## ANALYTICAL AND NUMERICAL RESULTS FOR A LONG JOSEPHSON JUNCTION WITH SURFACE LOSSES.

S. Pagano

Laboratory of Applied Mathematical Physics, The Technical University of Denmark  
DK-2800 Lyngby, Denmark.

N.F. Pedersen and S. Sakai\*

Physics Laboratory I, Technical University of Denmark, DK-2800 Lyngby, Denmark

A. Davidson

IBM Research, P.O. Box 218, Yorktown Heights, N.Y. 10598, U.S.A.

Abstract.

In this paper we show several analytical approaches to study the effect of dissipation on fluxon motion; our attention is mainly devoted to the surface impedance term which is the main quantity responsible for qualitative dynamical changes in the junction.

Introduction.

Soliton (fluxon) dynamics in the long Josephson junction (Josephson transmission line or JTL) has for many years been one of the most active research areas within the topic of Josephson tunneling. Fluxons show particle-like behavior in the fact that they carry energy and momentum, they are structurally stable in the sense that small perturbations do not destroy them, and they can travel at almost the speed of light within the JTL. All these features make fluxons excellent candidates for being the building blocks of new fast electronic devices, as has recently been demonstrated experimentally [1].

In view of this it is important to study the effects of various forms of dissipation on the fluxon motion, since these dissipations are responsible for distortion and even decay (switching) of the fluxons. Though a number of numerical simulations have been done to study this effect [2], very few analytical results are known. This is mainly due to the fact that the model equation for a Josephson transmission line, the perturbed sine-Gordon equation, has no known general analytic solution. Hence the main results are given in terms of a perturbative analysis around known solutions of the sine-Gordon equation (Ref. 3).

From numerical simulations [2] it has been shown that due to the presence of surface damping a number of new phenomena occur: (i) A distortion of the pulse shape of the fluxon together with a non-Lorenzian contraction; this is in contrast to the relativistic contraction present in the solution of the non-dissipative sine-Gordon system. (ii) The occurrence of an overshoot in the fluxon pulse accompanied with damped oscillations. (iii) A decrease in the maximum bias that can sustain pure fluxon motion, with a corresponding decrease of the energy; thus the pure soliton solutions become unstable against the rotating solution.

In the first section we show an analytical approach for solving the perturbed sine-Gordon equation with a piecewise linear approximation of the non-linear sine term. In the second section we consider a phase-space analysis that, although very simple, gives surprisingly good results in predicting the frequency and the damping constant of the overshoot oscillations observed numerically, as well as the change in the pulse shape of the fluxon. Finally we introduce a new perturbation approach that gives a surprisingly good agreement with the results of numerical computations.

\* Permanent address: Electrotechnical Laboratory, I-1-4, Nakano, Sakura-mura, Hitachi-gun, Ibaraki 305, Japan

Manuscript received September 30, 1986.

Analytic results for triangular current-phase relation.

The JTL is modeled by a perturbed sine-Gordon equation

$$\frac{d\phi}{dx} - \frac{d^2\phi}{dx^2} - \sin\phi - \alpha\dot{\phi} + \beta\ddot{\phi}_{ext} + \eta = 0 \quad (1)$$

where  $\phi$  is the phase difference between the two superconductors forming the junction,  $\alpha$  is the normalized parallel conductance,  $\beta$  is the normalized surface conductance and  $\eta$  is the bias current normalized to the maximum Josephson current; space is normalized to the Josephson penetration length  $\lambda$ , and time is normalized to the inverse of the Josephson plasma frequency  $\omega_0 = E/\lambda$ , where  $E$  is the speed of light in the Josephson transmission line.

In what follows we will consider the case in which the length of the junction is big enough to disregard the effects of the boundaries in order to concentrate our attention on the stationary fluxon motion.

In general when  $\alpha$ ,  $\beta$  and  $\eta$  are different from zero Eq. 1 can not be solved analytically. To extract some analytical information one can approximate the sine term in Eq. 1 by using a triangular current-phase relation with  $2\pi$  periodicity (Fig. 1)  $f(\phi)$  defined by

$$f(\phi) = \begin{cases} k(\phi - 2\pi), & -\pi/2 + 2\pi n \leq \phi \leq \pi/2 + 2\pi n \\ -k(\phi - \pi - 2\pi n), & \pi/2 + 2\pi n \leq \phi \leq 3\pi/2 + 2\pi n \end{cases} \quad (2)$$

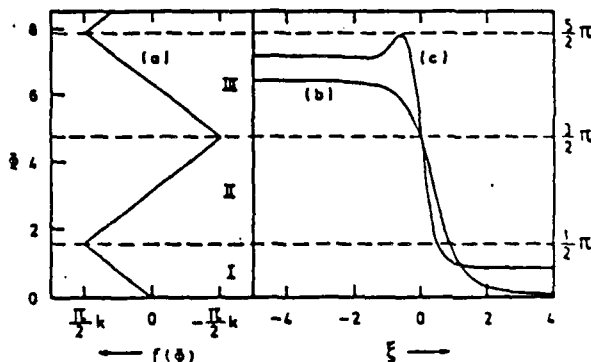


Fig. 1. a) Triangular current-phase relation  $f(\phi)$ . b,c) Fluxon line shapes with  $\alpha = 0.02$ ,  $\beta = 0.01$ , and  $I = 2/\pi$ . (b)  $u = 0.9$  giving  $\eta = 0.079$ . (c)  $u = 1.0$  giving  $\eta = 0.569$ .

The main idea of this procedure is that now Eq. 1 is a piecewise linear equation, i.e. the phase space is divided in regions (regions I, II and III in Fig. 1) in which Eq. 1 is linear and the corresponding solution can be found by elementary analysis. Caution has to be taken to properly join the solutions at the boundary of the different regions of the phase-space. The procedure, requiring rather lengthy calculations, has been carried out in Ref. 4, using a traveling-wave assumption of the solution to Eq. 1, which is then reduced to a third order ordinary differential equation (ODE):

$$-\alpha u \dot{\phi}_{fff} + (1-u^2) \dot{\phi}_{ff} + \alpha u \dot{\phi}_f - f(\phi) + \eta = 0 \quad (3)$$

where  $u$  is the velocity of the solution and  $f = \kappa - u\dot{u}$ . The solution in the three regions of Fig. 1 is given by

$$\begin{cases} A_1 \exp(q_1 \phi) + B_1 \exp(r_1 \phi) \\ + C_1 \exp(q_2 \phi) + D_1 \exp(r_2 \phi) \end{cases} \quad (4)$$

$$\begin{cases} A_2 \exp(q_3 \phi) + B_2 \exp(r_3 \phi) \\ + C_2 \exp(q_4 \phi) + D_2 \exp(r_4 \phi) \end{cases} \quad (5)$$

where  $A_i, C_i, C_2, B_1, B_2, B_3$  are constants and  $q_1, q_2, q_3, q_4$  and  $r_1, r_2, r_3, r_4$  are the roots of the characteristic polynomium  $P_\pm$  of Eq. 3 (the  $q$ 's are related to  $P_+$  and the  $r$ 's to  $P_-$ .)

$$P_\pm = \alpha u x^2 - (1-u^2)x^0 - \alpha u x \pm k = 0 \quad (6)$$

Due to the form of  $P_\pm$  we have, for  $P_+$ , always a negative real root  $q_1$  and for  $q_2$  and  $q_3$  either two positive real roots or a couple of complex conjugate roots with positive real part. For  $P_-$  we have always a positive root  $r_4$  and for  $r_1$  and  $r_2$  either two negative roots or a couple of complex conjugate ones with negative real part.

This information, together with the asymptotic conditions on the solution  $\phi$  at  $\phi \rightarrow \infty$  gives Eq. 4. The values of the constants  $A_1, B_1, B_2, B_3, C_1$  and  $C_2$  are determined by the matching conditions of  $\phi, \dot{\phi}_f$  and  $\dot{\phi}_{fff}$  at the border of the regions in Fig. 1 [4]. The main results of this approach are the following. The system parameters for the observation of the overshoot in the fluxon shape, (two complex conjugate roots in  $P_+$ ) is given by

$$\beta > 4\alpha^2/27k^2 \quad (6)$$

In presence of the overshoot, Fig. 2a, the period of the oscillations and their decay rate can be computed respectively from the imaginary and the real part of the two complex conjugate roots  $q_{\pm}$  of  $P_+$ . In Fig. 2a the absolute value of  $\dot{\phi}_f$  is shown in a log scale; for both the period and the decay rate of the oscillations a surprising similarity with the numerical results of the integration of equation Eq. 1, Fig. 2b [2], is found. The current-velocity relationship for the fluxon can be derived analytically [4] and in Fig. 3 a comparison of

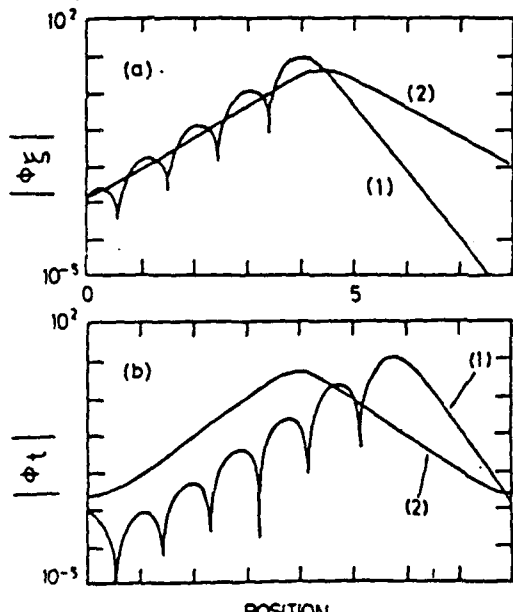


Fig. 2. Fluxon line shapes. (a) Analytical results. (b) Numerical integration of Eq. 1. The parameters are:  $\alpha = 0.02$ ,  $\beta = 0.01$ ,  $k = 2/\pi$ . (a-1)  $u = 0.9$ ,  $\eta = 0.079$ ; (a-2)  $u = 1$ ,  $\eta = 0.569$ , (b-1)  $\eta = 0.1$ , (b-2)  $\eta = 0.675$ .

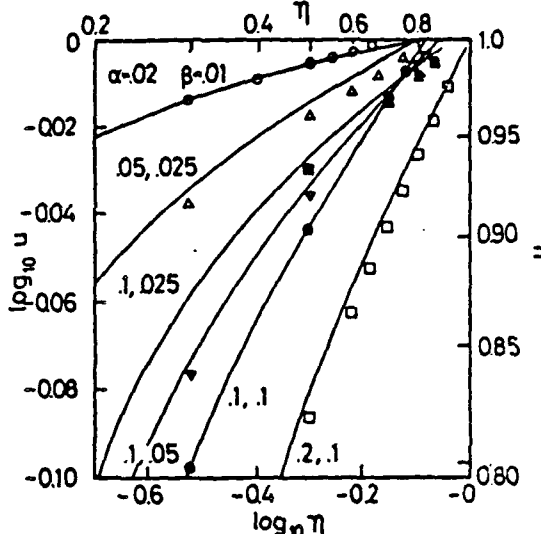


Fig. 3. Comparison of the  $\eta$ - $u$  curves computed analytically (solid curves) and the results [2] from numerical integration of Eq. 1 (marks) for various values of the parameters  $\alpha$  and  $\beta$ .

the computed  $\eta$ - $u$  curve with the results of a numerical simulation of Eq. 1 is shown. In this calculation the value of  $k$  (Eq. 2) is chosen to be  $8/\pi$  after a comparison of the junction coupling energy per unit length with that of Eq. 1. As shown in Fig. 3 the analytical results obtained are very close to the numerical ones for the original system.

The numerical methods used in this paper were simple and direct. An annular geometry was assumed, and the simple finite difference equation corresponding to Eq. 1 was solved. Usually an annulus of normalized length eight was used, with a total of 400 finite elements making up the ring. The time step in the simulations was usually about  $0.005/\omega_0$ . Situations with light damping needed smaller time steps; heavier damping could tolerate larger steps. All results were tested against variation with the spatial grid and time step. Initial conditions appropriate for creating a single soliton were approximated by a linear ramp in phase  $2\pi$  over the length of the junction, and the transients due to the relaxation to the true soliton were allowed to decay before any measurements were made. The reproducibility of the results despite variations in spatial grid and time step is the main reason for confidence in the numerical results.

#### Phase space analysis.

In this section we shall develop a phase-space analysis for the perturbed sine-Gordon equation Eq. 1 in order to investigate the effect of the surface loss on fluxon.

As in the preceding section we assume a travelling wave solution to Eq. 1 on an infinite JTL with a velocity  $u$ . We obtain

$$-\alpha u \dot{\phi}_{fff} + (1-u^2) \dot{\phi}_{ff} + \alpha u \dot{\phi}_f - \sin \phi + \eta = 0 \quad (7)$$

To this third order ODE is associated a three-dimensional phase-space in which the fluxon solution represents a separatrix, in the sense that it connects two fixed points of the phase-space in infinite time. The fixed points involved are obviously given by  $F = (\phi, \dot{\phi}, \ddot{\phi}_{fff}) = (\arcsin \eta, 0, 0)$ .

In the following a linearized analysis of the dynamics around the fixed points  $P$  will be performed.

Assuming a solution of Eq. 6 given by

$$\phi(f) = \arcsin \eta + \tilde{\phi}(f) + i|\tilde{\phi}'(f)| \quad (8)$$

we obtain to first order in  $\bar{q}$  the linear equation

$$-\alpha u \bar{\theta}_{gg} + (1-u^2) \bar{\theta}_{gg} + \alpha u \bar{\theta}_g - \sqrt{1-\eta^2} \bar{\theta} = 0 \quad (9)$$

whose solution is determined by the roots  $q$  of the associated polynomium

$$P(q) = q^2 - \frac{1-u^2}{\alpha u} q^2 - \frac{\alpha}{\beta} q + \frac{\sqrt{1-\eta^2}}{\alpha u} = 0 \quad (10)$$

This polynomium Eq. 10 is similar to Eq. 4, except for the last term, and it will show the same zoology of roots. The phase portrait near the fixed point is shown in Figs. 4a,b. Figure 4a corresponds to the case of three real roots, that gives rise to a smooth fluxon shape with no overshoot. In Fig. 4b the case of complex conjugate roots is considered and the oscillating behaviour of the overshoot is clearly identified by the spiraling of the phase-curve outwards from the fixed point.

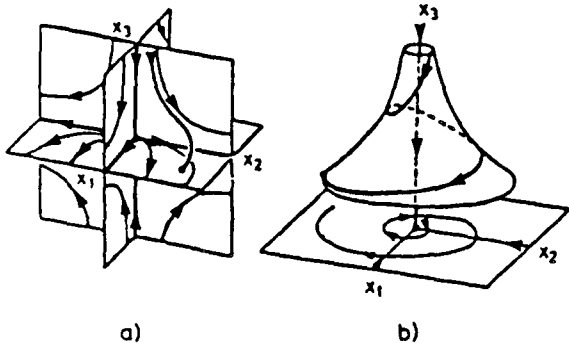


Fig. 4. Phase portrait near the fixed points. (a) two positive roots and one negative (b) one negative root and two complex conjugate.

This kind of analysis cannot give the threshold for the appearance of the oscillating overshoot, as the one in the first section, because the relationship between the bias and the velocity  $u$  of the fluxon is not known. However it is known from numerical integration that the velocity of the fluxon will rapidly tend to unity when the bias is increased. Assuming a unit velocity in Eq. 10, one can derive an expression for the threshold for observing overshoot in the fluxon, in the same way as in Eq. 6. The result is

$$\beta > 4\alpha^2/(27(1-\eta^2)) \quad (11)$$

The validity of this condition is limited by the fact that  $\eta$  must be consistent with a fluxon velocity very close to unity.

Additional results can be found by computing the (complex) roots of Eq. 10 using standard methods; that gives the decay rate  $\mu$  and the frequency  $\omega$  of the oscillations of the overshoot. In the case  $u=1$  and if  $\alpha^2/27(1-\eta^2) \ll 1$  (which does not introduce major restrictions) we can obtain fairly simple expressions for  $\mu$  and  $\omega$

$$\mu = -.5 ((1-\eta^2)/\alpha^2)^{1/4} \quad (12)$$

$$\omega = \sqrt{3}/2 ((1-\eta^2)/\alpha^2)^{1/4} \quad (13)$$

We have compared the above results with the ones obtained by the numerical integration of Eq. 1 [2] and obtain a very good agreement (within 2-3%).

Another interesting result that can be obtained by the phase-space analysis regards the slope of the leading and the trailing edge of the fluxon.

It is well known that, in the absence of dissipation, the slopes of the leading and the trailing edge of the fluxon are equal, i.e. the pulse shape is symmetric. The presence of dissipative terms may break

this symmetry by changing the slopes of the fluxon edges, as has been observed in numerical integrations.

Let us assume for simplicity that we have only one dissipative term in Eq. 1, namely the  $\alpha$  term. Using the same procedure as shown above, we obtain the characteristic polynomium in the form:

$$P(q) = q^2 + \alpha u/(1-u^2)q - (1-\eta^2)^{1/2}/(1-u^2) = 0 \quad (14)$$

the roots of which are given by

$$q_{1,2} = -\alpha u/2(1-u^2) \pm ((\alpha u/2(1-u^2))^2 + (1-\eta^2)^{1/2}/(1-u^2))^{1/2} \quad (15)$$

In a neighborhood of the fixed points, the solution  $\bar{\theta}(f)$  will then be given by

$$\begin{aligned} \bar{\theta}^1(f) &= \arcsin \eta + A \exp(-q_1 f) \\ \bar{\theta}^2(f) &= \arcsin \eta + B \exp(-q_2 f) + \dots \end{aligned} \quad (16)$$

where  $\bar{\theta}^1$  represents the leading edge of the fluxon and  $\bar{\theta}^2$  the trailing one.

From Eq. 15 it is seen that when  $\alpha$  is very small, the two exponents are equal in magnitude, but when  $\alpha$  is not small a difference in the magnitude of the exponents is found. This difference becomes more and more enhanced as  $\eta$  tends to unity, reproducing the behaviour observed in the numerical calculations. The same procedure that leads to Eq. 15 can be applied in the case  $\beta \neq 0$ , however the calculations are more lengthy to carry out.

#### Perturbational Methods.

In the previous section it has been shown that is possible to derive analytical results concerning the influence of the dissipative terms on the fluxon dynamics. Unfortunately, the lack of knowledge about the relationship between the bias current and the fluxon velocity ( $\eta$ - $u$  curve) limits the amount of information that is possible to obtain from such a procedure. Since the exact waveform of the fluxon in presence of bias and dissipations is not known, various perturbative methods have been used to derive the  $\eta$ - $u$  curve. The classical one [3] assumes the kink solution of the sine-Gordon equation as an approximation to the solutions of Eq. 1, i.e.

$$\phi(x,t) = 4 \operatorname{arctg}(\exp(Y_L(x-ut))) \quad (17)$$

where  $Y_L$  is the Lorentz factor  $(=1/(1-u^2))^{1/2}$ . Inserting Eq. 17 into Eq. 1 and imposing a power balance between the energy output due to dissipation and the energy input due to the bias current, the following expression for the  $\eta$ - $u$  curve is obtained [3]

$$\eta = (4/\pi)u Y_L((\alpha + \beta Y_L^2)/3) \quad (18)$$

Although this expression represents the qualitative behavior of the fluxon as observed both experimentally and in numerical simulations quite well, it fails to describe the high velocity region. In fact, when  $u \rightarrow 1$  Eq. 18 predicts that the bias goes to infinity, in contrast to numerical and experimental results.

The problem lies in the form of the solution assumed in Eq. 17, which implies that the fluxon becomes more and more narrow as the velocity approaches unity. It has been observed numerically that when  $\beta \neq 0$  the presence of  $\alpha$ -dissipation determines a lower limit in the fluxon contraction. Ferrigno and Pace [5] have found, ( $\beta=0$ ) similar results by using solution  $\phi(x,t) = \arcsin \eta + \eta \phi(x,t)$ , where  $\phi(x,t)$  is given by Eq. 17 with a different contraction factor  $Y_L$ :

$$Y_L = (1-\eta^2)^{1/4}/(1-u^2)^{1/4} \quad (19)$$

This leads to a  $\eta$ - $u$  relationship given by  $\eta = (4/\pi)\gamma_p$ , predicting that  $\eta \rightarrow 1$  and  $\gamma_p \rightarrow \pi/4a$  for  $u \rightarrow 1$ . Both the perturbation approach in [3] and in [5] have their main limitation in the fact that the perturbative terms ( $\alpha\beta_{xx} + \eta$ ) in [3] and ( $\eta + \eta\cos\theta + \alpha\beta$ ) in [5] are considered very small; while for  $\eta \rightarrow 1$  this is not true. Moreover the presence of the  $\beta$  term distorts the shape of the fluxon considerably from the one assumed in Eq. 14 making the ansatz about the solution to Eq. 1 unrealistic.

A possible way to handle the first of the two problems exposed can be to rewrite Eq. 1 as

$$\eta' - \eta_{xx} - \sin\theta \cdot \eta - \alpha'\beta_{xx}\eta_x = -\alpha'\beta_{xx}\theta_x - \beta\beta_{xx} + \alpha\beta \quad (20)$$

The left side of Eq. 20 has an exact solution [6] for any value of  $\eta$ :

$$\eta(x,t) = 4\arctg(\exp(\gamma(x-ut))) + \arcsin\eta \quad (21)$$

where  $\gamma = \gamma_p$  is given by Eq. 19 and  $\alpha' = -\eta^2/2u^2\gamma^2$ . Note that typically  $\alpha' \ll 1$  even when  $\eta \rightarrow 1$ . Inserting Eq. 21 into Eq. 20 and imposing a power balance on the terms of the right side in Eq. 20 we obtain

$$\eta' = (4/\pi u)\gamma(\alpha + \beta\gamma^2/3) \quad (22)$$

which is the same as Eq. 18 but with a different fluxon contraction term. It can easily be shown that the ansatz Eq. 21 always leads to Eq. 22 for any choice of  $\gamma$ . In the case  $\beta=0$  the expression for  $\gamma$  (Eq. 19) can be derived by minimizing the power balance energy (Eq. 23 to be derived below) with respect to  $\gamma$ . The power balance energy for a general contraction factor  $\gamma$  can be computed from Eq. 1 by multiplying Eq. 1 with  $\eta_{xx}$ , integrating once with respect to time and integrating all over the space. To perform the integration we have assumed the form Eq. 21 for  $\eta$  with  $\gamma$  as an independent parameter and the power balance relation Eq. 22. As a result the power balance energy is obtained

$$E = 4(\gamma(\beta + u\theta) + \sqrt{1-\gamma^2}) - 2u\beta\gamma^2 \quad (23)$$

where  $u$  is given by Eq. 22.

In the case  $\beta \neq 0$  the minimizing procedure cannot be applied because, as it has been discussed in the

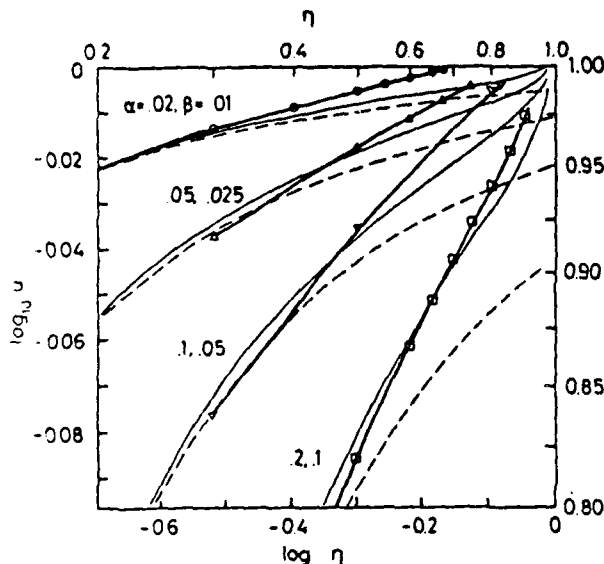


Fig. 5. Comparison between  $\eta$ - $u$  curves obtained by standard perturbative scheme (dashed curve), the one closed (full curve) and numerical integration of Eq. 1 (solid curve connecting marks), for various values of the parameters  $\alpha$  and  $\beta$ .

previous sections, the effect of the  $\beta$  term is to strongly deform the fluxon shape making the ansatz Eq. 21 not valid anymore.

In the case  $\beta \ll 1$  the expression Eq. 19 for  $\gamma$  can still be considered a good approximation, supporting the result obtained by the perturbative analysis.

We have checked the expression Eq. 22 with numerical results from the integration of Eq. 1 obtaining a much better agreement than for the standard perturbation result Eq. 18. In Fig. 5  $\eta$ - $u$  curves obtained from Eq. 22 are compared to numerical results from [2] in the critical region of high bias and velocity values. As expected a deviation is found when  $\beta$  is not small compared to  $\alpha$  and when the velocity of the fluxon is close to 1, i.e., when the overshoot is present and the assumption Eq. 21 is not valid anymore.

As a final remark we note that Eq. 22 predicts an increase of the width of the fluxon when the  $\beta$  term is present. In particular in the limit case  $\eta \rightarrow 1$  and  $u \rightarrow 1$  the value of  $\gamma$  has a correction with respect to the value found in ref. 5 for  $\beta=0$ , that to the first order in  $\beta$ ,  $\gamma$  is given by

$$\gamma = \pi/4a (1 - 1/(3(1 + 16a^2/\pi^2\beta))) \quad (24)$$

### Conclusion.

We have developed a number of analytical methods to study the effect of the surface impedance damping on the fluxon motion in a JTL.

A simple piecewise linear approximation of the sine term in the perturbed sine-Gordon equation (PSGE) that models JTL's allows to derive analytical solutions. It is shown to be very accurate in describing the dynamics of the original non-linear equations, especially with regard to the effect of the surface damping term. A phase-space analysis of the PSGE in the travelling wave assumption is able to predict quantitatively the dynamical effects of the surface damping in terms of the frequency and decay rate of the oscillations connected with the overshoot in the fluxon shape and the asymmetry in the fluxon shape. Finally, a new perturbative scheme based on the solution of PSGE with quadratic damping is derived, leading to a generalization of earlier results, obtained in absence of surface damping.

### Acknowledgments.

S.P. wish to acknowledge the "Fondazione Angelo delle Ricci", Florence-Italy, and the European Research Office of the United States Army (through contract No. DAJA-US-85-C-0042) for financial support during the period in which this work was performed. S.S. is grateful for the hospitality of Physics Lab. I, The Technical University of Denmark, during his sabbatical.

### References.

1. S. Sakai, H. Akoh, and H. Hayakawa, Jpn. J. App. Phys. **23**, L610 (1984); ibid **24**, L749 (1985); ibid **24**, L771 (1985).
2. A. Davidson, N.F. Pedersen, and S. Pagano, Appl. Phys. Lett. **48**, 1306 (1986).
3. D.W. McLaughlin and A.C. Scott, Phys. Rev. A **18**, 1652 (1978).
4. S. Sakai and N.F. Pedersen, Phys. Rev. B (in print).
5. A. Ferrigno and S. Pace, Phys. Lett. **112A**, 77 (1985).
6. N.F. Pedersen, K. Saernark, Physica **69**, 572 (1973); R.D. Parmentier, Solitons in Action, I. Longen and A.C. Scott, eds. (Academic Press, N.Y. 1973) p173.

Physica 26D (1987) 396-402  
 North-Holland, Amsterdam

## PARAMETRIC ADIABATIC PERTURBATIONS ON THE SINE-GORDON BREATHER SOLUTION

S. PAGANO

*Laboratory of Applied Mathematical Physics, The Technical University of Denmark, DK-2800 Lyngby, Denmark*

M. SALERNO\*

*Dipartimento di Fisica Teorica e SMSA, Università degli Studi di Salerno, I-84100 Salerno, Italy*

M.R. SAMUELSEN\*\*

*Dipartimento di Fisica, Università degli Studi di Salerno, I-84100 Salerno, Italy*

Received 15 July 1986

Revised manuscript received 17 November 1986

Breather dynamics in the sine-Gordon system with changing sine term coefficient is investigated. It is shown that for adiabatic changes the frequency of the breather in rescaled time is constant while the velocity changes just as the velocity of a kink.

### 1. Introduction

During the past years a great deal of interest has been devoted to the study of soliton dynamics in various physical systems [1]. One of the systems where soliton propagation is more accessible to experimental measurements is the long Josephson junction [2]. In this case the dynamics is governed by the sine-Gordon equation and soliton's (fluxon's) resonant motion manifests itself with the presence of dc singularities in the current-voltage characteristic of the junction [2, 3]. In this context several physical situations such as smooth spatial modulation of the Josephson supercurrent, slow temperature drift of the junction, etc... are modelled, (neglecting dissipation and bias), by the following simple perturbed sine-Gordon equation in normalized form

$$\phi_{xx} - \phi_{tt} = (1 + \alpha(x, t)) \sin(\phi) \\ = \left( \frac{m(x, t)}{8} \right)^2 \sin(\phi). \quad (1)$$

Here  $\phi(x, t)$  is the field variable, i.e. the macroscopic phase difference across the junction,  $\alpha(x, t) \sin(\phi)$  represents a nondissipative perturbation with  $\alpha$  a slowly changing function of space and time, and  $m(x, t)$  is the instantaneous  $2\pi$ -kink mass.

In a previous paper [4] the effects of such a perturbation on a  $2\pi$ -kink motion were investigated by assuming an adiabatic "switch on" of the perturbation. The analysis was performed without the need of perturbation theory, by using the conservation laws of system (1). The results were also found in good agreement with numerical experiments.

In the present paper we will continue this analysis by investigating the effects of the same perturbation on the other soliton solution of the sine-Gordon equation: the breather. A breather is a bound state of a soliton and an anti-soliton that is described by two parameters: the velocity with which the whole structure moves and the internal frequency of oscillation [5]. This will require the use of two conservation laws of eq. (1) to determine the perturbed breather dynamics. In section 2, by using the energy and the momentum of

\*Also G.N.S.M. sezione di Salerno, I-84100 Salerno, Italy.

\*\*Permanent address: Physics Laboratory 1, The Technical University of Denmark, DK-2800 Lyngby, Denmark.

eq. (1) we compute the rate of change of the internal frequency and of the velocity of a sine-Gordon breather under the influence of perturbations of type  $\alpha \sin(\phi)$  with  $\alpha$  either a function of space or of time. In the analysis we will assume an adiabatic switch on of the perturbation, thus avoiding the creation of background radiation into the system. As a result we find that the internal frequency in "rescaled" coordinate is constant

while the velocity exactly follows the same changes as those found in ref. 4 for a  $2\pi$ -kink. In section 3 the adiabatically "switching" process is numerically simulated for the  $\alpha(t)\sin(\phi)$  kind of perturbation. The comparison between numerical and analytical results confirms the validity of our simple approach. Finally in section 4 we estimate the limits of validity of the adiabatic assumption and summarize the main results of the paper.

## 2. Analysis

Let us start by defining the energy  $H(t)$  and the momentum  $P(t)$  for eq. (1) as

$$H \equiv \int_{-\infty}^{+\infty} \left( \frac{1}{2}\phi_t^2 + \frac{1}{2}\phi_x^2 + (1 + \alpha)(1 - \cos(\phi)) \right) dx, \quad (2)$$

$$P \equiv - \int_{-\infty}^{+\infty} \phi_x \phi_t dx \quad (3)$$

and by considering their time derivatives. With the help of eq. (1) we get

$$\frac{dH}{dt} = \int_{-\infty}^{+\infty} \alpha_t (1 - \cos(\phi)) dx, \quad (4)$$

$$\frac{dP}{dt} = - \int_{-\infty}^{+\infty} \alpha_x (1 - \cos(\phi)) dx, \quad (5)$$

from which it is clear that when  $\alpha_t = 0$  (i.e.  $\alpha \equiv \alpha(x)$ ) the energy is conserved [4, 6], while when  $\alpha_x = 0$  (i.e.  $\alpha \equiv \alpha(t)$ ) the momentum is conserved [4]. In the adiabatic case with a spatial localized entity, the derivative of  $\alpha$  in eqs. (4), (5) can be taken outside the integrals and one is left with the spatial integral of  $(1 - \cos(\phi))$  in both equations. (For a  $2\pi$ -kink these equations provide the same informations.) In order to find the rate of change of the breather frequency it is convenient to introduce the rescaled spatial and time variables  $z, \tau$ ,

$$dz = (1 + \alpha)^{1/2} dx, \quad d\tau = (1 + \alpha)^{1/2} dt, \quad (6)$$

in terms of which eq. (1) is rewritten as

$$\phi_{zz} - \phi_{\tau\tau} - \sin(\phi) = \phi_\tau \frac{\partial \ln(m)}{\partial \tau} - \phi_z \frac{\partial \ln(m)}{\partial z}, \quad (7)$$

where the last two terms represent perturbations to the pure sine-Gordon equation. Eq. (6) shows that the velocity is the same in the original and in the rescaled variables

$$v = \frac{dz}{d\tau} = \frac{dx}{dt}, \quad (8)$$

while the re-scaled frequency  $\omega'$  is related to the original frequency  $\omega$  by

$$\omega' = \frac{d\phi}{d\tau} = (1 + \alpha)^{-1/2} \frac{d\phi}{dt} = (1 + \alpha)^{-1/2} \omega. \quad (9)$$

For adiabatic changes of the mass  $m$  the instantaneous breather solution of eq. (7) is written as

$$\phi = 4 \tan^{-1} \left\{ \frac{\Gamma(\omega')^{-1} \sin [\omega' \Gamma(v)(\tau - vt) + \Phi_0]}{\omega' \cosh [\Gamma(\omega')^{-1} \Gamma(v)(z - vt)]} \right\}, \quad (10a)$$

$$= 4 \tan^{-1} \left\{ \frac{\Gamma(\omega')^{-1} \sin [\omega' \tau \Gamma(v)^{-1} - \omega' \Gamma(v)v(z - vt) + \Phi_0]}{\omega' \cosh [\Gamma(\omega')^{-1} \Gamma(v)(z - vt)]} \right\}, \quad (10b)$$

where

$$\Gamma(\beta) = (1 - \beta^2)^{-1/2}. \quad (11)$$

Inserting eq. (10) into eq. (2) and using eq. (6) we get for the energy

$$H = 16(1 + \alpha)^{1/2} \Gamma(\omega')^{-1} \Gamma(v) = 2m \Gamma(\omega')^{-1} \Gamma(v). \quad (12)$$

Similarly, from eq. (3) we get for the momentum

$$P = 16(1 + \alpha)^{1/2} \Gamma(\omega')^{-1} \Gamma(v)v = 2m \Gamma(\omega')^{-1} \Gamma(v)v. \quad (13)$$

In order to use eqs. (4), (5) we have to perform the spatial integral of  $(1 - \cos(\phi))$ . Since the changes are adiabatic the breather parameters  $v$  and  $\omega'$  will change very little during one period of oscillation. Therefore we can first take the time average of  $(1 - \cos(\phi))$  and then do the spatial integration. With the use of eqs. (10) and (6), after some lengthy calculations we get

$$\frac{1}{T} \int_0^T dt \int_{-\infty}^{+\infty} (1 - \cos(\phi)) dx = \frac{8\Gamma(\omega')^{-1}}{\Gamma(v)(1 + \alpha)^{1/2}}. \quad (14)$$

From eqs. (4) and (5) together with eqs. (12), (13), (14) we have

$$\frac{1}{2} \frac{d}{dt} (H^2 - P^2) = 128(1 - \omega'^2)(\alpha_t + v\alpha_x). \quad (15)$$

Observing that

$$\frac{d\alpha}{dt} = \alpha_t + v\alpha_x, \quad (16)$$

eq. (15) implies

$$\frac{d}{dt} (1 - \omega'^2) = 0, \quad (17)$$

independently of how the change of  $\alpha(x, t)$  is made, the only requirement being its adiabaticity, the frequency parameter in the rescaled time  $\omega'$  is constant. The frequency  $\omega$  in the original time is then easily obtained from eq. (9).

To compute the rate of change of the breather's velocity we observe that since  $\omega'$  is constant there is no substantial difference between the breather problem analyzed here and the  $2\pi$ -kink problem analyzed in ref. 4. We have only to replace  $\Gamma(\omega')^{-1}$  by  $\frac{1}{2}$  in eqs. (12), (13), (14) and take over the results from ref. 4. These results depend on  $\alpha(x, t)$  and on the initial velocity. Here we consider only the cases  $\alpha_x = 0$  and  $\alpha_t = 0$ .

*Case  $\alpha_x = 0$ .* In this case the momentum  $P$  is a conserved quantity. Thus from eqs. (5), (13), (17) it follows (in = initial)

$$(1 + \alpha)^{1/2} v \Gamma(v) = \text{constant} = v_{\text{in}} \Gamma(v_{\text{in}}), \quad (18)$$

this giving for the breather velocity

$$v = v_{\text{in}} / [1 + \alpha(1 - v_{\text{in}}^2)]^{1/2}. \quad (19)$$

*Case  $\alpha_t = 0$ .* In this case the energy is the conserved quantity (see eq. (4)), this implying (eqs. (12), (17))

$$(1 + \alpha)^{1/2} \Gamma(v) = \text{constant} = \Gamma(v_{\text{in}}), \quad (20)$$

from which it follows that

$$v = [v_{\text{in}}^2 - \alpha(1 - v_{\text{in}}^2)]^{1/2}. \quad (21)$$

In the next section we will compare the results referring to the  $\alpha_x = 0$  type of perturbation with those obtained by a direct numerical integration of system (1).

### 3. Numerical experiment

We have integrated numerically eq. (1) assuming periodic boundary conditions over a normalized length  $L = 40$ . This value has been chosen in order to avoid interferences between the tails of the breather-like solution during the time evolution of the system. The numerical algorithm is based on an explicit finite difference scheme derived by Ablowitz et al. [7] that, with a choice of the spatial and temporal step size of 0.1 ensures stability and accuracy of the calculation [8].

In all numerical experiments we have restricted ourselves to the case  $\alpha = \alpha(t)$  since the other one ( $\alpha = \alpha(x)$ ) requires a much more complex code to

be implemented on a finite length model and does not give a deeper understanding of the system. Each numerical integration has been carried out in the following way: a) The initial condition is set in the form of a "pure" sine-Gordon breather and  $\alpha$  is set to zero; b)  $\alpha$  is changed (increased or decreased) at a constant rate and the frequency and the velocity of the solution are measured at each oscillation period of the solution itself. A value of the rate of change of  $\alpha$  of  $10^{-3}$  has been chosen in such a way that it ensures us that no spurious dynamical effects, like phonon creation, are generated.

The most interesting part of the numerical procedure is the way that both the velocity and the

frequency of the solution are measured. The problem lays in the fact that a moving breather does not have a constant profile, but oscillates in an un-harmonic way.

The program locates the maximum  $M_x$  of the solution and its  $x$  coordinate at each time step, using a parabolic interpolation between adjacent spatial grid points.  $M_x$  evolves in time in an oscillatory way, reaching a maximum value  $M_{x,i}$  once per period of oscillation of the solution.  $M_{x,i}$  is evaluated together with the corresponding time value, again using a parabolic interpolation between adjacent time points. Once that the positions  $x_0$  and  $x_1$ , and the two corresponding times  $t_0$  and  $t_1$  of the two consecutive maximums  $M_{x,i}$  are known, then the velocity and the frequency of the solution are calculated as

$$v = \frac{(x_1 - x_0)}{(t_1 - t_0)} \quad \text{and} \quad \omega = \frac{2\pi}{(t_1 - t_0)}. \quad (22)$$

In eq. (9) we have given the connection between the original frequency  $\omega$  and the rescaled frequency  $\omega'$ . From eq. (10a) we see that the rescaled frequency  $\omega'_1$  measured at a given point is

$$\omega'_1 = \omega' I'(v) \quad (23)$$

and from eq. (10b) that the rescaled frequency  $\omega'_2$  measured in the frame moving with the breather ( $z = vt$ ) is

$$\omega'_2 = \omega' I'(v)^{-1}. \quad (24)$$

These relativistic effects are important when comparing to numerical experiments. Indeed, the method we have used to compute the solution frequency corresponds to a measurement in the original time, so in order to compute the corresponding value of the parameter  $\omega'$  in eq. (17), eq. (23) must be used. The results of the numerical integration are shown in figs. 1 and 2. In fig. 1a the case of a resting breather ( $v = 0$ ) is analyzed.

The initial values of the frequencies  $\omega$  are varied from 0.1 to 0.9 and the corresponding frequency

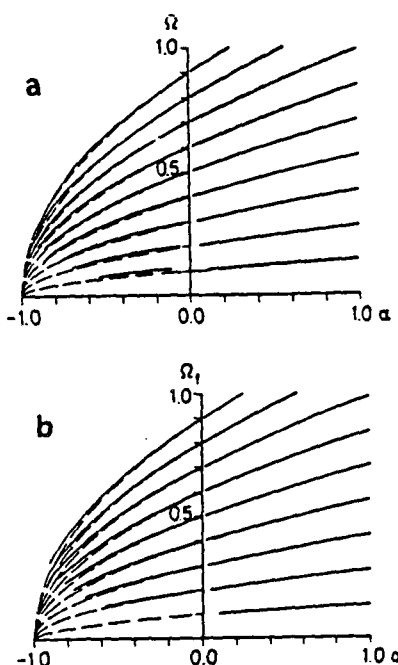


Fig. 1. a) Frequency  $\omega$  of the breather as function of  $\alpha = \sigma(t)$  for different starting frequency values. The dashed curves are the theoretical predictions (eqs. (9), (17)) and the full curves are the numerical results. (When the dashed curves are not visible they coincide with the full ones.) The initial velocity is set to zero and the line length is  $L = 20$ . b) Same as in fig. 1a but with an initial velocity of 0.5 and line length  $L = 40$ .

changes are computed, both from an increase of  $\alpha$  up to  $\alpha = 1$  and for a decrease of  $\alpha$  down to  $\alpha = -1$ . A comparison of the numerical results (full curves) with the prediction of eqs. (9), (17) (dashed curves) shows that an excellent agreement is reached, except for the region where the breather-like solution becomes so wide that the influence of the periodic boundary conditions cannot be neglected (in this case the spatial length was 20). In fig. 1b a similar comparison is shown, corresponding this time to a moving breather with an initial velocity  $v = 0.5$ . Again a very good agreement is reached, apart from a region where the same considerations made before apply (this time the spatial length is 40). Once that it has been shown that the change of the frequency  $\omega$  with  $\alpha$  does not depend on the initial velocity of the breather, as predicted by eq. (17), a number of

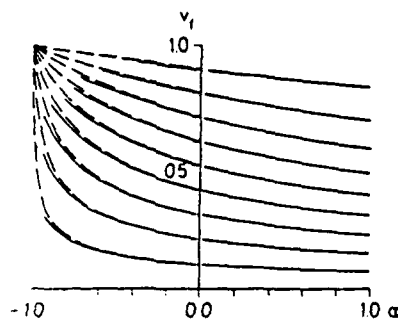


Fig. 2. Velocity  $v$  of the breather as function  $\alpha = \alpha(t)$  for different setting of initial velocities. The initial frequency is 0.5. The dashed curves are the theoretical predictions (eq. (19)) while the full ones are the numerical results. (When the dashed curves are not visible they coincide with the full ones.)

integrations with a fixed initial frequency  $\omega = 0.5$  and with initial velocities ranging from 0.1 to 0.9 have been performed. The results are plotted in fig. 2 where the velocity of the solution is plotted as a function of  $\alpha$  both for an increase of  $\alpha$  up to  $\alpha = 1$  and for a decrease down to  $\alpha = -1$ . Again a very good agreement is found, except for the points lying in the previously discussed region, verifying the results (eq. (19)) obtained from our analysis.

#### 4. Conclusion

In this paper we have considered the effects of changes in  $\alpha$  in eq. (1) on a breather solution. We have shown that as long as the changes are adiabatic the rescaled frequency parameter  $\omega'$  is constant and the velocity changes just as the velocity of a kink. Finally we have done a numerical test in order to estimate the limits of validity of the adiabatic assumption. To perform this test we have used the following expression for  $\alpha(t)$ :

$$\alpha(t) = \frac{A}{\pi} \left\{ \frac{1}{2}\pi + A^{-1} \tan^{-1} [\pi s(t - \frac{1}{2}T_F)] \right\}, \quad (25)$$

where  $T_F$  is the integration time,  $s$  is the maximum slope of  $\alpha(t)$  and  $A$  is the final value of  $\alpha$ .

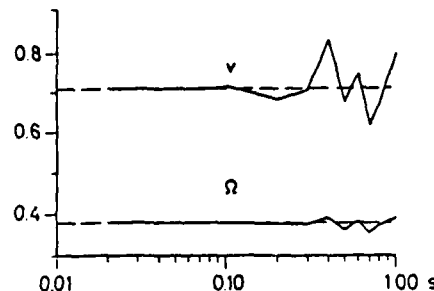


Fig. 3. Dependence of the change of  $v$  and  $\omega$  on the rate of changes of  $\alpha(t)$  (see eq. (25)). The initial frequency and velocity are both set to 0.5, and  $\alpha$  is changed according to eq. (25) ( $A = 1$ ,  $T_F = (20.4/s) + 100$ ). The final frequency and velocity are plotted as functions of  $s$ . The dashed lines correspond to the theoretical predictions in the adiabatic approximations (eqs. (9), (19)).

The results are summarized in fig. 3 where the final values of  $\omega$  and  $v$  are reported as function of  $s$  ( $\omega_{in} = 0.5$ ,  $v_{in} = 0.5$ ,  $A = 1$ ) and  $T_F$  is adjusted in order to give  $\alpha(T_F) \geq 0.99A$ . The figure shows that up to a value of  $s = 0.1$ , corresponding to a time of change of  $\alpha$  comparable with the oscillation period of the breather, there is no appreciable deviation of the numerical results from the theoretical predictions based on the adiabatic assumption.

#### Acknowledgements

S.P. wish to thank the "Fondazione A. Della Riccia", Florence, Italy, for financial support. Financial support from the Thomas B. Thrives Fond (M.S.) and from the European Research Office of the United States Army (contract No. DAJA-US-85-C-0042) (M.S. and S.P.) is also acknowledged. M.R.S. wish to thank the University of Salerno for the kind hospitality received.

#### References

- [1] See Solitons and Condensed Matter Physics, A. Bishop and T. Schneider, eds., Springer Series in Solid-State Sciences, vol. 8, (Springer, Berlin, 1978).

- [2] See for example A. Barone and G. Paterno, Physics and Applications of the Josephson Effect (Wiley, New York, 1982).
- [3] O.H. Olsen, N.F. Pedersen, M.R. Samuelsen, H. Svensmark and D. Weiner, Phys. Rev. B 33 (1986) 168.
- [4] M. Salerno, M.R. Samuelsen, P.S. Lomdhal and O.H. Olsen, Phys. Lett. A 108 (1985) 241.
- [5] A.C. Scott, Phys. Scripta 20 (1979) 509.
- [6] P.L. Christiansen and O.H. Olsen, Wave Motion 4 (1982)
- [163.] J.P. Leon, G. Reinisch and J.C. Fernandez, Phys. Rev. B 127 (1983) 5817.
- [7] M.J. Ablowitz, M.D. Kruskal and J.F. Ladik, SIAM J. Appl. Math. 36 (1979) 428.
- [8] J.C. Eilbeck, in: Soliton in Condensed Matter Physics, Springer Series in Solid State Sciences, vol. 8 (Springer, Berlin, 1978).

## Stability of the McCumber curve for long Josephson tunnel junctions

G. Costabile, S. Pagano,\* and R. D. Parmentier

*Dipartimento di Fisica, Università di Salerno, I-84100 Salerno, Italy*

(Received 3 July 1986; revised manuscript received 1 June 1987)

The stability of the McCumber solution of the perturbed sine-Gordon equation that describes the dynamics of a long Josephson junction may conveniently be studied within the context of a Fourier-Galerkin approximation. In the absence of an externally applied magnetic field, this procedure predicts analytically how the number, locations, and widths of the unstable regions of the McCumber curve depend on the junction parameters. These instabilities are of physical interest because they evolve into the fluxon oscillations associated with zero-field steps. In the presence of a small applied magnetic field, the same procedure provides a technique for studying Fiske steps.

### I. INTRODUCTION

The determination of instability regions associated with the McCumber curve in the current-voltage ( $I$ - $V$ ) characteristics of long, narrow (hysteretic) Josephson tunnel junctions has attracted research interest because the existence of such instability regions is directly connected with the experimental observation of zero-field steps (ZFS's) in the  $I$ - $V$  characteristics of such junctions. This connection was first pointed out in 1973 by Fulton and Dynes,<sup>1</sup> on the basis of observations on a mechanical analog of the long Josephson junction. Later, the problem was studied analytically by Burkov and Lifsic.<sup>2</sup> More recently, Pagano *et al.*<sup>3</sup> have considered the problem in some detail, reporting analytical, numerical, and experimental results. Briefly, the picture that emerges from these studies is as follows: To observe ZFS's experimentally, one raises the bias current applied to the junction from zero up to the critical value, whereupon the junction switches from the zero-voltage state to the gap state. The bias current is then reduced to some nonzero value; during this phase the McCumber curve in the  $I$ - $V$  plane is traced out. Raising the current again then allows tracing out the ZFS's.

This situation may be understood theoretically by performing a stability analysis of the particular solution, corresponding to the McCumber curve, of the perturbed sine-Gordon equation that describes the dynamics of the junction. The simplest case is that in which there is no external magnetic field applied to the junction. In this case it is particularly convenient to perform a multimode, i.e., Fourier-Galerkin, decomposition of the model equation since the McCumber solution corresponds to excitation of only the zero-order mode. The stability of this solution is governed by the higher-order mode equations, which, in the linear approximation, reduce to a set of uncoupled, damped Lamé equations, for which exact, analytic solutions have been found. Such Lamé equations exhibit parametrically excited unstable solutions in some regions of their parameter space; these instabilities evolve with time into the fluxon oscillations associated with the ZFS's.

The application of an external magnetic field provides a mixing mechanism between the various mode equations, thus rendering the analysis less tractable. For a sufficiently small field, however, we can once again linearize the higher-order mode equations. In this approximation, the essential effect of the field is simply to add an inhomogeneous driving term to the odd-order mode equations. This term is responsible for the appearance of (odd-order) Fiske steps (FS's) in the  $I$ - $V$  characteristic of the junction.

### II. MATHEMATICAL MODEL

The mathematical model of the overlap-geometry Josephson junction is, in normalized form, the perturbed sine-Gordon equation<sup>4</sup>

$$\phi_{xx} - \phi_{tt} - \sin\phi = \alpha\phi, -\beta\phi_{xxt} - \gamma, \quad (1a)$$

$$\phi_x(0, t) = \phi_x(L, t) = \eta. \quad (1b)$$

Here,  $\phi(x, t)$  is the usual Josephson phase variable,  $x$  is distance along the junction normalized to the Josephson penetration length, and  $t$  is time normalized to the inverse of the Josephson plasma angular frequency. The model contains five parameters:  $\alpha$ ,  $\beta$ ,  $\gamma$ ,  $L$ , and  $\eta$ . The term in  $\alpha$  represents shunt loss due to quasiparticle tunneling (assumed Ohmic), the term in  $\beta$  represents dissipation due to the surface resistance of the superconducting films,  $\gamma$  is the spatially uniform bias current normalized to the maximum zero-voltage Josephson current,  $L$  is the normalized junction length, and  $\eta$  is the normalized external magnetic field, applied in the plane of the junction and perpendicular to its long dimension. In recent years this model has been shown to describe a wide range of experimentally observed Josephson phenomena, often to a surprising level of detail.

A number of approaches have been employed in the literature to solve Eqs. (1). One of these, which has been found convenient in particular for the study of periodic limit cycle behavior, is the Fourier-Galerkin approximation, i.e., projection onto a truncated series of Fourier spatial modes whose amplitudes are unknown functions

of time. To illustrate this approach we consider first the case of homogeneous boundary conditions, i.e.,  $\eta=0$  in Eq. (1b). We take as a solution ansatz the form

$$\phi(x,t) = \sum_{j=0}^N \phi_j(t) \cos(j\pi x/L), \quad (2)$$

where  $N$  is some finite number. The choice of this form stems from considering, at any instant of time, a reflection of the function  $\phi(x,t)$  in the interval  $x=0$  to  $L$  onto the interval  $x=0$  to  $-L$  in such a way as to construct a periodic, continuous, smooth, even function with spatial periodicity  $2L$ . In the limit  $N \rightarrow \infty$  the representation of Eq. (2) is exact; the practical usefulness of this approach depends upon being able to obtain a "reasonable" description of the system behavior using a relatively small value of  $N$ .

Inserting Eq. (2) into Eqs. (1), and using the orthogonality properties of the trigonometric functions, we obtain the following set of ordinary differential equations for the mode amplitudes  $\phi_j(t)$ :

$$\ddot{\phi}_0 + \alpha\dot{\phi}_0 = \gamma - (1/L) \int_{x=0}^L \sin\phi \, dx, \quad (3a)$$

$$\begin{aligned} \ddot{\phi}_m + (\alpha + \beta\omega_m^2)\dot{\phi}_m + \omega_m^2\phi_m \\ = -(2/L) \int_{x=0}^L \sin\phi \cos(m\pi x/L) \, dx, \quad (3b) \end{aligned}$$

$$m = 1, 2, \dots, N$$

in which  $\omega_m \equiv m\pi/L$ , and  $\phi$  is given by Eq. (2), and overdots denote derivatives with respect to  $t$ .

### III. McCUMBER STABILITY ANALYSIS

A McCumber solution of Eqs. (1) is one without spatial structure; in terms of the elastically coupled pendulum-chain analog of the sine-Gordon system it has all of the pendula rotating in synchronism "over the top." In terms of Eqs. (3) it is represented by a configuration having  $\phi_0 \neq 0$  and  $\phi_m(t) \equiv 0$ ,  $m = 1, 2, \dots, N$ . In this situation Eq. (3a) becomes

$$\ddot{\phi}_0 + \alpha\dot{\phi}_0 = \gamma - \sin\phi_0, \quad (4)$$

and all of Eqs. (3b) become identically zero. In the absence of loss and bias ( $\alpha = \gamma = 0$ ), the rotating solution of Eq. (4) is exactly

$$\phi_0(t) = 2 \operatorname{am}(t/k; k), \quad (5)$$

where  $\operatorname{am}$  is the Jacobian elliptic amplitude function<sup>5</sup> of modulus  $k$ , with  $0 \leq k \leq 1$ . For nonzero  $\alpha$  and  $\gamma$  we assume that Eq. (5) solves Eq. (4) in the power-balance approximation, i.e., we equate the average power furnished by the bias supply,  $P_{\text{in}} = \gamma \langle \dot{\phi}_0 \rangle$ , to the average power dissipated,  $P_{\text{out}} = \alpha \langle \dot{\phi}_0^2 \rangle$ , where angular brackets denote a time-averaged value. Carrying out this operation yields the following expressions for the McCumber branch of the  $I-V$  characteristic of the junction:

$$\gamma = 4\alpha E(k)/\pi k, \quad (6a)$$

$$1 - \langle \phi_0 \rangle = \pi/k K(k), \quad (6b)$$

where  $K(k)$  and  $E(k)$  are, respectively, the complete elliptic integrals of first and second kinds.<sup>5</sup>

To study the stability of this solution we suppose now that the  $\phi_m(t)$ ,  $m = 1, 2, \dots, N$ , are all small but nonzero. Defining

$$\epsilon \equiv \sum_{j=1}^N \phi_j(t) \cos(j\pi x/L), \quad (7)$$

we expand  $\sin\phi$  to linear terms as

$$\sin\phi = \sin(\phi_0 + \epsilon) = \sin\phi_0 + \epsilon \cos\phi_0. \quad (8)$$

Inserting Eq. (8) into Eqs. (3), and utilizing once again the orthogonality of the cosines, we obtain

$$\ddot{\phi}_0 + \alpha\dot{\phi}_0 = \gamma - \sin\phi_0, \quad (9a)$$

$$\ddot{\phi}_m + (\alpha + \beta\omega_m^2)\dot{\phi}_m + \omega_m^2\phi_m = -\phi_m \cos\phi_0, \quad m = 1, 2, \dots, N. \quad (9b)$$

The equation for  $\phi_0$ , Eq. (9a), is exactly the same as in the unperturbed case, Eq. (4). Equations (9b) represent a set of  $N$  uncoupled, linear, parametrically excited oscillators in which the  $\phi_0$  term is the parametric driver. Since these equations are uncoupled, they may be solved independently, which greatly simplifies the analysis.

Inserting the expression of Eq. (5) for  $\phi_0$  into the generic member of Eqs. (9b), we obtain explicitly, for the  $n$ th mode, the equation

$$\ddot{\phi}_n + (\alpha + \beta\omega_n^2)\dot{\phi}_n + [\omega_n^2 + 1 - 2 \operatorname{sn}^2(t/k; k)]\phi_n = 0, \quad (10)$$

where  $\operatorname{sn}$  is the Jacobian elliptic sine function of modulus  $k$ . Defining the new time variable,  $\tau \equiv t/k$ , we transform Eq. (10) into

$$\ddot{\phi}_n + k(\alpha + \beta\omega_n^2)\dot{\phi}_n + [k^2(\omega_n^2 + 1) - 2k^2\operatorname{sn}^2(\tau; k)]\phi_n = 0, \quad (11)$$

where overdots now denote derivatives with respect to  $\tau$ . We may eliminate the first derivative term in Eq. (11) by means of the standard transformation

$$\phi_n(\tau) = y(\tau) \exp[-\frac{1}{2}k(\alpha + \beta\omega_n^2)\tau], \quad (12)$$

under which Eq. (11) becomes

$$\ddot{y} + [k^2[\omega_n^2 + 1 - \frac{1}{4}(\alpha + \beta\omega_n^2)^2] - 2k^2\operatorname{sn}^2(\tau; k)]y = 0. \quad (13)$$

Equation (13) is Lamé's equation. A detailed discussion of the exact analytic solution of this equation (in somewhat more generalized form) may be found in Whittaker and Watson<sup>6</sup> (who attribute the original solution to lecture notes of Hermite dating from 1872). Following their discussion, we find two linearly independent solutions of Eq. (13) to be

$$y_+(\tau) = [H(\tau - \tau_0)/\theta(\tau)] \exp[+Z(\tau_0)\tau], \quad (14a)$$

$$y_-(\tau) = [H(\tau + \tau_0)/\theta(\tau)] \exp[-Z(\tau_0)\tau], \quad (14b)$$

where  $H$ ,  $\theta$ , and  $Z$  are, respectively, the eta, theta, and zeta functions of Jacobi,<sup>5</sup> provided the constant  $\tau_0$

satisfies the equation

$$\begin{aligned} \text{cn}^2(\tau_0; k) \text{ds}^2(\tau_0; k) - \text{ns}^2(\tau_0; k) \\ = -k^2[\omega_n^2 + 1 - \frac{1}{4}(\alpha + \beta\omega_n^2)^2], \quad (15) \end{aligned}$$

where cn, ds, and ns are Jacobian elliptic functions.<sup>5</sup> Using various identities amongst these functions,<sup>5</sup> we may simplify Eq. (15) to

$$\text{sn}^2(\tau_0; k) = 1/k^2 - \omega_n^2 + \frac{1}{4}(\alpha + \beta\omega_n^2)^2. \quad (16)$$

The nature of the functions in Eqs. (14) depends on the value assumed by the right-hand side of Eq. (16). We may *a priori* distinguish four possible cases.

*Case 1:*  $0 \leq 1/k^2 - \omega_n^2 + \frac{1}{4}(\alpha + \beta\omega_n^2)^2 \leq 1$ . Using various results from Ref. 5, we may establish that  $\tau_0$  is real,  $0 \leq \tau_0 \leq K(k)$ ,  $H/\theta$  is real and periodic, and  $Z(\tau_0) \geq 0$ . Hence, from Eqs. (14) and (12), the stability boundaries of Eq. (11) are given by

$$\delta \equiv Z(\tau_0) - \frac{1}{2}k(\alpha + \beta\omega_n^2) = 0. \quad (17)$$

$\delta < 0$  implies stability;  $\delta > 0$  implies instability.

*Case 2:*  $1/k^2 - \omega_n^2 + \frac{1}{4}(\alpha + \beta\omega_n^2)^2 < 0$ . We may establish that  $\tau_0$  is pure imaginary,  $Z(\tau_0)$  is pure imaginary, and  $H/\theta$  is complex, but periodic. Hence,  $\text{Re}(\delta) = -\frac{1}{2}k(\alpha + \beta\omega_n^2) < 0$ , which implies stability.

*Case 3:*  $1 < 1/k^2 - \omega_n^2 + \frac{1}{4}(\alpha + \beta\omega_n^2)^2 \leq 1/k^2$ . We may establish that  $\tau_0$  is complex,  $\text{Re}(\tau_0) = K(k)$ ,  $Z(\tau_0)$  is pure imaginary, and  $H/\theta$  is complex, but periodic. Hence, as in case 2,  $\text{Re}(\delta) = -\frac{1}{2}k(\alpha + \beta\omega_n^2) < 0$ , which implies stability.

*Case 4:*  $1/k^2 < 1/k^2 - \omega_n^2 + \frac{1}{4}(\alpha + \beta\omega_n^2)^2 < \infty$ , i.e.,  $\alpha + \beta\omega_n^2 > 2\omega_n$ . We may establish that  $\tau_0$  is complex,  $\text{Im}(\tau_0) = K(k')$ , where  $k'$  is the complementary modulus, and  $H/\theta$  is complex, but periodic; however, the nature of  $Z(\tau_0)$  is not (at least to us) completely clear. However, we note that for "physically reasonable" parameters case 4 is unlikely: e.g., with  $\alpha = 0.05$  and  $\beta = 0.02$ , case 4 is obtained only if  $L/n < 0.0314$  or if  $L/n > 126$ , where  $L$  is the normalized junction length and  $n$  is the order of the ZFS.

Consequently, in practice, the only physically relevant situation is case 1. The computational procedure involves fixing the parameters  $\alpha$ ,  $\beta$ ,  $L$ , and  $n$ , and iterating Eqs. (16) and (17) until a value of  $k$  is found which gives  $\delta = 0$ . The stability boundaries in current and voltage are then found by inserting this value of  $k$  into Eqs. (6). The necessary calculations may be carried out readily using a programmable pocket calculator.

As a check on this theory we have compared our present results with those obtained by Pagano *et al.*<sup>3</sup> by means of a perturbation expansion of Eqs. (9b) in the high-voltage region of the McCumber curve. We have also compared our results with those obtained by a direct numerical implementation of Floquet theory.<sup>7</sup> Agreement was found in all cases.

#### IV. SOME PARTICULAR RESULTS

Suppose we wish to establish a stability boundary at  $V = 0$ , i.e., we impose  $\delta(V=0)=0$ . From Eq. (6b),  $V=0$

corresponds to  $k=1$ . For  $k=1$ , both  $\text{sn}(\tau_0; k)$  and  $Z(\tau_0)$  reduce to  $\tanh(\tau_0)$ , so that, from Eqs. (16) and (17), the condition for  $\delta(V=0)=0$  is

$$[1 - \omega_n^2 + \frac{1}{4}(\alpha + \beta\omega_n^2)^2]^{1/2} = \frac{1}{2}(\alpha + \beta\omega_n^2), \quad (18)$$

i.e.,  $L/n = \pi$ . For  $L/n > \pi$ , we have  $\delta(V=0) > 0$ , which implies instability. From these facts one might be tempted to infer that for all  $L/n \geq \pi$  the instability region in voltage extends from some maximum value, say  $V_m$ , down to  $V=0$ . Numerical calculations show this to be almost, but not quite, correct: For  $L/n$  very slightly greater than  $\pi$ , the instability region may consist of two disjoint pieces separated by a region of stability. For example, for  $\alpha = 0.05$ ,  $\beta = 0.02$ , and  $L/n = 3.142$ , the McCumber curve is unstable from  $V=0$  to 0.287 and from  $V=0.589$  to 2.39; but already for  $L/n = 3.143$  the intermediate stable region becomes unstable, and the instability region extends smoothly down to  $V=0$ .

Another consequence of this theory is that instability regions corresponding to the same value of  $\alpha$ ,  $\beta$ , and  $L$ , but different  $n$ , can overlap. This situation is illustrated in Fig. 1, which shows the instability regions for  $\alpha = 0.05$ ,  $\beta = 0.02$  and  $n = 1, 2, 3$ , as a function of  $L$ . For different values of  $\alpha$  and  $\beta$  the form of the instability regions remains quite similar to that shown, the major difference being that the "peak points," i.e., the points where the width of a region goes to zero, move to higher voltages for smaller  $\alpha$  and/or  $\beta$ . The numbers in parentheses in Fig. 1 indicate which McCumber regions are unstable in the various zones of the  $V$ - $L$  plane. The existence of overlapping instability regions might imply the existence of a switching mechanism between different ZFS's, but a verification of this hypothesis lies beyond the scope of a linear stability theory. In any case, the above two observations suggest a simple explanation for the frequently observed experimental fact that it is often difficult to bias on low-order ZFS's in longer junctions: If the low-order instability regions overlap, and if the lowest region or regions extend down to  $V=0$ , then it seems not unlikely that in descending along the

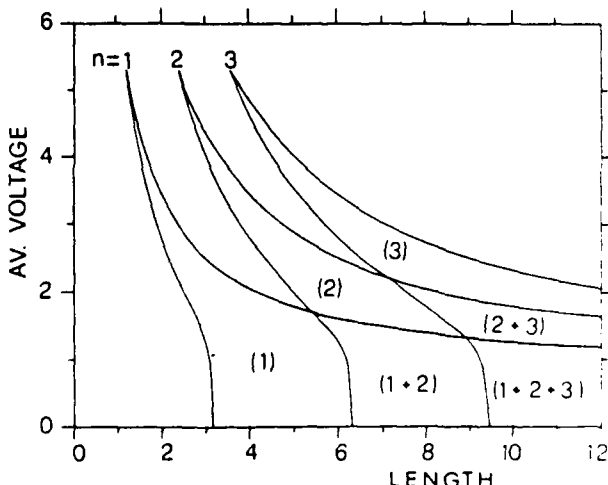


FIG. 1. Junction-length dependence of instability regions for  $\alpha = 0.05$  and  $\beta = 0.02$ . Numbers in parentheses indicate which McCumber regions are unstable.

McCumber curve one might switch directly to the zero-voltage state, skipping over the intervening ZFS's.

A linear stability analysis can provide estimates of the stability boundaries along the McCumber curve, but it cannot furnish the time evolution of an unstable solution. This question was addressed in Ref. 3, where it was shown by direct numerical integration of Eqs. (3) how such an unstable solution evolves into the fluxon oscillation associated with a ZFS. The existence of such a dynamic route is also suggested by the following analytic argument: Suppose in Eqs. (3) that only one spatial mode, say the  $n$ th, is excited, but that its amplitude is not restricted to be small. In this case Eqs. (3) can be written explicitly as

$$\ddot{\phi}_n + \alpha \dot{\phi}_n = \gamma - J_0(\phi_n) \sin \phi_0, \quad (19a)$$

$$\ddot{\phi}_n + (\alpha + \beta \omega_n^2) \dot{\phi}_n + \omega_n^2 \phi_n = -2J_1(\phi_n) \cos \phi_0, \quad (19b)$$

where  $J_0$  and  $J_1$  are Bessel functions of the first kind. With the assumption that  $\phi_0 = \omega t$ , with  $\omega$  constant, Eq. (19b) becomes just the equation derived by Takanaka<sup>8</sup> to study the  $I$ - $V$  profile of ZFS's. In fact, all of Takanaka's results are reproduced by applying the Krylov-Bogoliubov approximation procedure<sup>9</sup> to Eqs. (19). Similarly, a two-mode approximation to Eqs. (3), together with the Krylov-Bogoliubov procedure, gives rise to the results of Chang *et al.*,<sup>10</sup> and an  $N$ -mode approximation to those of Enpuku *et al.*<sup>11</sup>

## V. MAGNETIC FIELD EFFECTS

In the presence of an external magnetic field,  $\eta \neq 0$  in Eq. (1b), the solution ansatz of Eq. (2) is no longer appropriate since it does not satisfy the boundary conditions. The expedient normally employed in this situation is to replace Eq. (2) by an ansatz of the form

$$\phi(x, t) = f(x) + \sum_{j=0}^N \phi_j(t) \cos(j\pi x/L), \quad (20)$$

where  $f(x)$  is some function that satisfies Eq. (1b). Several different such ansätze have been used by various authors: Enpuku *et al.*<sup>11</sup> use  $f(x) = \eta x$ . Watanabe and Ishii<sup>12</sup> use the procedure, due to Olsen and Samuelsen,<sup>13</sup> of choosing an  $f(x)$  that corresponds to two static virtual fluxons placed outside the two ends of the junction. Kawamoto<sup>14,15</sup> uses, respectively, in the two papers cited, a static fluxon lattice array and a static fluxon-antifluxon array for  $f(x)$ .

The basic mathematical requirement on  $f(x)$  is that it must satisfy Eq. (1b). In addition, a "good" choice for  $f(x)$  presumably should be computationally simple and should lead to a relatively rapid convergence of the truncated Fourier series in Eq. (20). Since we are not aware of how to guarantee *a priori* this second condition, we shall, in what follows, use the Enpuku *et al.*<sup>11</sup> ansatz,  $f(x) = \eta x$ , because of its simplicity. This choice [with the substitution of Eq. (20) for  $\phi$ ] leaves the form of the dynamical equations, Eqs. (3), unchanged.

The main effect of the introduction of the magnetic field is that now there is, in general, always an excitation of the spatial modes that does not any longer allow a

separation of the junction dynamics into independent oscillators, as in the discussion leading up to Eqs. (9). Consequently, in order to make some analytical progress, we now assume that  $\eta L \ll 1$ , and we assume that this implies that  $\epsilon$  in Eq. (7) is small. Expanding  $\sin \phi$  to linear terms in small quantities, we may write Eqs. (3) as

$$\ddot{\phi}_0 + \alpha \dot{\phi}_0 = \gamma - \sin(\phi_0 + \eta L/2), \quad (21a)$$

$$\begin{aligned} \ddot{\phi}_m + (\alpha + \beta \omega_m^2) \dot{\phi}_m + (\omega_m^2 + \cos \phi_0) \phi_m \\ = (4\eta L/m^2\pi^2) P_m \cos \phi_0, \end{aligned} \quad (21b)$$

where  $m = 1, 2, \dots, N$ , and  $P_m = (0, 1)$  for  $m$  (even, odd).

With the substitution  $\phi'_0 = \phi_0 + \eta L/2$ , Eq. (21a) becomes identical to Eq. (9a). Equations (21b) differ from Eqs. (9b) only by the presence of the inhomogeneous driving term  $(4\eta L/m^2\pi^2) P_m \cos \phi_0$ , which is present only for odd  $m$ . Since Eqs. (21b) are, by construction, once again linear, their total solution is just the sum of the homogeneous solution, i.e., that found in Sec. III above, plus a particular integral. The homogeneous solution shows exponential growth when the dominant frequency of  $\cos \phi_0$  is approximately  $2\omega_m$  (for any  $m$ ). Outside of the instability regions the homogeneous solution tends asymptotically to zero. The particular integral, on the other hand, is essentially a resonance having a peak response when the dominant frequency of  $\cos \phi_0$  is approximately  $\omega_m$  (for odd  $m$ ). Thus, in the context of the linear approximation, the appearance of ZFS's may be attributed to a parametrically excited resonance of the multimode equations, whereas the appearance of the odd-order FS's derives from a directly excited resonance of these equations. A complete analysis of magnetic field effects, and in particular an analysis of the even-order FS's, requires going beyond the linear approximation. This may be effected by perturbation theory, as in Ref. 3, or else by a direct numerical integration of Eqs. (3), in either case using the ansatz of Eq. (20) for  $\phi$ .

## VI. CONCLUSIONS

The linear stability analysis described above provides a simple explanation for a number of frequently observed experimental facts, e.g., the fact that it is often difficult to bias on low-order ZFS's in longer junctions. Moreover, it underscores the fact, first suggested by Chang *et al.*,<sup>10</sup> that both ZFS's and FS's might be described within the context of a single, unified model. It should be noted, however, that this analysis applies only to the mechanism of switching from the McCumber curve. There presumably exist also other mechanisms for biasing on steps (both ZFS's and FS's); the study of these will presumably require other tools.

## ACKNOWLEDGMENTS

This work was initiated while two of us (S.P. and R.D.P.) were guests at the Laboratory of Applied Mathematical Physics of The Technical University of Denmark (DTU); it was further developed while the

third of us (G.C.) was a guest at Physics Laboratory I of the same institution. We are all grateful for the hospitality received at DTH. We gratefully acknowledge financial support from the European Research Office of the United States Army through Contract No. DAJA-45-85-C-0042, the Thomas B. Thriges Fond (Denmark),

the Fondazione Angelo della Riccia (Italy), and the Gruppo Nazionale di Struttura della Materia/Consiglio Nazionale delle Ricerche—Centro Interuniversitario di Struttura della Materia/Ministero della Pubblica Istruzione (Italy).

\*Present address: Istituto di Cibernetica del CNR, I-80072 Arco Felice (NA), Italy.

<sup>1</sup>T. A. Fulton and R. C. Dynes, Solid State Commun. **12**, 57 (1973).

<sup>2</sup>S. E. Burkov and A. E. Lifsic, Wave Motion **5**, 197 (1983).

<sup>3</sup>S. Pagano, M. P. Soerensen, R. D. Parmentier, P. L. Christiansen, O. Skovgaard, J. Mygind, N. F. Pedersen, and M. R. Samuelsen, Phys. Rev. B **33**, 174 (1986).

<sup>4</sup>P. S. Lomdahl, O. H. Soerensen, and P. L. Christiansen, Phys. Rev. B **25**, 5737 (1982).

<sup>5</sup>M. Abramowitz and I. A. Stegun, *Handbook of Mathematical Functions*, 9th ed. (Dover, New York, 1970), Chaps. 16 and 17.

<sup>6</sup>E. T. Whittaker and G. N. Watson, *A Course of Modern Analysis*, 4th ed. (Cambridge University Press, Cambridge, 1927), Sec. 23.71.

<sup>7</sup>B. A. Asner, Jr., Int. J. Non-Linear Mech. **15**, 127 (1980).

<sup>8</sup>K. Takanaka, Solid State Commun. **29**, 443 (1979).

<sup>9</sup>N. Minorsky, *Nonlinear Oscillations* (Van Nostrand, Princeton, 1962), Chap. 14.

<sup>10</sup>J.-J. Chang, J. T. Chen, and M. R. Scheuermann, Phys. Rev. B **25**, 151 (1982).

<sup>11</sup>K. Enpuku, K. Yoshida, and F. Irie, J. Appl. Phys. **52**, 344 (1981).

<sup>12</sup>K. Watanabe and C. Ishii, in *Proceedings of LT-17, Part I—Contributed Papers*, edited by U. Eckern, A. Schmid, H. Weber, and H. Wühl (North-Holland, Amsterdam, 1984), p. 705.

<sup>13</sup>O. H. Olsen and M. R. Samuelsen, J. Appl. Phys. **52**, 6247 (1981).

<sup>14</sup>H. Kawamoto, Prog. Theor. Phys. **66**, 780 (1981).

<sup>15</sup>H. Kawamoto, Prog. Theor. Phys. **70**, 1171 (1983).

## Chaotic Behaviour of a Pendulum with Variable Length.

M. BARTUCCHELLI (\*), P. L. CHRISTIANSEN, V. MUTO and M. P. SOERENSEN

*Laboratory of Applied Mathematical Physics  
The Technical University of Denmark, DK-2800 Lyngby, Denmark*

N. F. PEDERSEN

*Physics Laboratory I  
The Technical University of Denmark, DK-2800 Lyngby, Denmark*

(ricovuto il 24 Giugno 1987)

**Summary.** — The Melnikov function for the prediction of Smale horseshoe chaos is applied to a driven damped pendulum with variable length. Depending on the parameters, it is shown that this dynamical system undertakes heteroclinic bifurcations which are the source of the unstable chaotic motion. The analytical results are illustrated by new numerical simulations. Furthermore, using the averaging theorem, the stability of the subharmonics is studied.

PACS. 05.45. — Theory and models of chaotic systems.  
PACS. 43.40.Ga — Nonlinear vibration.

### 1. — Introduction.

In this paper we investigate the heteroclinic and subharmonic bifurcations of a pendulum with variable length using the so-called Melnikov method (¹).

This method is a global perturbation theory which is able to analytically predict the occurrence of homoclinic (heteroclinic) and subharmonic bifur-

(\*) Present address: Mathematics Department, Queen Mary College University of London, Mile End Road, London, E1 4NS, England.

(¹) V. K. MELNIKOV: *Trans. Moscow Math. Soc.*, 12, 1 (1963).

tions when some parameters of the system are varied. Further, it gives sufficient conditions for the occurrence of transversal intersection between the stable and unstable branches of the homoclinic (heteroclinic) orbits. When such a transversal intersection occurs, it can be shown, using the Birkhoff-Smale theorem (2), that the set of nonwandering points (2) contains an invariant Cantor set; moreover, some iterate of the Poincaré map restricted to this Cantor set is equivalent to a shift on two symbols (*i.e.* a horseshoe) (2). This invariant hyperbolic Cantor set is structurally stable, this guarantees that we can perturb it slightly without destroying it. However, it is important to realize that this invariant set is not an attractor. This means that the existence of homoclinic (heteroclinic) points does not imply stable chaotic behaviour. Nevertheless, it is quite difficult to predict the asymptotic behaviour of an orbit because the stable manifold behaves like an uncountable set of saddle separatrices, *i.e.* two orbits starting on different sides of the stable manifold will ultimately separate exponentially fast (this is equivalent to saying «sensitive dependence upon initial conditions», *i.e.* chaos).

Also the occurrence of the so-called homoclinic (heteroclinic) tangencies in dissipative systems is very important. Works of Newhouse (3-5) and Gavrilov-Silnikov (6,7) indicate that there are infinite sets of «stable» periodic orbits of arbitrarily long periods. These orbits are created through saddle-node bifurcations and throughout the bifurcations they double their periods repeatedly. Such bifurcations can be expected to occur within chaotic regimes. Moreover, we can expect an infinite number of periodic sinks for parameter values near the homoclinic tangencies. Several examples exist of systems for which homoclinic tangencies occur (8). Thus we expect this wild behaviour to be found in many other systems.

The paper is organized as follows: Sect. 2 describes the physical model. Section 3 contains the heteroclinic Melnikov function. Section 4 deals with the subharmonic Melnikov functions. In sect. 5 the stability of the subharmonic solutions is discussed using second-order averaging. Finally, sect. 6 contains the conclusion. Throughout the paper one can see how Melnikov's theory gives global results, which enable us to prove the onset of chaos for periodically perturbed nonlinear systems like the pendulum with variable length.

(2) J. GUCKENHEIMER and P. J. HOLMES: *Nonlinear Oscillations, Dynamical Systems and Bifurcations of Vector Fields*, Appl. Math. Sci., Vol. 42 (Springer-Verlag, Berlin, 1983).

(3) S. E. NEWHOUSE: *Topology*, 13, 9 (1974).

(4) S. E. NEWHOUSE: *Publ. Math. IHES*, 50, 101 (1979).

(5) S. E. NEWHOUSE: *Lectures on dynamical systems*, in *Dynamical Systems, C.I.M.E. Lectures, Bressanone, Italy, June 1978, Progress in Mathematics*, No. 8 (Birkhäuser, Boston, Mass., 1980), p. 1.

(6) N. K. GAVRILOV and L. P. SILNIKOV: *Math. USSR Sb.*, 88, 467 (1972).

(7) N. K. GAVRILOV and L. P. SILNIKOV: *Math. USSR Sb.*, 90, 139 (1973).

We hope that it will be possible to make real experiments on this system as in other comparable systems (8) in order to test the physical validity of Melnikov's theory.

Steps in this direction, that is, examples in which Melnikov's theory has been compared with real experiments, are those described in ref. (9-14).

## 2. - The physical model.

We consider a simple damped pendulum with unit mass and variable length in the gravity field, driven by an oscillating external torque. It can be shown that the equation of motion which governs this system is (15)

$$(1) \quad \frac{d}{d\tau} \left( l \frac{dx}{d\tau} \right) + lg \sin x = -r \frac{dx}{d\tau} + r_1 \sin (\omega_1 \tau),$$

$r, r_1$  and  $\omega_1$  being nonnegative constants. Here  $x(\tau)$  is the angular displacement from the vertical at time  $\tau$ .  $r$  is the damping constant,  $r_1$  is the amplitude of the oscillating external torque with frequency  $\omega_1$  and  $g$  denotes the gravitational constant. The length  $l(\tau)$  of the pendulum is assumed to vary with time  $\tau$  according to

$$(2) \quad l(\tau) = a + b \sin (\omega \tau), \quad a \gg b > 0, \quad \omega > 0.$$

Introducing  $H = b/a \ll 1$  and  $\omega_0^2 = g/a$ , eqs. (1) ... 1 (2) lead to

$$(3) \quad (1 + 2H \sin (\omega \tau)) \frac{d^2x}{d\tau^2} + 2\omega H \cos (\omega \tau) \frac{dx}{d\tau} + \omega_0^2 (1 + H \sin (\omega \tau)) \sin x = -\frac{r}{a^2} \frac{dx}{d\tau} + \frac{r_1}{a^2} \sin (\omega_1 \tau).$$

(8) M. BARTUCELLI, P. L. CHRISTIANSEN, N. F. PEDERSEN and M. P. SOERENSEN: *Phys. Rev. B*, **33**, 4686 (1986).

(9) Z. G. GENCHEV, Z. G. IVANOV and B. N. TORDOROV: *IEEE Trans. Circuits Syst., CAS-30*, 633 (1983).

(10) B. P. KOCH, R. W. LEVEN, B. POMPE and R. WILKE: *Phys. Lett. A*, **96**, 219 (1983).

(11) B. P. KOCH and R. W. LEVEN: *Physica D (Utrecht)*, **16**, 1 (1985).

(12) R. W. LEVEN, B. POMPE, C. WILKE and B. P. KOCH: *Physica D (Utrecht)*, **16**, 371 (1985).

(13) F. M. A. SALAM and S. S. SAstry: *The complete dynamics of the forced Josephson junction circuit: the regions of chaos*, in *Chaos in Nonlinear Dynamical Systems*, edited by J. CHANDRA (SIAM, Philadelphia, Penn., 1984), p. 43.

(14) F. C. MOON, J. CUSUMANO and P. J. HOLMES: *Physica D (Utrecht)*, **24**, 383 (1987).

(15) T. LEVI-CIVITA and U. AMALDI: *Lezioni di meccanica razionale* (Zanichelli, Bologna, 1927).

This equation is valid to order  $O(H)$ . Dividing eq. (3) by  $\omega_0^2$  and redefining time  $\tau$  as  $t = \omega_0 \tau$ , we obtain

$$(4) \quad \left(1 + 2H \sin\left(\frac{\omega}{\omega_0} t\right)\right) \ddot{x} + 2 \frac{\omega}{\omega_0} H \cos\left(\frac{\omega}{\omega_0} t\right) \dot{x} + \left(1 + H \sin\left(\frac{\omega}{\omega_0} t\right)\right) \sin x = \\ = -\frac{r}{\omega_0 a^2} \ddot{x} + \frac{r_1}{\omega_0^2 a^2} \sin\left(\frac{\omega_1}{\omega_0} t\right).$$

Dots denote derivatives with respect to the normalized time  $t$ . We now redefine the parameters in eq. (4) according to

$$(5) \quad \begin{cases} \frac{r}{\omega_0 a^2} = \varepsilon \beta, & \frac{r_1}{\omega_0^2 a^2} = \varepsilon \varrho_1, \\ \frac{\omega_1}{\omega_0} = \bar{\omega}_1, & \frac{\omega}{\omega_0} = \bar{\omega} \quad \text{and} \quad \frac{\omega}{\omega_0} H = \varepsilon \bar{\omega} \bar{H}, \end{cases}$$

where  $\varepsilon \ll 1$ . Assuming  $H \ll (\omega/\omega_0)H \ll 1$ ,  $H \ll \varepsilon \beta$  and  $H \ll \varepsilon \varrho_1$ , eq. (4) (after dropping the bars) finally reduces to

$$(6) \quad \ddot{x} + \sin x = \varepsilon [-\beta \dot{x} + \varrho_1 \sin(\omega_1 t) - 2\omega H \cos(\omega t)].$$

### 3. - The heteroclinic Melnikov function.

Equation (6) can be written as a system of two first-order ordinary differential equations, i.e.

$$(7) \quad \begin{cases} \dot{x} = y, \\ \dot{y} = -\sin x + \varepsilon [-\beta \dot{x} + \varrho_1 \sin(\omega_1 t) - 2H\omega \cos(\omega t)\dot{x}]. \end{cases}$$

When  $\varepsilon = 0$ , system (7) becomes the classical simple-pendulum equations

$$(8) \quad \begin{cases} \dot{x} = y, \\ \dot{y} = -\sin x, \end{cases}$$

which is known to be a completely integrable system. Indeed, eq. (8) is a Hamiltonian system with the Hamiltonian given by

$$(9) \quad \mathcal{H}(x, y) = \frac{y^2}{2} + (1 - \cos x).$$

Besides, the unperturbed system (9) has the following solutions:

- a) Oscillations with energy  $\mathcal{H}(x, y) < 2$ .
- b) Complete revolution (rotations) with energy  $\mathcal{H}(x, y) > 2$ .
- c) Aperiodic motion with energy  $\mathcal{H}(\bar{x}, \bar{y}) = 2$ .

The orbits corresponding to cases a) and b) are periodic orbits.

In order to compute the heteroclinic Melnikov function (2,16) it is necessary to know the so-called heteroclinic solutions (2) of the unperturbed system (8).

They are given by

$$(10) \quad \begin{cases} \bar{x}(t - t_0) = \pm 2 \operatorname{tg}^{-1} [\sinh(t - t_0)], \\ \bar{\dot{x}}(t - t_0) = \bar{y}(t - t_0) = \pm 2 \operatorname{sech}(t - t_0). \end{cases}$$

This case corresponds to case c) described above. The Melnikov function for system (7) is (2)

$$(11) \quad M^\pm(t_0) := \int_{-\infty}^{\infty} \bar{y}(t - t_0) [-\beta \bar{y}(t - t_0) + \varrho_1 \sin(\omega_1 t) - 2H\omega \cos(\omega t) \bar{y}(t - t_0)] dt.$$

Making the following change of variables in formula (11):  $t \rightarrow t + t_0$ , we obtain

$$(12) \quad M^\pm(t_0) := \int_{-\infty}^{+\infty} \bar{y}(t) \{-\beta \bar{y}(t) + \varrho_1 \sin[\omega_1(t + t_0)] - 2H\omega \cos[\omega(t + t_0)] \bar{y}(t)\} dt,$$

which is more convenient in calculations. Substituting formula (10) into formula (12) and making the calculations, we arrive at the following result:

$$(13) \quad M^\pm(t_0) := -8\beta \pm 2\pi\varrho_1 \sin(\omega_1 t_0) \operatorname{sech}\left(\frac{\pi}{2}\omega_1\right) - 8\pi\omega^2 H \cos(\omega t_0) \operatorname{cosech}\left(\frac{\pi}{2}\omega\right).$$

If  $\sin \omega_1 t_0 = \pm 1$  and  $\cos \omega t_0 = -1$ , corresponding to the ratios  $\omega_1/\omega = (1+4s)/(2+t)$  and  $\omega_1/\omega = (3+4s)/(2+4t)$ , where  $s, t$  are integers, the

(16) B. D. GREENSPAN and P. J. HOLMES: *Heteroclinic orbits, subharmonics and global bifurcations in forced oscillations*, in *Nonlinear Dynamics and Turbulence*, edited by G. BARENBLATT, G. IOOSS and D. D. JOSEPH (Pitman, London, 1983), p. 172.

Melnikov function will have infinitely many zeros when

$$(14) \quad \varrho_1 > \cosh\left(\frac{\pi}{2}\omega_1\right) \left[ \frac{4\beta}{\pi} - 4H\omega^2 \operatorname{cosech}\left(\frac{\pi}{2}\omega\right) \right];$$

the corresponding condition on  $H$  becomes

$$(15) \quad H > \frac{\sinh((\pi/2)\omega)}{\omega^2} \left[ \frac{\beta}{\pi} - \frac{\varrho_1}{4} \operatorname{sech}\left(\frac{\pi}{2}\omega_1\right) \right].$$

The equalities in formulae (14) and (15) characterize the onset of the heteroclinic bifurcations with an approximation of  $O(1)$  for sufficiently small  $\varepsilon$ . Furthermore, the strict inequalities (14) and (15) characterize the existence of transverse heteroclinic intersection points between the local stable and unstable branches of the heteroclinic orbits (10). It may be shown (2) that, if the stable and unstable branches of the heteroclinic orbits (10) intersect transversely once, then they intersect each other infinitely many times. The presence of such intersecting orbits implies that the Poincaré map has the so-called Smale horseshoe (2). A Smale horseshoe contains a countable set of unstable periodic orbits, an uncountable set of bounded, nonperiodic orbits and a dense orbit. It should be noticed that even though the Smale horseshoe is extremely complicated and contains an uncountable infinity of nonperiodic or chaotic orbits, it is not an attractor. However, it can exert a dramatic influence on the behaviour of orbits which pass close to it. These orbits will display a sensitive

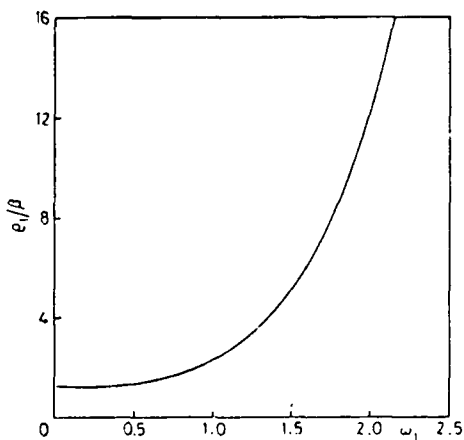


Fig. 1.

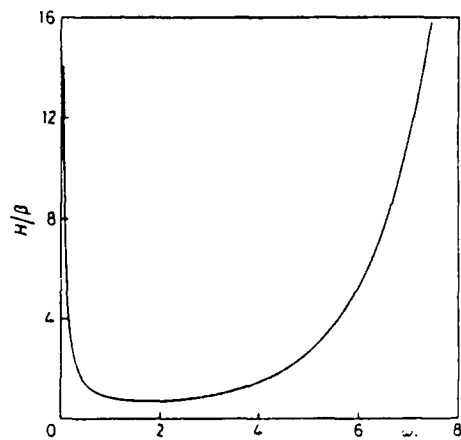


Fig. 2.

Fig. 1. - Heteroclinic bifurcation curve in the  $(\omega_1, \varrho_1)$ -plane (eq. (14)). Smale horseshoe chaos above curve.  $H/\beta = 0.2$ .

Fig. 2. - Heteroclinic bifurcation curve in the  $(\omega_1, H)$  parameter plane (eq. (15)). Smale horseshoe chaos above curve.  $\varrho_1/\beta = 0.2$ .

dependence on initial conditions. Thus system (7) has a Smale horseshoe in its dynamics when inequalities (14) and (15) are strictly satisfied. The bifurcation curves in parameter space which separate regions with and without Smale horseshoe chaos are given by the equalities in formulae (14) and (15). These curves are shown in fig. 1 and 2, where  $\varrho_1/\alpha$  and  $H/\alpha$  are depicted as functions of  $\omega_1$ . In both figures we have chosen the ratio  $\omega_1/\omega = (1 + 4s)/(2 + 4t)$  with  $s = t = 1$ .

#### 4. - Subharmonic Melnikov functions.

In order to apply the subharmonic Melnikov functions (2) we need to know the analytical expressions of the periodic solutions of the unperturbed problem. In fact, the subharmonic Melnikov function for system (8) is defined as follows (2):

$$(16) \quad M^{m/n}(t_0) := \int_0^{mT} f[q^\alpha(t)] \wedge g[q^\alpha(t), (t + t_0)] dt.$$

Here  $q^\alpha(t)$  is a periodic orbit of the unperturbed system with period  $T^\alpha = (m/n)T$ ,  $m$  and  $n$  relatively prime,  $T$  is the period of the perturbation *e.g.*

For system (8) we have two qualitatively different periodic solutions: the oscillating and the rotating solutions. The analytical expressions are

$$(17) \quad \begin{cases} x_{os}(t - t_0, k) = \pm 2 \sin^{-1}[k \operatorname{sn}(t - t_0, k)], \\ y_{os}(t - t_0, k) = \pm 2k \operatorname{cn}(t - t_0, k), \end{cases}$$

for the oscillating case, and

$$(18) \quad \begin{cases} x_{ro}(t - t_0, k) = \pm 2 \sin^{-1}\left\{\operatorname{sn}\left[k(t - t_0), \frac{1}{k}\right]\right\}, \\ y_{ro}(t - t_0, k) = \pm 2k \operatorname{dn}\left[k(t - t_0), \frac{1}{k}\right], \end{cases}$$

for the rotating case. We note that «os» and «ro» stand for oscillating and rotating, respectively.

In eqs. (17) and (18)  $\operatorname{sn}$ ,  $\operatorname{en}$  and  $\operatorname{dn}$  are the Jacobi elliptic functions, and  $k$  is the elliptic modulus (17). Moreover, for system (7) we see that the period

(17) P. F. BYRD and M. D. FRIEDMAN: *Handbook of Elliptic Integrals for Engineers and Physicists* (Springer-Verlag, Berlin, 1971).

of the perturbation is

$$(19) \quad T = pT_1 = qT_2,$$

where  $\omega_1/\omega = p/q$  with  $p$  and  $q$  relatively prime and where  $T_1 = 2\pi/\omega_1$ ,  $T_2 = 2\pi/\omega$  are the periods of  $\sin \omega_1 t$  and  $\cos \omega t$ , respectively.

We now compute the subharmonic Melnikov functions for these resonant periodic orbits. The resonance conditions are

$$(20) \quad 4K(k) = \frac{m}{n} T = \frac{m}{n} p \frac{2\pi}{\omega_1}, \quad 4K(k) = \frac{m}{n} T = \frac{m}{n} q \frac{2\pi}{\omega}$$

for the oscillating motion ( $k < 1$ ) and

$$(21) \quad \frac{2K(1/k)}{k} = \frac{m}{n} T = \frac{m}{n} p \frac{2\pi}{\omega_1}, \quad \frac{2K(1/k)}{k} = \frac{m}{n} T = \frac{m}{n} q \frac{2\pi}{\omega}$$

for the rotating motion ( $k > 1$ ).

In (20) and (21),  $m$  and  $n$  are relatively prime natural numbers and  $K(k)$  denotes the complete elliptic integral of the first kind (\*).

The subharmonic Melnikov function (16) reads

$$(22) \quad M_{os}^{m/n}(t_0) = \int_0^{m\pi} [y_{os}(t, k) [-\beta y_{os}(t, k) + \varrho_1 \sin(\omega_1 t + \omega_1 t_0) - \\ - 2H\omega \cos(\omega t + \omega t_0) y_{os}(t, k)] dt$$

for the oscillating case and

$$(23) \quad M_{ro}^{m/n}(t_0) = \int_0^{m\pi} [y_{ro}(t, k) [-\beta y_{ro}(t, k) + \varrho_1 \sin(\omega_1 t + \omega_1 t_0) - \\ - 2H\omega \cos(\omega t + \omega t_0) y_{ro}(t, k)] dt$$

for the rotating case. Now inserting (17) into (22) and (18) into (23), respectively, we get for the two subharmonic Melnikov functions

$$(24) \quad M_{os}^{m/n}(t_0) = -4\beta k^2 \int_0^{m\pi} \operatorname{cn}^2(t, k) dt \pm 2\varrho_1 k \int_0^{m\pi} \sin(\omega_1 t + \omega_1 t_0) \operatorname{cn}(t, k) dt + \\ - 8H\omega k^2 \int_0^{m\pi} \cos(\omega t + \omega t_0) \operatorname{cn}^2(t, k) dt,$$

$$(25) \quad M_{ro}^{m/n}(t_0) = -4\beta k^2 \int_0^{m\pi} \operatorname{dn}^2\left(kt, \frac{1}{k}\right) dt \pm 2\varrho_1 k \int_0^{m\pi} \sin(\omega_1 t + \omega_1 t_0) \operatorname{dn}\left(kt, \frac{1}{k}\right) dt - \\ - 8k^2 H\omega \int_0^{m\pi} \cos(\omega t + \omega t_0) \operatorname{dn}^2\left(kt, \frac{1}{k}\right) dt.$$

The second integral of expression (24) vanishes except for  $n = 1$  and odd  $mp$ , while the third one vanishes except for  $n = 1$  and even  $mq$ . In these cases we obtain

$$(26) \quad M_{\text{os}}^{m/1}(t_0) = -16\beta[E(k) - k'^2 K(k)] \pm 4\pi\varrho_1 \operatorname{sech}(\omega_1 K'(k)) \sin(\omega_1 t_0) - \\ - 16\pi H\omega^2 \operatorname{cosech}(\omega K'(k)) \cos(\omega t_0).$$

For the rotating motion we have that the second and third integrals of expression (25) vanish except for  $n = 1$ . In this case we obtain

$$(27) \quad M_{\text{ro}}^{m/1}(t_0) = -8\beta k E(1/k) \pm 2\pi\varrho_1 \operatorname{sech}\left(\frac{\omega_1 K'(1/k)}{k}\right) \sin(\omega_1 t_0) - \\ - 8\pi H\omega^2 \operatorname{cosech}\left(\frac{\omega K'(1/k)}{k}\right) \cos(\omega t_0).$$

In (26) and (27),  $K'(k) = K(k')$ , and  $k'$  is the complementary modulus, which is related to  $k$  by  $k'^2 = 1 - k^2$  (17). Rearranging eqs. (26), (27) we find two necessary conditions for the occurrence of subharmonics of periods  $mT$  with an accuracy of  $O(1)$ ; these conditions are

$$(28) \quad \varrho_{1,\text{os}} \geq \cosh(\omega_1 K'(k)) \left[ \frac{4\beta}{\pi} (E(k) - k'^2 K(k)) - 4H\omega^2 \operatorname{cosech}(\omega K'(k)) \right]$$

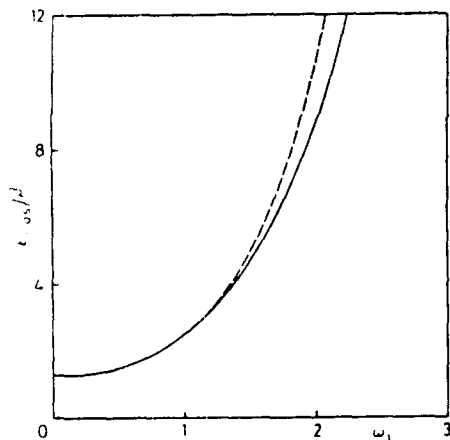


Fig. 3.

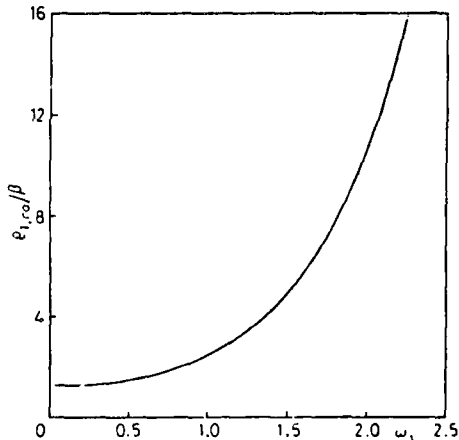


Fig. 4.

Fig. 3. - Subharmonic curves for the oscillating case and heteroclinic bifurcation curve in the  $(\omega_1, \varrho_1)$  parameter plane (eqs. (28) and (14)). Solid curve:  $mp = 3, mq = 2$ . Dashed curve:  $mp = 6, mq = 4$  and (overlapping)  $mp = 9, mq = 6$  and (overlapping) heteroclinic curve.  $H/\beta = 0.2$ .

Fig. 4. - Subharmonic curves for the rotating case and heteroclinic bifurcation curve in the  $(\omega_1, \varrho_1)$  parameter plane (eqs. (29) and (14)). Solid curve:  $(mp, mq) = (3, 2), (6, 4), (9, 6)$  and heteroclinic curve overlapping.  $H/\beta = 0.2$ .

and

$$(29) \quad \varrho_{1,\infty} > \cosh\left(\frac{\omega_1 K'(1/k)}{k}\right) \left[ \frac{4\beta k}{\pi} E\left(\frac{1}{k}\right) - 4H\omega^2 \operatorname{cosech}\left(\frac{\omega_1 K'(1/k)}{k}\right) \right].$$

The subharmonic bifurcation curves corresponding to formulae (28) and (29) are shown in fig. 3 and 4, respectively. In fig. 5 and 6 we show enlargements of these curves.

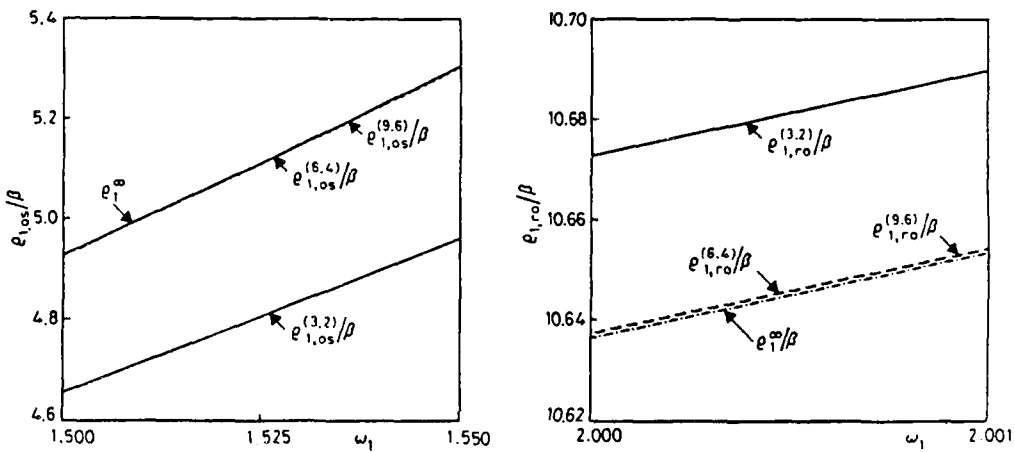


Fig. 5.

Fig. 6.

Fig. 5. – Enlargement of fig. 3 in the region  $1.50 < \omega_1 < 1.55$ . ( $mp, mq$ ) indicated in the superscripts.

Fig. 6. – Enlargement of fig. 4 in the region  $2.000 < \omega_1 < 2.001$ . ( $mp, mq$ ) indicated in the superscripts.

Similarly, we can obtain the expressions for the occurrence of subharmonics in the  $(\omega_1, H)$  parameter plane. They are the following ones:

$$(30) \quad H_{\infty} > \frac{\sinh(\omega_1 K'(k))}{\omega^2} \left[ \frac{\beta}{\pi} (E(k) - k'^2 K(k)) - \frac{\varrho_1}{4} \operatorname{sech}(\omega_1 K'(k)) \right] = R_{\infty}^{(mp, mq)},$$

$$(31) \quad H_{\infty} > \frac{\sinh((\omega_1 K'(1/k))/k)}{\omega^2} \left[ \frac{\beta k}{\pi} E(1/k) - \frac{\varrho_1}{4} \operatorname{sech}\left(\frac{\omega_1 K'(1/k)}{k}\right) \right] = R_{\infty}^{(mp, mq)}.$$

As above, the subharmonic bifurcation curves corresponding to formulae (30) and (31) are shown in fig. 7a-d) and fig. 8, respectively. In fig. 9 we show the enlargement of the rotating case in the interval  $3.000 < \omega_1 < 3.001$ .

In the oscillating case the resonance condition (20) can be solved for each choice of  $mp, mq$  with  $2\pi mp/n\omega_1 > 2\pi$  and  $2\pi mq/n\omega > 2\pi$ . The curves in fig. 3 and 7 are restricted accordingly.

Formulae (28)-(31) converge to formulae (14) and (15), respectively, because

$$(32) \quad \frac{1}{2} \lim_{m \rightarrow \infty} M_{os}^m(t_0) = \lim_{m \rightarrow \infty} M_{ro}^m(t_0) = M^\pm(t_0).$$

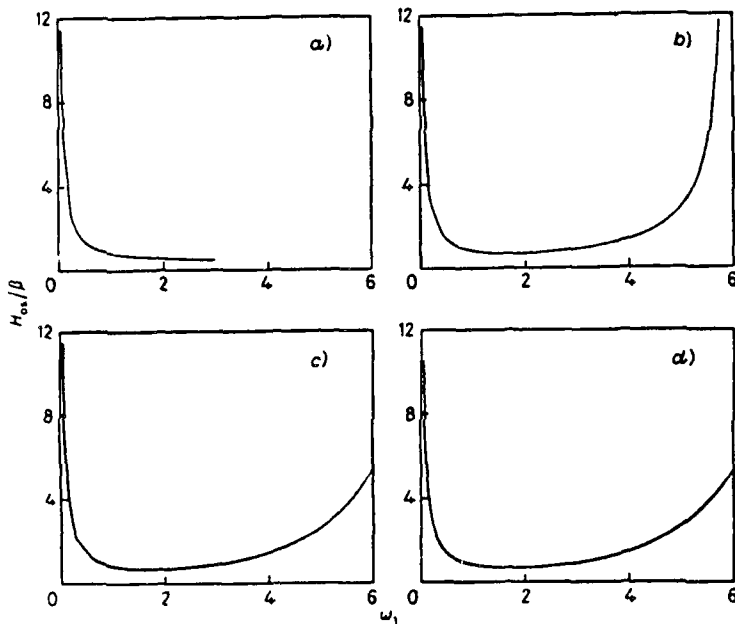


Fig. 7. – Subharmonic curves for the oscillating case, (a-c)), and heteroclinic bifurcation curve, (d)), in the  $(\omega_1, H)$  parameter plane (eq. (30)) for  $mp = 3, 6, 9$  and  $mq = 2, 4, 6$  and eqs. (15) and (30), respectively.  $\varrho_1/\beta = 0.2$ .

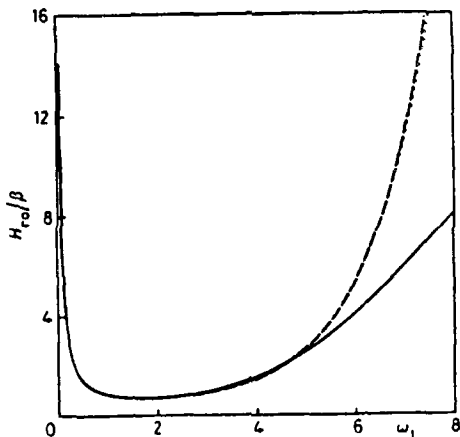


Fig. 8. – Subharmonic curves for the rotating case and heteroclinic bifurcation curve in the  $(\omega_1, H)$  parameter plane (eqs. (31) and (15)). Solid curve:  $(mp, mq) = (3, 2)$ ; dotted curve:  $(6, 4)$ ; dashed curve:  $(9, 6)$  and heteroclinic (overlapping).  $\varrho_1/\beta = 0.2$ .

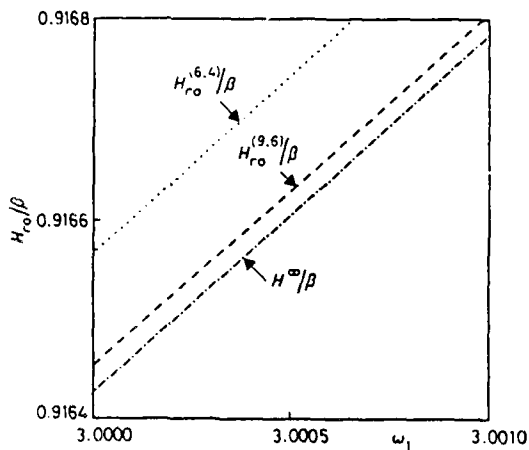


Fig. 9. - Enlargement of fig. 8 in the region  $3.000 < \omega_1 < 3.001$ .

The figures demonstrate the convergence is extremely rapid.

From this it follows that the heteroclinic bifurcations are the limit of a sequence of subharmonic saddle-node bifurcations. Furthermore, we can define the convergence rates as

$$\delta = \lim_{mq \rightarrow \infty} \frac{R^{(mq, mp)} - R^{(mq-i, mp)}}{R^{(mq+i, mp)} - R^{(mq, mp)}}$$

and

$$\delta_i = \lim_{mq \rightarrow \infty} \frac{R^{(mq, mp)} - R^{(mq, mp-i)}}{R^{(mq+1, mp)} - R^{(mq, mp)}},$$

where  $i = 2$  in the oscillating regime and  $i = 1$  in the rotating one. Making the calculations we find that  $\delta = \exp[2\pi/\omega]$  and  $\delta_i = \exp[2\pi/\omega_i]$  in both regimes.

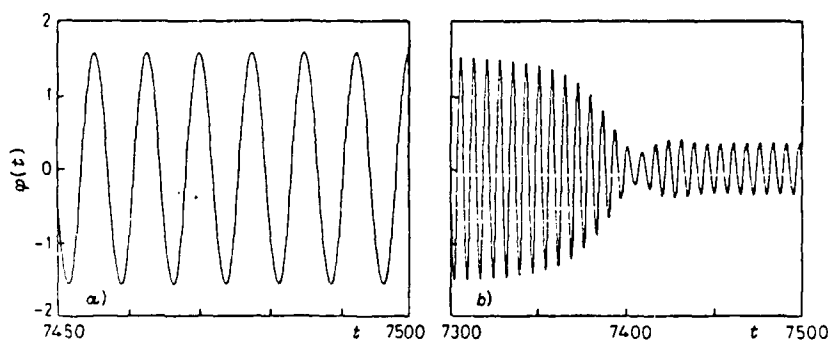


Fig. 10. - Numerical solution of eq. (6) for  $2 \sin^{-1} k = 1.6$ ,  $\beta = 0.1$ ,  $\rho_1 = 0.1$ ,  $\omega_1 = \pi mp/2K(k)$  and  $\omega = \pi mq/2K(k)$  with  $mp = 1$  and  $mq = 2$ . a)  $H = 0.0144$ , b)  $H = 0.0143$ .

The previous predictions by Melnikov theory for subharmonic bifurcations were tested by a numerical simulation. For parameter values  $2 \sin^{-1} k = 1.6$ ,  $\beta = 0.1$ ,  $\varrho_1 = 0.1$ ,  $\omega_1 = \pi mp/2K(k)$  and  $\omega = \pi mq/2K(k)$  with  $mp = 1$  and  $mq = 2$ , eq. (30) yields the critical value  $H_{*} = 0.0147$ . Figure 10 shows the numerical solution to eq. (6) for the same values of  $k$ ,  $\beta$ ,  $\varrho_1$ ,  $\omega_1$  and  $\omega$ . For  $H = 0.0144$  we get the stable subharmonic solution shown in fig. 10a), while a decrease in  $H$  to  $H = 0.0143$  makes this subharmonic solution unstable as seen in fig. 10b). The prediction by Melnikov theory thus only deviates by 3 %. However, it is important to notice that we cannot use subharmonic Melnikov's method for proving that the stable and unstable manifolds of the hyperbolic orbits intersect transversally. This is because the subharmonic Melnikov function is exponentially small and the remainder in the perturbative series becomes important (18).

### 5. - Stability analysis of subharmonic orbits.

In this section we shall use the following perturbation method (1,2,18) in order to get information on the stability of the subharmonic orbits. We consider the perturbed system (7); because it is a Hamiltonian system when  $\varepsilon = 0$ , a symplectic change of co-ordinate to action-angle variables can be found:

$$(33) \quad \begin{cases} I = I(x, y), \\ \theta = \theta(x, y). \end{cases}$$

Using transformations (33) system (7) becomes

$$(34) \quad \begin{cases} \dot{I} = \varepsilon g \frac{\partial I}{\partial y} = \varepsilon H(I, \theta, t), \\ \dot{\theta} = \Omega(I) + \varepsilon g \frac{\partial \theta}{\partial y} = \Omega(I) + \varepsilon G(I, \theta, t), \end{cases}$$

where

$$(35) \quad g = -\beta \dot{x} + \varrho_1 \sin \omega_1 t - 2H\omega \cos(\omega t) \dot{x}$$

is the perturbation, and

$$(36) \quad \Omega(I^\alpha) = \frac{\partial \mathcal{H}}{\partial I} \Big|_{I=I^\alpha} = \frac{2\pi}{T^\alpha}$$

is the angular frequency of the unperturbed orbit  $[x^\alpha(t - t_0), y^\alpha(t - t_0)]$  with

---

(18) P. HOLMES: *Physica D (Utrecht)*, 5, 335 (1982).

action  $I^\alpha = I[x^\alpha(t - t_0), y^\alpha(t - t_0)]$ , and

$$(37) \quad T^\alpha = \frac{mp}{n} T_1 = \frac{mq}{n} T_2.$$

If we now consider small perturbations of a resonant orbit  $T^\alpha$ , we can approximate the variations of the action-angle variables as follows:

$$(38) \quad \begin{cases} I = I^\alpha + \sqrt{\varepsilon} h(t), \\ \theta = \Omega(I^\alpha)t + \varphi(t). \end{cases}$$

Making the derivatives with respect to time, we obtain

$$(39) \quad \begin{cases} \dot{h} = \sqrt{\varepsilon} F(I^\alpha, \Omega^\alpha t + \varphi, t) + \varepsilon F'(I^\alpha, \Omega^\alpha t + \varphi, t)h + O(\varepsilon^{\frac{3}{2}}), \\ \dot{\varphi} = \sqrt{\varepsilon} \Omega'(I^\alpha)h + \varepsilon \left[ G(I^\alpha, \Omega^\alpha t + \varphi, t) + \Omega''(I^\alpha) \frac{h^2}{2} \right] + O(\varepsilon^{\frac{3}{2}}), \end{cases}$$

where the primes denote  $\partial/\partial I$

If  $\Omega'(I^\alpha)$  is bounded we can apply the averaging theorem (19) for  $\sqrt{\varepsilon}$  sufficiently small. This yields, with an averaging transformation  $(h, \varphi) \rightarrow (\bar{h}, \bar{\varphi})$ ,

$$(40) \quad \begin{cases} \dot{\bar{\varphi}} = \sqrt{\varepsilon} \Omega' \bar{h} + \varepsilon \left[ \frac{\Omega'' \bar{h}^2}{2} + \bar{G}_m(\bar{\varphi}) \right] + O(\varepsilon^{\frac{3}{2}}), \\ \dot{\bar{h}} = \sqrt{\varepsilon} \frac{1}{2\pi} M_m(\bar{\varphi}/\Omega^\alpha) + \varepsilon \bar{F}'_m(\bar{\varphi}) \bar{h} + O(\varepsilon^{\frac{3}{2}}), \end{cases}$$

where  $\bar{F}'_m$  and  $\bar{G}_m$  are the averages of  $F'$  and  $G$ . For more details, see (18).

Let us start with the action transformation: In order to deduce the expression of the action variable  $I$  it is convenient to write the Hamiltonian  $\mathcal{H} = \mathcal{H}(x, y) = y^2/2 + (1 - \cos x)$  as a function of the elliptic modulus. Both in the oscillating case and in the rotating one we obtain

$$(41) \quad \mathcal{H}(k) = 2k^2,$$

where  $0 < k < 1$  and  $k > 1$  in the oscillating and rotating cases, respectively. Using formula (41) and standard methods for the computation of the action

---

(19) J. K. HALE: *Ordinary Differential Equations* (J. Wiley & Sons, New York, N. Y., 1969).

variable (30) we arrive at the formulae

$$(42) \quad I_{\text{ss}}^{\alpha} := I_{\text{ss}}(k) = \frac{8}{\pi} [E(k) - k'^2 K(k)]$$

for the oscillating case, and

$$(43) \quad I_{\text{ro}}^{\alpha} := I_{\text{ro}}(k) = \frac{4}{\pi} k E(1/k)$$

for the rotating one.

The expressions for  $\Omega(I^{\alpha})$  given by formula (36) are

$$(44) \quad \Omega_{\text{ss}}(I^{\alpha}) = \frac{\pi}{2K(k)} = \frac{\omega}{mq} = \frac{\omega_1}{mp}$$

and

$$(45) \quad \Omega_{\text{ro}}(I^{\alpha}) = \frac{\pi k}{K(1/k)} = \frac{\omega}{mq} = \frac{\omega_1}{mp},$$

where  $k$  is given by relationships (20) and (21), respectively. Using the identity  $\Omega'(I^{\alpha}) := \partial\Omega(I)/\partial I|_{I=I^{\alpha}}$  and formulae (42)-(45) we obtain the following expressions:

$$(46) \quad \Omega'_{\text{ss}}(I^{\alpha}) = -\frac{\pi^2 [E(k) - k'^2 K(k)]}{16k^2 k'^2 K^3(k)} < 0$$

and

$$(47) \quad \Omega'_{\text{ro}}(I^{\alpha}) = -\frac{\pi^2 k^2 E(1/k)}{4k'^2 K^3(1/k)} > 0.$$

Further, we have  $\Omega''(I^{\alpha}) := \partial^2\Omega(I)/\partial I^2|_{I=I^{\alpha}}$  and from this we get

$$(48) \quad \Omega''_{\text{ss}}(I^{\alpha}) = -\frac{\pi^3}{128kK(k)} \frac{d}{dk} \left[ \frac{E(k) - k'^2 K(k)}{k^2 k'^2 K^3(k)} \right]$$

and

$$(49) \quad \Omega''_{\text{ro}}(I^{\alpha}) = -\frac{\pi^3}{16K(1/k)} \frac{d}{dk} \left[ \frac{k^2 E(1/k)}{k'^2 K^3(1/k)} \right].$$

Finally, from (26) and (27) we obtain

$$(50) \quad M^n(\varphi/\Omega^{\alpha}) = M_{\text{ss}}^n(\varphi/\Omega^{\alpha}) = -16\beta[E(k) - k'^2 K(k)] + \\ \pm 4\pi\varrho_1 \operatorname{sech}(\omega_1 K'(k)) \sin(mp\varphi) - 16\pi H \omega^2 \operatorname{cosech}(\omega K'(k)) \cos(mq\varphi)$$

---

(20) I. PERCIVAL and D. RICHARDS: *Introduction to Dynamics* (Cambridge University Press, Cambridge, 1982).

and

$$(51) \quad M^m(\varphi/\Omega^\alpha) = M_{ro}^m(\varphi/\Omega^\alpha) = -8\beta k E(1/k) \pm \\ \pm 2\pi\varrho_1 \operatorname{sech}\left(\frac{\omega_1 K'(1/k)}{k}\right) \sin(mp\varphi) - 8\pi H \omega^2 \operatorname{cosech}\left(\frac{\omega K'(1/k)}{k}\right) \cos(mq\varphi).$$

We first consider system (40) to the order  $O(\sqrt{\varepsilon})$ , and dropping the bars we get

$$(52) \quad \dot{\varphi} = \sqrt{\varepsilon} \Omega'_{os}(I^\alpha) h, \quad \dot{h} = \sqrt{\varepsilon} \frac{1}{2\pi} M_{os}^m(\varphi/\Omega^\alpha)$$

for the oscillating case and

$$(53) \quad \dot{\varphi} = \sqrt{\varepsilon} \Omega'_{ro}(I^\alpha) h, \quad \dot{h} = \sqrt{\varepsilon} \frac{1}{2\pi} M_{ro}^m(\varphi/\Omega^\alpha)$$

for the rotating one.

Such systems have fixed points at  $h = 0$  and at the values of  $\varphi$  for which  $M_{os}^m(\varphi/\Omega^\alpha) = 0$  and  $M_{ro}^m(\varphi/\Omega^\alpha) = 0$ , respectively. For both systems, such fixed points are saddles, if  $\partial M^m / \partial \varphi > 0$ , and centres, if  $\partial M^m / \partial \varphi < 0$ .

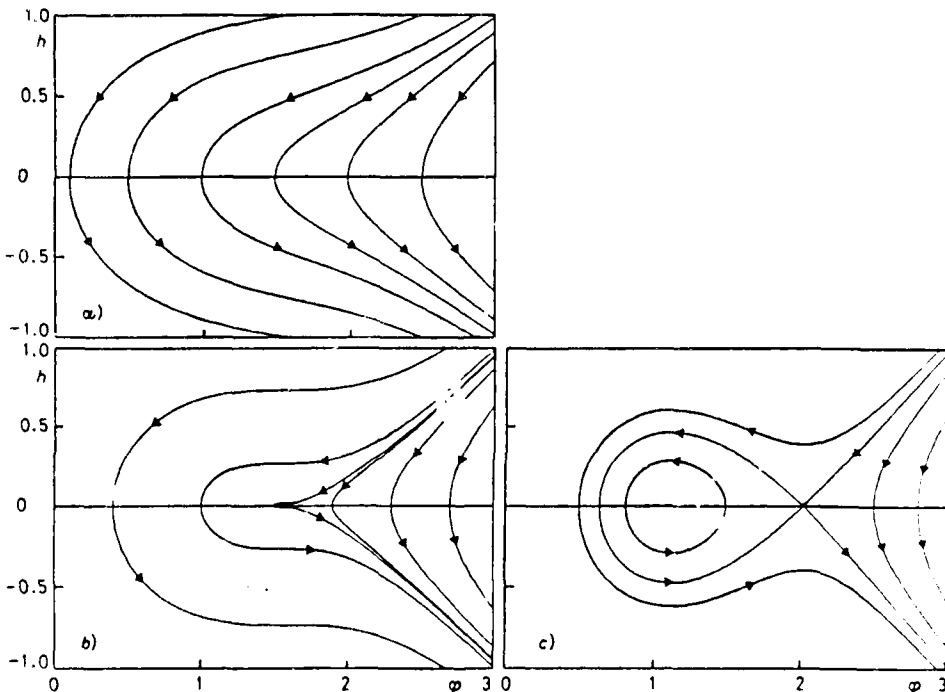


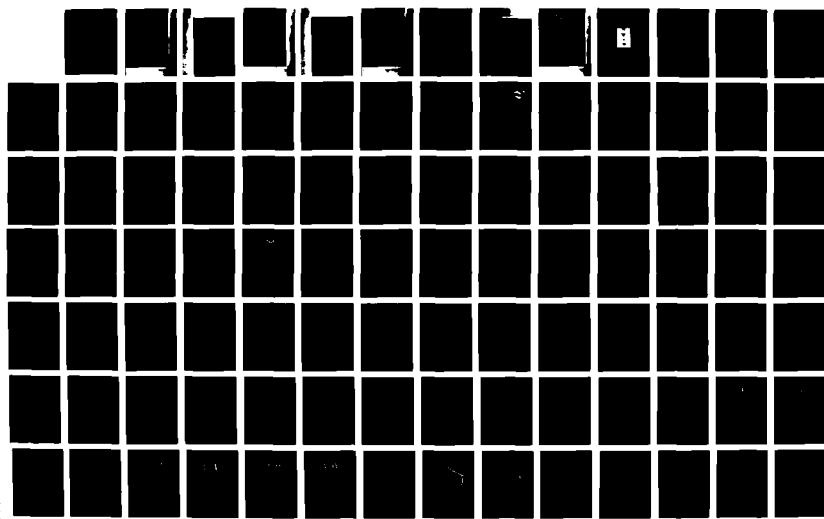
Fig. 11. - Phase portraits of system (52) for the oscillating case with  $2 \sin^{-1} k = 1.6$ ,  $\beta = 0.1$ ,  $\varrho_1 = 0.1$ ,  $\varepsilon = 1$ ,  $mp = 1$  and  $mq = 2$ . a)  $H = 0.002 < R_{os}^{(mp,mq)} = -0.014706$  (eq. (28)). No periodic points. b)  $H = R_{os}^{(mp,mq)}$ . Doubly degenerate points. c)  $H = 0.03 > R_{os}^{(mp,mq)}$ . Saddles and centres.

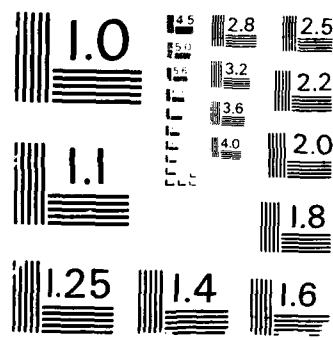
RD-R205-469 COHERENCE AND CHAOS PHENOMENA IN JOSEPHSON OSCILLATORS 2/3  
FOR SUPERCONDUCTIN (U) TECHNICAL UNIV OF DENMARK  
LYNGBY LAB OF APPLIED MATHEMATICAL P

UNCLASSIFIED P L CHRISTIANSEN ET AL 25 JAN 89

F/G 9/1

NL





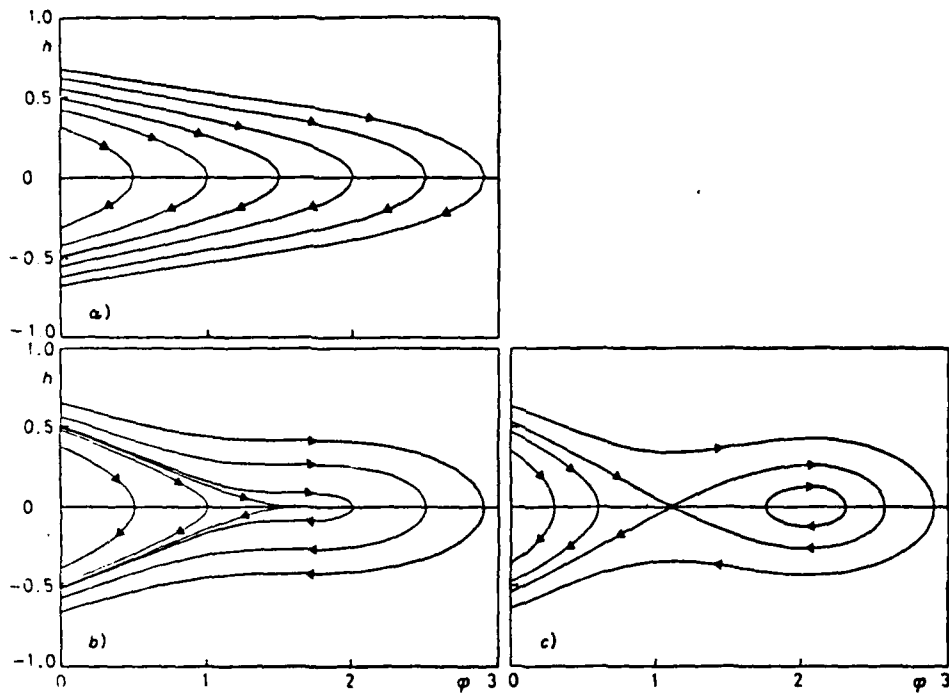


Fig. 12. - Phase portraits of system (53) for the rotating case with  $k = 1/0.95$ ,  $\beta = 0.1$ ,  $\varrho_1 = 0.1$ ,  $\varepsilon = 1$ ,  $mp = 1$  and  $mq = 2$ . a)  $H = 0.02 < R_{ro}^{(mp,mq)} = 0.114\,642$  (eq. (29)). No periodic points. b)  $H = R_{ro}^{(mp,mq)}$ . Doubly degenerate points. c)  $H = 0.2 > R_{ro}^{(mp,mq)}$ . Saddles and centres.

In fig. 11a)-c) and 12a)-c), we show the phase portraits of systems (52) and (53), respectively, corresponding to the choices of  $mp = 1$  and  $mq = 2$ , and the plus sign in formula (50), which gives

$$\begin{aligned} M_{ro}(\varphi/\Omega^2) = & -16\beta[E(k) - k'^2 K(k)] + 4\pi\varrho_1 \operatorname{sech}(\omega_1 K'(k)) \sin \varphi - \\ & - 16\pi H \omega^2 \operatorname{cosech}(\omega K'(k)) \cos(2\varphi), \end{aligned}$$

and corresponding to the choices of  $mp = 1$ ,  $mq = 2$  and the plus sign in formula (51), which gives

$$\begin{aligned} M_{ro}(\varphi/\Omega^2) = & -8\beta k E(1/k) + 2\pi\varrho_1 \operatorname{sech}\left(\frac{\omega_1 K'(1/k)}{k}\right) \sin \varphi - \\ & - 8\pi H \omega^2 \operatorname{cosech}\left(\frac{\omega K'(1/k)}{k}\right) \cos 2\varphi. \end{aligned}$$

These figures show the three cases of  $H_{ro}$  and  $H_{ro}$  less than, equal to and larger than the values of the corresponding subharmonic bifurcation curves.

Then, according to the averaging theorem (19) we have that the full system (7) has saddle-type orbits near the saddle points of (52) and (53) and periodic orbits near the centres.

Furthermore, we note that systems (52) and (53) are Hamiltonian systems with Hamiltonians given by

$$\mathcal{H} = \sqrt{\varepsilon} \left[ \frac{\Omega'(I^\alpha)}{2} h^2 + V(\varphi) \right],$$

where

$$V = -\frac{1}{2\pi} \int M^m(\varphi/\Omega^\alpha) d\varphi,$$

i.e. explicitly

$$(54) \quad \mathcal{H}_{ss} = \sqrt{\varepsilon} \left\{ \frac{\Omega'_{ss}(I^\alpha)}{2} h^2 - \frac{1}{2\pi} \left[ -16\beta(E(k) - k'^2 K(k)\varphi) \mp 4\pi\varrho_1 \operatorname{sech}(\omega_1 K'(k)) \frac{\cos(mp\varphi)}{mp} - 16\pi H\omega^2 \operatorname{cosech}(\omega K'(k)) \frac{\sin(mq\varphi)}{mq} \right] \right\},$$

$$(55) \quad \mathcal{H}_{ro} = \sqrt{\varepsilon} \left\{ \frac{\Omega'_{ro}(I^\alpha)}{2} h^2 - \frac{1}{2\pi} \left[ -8\beta k E(1/k)\varphi \mp 2\pi\varrho_1 \operatorname{sech}\left(\frac{\omega_1 K'(1/k)}{k}\right) \frac{\cos(mp\varphi)}{mp} - 8\pi H\omega^2 \operatorname{cosech}\left(\frac{\omega K'(1/k)}{k}\right) \frac{\sin(mq\varphi)}{mq} \right] \right\}.$$

Since systems (52) and (53) are structurally unstable, it is necessary to take into account the  $O(\varepsilon)$  terms in system (40), where

$$\overline{F'_m(\varphi)} = \frac{1}{mT} \int_0^{mT} F'(\Omega^\alpha t + \varphi, I^\alpha, t) dt$$

and

$$\overline{G_m(\varphi)} = \frac{1}{mT} \int_0^{mT} G(\Omega^\alpha t + \varphi, I^\alpha, t) dt$$

with

$$F'(\theta, I, t) = \frac{\partial}{\partial I} F(\theta, I, t),$$

$$F(\theta, I, t) = \frac{1}{\Omega(I)} [-\beta \dot{x} + \varrho_1 \sin(\omega_1 t) - 2H\omega \cos(\omega t) \dot{x}] \dot{x}$$

and

$$G(\theta, I, t) = -\frac{\partial x}{\partial I} [-\beta \dot{x} + \varrho_1 \sin(\omega_1 t) - 2H\omega \cos(\omega t) \dot{x}].$$

Making the calculation we obtain

$$\widehat{F_m'(\varphi)} = -\beta(AJ_1 + BJ'_1) \pm \varrho_1(AJ_2 + BJ'_2) \sin(mp\varphi) - H(AJ_3 + BJ'_3) \cos(mq\varphi)$$

and

$$\widehat{G_m(\varphi)} = \pm \varrho_1(AJ_2 + BJ'_2) \frac{\cos(mp\varphi)}{mp} + H(AJ_3 + BJ'_3) \frac{\sin(mq\varphi)}{mq},$$

$$J_1 = J_1(m) = 16[E(k) - k'^2 K(k)], \quad J'_1 = \frac{d}{dk} J_1,$$

$$J_2 = J_2(m, \omega_1) = 4\pi \operatorname{sech} \frac{mp\pi K'(k)}{2K(k)}, \quad J'_2 = \frac{d}{dk} J_2,$$

$$J_3 = J_3(m, \omega) = 16\pi\omega^2 \operatorname{cosech} \frac{mq\pi K'(k)}{2K(k)}, \quad J'_3 = \frac{d}{dk} J_3,$$

$$A = A(m) = -\frac{\Omega'_{\text{ro}}(I^*) mp}{2\pi\omega_1} > 0,$$

$$B = B(m) = \frac{\omega_1}{8\pi mp k} > 0$$

in the oscillating case, and

$$\widehat{F_m'(\varphi)} = -\beta(AK_1 + BK'_1) \pm \varrho_1(AK_2 + BK'_2) \sin(mp\varphi) - H(AK_3 + BK'_3) \cos(mq\varphi),$$

$$\widehat{G_m(\varphi)} = \pm \varrho_1(AK_2 + BK'_2) \frac{\cos(mp\varphi)}{mp} + H(AK_3 + BK'_3) \frac{\sin(mq\varphi)}{mq}$$

with

$$K_1 = K_1(m) = 8kE(1/k), \quad K'_1 = \frac{d}{dk} K_1,$$

$$K_2 = K_2(m, \omega_1) = 2\pi \operatorname{sech} \frac{mp\pi K'(1/k)}{K(1/k)}, \quad K'_2 = \frac{d}{dk} K_2,$$

$$K_3 = K_3(m, \omega) = 8\pi\omega^2 \operatorname{cosech} \frac{mq\pi K'(1/k)}{K(1/k)}, \quad K'_3 = \frac{d}{dk} K_3,$$

$$A = A(m) = -\frac{mp\Omega'_{\text{ro}}(I^*)}{2\pi\omega_1} < 0,$$

$$B = B(m) = \frac{\omega_1}{8\pi mp k}$$

in the rotating case.

The traces of the linearized system (40) read

$$(56) \quad \text{Tr}_{ss}(L) = -\varepsilon\beta[AJ_1 + BJ'_1]$$

in the oscillating case, and

$$(57) \quad \text{Tr}_{ro}(L) = -\varepsilon\beta[AK_1 + BK'_1]$$

in the rotating one.

They are both constants. Thus according to Bendixon's criterion (2) it follows that system (40) cannot have closed trajectories.

In fig. 13a-d) we show the phase portraits of system (40) in the oscillating case. In the rotating case one obtains analogous results.

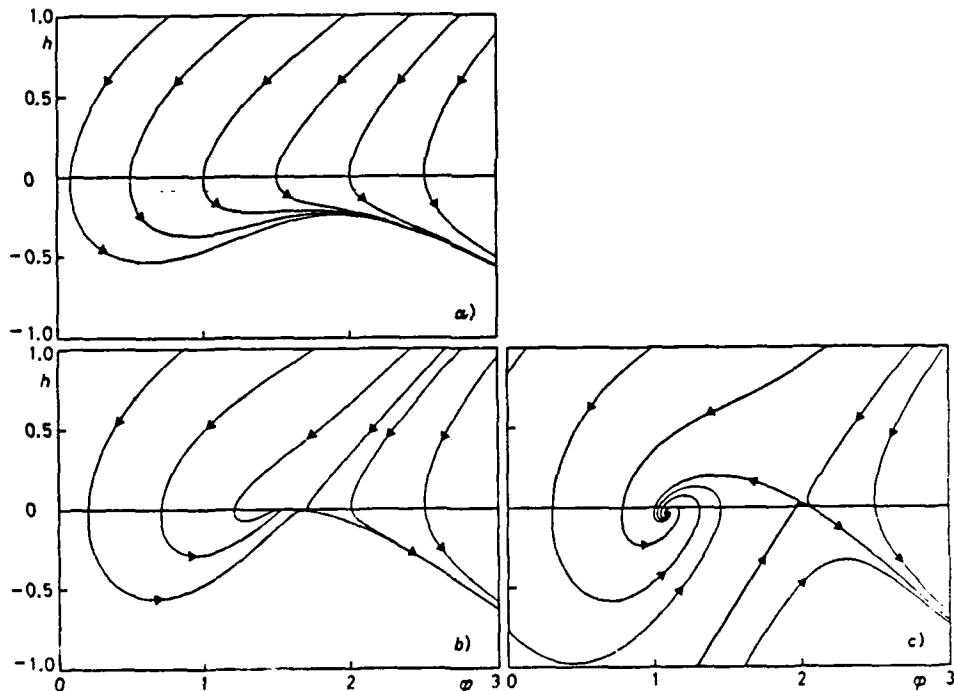


Fig. 13. - Phase portraits of system (40) in the oscillating case with  $2 \sin^{-1} k = 1.6$ ,  $\beta = 0.1$ ,  $\rho_1 = 0.1$ ,  $\varepsilon = 1$ ,  $mp = 1$  and  $mq = 2$ . a)  $H = 0.002 < R_{ss}^{(mp,mq)} \approx 0.014706$  (eq. (28)). No periodic points. b)  $H = R_{ss}^{(mp,mq)}$ . Doubly degenerate points. c)  $H = 0.03 > R_{ss}^{(mp,mq)}$ . Sink and saddle points.

It is important to note that these results are not uniformly valid. Indeed, the factor  $\Omega'(I^\alpha)$  becomes unbounded as  $\alpha \rightarrow \infty$ . Therefore, as  $\alpha$  increases, averaging is valid in smaller and smaller regions  $0 < \varepsilon \ll \varepsilon_0(m)$ .

### 6. - Conclusion.

In this paper we have investigated the onset of chaos for a perturbed pendulum with variable length. We show that this system exhibits Smale horseshoe chaos for certain ranges of parameter values. The bifurcation diagram shown in fig. 2 gives some insight into the behaviour of the system. One can see that when  $\omega_1$  goes to zero we do not get Smale horseshoe chaos. This is in agreement with the well-known classical phenomenon that the action variable is an adiabatic invariant for this system when its length is varied sufficiently slowly.

Furthermore, by using the subharmonic Melnikov's functions we have obtained the bifurcation diagrams for the occurrence of subharmonic orbits. These subharmonic bifurcation curves converge (rapidly) to the heteroclinic bifurcation curve. This result implies that the heteroclinic bifurcation is the limit of a countable sequence of subharmonic saddle-node bifurcations.

Moreover, making use of the averaging theorem, the stability of the subharmonics was investigated. Indeed, according to the averaging theorem the equilibria of the averaged system correspond to cycles of the perturbed system. We have found that the fixed points of the averaged system are sinks and saddles which are created through saddle-node bifurcations. This implies that the perturbed system, at least on a time scale of  $1/\epsilon$  (for  $\epsilon$  sufficiently small), has a hyperbolic periodic orbit of the same stability type as the fixed points of the averaged system.

\* \* \*

The financial support of the Consiglio Nazionale delle Ricerche, Roma, Italy, to two of the authors (MB and VM) and of the European Research Office of the United States Army (through contract No. DAJA-45-85-C-0042) is acknowledged.

### ● RIASSUNTO

In questo articolo si applica la teoria di Melnikov per predire analiticamente la presenza di caos (Smale-horseshoe) in un pendolo con lunghezza variabile in presenza di dissipazione e di un termine forzante. Si mostra che tale sistema dinamico presenta una cascata di biforcazioni eterocliniche quando i parametri che entrano nell'equazione differenziale che lo descrive sono variati. La presenza di queste biforcazioni è la sorgente del moto caotico. Si studia inoltre la stabilità dello subarmonico facendo uso del teorema della media temporale.

Резюме не получено.

## Note

### Split-Step Spectral Method for Nonlinear Schrödinger Equation with Absorbing Boundaries

By application of spectral methods [1] the computational solution of nonlinear partial differential equations has been improved in accuracy as well as efficiency in particular on vector computers. Fourier spectral methods [2] require periodic boundary conditions often in contrast to the actual physical problems where modelling by outflow boundary conditions may be appropriate in many cases.

In this note we consider the cubic nonlinear Schrödinger equation (NLS) which occurs in nonlinear optics [3], deep water wave theory [4], plasma physics [5], biomolecular dynamics [6], e.g. The equation can be solved numerically by the split-step Fourier method (SSFM) described in [7, 8]. We generalize the method by including an additional term in the partial differential equation with the effect of absorbing outgoing radiation at the boundaries. The applications of SSFM requires periodic boundary conditions. However, the drawback of these conditions is eliminated by our new method.

The NLS with periodic boundary conditions is given by

$$iu_t + \frac{1}{2}u_{xx} + |u|^2 u = 0, \quad (1a)$$

$$u(-L/2, t) = u(L/2, t), \quad \text{and} \quad u_x(-L/2, t) = u_x(L/2, t) \quad (1b)$$

$-L/2 \leq x \leq L/2$ ,  $-\infty < t < \infty$ , and  $u = u(x, t)$ .

The SSFM in its original form consists of two steps. First, the nonlinear part of Eq. (1a),  $iu_t + |u|^2 u = 0$ , is solved by means of the simple wave solution  $u(x, t) = u(x, 0) \exp(i|u(x, 0)|^2 t)$ . Second, the linear part of Eq. (1a),  $iu_t + \frac{1}{2}u_{xx} = 0$ , is solved by means of Fourier transformation.

Our modified version of NLS is

$$iu_t + \frac{1}{2}u_{xx} + |u|^2 u + i\gamma(x) u = 0, \quad (2a)$$

$$u(-L/2, t) = u(L/2, t), \quad \text{and} \quad u_x(-L/2, t) = u_x(L/2, t), \quad (2b)$$

where the real function  $\gamma(x)$  in the absorbing term,  $i\gamma(x) u$ , is given by

$$\gamma(x) = \gamma_0 (\operatorname{sech}^2[\alpha(x - L/2)] + \operatorname{sech}^2[\alpha(x + L/2)]). \quad (2c)$$

As seen in Fig. 1 we introduce smooth losses at the boundaries  $x = -L/2$  and  $x = L/2$  through this choice of  $\gamma$ .

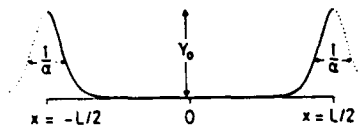


FIG. 1. The absorption function  $\gamma(x)$  (2c) introduces losses in the neighborhood of the periodic boundaries at  $x = \pm L/2$ . Parameters  $\gamma_0$  and  $\alpha$  in (2c) must be chosen such that the scattering from the "absorption walls,"  $\text{sech}^2[\alpha(x \mp L/2)]$ , is small.

In the corresponding new generalized split-step method we first solve the non-linear part of Eq. (2a)

$$i\tilde{u}_t + |\tilde{u}|^2 \tilde{u} + i\gamma(x) \tilde{u} = 0 \quad (3)$$

for which we have found the exact solution

$$\tilde{u}(x, t) = \tilde{u}(x, 0) \exp\{i|\tilde{u}(x, 0)|^2 (1 - e^{-2\gamma t})/2\gamma - \gamma t\} \quad (4)$$

by inspection. Second, the linear part,  $i\tilde{u}_t + \frac{1}{2}\tilde{u}_{xx} = 0$ , is solved in Fourier space by

$$\tilde{U}(k, t) = \tilde{U}(k, 0) \exp\{-ik^2 t/2\}. \quad (5)$$

Also in our generalized SSFM the solution is advanced one time step  $\Delta t$  by (i) obtaining  $\tilde{u}(x, \Delta t)$  from  $u(x, 0)$  by means of (4) with  $\tilde{u}(x, 0) = u(x, 0)$ , (ii) inserting the Fourier transform of  $\tilde{u}(x, \Delta t)$  as  $\tilde{U}(k, 0)$  in (5)

$$\tilde{U}(k, \Delta t) = \int_{-\infty}^{\infty} \tilde{u}(x, \Delta t) \exp\{ikx\} dx \exp\{-ik^2 \Delta t/2\}, \quad (6)$$

and (iii) transforming the resulting  $\tilde{U}(k, \Delta t)$  back to  $x$ -space

$$u(x, \Delta t) = \frac{1}{2\pi} \int_{-\infty}^{\infty} \tilde{U}(k, \Delta t) \exp\{-ikx\} dk. \quad (7)$$

This method is second-order accurate in  $\Delta t$  and all orders in  $\Delta x$  and is unconditionally stable according to linear analysis [8].

Figure 2 shows the time development of the initial condition

$$u(x, 0) = (1 + 0.6 \cos 7x) \text{ sech } x \quad (8)$$

in two cases: (a) subjected to the classical NLS dynamics given by (1) and (b) subjected to the NLS dynamics with absorption given by (2). The initial condition (8) describes an NLS 1-soliton [9] with radiation superposed. In case (a) the radiation cannot escape from the system owing to the spatial periodicity and eventually destroys the 1-soliton. In case (b) the radiation is essentially absorbed already at the first passage of the boundary leaving the 1-soliton undisturbed.

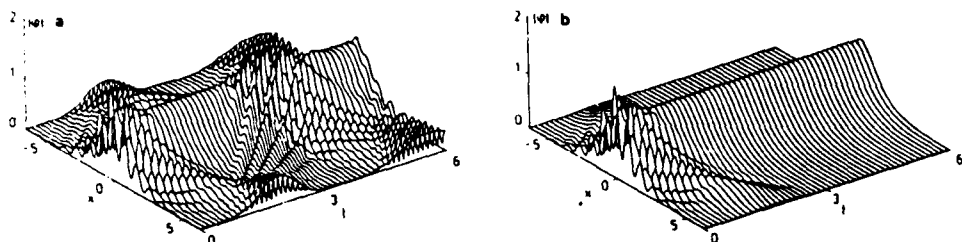


FIG. 2. Evolution of NLS 1-soliton (8) with dynamics given by (a) classical NLS (1), (b) NLS with absorption (2). Parameters  $L = 12.8$ ,  $\gamma_0 = 20$ , and  $\alpha = 1$ . Resolution  $\Delta x = 0.1$  and  $\Delta t = 0.005$ .

The difference between Figs. 2a and 2b demonstrates the importance of adding absorption in the NLS equation. This new trick makes the SSFM much more applicable to the physical problems mentioned in the introduction.

#### ACKNOWLEDGMENTS

The financial support of the Danish Council for Scientific and Industrial Research and of the European Research Office of the United States Army through Contract DAJA-45-85-C-0043 is acknowledged.

#### REFERENCES

1. D. GOTTLIEB AND S. A. ORSZAG, *Numerical Analysis of Spectral Methods: Theory and Applications*, CBMS-NSF Regional Conf. Ser. in Appl. Math. Vol. 26 (Soc. Indus. Appl. Math., Philadelphia, 1977), p. 1.
2. D. GOTTLIEB, M. Y. HUSSAINI, AND S. A. ORSZAG, in *Proceedings, Symposium on Spectral Methods for PDE*, edited by R. G. Voigt, D. Gottlieb, and M. Y. Hussaini, SIAM Monograph, Soc. Indus. Appl. Math., Philadelphia, 1984), p. 1.
3. A. HASEGAWA AND F. TAPPERT, *Appl. Phys. Lett.* **23**, 142 (1973).
4. D. J. BENNEY AND A. C. NEWELL, *J. Math. Phys.* **46**, 133 (1967).
5. G. J. MORALES AND Y. C. LEE, preprint, UCLA, 1975 (unpublished).
6. A. S. DAVYDOV, *Phys. Scripta* **20**, 387 (1979).
7. T. R. TAHAN AND M. J. ABLOWITZ, *J. Comput. Phys.* **55**, 203 (1984).
8. R. H. HARDIN AND F. D. TAPPERT, *SIAM Rev. Chronicle* **15**, 423 (1973).
9. J. SATSUMA AND N. YAJIMA, *Prog. Theor. Phys. Supp.* **55**, 284 (1974).

RECEIVED: June 24, 1986; REVISED: November 20, 1986

F. IF  
P. BERG  
P. L. CHRISTIANSEN  
O. SKOVGAARD

*Laboratory of Applied Mathematical Physics  
The Technical University of Denmark  
DK-2800 Lyngby, Denmark*

Printed by Catherine Press, Ltd., Tempelhof 41, B-8000 Brugge, Belgium

## Nonlinear dynamics

# Observations of real solitons

Peter L. Christiansen

SOLITONS are localized nonlinear waves that can propagate and interact like particles. Theoretical studies show that phenomena such as water waves, light pulses in optical fibres, magnetic-flux quanta in superconducting devices and coherent excitations of biomolecules can be solitons. Computer simulations show that solitons can form in the presence of such realistic features as frictional loss mechanisms, external driving forces and thermal fluctuations. The solitons will exist under these circumstances for sufficiently long to be important features in the time evolution of the wave excitations. Experimental demonstrations of soliton dynamics, however, are still scarce. Therefore, two recent papers by Fujimaki, Nakajima and Sawada<sup>1</sup> and by Wu, Wheatley, Putterman and Rudnick<sup>2</sup> showing solitons in real systems are most noteworthy.

The work by Fujimaki *et al.* deals with collision of solitons on an electronic Josephson transmission line (JTL), 1.8 mm long, composed of a sequence of 31 discrete Josephson junctions (interleaved superconducting and insulating layers). In the continuum version of the JTL, the Josephson effect (superconducting electrons tunnelling through the insulating layers) results from the weak coupling between pairs of superconducting thin films. This overlap geometry is modelled very accurately by the sine-Gordon equation originally developed by particle physicists. In 1962, Perring and Skyrme<sup>3</sup> showed that this nonlinear partial differential equation possesses solutions that they termed 'kink' and 'antikink', after

their shapes, which can propagate and interact with each other completely non-destructively, suffering only phase shifts as a result of the interaction.

In certain respects, Perring and Skyrme's paper foreshadows the pioneering work by Zabusky and Kruskal on the Korteweg-de Vries equation (originally formulated to describe shallow water

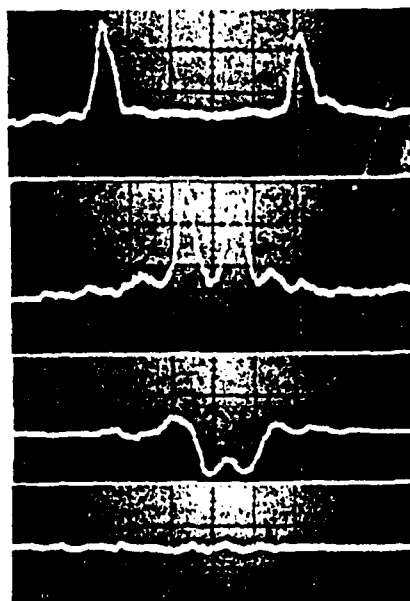


**Fig. 2** Fluxon-antifluxon annihilation process observed at *a* 0, *b* 8, *c* 16 and *d* 24 ps after the fluxons are launched. The width of the picture is 1.8 mm. (Courtesy of A. Fujimaki.)

waves), which introduced the soliton concept. The derivative of Perring and Skyrme's kinks corresponds to the solitons. An isolated kink solution to the sine-Gordon equation cannot be destroyed and is therefore a 'topological' soliton. In the JTL theory, these solitons carry magnetic-flux quanta (current vortices) and are termed fluxons. Correspondingly, negative magnetic flux quanta are carried by antifluxons. One consequence of the theory is that the fluxons behave as relativistic particles (their effective mass increases with increased velocity). In both papers<sup>1,2</sup> the analysis was directly inspired by computational results.

The superconducting circuit, made using standard lead-based technology, consists of two fluxon generators, the JTL and a sampler to measure the flux in the JTL (Fig. 1); all are based on the Josephson effect. A fluxon is injected into the JTL when a control current  $I_c$  to the fluxon generator exceeds a critical value. A bias current  $I_b$ , perpendicular to the JTL controls the velocity  $v$  of the fluxons (which is

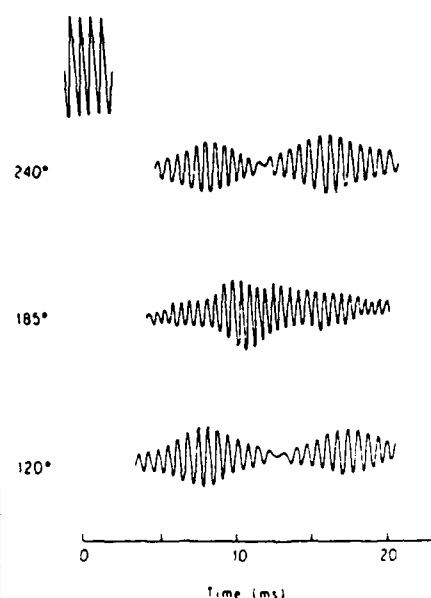


**Fig. 3** Collision of clockwise and anticlockwise envelope solitons travelling around a thin cylindrical shell. The shape of the envelope persists because of the balance between amplitude dispersion and the nonlinearity of the elastic medium. Without this balance the wave packet would disperse. The top trace shows the excitation pulse. (From ref. 2.)

typically  $4 \times 10^7 \text{ m s}^{-1}$ ), and must also exceed a minimum value. The sampler detects only at one central point, so that the flux across the whole JTL cannot be measured in one go.

Instead, a variable delay  $2\Delta t$  can be introduced between the two fluxon generators, effectively moving the fluxon-antifluxon pair left or right by a distance  $v\Delta t$ . A single scan, such as shown in Fig. 2, is obtained by sweeping  $\Delta t$ . The time sequence shown in Fig. 2 is obtained by introducing a second delay  $\Delta S$  before firing the sampler.

Fujimaki *et al.* thus observe the collision of a fluxon and an antifluxon, in which the two merge, interact and dissipate their energy via a 'breather mode' (the soliton and antisoliton bound together in a localized, lower-energy state) into linear oscillations ('radiation') which are finally absorbed by shunt resistances (Fig. 2). This agrees well with computational results and can also be understood in terms of fluxon perturbation theory. In other cases, the fluxons can survive the collision. The fringes in the traces are non-solitonic effects inevitable in real versions of such idealized mathematical concepts. The authors also demonstrate the relativistic nature of the fluxons by showing that the product of the pulse height and the pulse width is independent of the fluxon velocity.

Wu *et al.*<sup>2</sup> observed envelope solitons in elastic solids for the first time. In contrast to topological solitons, envelope solitons are wave packets with a soliton-shaped envelope (Fig. 3). Earlier experiments with fluid surface waves have been

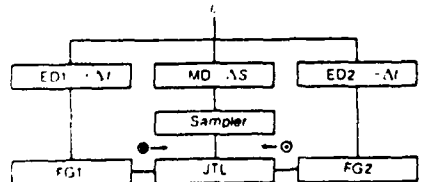


**Fig. 1** Simplified block diagram of the fluxon experiment of Fujimaki *et al.* The fluxon and antifluxon (cross and dot, respectively) are injected into the Josephson transmission line (JTL), made of 31 Josephson junctions, each a  $4 \times 4 \mu\text{m}^2$  sandwich of two superconducting films and one insulating) by the fluxon generators FG1 and FG2. Electronic delays ED1 and ED2 delay the fluxon and advance the antifluxon by  $\Delta t$ , effectively shifting the system  $v\Delta t$  leftwards along the JTL. The sampler records the flux density at the midpoint of the JTL after a variable mechanical time delay ( $\Delta S$ ) of  $\Delta S$ . The whole process is initiated when the control current  $I_c$  exceeds a critical value. (From ref. 1.)

interpreted in terms of envelope solitons<sup>6</sup>. Wu *et al.*<sup>7</sup> excite flexural wave packets by an acoustic horn driver on a circular-cylindrical thin elastic shell. The waves propagate clockwise and anticlockwise around the cylinder. Their nonlinear interaction is seen by means of transducers mounted on the shell. The reason for using thin shells is that this system is very dispersive and has a high nonlinear response, making the generation of solitons feasible, and a large quality factor, so that they persist. Such a combination of parameters generally makes soliton formation in off-equilibrium (highly distorted) systems accessible to observation.

As in other quickly varying hyperbolic

classical fields, the slow modulations of the flexural waves on the shell are described by the nonlinear Schrödinger equation. The parameters in the interacting envelope soliton solutions of this equation can be fitted perfectly to the observed data, thus implying the existence of envelope solitons.

Solitons are not of interest to physicists alone. Davydov<sup>8</sup> has proposed application of envelope solitons to understand energy storage and transport in protein chains. Our computer studies<sup>9</sup> of the quantum model of  $\alpha$ -helical proteins show that the solitons have long lifetimes at biological temperatures. Unfortunately, experimental evidence of this mechanism

remains to be obtained. □

- 1 Fujimaki, A., Nakajima, K. & Sawada, Y. *Phys Rev Lett* **59**, 2895-2898 (1987)
- 2 Wu, J., Wheatey, J., Puterman, S. & Rudnick, I. *Phys Rev Lett* **59**, 2744-2747 (1987)
- 3 Perring, J. K. & Skyrme, T. H. R. *Nucl Phys* **31**, 550 (1962)
- 4 Zabusky, N. J. & Kruskal, M. D. *Phys Rev Lett* **15**, 240-243 (1965)
- 5 Pedersen, N. F., Samuelsen, M. R. & Welner, D. *Phys Rev B* **30**, 4057-4059 (1984)
- 6 Yuen, H. C. & Lake, B. M. *Phys Fluids* **18**, 956-960 (1975)
- 7 Davydov, A. S. *J. Theor Biol.* **30**, 559-569 (1971)
- 8 Cruzeiro, L., Halding, J., Christiansen, P. L., Skovgaard, O. & Scott, A. C. *Phys Rev A* (in the press)

Peter L. Christiansen is at the Centre for Modelling Nonlinear Dynamics and Irreversible Thermodynamics (MIDIT), The Technical University of Denmark, DK-2800 Lyngby, Denmark

## Thermal sine-Gordon system in the presence of different types of dissipation

M. Salerno,<sup>\*</sup> M. R. Samuelsen,<sup>†</sup> and H. Svensmark<sup>†</sup>

Modellering Ikke-Lineær Dynamik og Irreversibel Termodynamik, The Technical University of Denmark, DK-2800 Lyngby, Denmark

(Received 30 November 1987)

The effects of thermal fluctuations on solitons and phonons of the sine-Gordon system are investigated in the presence of a  $\alpha\phi_{xx} - \beta\phi_{xxx}$  dissipation. The analysis requires the assumption of a more general autocorrelation function for the noise than the one used in previous works. We verify that this leads to the correct results for the average kinetic energies of solitons and phonons in the system. We also evaluate the linewidth for a Josephson oscillator in the presence of both  $\alpha$  and  $\beta$  dissipation, and lastly we briefly discuss the extension of the theory to more general dissipative terms.

## I. INTRODUCTION

The effects of thermal fluctuations both on solitons and phonons of the sine-Gordon system are relevant in the description of many physical systems in contact with a heat reservoir.<sup>1-8</sup> In the context of Josephson junctions, for example, it was shown that thermal fluctuations in the fluxon velocity are directly related to the appearance of a very narrow oscillator linewidth.<sup>4,5</sup> The coupling of the sine-Gordon system to the heat reservoir can be schematized as shown in Fig. 1, where *A* represents an ordered flow of energy from the system to the heat reservoir (due to dissipation) and *B* represents a disordered flow of energy from the reservoir to the system (thermal fluctuations). This means that the loss term in the sine-Gordon equation is intrinsically connected to a noise term (dependent on temperature) representing the effect of the reservoir on the system. This scheme leads to the following thermal sine-Gordon (TSG) equation:

$$\phi_{xx} - \phi_{xx} - \sin\phi = \eta + \Gamma(\phi) + n(x, t), \quad (1)$$

where  $\Gamma(\phi)$  represents a generic dissipation and  $n(x, t)$  is the stochastic force associated with the loss. [In Eq. (1) a bias term  $\eta$  which represents ordered energy input into the system, suitable for many practical applications, is also included.] In recent papers the TSG equation was studied by assuming a loss term proportional to  $\phi$ , [i.e.,  $\Gamma(\phi) = \alpha\phi$ , in Eq. (1)], and an autocorrelation function for the noise given by

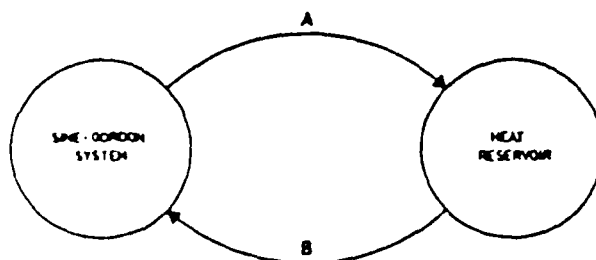


FIG. 1. Schematized representation of the thermal sine-Gordon system. *A* represents ordered flow of energy from the sine-Gordon system to the heat reservoir and *B* represents disordered flow from the reservoir to the system.

$$\langle n(x, t)n(x', t') \rangle = 16\alpha \frac{k_B T}{E_0} \delta(x - x') \delta(t - t'). \quad (2)$$

In Eq. (2)  $\langle \dots \rangle$  means ensemble average,  $E_0$  is the rest energy of the soliton (used to fix the scale in energy),  $k_B$  is the Boltzmann constant, and  $T$  is the temperature. The prefactor in Eq. (2) was determined by applying the fluctuation-dissipation theorem to a soliton with small velocity.<sup>6</sup> Among other results, it was shown that as a consequence of the thermal reservoir, solitons have an average energy of  $\frac{1}{2}k_B T$  per mode.<sup>6,7</sup> This analysis was also applied to a Josephson junction, leading to an expression for the oscillator linewidth in agreement with experimental measurements.<sup>8</sup> In the context of the Josephson junction however, besides a loss term proportional to  $\phi_{xx}$ , it is of interest to include a loss proportional to  $\phi_{xxx}$ , which is due to normal surface currents through the junction. This kind of dissipation is found to be responsible for several interesting phenomena such as bunching of fluxons,<sup>9</sup> and appearance of strong deformations on the fluxon tail.<sup>10</sup> The aim of the present paper is to extend the analysis in Ref. 6 to include this  $\phi_{xxx}$  dissipative term. More precisely we will consider  $\Gamma$  in Eq. (1) to be given by

$$\Gamma(\phi) \equiv \alpha\phi_{xx} - \beta\phi_{xxx}, \quad \alpha, \beta \in \mathbb{R}^+ \quad (3)$$

and assume for the noise the following autocorrelation function:

$$\begin{aligned} \langle n(x, t)n(x', t') \rangle &= 16 \frac{k_B T}{E_0} \delta(t - t') \\ &\times \left[ \alpha - \beta \frac{\partial^2}{\partial x^2} \right] \delta(x - x'). \end{aligned} \quad (4)$$

The effects of the noise term (4) in Eq. (1), will be then studied in the cases of pure soliton and pure fluxon motion, respectively, in Secs. II and III. As a result we find that the "thermal" solitons and phonons will still have an average energy of, respectively,  $\frac{1}{2}k_B T$  and  $k_B T$  per mode; however, the presence of the  $\beta$  term in (3) will decrease the diffusion constant of a soliton by a factor  $\alpha/(\alpha + \beta/3)$ . In Sec. III we also relate the above results to the Josephson junctions by showing that there will be

no change in the linewidth expression given in Ref. 5 due to the presence of the  $\beta$  dissipation. Finally in Sec. IV we give a short summary of the main results, including a brief discussion on the generalization of the above-mentioned results to higher-order dissipative terms of the type  $\sum_{i=1}^m \alpha_i D_x^{2i} \phi$ , with  $\alpha_i \in R$ ,  $D_x \equiv \partial/\partial x$ , and  $m \in N$ .

## II. THERMAL PHONONS

In this section we consider the TSG equation

$$\phi_{xx} - \phi_{tt} - \sin\phi = \eta + \alpha\phi - \beta\phi_{xtt} + n(x, t) \quad (5)$$

in the small-amplitude limit and with no solitons in the system. Phonon modes  $\psi$  are seen as small oscillations around the ground state  $\phi_0 = -\sin^{-1}\eta$  satisfying the boundary conditions

$$\psi_x(0, t) = \psi_x(L, t) = 0. \quad (6)$$

The field  $\phi(x, t)$  in the small-amplitude limit can be written as

$$\phi(x, t) = -\sin^{-1}\eta + \psi(x, t) \text{ with } \|\psi\| \ll 1. \quad (7)$$

By substituting (7) in (5) we get the following stochastic equation for thermal phonons:

$$\psi_{xx} = \psi_{tt} - (1 - \eta^2)^{1/2}\psi + \alpha\psi_t - \beta\psi_{xtt} + n(x, t). \quad (8)$$

When  $\alpha = 0$ ,  $\beta = 0$ , and  $n(x, t) \equiv 0$ , these phonons are just classical Klein-Gordon modes with energy given by

$$H_{ph} = \frac{E_0}{16} \int_0^L dx [\psi_x^2 + \psi_t^2 + \psi^2(1 - \eta^2)^{1/2}] \quad (9)$$

(here  $L$  is the length of the system). The general solution of Eq. (8) can then be expressed in terms of the complete set  $\phi_n$  of orthonormal Klein-Gordon modes as

$$\psi(x, t) = \sum_n A_n(t) \phi_n(x) = \sqrt{2/L} \sum_n A_n(t) \cos(k_n x) \quad (10)$$

with  $k_n = \hbar\pi/L$  and  $\sqrt{2/L}$  just a normalization factor. Inserting (10) in (8) and projecting the resulting equation along the unperturbed eigenstate we get

$$A_{n,tt} + (\alpha + \beta k_n^2) A_{n,t} + \omega_n^2 A_n = \epsilon_n(t), \quad (11)$$

where

$$\epsilon_n(t) = \sqrt{2/L} \int_0^L n(x, t) \cos(k_n x) dx \quad (12)$$

and

$$\omega_n^2 = (1 - \eta^2)^{1/2} + k_n^2. \quad (13)$$

By using (4) we obtain for the autocorrelation function and for the power spectrum of the normal process  $\epsilon_n(t)$  the following expressions:

$$R_{\epsilon_n}(t - t') \equiv \langle \epsilon_n(t') \epsilon_n(t) \rangle$$

$$= 16(\alpha + \beta k_n^2) \frac{k_B T}{E_0} \delta(t - t'), \quad (14)$$

$$S_{\epsilon_n}(\omega) = 16(\alpha + \beta k_n^2) \frac{k_B T}{E_0}. \quad (15)$$

By identifying  $\alpha + \beta k_n^2$  with  $\alpha$  we see that Eqs. (11), (14), and (15) coincide, respectively, with Eqs. (3.9), (2.12), and (2.13) of Ref. 6. One can follow the same analysis of Ref. 6 to show that the average energy per phonon mode is

$$\langle H_n \rangle = k_B T. \quad (16)$$

[This easily follows by solving by harmonic analysis Eq. (11) and by using Eq. (9).] It is worth remarking that this result does not depend on the particular boundary conditions used, nor on the smallness requirements of  $\alpha$ ,  $\beta$ , and  $\eta$ .

## III. THERMAL SOLITONS

In this section we concentrate on the effect of the  $\alpha$ ,  $\beta$ ,  $\eta$ , and  $n(x, t)$  terms in Eq. (5) on an unperturbed sine-Gordon soliton

$$\phi = 4 \tan^{-1} \exp[\gamma(u)(x - ut)], \quad (17)$$

$$\gamma(u) = (1 - u^2)^{-1/2}.$$

Note that the  $\eta$  in (5) shifts the ground state from 0 to  $-\sin^{-1}\eta$ ; therefore a soliton in our system should be seen as a  $2\pi$  kink from  $-\sin^{-1}\eta$  to  $2\pi - \sin^{-1}\eta$ .

An equation of motion for the perturbed soliton can be easily obtained by defining the momentum

$$P = -\frac{1}{i} \int_{-\infty}^{+\infty} \phi_x \phi_t dx \quad (18)$$

and differentiating it with respect to time, this giving

$$\frac{dP}{dt} = \frac{\pi\eta}{4} + \frac{\alpha}{8} \int \phi_x \phi_t dx + \frac{\beta}{8} \int \phi_{xx} \phi_{xt} dx + \epsilon(t), \quad (19)$$

where

$$\epsilon(t) = -\frac{1}{i} \int_{-\infty}^{+\infty} \phi_x n(x, t) dx. \quad (20)$$

With neglect of thermal noise, Eq. (19) has stationary  $2\pi$ -kink  $\phi^*$  solutions moving with the power-balance velocity  $u_0$ , for small perturbations, satisfying<sup>11</sup>

$$\frac{\pi\eta}{4} (1 - u_0^2)^{3/2} - \alpha u_0 (1 - u_0^2) - \frac{\beta}{3} u_0 = 0 \quad (21)$$

and with momentum

$$P_0 = u_0 \gamma(u_0). \quad (22)$$

In the stationary case, the integrals in Eq. (19) can be written as

$$-u \left[ \frac{\alpha}{8} \int (\phi_x^*)^2 dx + \frac{\beta}{8} \int (\phi_{xx}^*)^2 dx \right] = -u \left[ \alpha \gamma_1(u) + \frac{\beta}{3} \gamma_2(u) \right] \equiv -\frac{\pi\eta(u)}{4}, \quad (23)$$

where we used Eq. (18) together with  $\phi'' = -u\phi'_x$ . Equation (22) defines the functions  $\gamma_1(u)$  and  $\gamma_2(u)$  which for small perturbations (or small velocities) reduce to the usual Lorentz factor in (17).

By inserting Eq. (23) into Eq. (19) we get for the momentum the following Langevin equation for  $P$ :

$$\frac{dP}{dt} = \frac{\pi\eta}{4} - \frac{\eta(u)}{4} + \epsilon(t). \quad (24)$$

The noise term  $\epsilon(t)$  in Eq. (24) introduces fluctuations in the momentum and, from (22), in the velocity of the kink according to

$$\frac{dp}{dt} \frac{\partial \Delta u}{\partial t} = -\frac{\pi}{4} \frac{\partial \eta}{\partial u} \Delta u + \epsilon(t), \quad (25)$$

where  $\Delta u$  measures the deviation of the  $2\pi$ -kink velocity from the power-balance value (21). The autocorrelation function and the power spectrum of the process  $\epsilon(t)$  in (25) are then easily evaluated by means of Eqs. (4) and (21). we write

$$R_\epsilon(t-t') = \frac{\pi}{2u} \frac{k_B T}{E_0} \eta(u) \delta(t-t'),$$

$$S_\epsilon(\omega) = \frac{\pi}{2u} \frac{k_B T}{E_0} \eta(u). \quad (26)$$

For small velocities (i.e.,  $\eta \approx 0$ ) we have from (23),

$$\eta(u) \approx \frac{4u}{\pi} \left| \alpha + \frac{\beta}{3} \right|. \quad (27)$$

Then Eq. (25) reduces to a Langevin equation for  $u$ ,

$$\frac{du}{dt} = - \left| \alpha + \frac{\beta}{3} \right| u + \epsilon(t). \quad (28)$$

By using (26) and (27), Eq. (28) is easily integrated by harmonic analysis, this giving

$$S_u(\omega) = \frac{S_\epsilon(\omega)}{\omega^2 + \left| \alpha + \frac{\beta}{3} \right|^2}, \quad (29)$$

from which it follows that

$$\langle u^2 \rangle = R_u(0) = \int_{-\infty}^{+\infty} \frac{d\omega}{2\pi} S_u(\omega) = \frac{k_B T}{E_0}. \quad (30)$$

The time average of the kinetic energy in the Brownian motion of the  $2\pi$  kink is then evaluated as

$$\langle E_{\text{kin}} \rangle = \frac{1}{2} E_0 \langle u^2 \rangle = \frac{1}{2} k_B T. \quad (31)$$

From Eq. (29) a diffusion constant  $D$  for the  $2\pi$ -kink motion can also be derived as

$$D = \frac{1}{E_0} \frac{k_B T}{\left| \alpha + \frac{\beta}{3} \right|}, \quad (32)$$

which is just the usual relation reported in Ref. 6 with  $\alpha$  identified with  $\alpha + \beta/3$ . The effect of the  $\beta$  dissipation on

the  $2\pi$ -kink motion is then to decrease its diffusion constant as one would have expected. We finally close this section by showing that the linewidth of a Josephson oscillator with  $\beta\phi_{xx}$  damping will still be given by the same expression reported in Ref. 6. To this end we return to Eq. (24) (which is valid for all  $u$ ) and rewrite it as

$$\frac{d}{dt} \Delta u + \frac{\pi}{4} \frac{\partial \eta}{\partial p} \Delta u = \frac{\partial u}{\partial p} \epsilon(t), \quad (33)$$

this leading to the following expression for the power spectrum of  $\Delta u$ :

$$S_{\Delta u}(\omega) = \left| \frac{\partial u}{\partial \eta} \right|^2 \left| \frac{\partial \eta}{\partial p} \right|^2 \frac{S_\epsilon(\omega)}{\omega^2 + \left( \frac{\pi}{4} \frac{\partial \eta}{\partial p} \right)^2}, \quad (34)$$

and by performing the same analysis of Ref. 5, one gets the following linewidth expression:

$$\Delta\nu = \frac{\pi k_B T}{\phi_0^2} \frac{R_D^2}{R_S}, \quad (35)$$

where  $R_D \propto \Delta u / \partial p$ ,  $R_S \propto u / p$ , and  $\phi_0$  is the flux quantum  $h/2e$  (for details we refer to Ref. 5).

#### IV. CONCLUSIONS

It has been shown that the effect of a thermal reservoir on solitons and phonons in the sine-Gordon system in the presence of  $\alpha\phi_x - \beta\phi_{xx}$  dissipations gives an average kinetic energy of, respectively,  $\frac{1}{2}k_B T$  and by  $k_B T$  per mode. The presence of the  $\beta$  term on the soliton is to decrease its diffusion constant. Furthermore, we showed that the above analysis in the case of the Josephson oscillators leads to the same linewidth expression as obtained in Ref. 5.

Finally, in closing the paper, we wish to point out that the above analysis can be generalized to dissipations of type  $\hat{\alpha}\phi$ , with  $\hat{\alpha}$  given by the following differential operator:

$$\hat{\alpha} = \sum_{n=0}^N (-1)^n \alpha_n D_x^{2n} \text{ where } D_x \equiv \frac{\partial}{\partial x}. \quad (36)$$

In this case we need to replace the autocorrelation function (4) for the noise  $n(x, t)$  by the following expression:

$$\langle n(x, t)n(x', t') \rangle = 16 \frac{k_B T}{E_0} \delta(t-t') \hat{\alpha} \delta(x-x') \quad (37)$$

in order to get the correct results. Indeed one easily sees that (36) and (37) will give little changes in the above results except for the substitutions of

$$(\alpha + \beta k_n^2) \rightarrow \alpha_0 + \sum_i \alpha_i k_n^{2i} \quad (38)$$

in the phonon case and

no change in the linewidth expression given in Ref. 5 due to the presence of the  $\beta$  dissipation. Finally in Sec. IV we give a short summary of the main results, including a brief discussion on the generalization of the above-mentioned results to higher-order dissipative terms of the type  $\sum_{i=1}^m \alpha_i D_x^{2i} \phi$ , with  $\alpha_i \in \mathbb{R}$ ,  $D_x \equiv \partial/\partial x$ , and  $m \in \mathbb{N}$ .

## II. THERMAL PHONONS

In this section we consider the TSG equation

$$\phi_{xx} - \phi_{tt} - \sin\phi = \eta + \alpha\phi_t - \beta\phi_{xxt} + n(x, t) \quad (5)$$

in the small-amplitude limit and with no solitons in the system. Phonon modes  $\psi$  are seen as small oscillations around the ground state  $\phi_0 = -\sin^{-1}\eta$  satisfying the boundary conditions

$$\psi_x(0, t) = \psi_x(L, t) = 0. \quad (6)$$

The field  $\phi(x, t)$  in the small-amplitude limit can be written as

$$\phi(x, t) = -\sin^{-1}(\eta) + \psi(x, t) \text{ with } \|\psi\| \ll 1. \quad (7)$$

By substituting (7) in (5) we get the following stochastic equation for thermal phonons:

$$\psi_{xx} = \psi_{tt} - (1 - \eta^2)^{1/2} \psi + \alpha\psi_t - \beta\psi_{xxt} + n(x, t). \quad (8)$$

When  $\alpha = 0$ ,  $\beta = 0$ , and  $n(x, t) \equiv 0$ , these phonons are just classical Klein-Gordon modes with energy given by

$$H_{ph} = \frac{E_0}{16} \int_0^L dx [\psi_x^2 + \psi_t^2 + \psi^2 (1 - \eta^2)^{1/2}] \quad (9)$$

(here  $L$  is the length of the system). The general solution of Eq. (8) can then be expressed in terms of the complete set  $\phi_n$  of orthonormal Klein-Gordon modes as

$$\psi(x, t) = \sum_n A_n(t) \phi_n(x) = \sqrt{2/L} \sum_n A_n(t) \cos(k_n x) \quad (10)$$

with  $k_n = n\pi/L$  and  $\sqrt{2/L}$  just a normalization factor. Inserting (10) in (8) and projecting the resulting equation along the unperturbed eigenstate we get

$$A_{n,tt} + (\alpha + \beta k_n^2) A_{n,t} + \omega_n^2 A_n = \epsilon_n(t), \quad (11)$$

where

$$\epsilon_n(t) = \sqrt{2/L} \int_0^L n(x, t) \cos(k_n x) dx \quad (12)$$

and

$$\omega_n^2 = (1 - \eta^2)^{1/2} + k_n^2. \quad (13)$$

By using (4) we obtain for the autocorrelation function and for the power spectrum of the normal process  $\epsilon_n(t)$  the following expressions:

$$R_{\epsilon_n}(t - t') \equiv \langle \epsilon_n(t') \epsilon_n(t) \rangle$$

$$= 16(\alpha + \beta k_n^2) \frac{k_B T}{E_0} \delta(t - t'), \quad (14)$$

$$S_{\epsilon_n}(\omega) = 16(\alpha + \beta k_n^2) \frac{k_B T}{E_0}. \quad (15)$$

By identifying  $\alpha + \beta k_n^2$  with  $\alpha$  we see that Eqs. (11), (14), and (15) coincide, respectively, with Eqs. (3.9), (2.12), and (2.13) of Ref. 6. One can follow the same analysis of Ref. 6 to show that the average energy per phonon mode is

$$\langle H_n \rangle = k_B T. \quad (16)$$

[This easily follows by solving by harmonic analysis Eq. (11) and by using Eq. (9).] It is worth remarking that this result does not depend on the particular boundary conditions used, nor on the smallness requirements of  $\alpha$ ,  $\beta$ , and  $\eta$ .

## III. THERMAL SOLITONS

In this section we concentrate on the effect of the  $\alpha$ ,  $\beta$ ,  $\eta$ , and  $n(x, t)$  terms in Eq. (5) on an unperturbed sine-Gordon soliton

$$\phi = 4 \tan^{-1} \exp[\gamma(u)(x - ut)], \quad (17)$$

$$\gamma(u) = (1 - u^2)^{-1/2}.$$

Note that the  $\eta$  in (5) shifts the ground state from 0 to  $-\sin^{-1}\eta$ ; therefore a soliton in our system should be seen as a  $2\pi$  kink from  $-\sin^{-1}\eta$  to  $2\pi - \sin^{-1}\eta$ .

An equation of motion for the perturbed soliton can be easily obtained by defining the momentum

$$P = -\frac{1}{\hbar} \int_{-\infty}^{+\infty} \phi_x \dot{\phi}_x dx \quad (18)$$

and differentiating it with respect to time, this giving

$$\frac{dP}{dt} = \frac{\pi\eta}{4} + \frac{\alpha}{8} \int \phi_x \dot{\phi}_x dx + \frac{\beta}{8} \int \phi_{xx} \phi_{xt} dx + \epsilon(t), \quad (19)$$

where

$$\epsilon(t) = -\frac{1}{\hbar} \int_{-\infty}^{+\infty} \phi_x n(x, t) dx. \quad (20)$$

With neglect of thermal noise, Eq. (19) has stationary  $2\pi$ -kink  $\phi^*$  solutions moving with the power-balance velocity  $u_0$ , for small perturbations, satisfying<sup>11</sup>

$$\frac{\pi\eta}{4} (1 - u_0^2)^{1/2} - \alpha u_0 (1 - u_0^2) - \frac{\beta}{3} u_0 = 0 \quad (21)$$

and with momentum

$$P_0 = u_0 \gamma(u_0). \quad (22)$$

In the stationary case, the integrals in Eq. (19) can be written as

$$-u \left[ \frac{\alpha}{8} \int (\phi_x^*)^2 dx + \frac{\beta}{8} \int (\phi_{xx}^*)^2 dx \right] = -u \left[ \alpha \gamma_1(u) + \frac{\beta}{3} \gamma_2(u) \right] \equiv -\frac{\pi\eta(u)}{4}, \quad (23)$$

## Stability of fluxon motion in long Josephson junctions at high bias

S. Pagano,\* M. P. Soerensen, P. L. Christiansen, and R. D. Parmentier<sup>†</sup>

Laboratory of Applied Mathematical Physics, The Technical University of Denmark, DK-2800 Lyngby, Denmark

(Received 29 September 1987; revised manuscript received 16 March 1988)

In long Josephson junctions the motion of fluxons is revealed by the existence of current steps, zero-field steps, in the current-voltage characteristics. In this paper we investigate the stability of the fluxon motion when high values of the current bias are involved. The investigation is carried on by numerical integration of the model equation, the perturbed sine-Gordon equation, simulating junctions of overlap and annular geometry. A detailed description of the mechanism for the switching from the top of the zero-field step for both geometries is reported. Moreover, the effect of the various dissipations and of the junction length on the switching-current value is investigated. A simple boundary model is able to describe, for junctions of overlap geometry, the qualitative dependence of the switching current on the system parameters.

MS code no. BJ3799 1988 PACS number(s): 74.50. + r, 02.70. + d

## 4. INTRODUCTION

It is well known that Josephson junctions can support, under appropriate conditions the motion of magnetic field quanta (fluxons). The evidence of such motion is observed experimentally as current singularities [zero-field steps (ZFS's)] in the current-voltage characteristic and as microwave emission, in junctions having physical lengths bigger than the Josephson penetration length  $\lambda_J$ .<sup>1</sup> Since 1973, an attempt has been made to explain the observed phenomena in terms of oscillatory solitonic solutions of the "perturbed" sine-Gordon equation (PSGE) describing the electrodynamic of a Josephson junction.<sup>2</sup> For a unidimensional geometry and in normalized units it has the form

$$\phi_{xx} - \phi_{tt} - \sin\phi \overset{\circ}{=} \alpha\phi_t - \beta\phi_{xxt} - \gamma. \quad (1)$$

Here,  $\phi$  is the usual Josephson phase variable,  $x$  is distance along the junction normalized to the Josephson penetration length  $\lambda_J$ ,  $t$  is time normalized to the inverse of the Josephson plasma angular frequency  $\omega_J$ ,  $\alpha$  is the normalized shunt conductance that takes into account tunneling of normal electrons across the junction,  $\beta$  is the normalized real part of the superconductor surface impedance,  $\gamma$  is the dc bias current normalized to the Josephson critical current, and the subscripts indicate partial derivatives. Equation (1), together with the appropriate boundary conditions, determined by the particular junction geometry employed, gives a very good description of the observed dynamical behavior of the junction, often to a surprising degree of accuracy. It has to be noted, however, that since exact analytic dynamical solutions of Eq. (1), are, in general, not known, all the information is obtained either by direct numerical integration of Eq. (1), or by perturbative methods based on the known analytical solutions of the unperturbed sine-Gordon equation [ $\alpha = \beta = \gamma = 0$  in Eq. (1)], or by some other approximation scheme.

The perturbative approach is very useful in describing the overall dynamics of fluxons in the junction, in partic-

ular when all the perturbing terms are small, but it fails in describing extreme situations such as the ones where the stability of the traveling solutions at high bias values is involved. In fact, the perturbative approach is unable to predict the maximum current amplitude of the ZFS's, i.e., the maximum dc bias current that can sustain fluxon propagation. The simplest power-balance perturbative scheme<sup>3</sup> predicts an infinite step current height, while the perturbative scheme proposed in Refs. 4 and 5 predicts a maximum normalized step height equal to one. In contrast, experimental and numerical results, by various authors, typically give a maximum step height between 0.4 and 0.8.<sup>6</sup> The main reason for the failure of the perturbative approach is that, being based on solutions of the pure sine-Gordon equation, it is not valid when the perturbative terms [the right-hand side of Eq. (1)] become large, as occurs when bias values that are not small are considered.

Since the question of the maximum current amplitude of the ZFS's is of considerable practical importance to the experimentalist, and since no completely adequate analytic or perturbative approach is presently available, we propose in this work to furnish a detailed numerical study of the question, with the hope of providing a springboard for future theoretical work. We note that a step in the same direction has recently been taken by Zhang and Wu.<sup>7</sup> With respect to their work, our work (i) considers junctions of both annular and overlap geometries,<sup>1,3</sup> (ii) describes in detail the instability mechanism for both geometries, and (iii) employs more than one numerical scheme, which in turn, (iv) pinpoints a numerical pitfall to be avoided. Like Zhang and Wu, we limit attention to dynamic states involving a single propagating fluxon. Moreover, we shall not consider, in this work, the effects of intrinsic and extrinsic noise and of barrier spatial nonuniformities<sup>8</sup> on the stability of the fluxon oscillations. The reasons for this choice are based on the facts that the cited effects, although often important in physical devices, can always be reduced by a careful shielding of the junction from electromagnetic interference, by lowering the working temperature and by

improving the fabrication processes. Then the maximum performances will be determined by the intrinsic instabilities of the fluxon oscillations, which are the subject of this work.

In Sec. II a description of the numerical methods used is reported. Junctions of annular geometry and of overlap geometry are then analyzed in order to identify the ranges of stable fluxon motion in each case. Finally, a quasianalytical model is presented which gives reasonable qualitative agreement with the numerical results for overlap geometry junctions.

## II. NUMERICAL METHODS

In order to numerically solve Eq. (1) with the appropriate boundary condition, two different numerical schemes have been employed. One is based on a Fourier-Galerkin spatial decomposition of the phase  $\phi$  as<sup>9</sup>

$$\begin{aligned}\phi(x,t) = & \eta x + \phi_0(t) + \sum_{n=1}^N \left[ \phi_n(t) \cos \left( \frac{n\pi x}{l} \right) \right. \\ & \left. + \psi_n(t) \sin \left( \frac{n\pi x}{l} \right) \right],\end{aligned}\quad (2)$$

where the  $\phi_n(t)$  and  $\psi_n(t)$  are unknown functions of time,  $l$  is the normalized junction length, and  $\eta$  is a constant chosen to take appropriately into account the boundary conditions. For the annular geometry junction the boundary conditions are

$$\begin{aligned}x & \neq c, \quad t \\ \phi(x,t) & = \phi(x, l + \theta) + 2m\pi,\end{aligned}\quad (3)$$

where  $m$  is the difference between the number of fluxons and antifluxons present along the junction (since the junction is a closed loop  $m$  is a conserved quantity). In this case,

$$\eta = \frac{2\pi m}{l}. \quad (4)$$

For the overlap geometry junction the boundary conditions are

$$\phi_x(0,t) = \phi_x(l,t) = \eta, \quad (5)$$

where now  $\eta$  represents the normalized value of the external magnetic field along the  $y$  direction in the junction plane. Moreover, the boundary conditions [Eq. (5)] impose that  $\psi_n = 0$  for all  $n$ . All the results obtained herein are referred to the case where no external magnetic field is applied.

Although other geometrical configurations are possible, only the above two have been considered because they are the most useful for the understanding of the junction dynamics.<sup>7</sup> Inserting Eq. (2) into Eq. (1) and using the orthogonality of the trigonometric functions, the following set of differential equations is obtained:

$$\ddot{\phi}_0 + \mu_0 \dot{\phi}_0 - \gamma = -\frac{1}{l} \int_0^l \sin \phi \, dx, \quad (6a)$$

$$\ddot{\phi}_n + \mu_n \dot{\phi}_n + \omega_n^2 \phi_n = -\frac{2}{l} \int_0^l \sin \phi \cos \left( \frac{n\pi x}{l} \right) dx, \quad n = 1, 2, \dots, N, \quad (6b)$$

$$\ddot{\psi}_n + \mu_n \dot{\psi}_n + \omega_n^2 \psi_n = -\frac{2}{l} \int_0^l \sin \phi \sin \left( \frac{n\pi x}{l} \right) dx, \quad n = 1, 2, \dots, N. \quad (6c)$$

Here  $\omega_n = (n\pi/l)$ ,  $\mu_n = \alpha + \omega_n^2 \beta$  and overhead dots denote time derivatives.

The set of equations (6) is solved using a sixth-order predictor-corrector method with variable step size,<sup>10</sup> while the right-hand sides of Eqs. (6) are evaluated by fast-Fourier-transform routine.<sup>11</sup> The accuracy of the numerical integration was checked by decreasing the time step and by increasing the number of spatial harmonic components considered. A typical value for the time step was  $\Delta t = 0.05$  while a choice of a number of spatial harmonics equal to twice the junction length was always appropriate.

The other numerical scheme employed was an implicit finite difference method<sup>12</sup> where the phase  $\phi$  is restricted to a square mesh

$$\phi \equiv \phi(\Delta x, q \Delta t). \quad (7)$$

The derivatives in Eq. (1) are approximated by a second-order Taylor expansion in the step size, with a time average over one time step for the  $x$  derivatives and inserted into Eq. (1). The boundary conditions are handled by introducing virtual extra points at the edge of the mesh in the usual way. A predictor-corrector loop is used to evaluate the nonlinear term in Eq. (1), enhancing in this way the stability of the whole scheme. Finally a set of linear algebraic equations with a tridiagonal coefficient matrix is obtained in the form

$$Ax = y, \quad (8)$$

where

$$x = (\phi_1^{q+1}, \dots, \phi_N^{q+1}) \quad (9)$$

and  $y$  is an appropriate function of the phase values at the mesh points and previous two time steps. Equation (8) is solved by the "double-sweep method"<sup>12</sup> which has been demonstrated to be stable as long as the matrix  $A$  is diagonally dominant, i.e., in this case

$$\frac{3(\beta + \Delta t)}{\alpha(\Delta x)^2 + 2(\Delta x)^2/\Delta t + 2\beta + 2\Delta t} < 1. \quad (10)$$

Again the accuracy of the results has been checked by halving both the space step  $\Delta x$  and the time step  $\Delta t$ . Although it may seem exaggerated to use two different numerical methods to solve the same equation, this was very useful to test the independence of the numerical results on the scheme used. This fact is very important when dealing with dynamical states parametrically driven to unstable regions. Another point to consider is that, al-

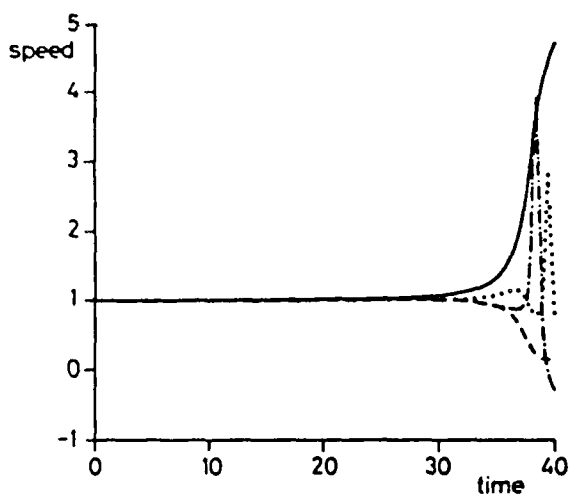


FIG. 1. Time evolution of the first four mode speeds. The modes considered are the 0th (solid curve), the 1st (dashed curve), the 2nd (dash-dotted curve), and the 3rd (dotted curve).

though the finite difference method seems to be more efficient for long junctions, the multimode method is able to give more physical information about the dynamical states investigated. For example, looking at the phase velocity of each mode in annular junctions is very useful to determine whether or not stationary motion conditions are achieved. The mode phase velocity is defined as

$$u_n = -\frac{F_n(\phi_i)}{F_n(\phi_x)}, \quad (11)$$

where  $F_n(Y)$  is the  $n$ th component of the spatial Fourier transform of  $Y$ . This definition is based on the idea that each Fourier component of the phase travels with a modulating velocity  $u_n$ , which is slowly varying on the time scale of the time step used in the integration scheme. In Fig. 1 a plot of the time dependence of the phase velocity of the first four modes is shown for the case of an annular geometry junction with  $l = 16$ ,  $\alpha = 0.18$ ,  $\beta = 0.01$ ,  $\gamma = 0.89$ ,  $m = 1$ . The parameter values correspond to the top of the first current singularity and the time evolution shows how the fluxon solution becomes unstable and breaks down at the time  $t \sim 35$ . In fact, as long as the fluxon is stable and travels along the junction, all the modes have the same velocity, the fluxon velocity, whereas when the solution becomes unstable it undergoes transitory state where all the modes behave differently and finally reaches a new stable configuration where again all the modes have the same velocity (not shown in the figure).

### III. ANNULAR GEOMETRY

In this section a study of the mechanism for the switching from the "fluxon" state (ZFSI) to the "rotating" state (McCumber branch) is carried out for junctions of annular geometry. The choice of the annular geometry is made because in such a system there are no collisions

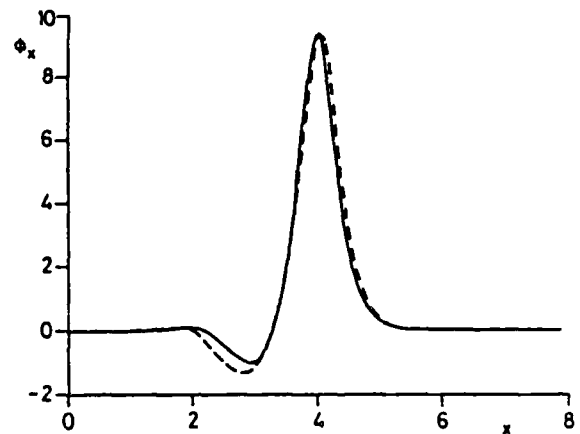


FIG. 2.  $\phi_x$  at two different bias levels:  $\gamma = 0.75$  (solid curve) and  $\gamma = 0.8$  (dashed curve).

of the fluxons with the boundaries; thus the resulting dynamics is smoother. Moreover, since junction normalized lengths  $l \gg 1$  are always considered, the motion of a single fluxon on an infinite Josephson transmission line is well approximated. This allows a reduction of Eq. (1) to a third-order ordinary differential equation (ODE) for the traveling phase profile, reducing the problem to the study of a low-dimensional system.

In Figs. 2-4 the initial condition of the fluxon line shape proposed by Ferrigno and Pace<sup>3</sup> is used,

$$\phi_0(x, t) = \sin^{-1} \gamma + 4 \tan^{-1} \left[ \exp \left( \frac{x - u_0 t}{\sqrt{1 - \gamma^2}} \right) \right] \times \frac{(1 - \gamma^2)^{1/4}}{(1 - u_0^2)^{1/2}}, \quad (12)$$

where  $u_0$  is computed from power-balance considerations<sup>3</sup>

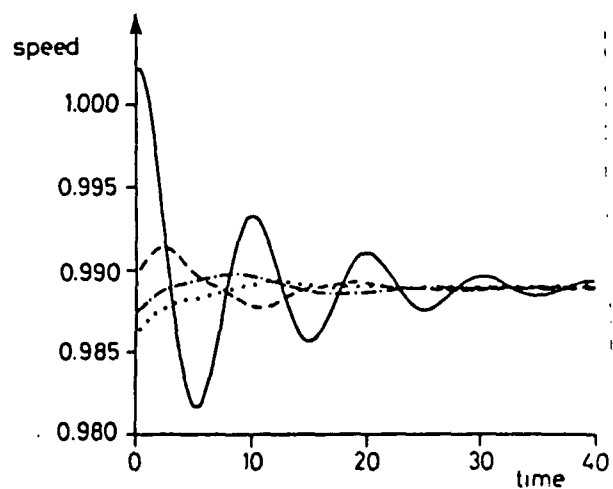


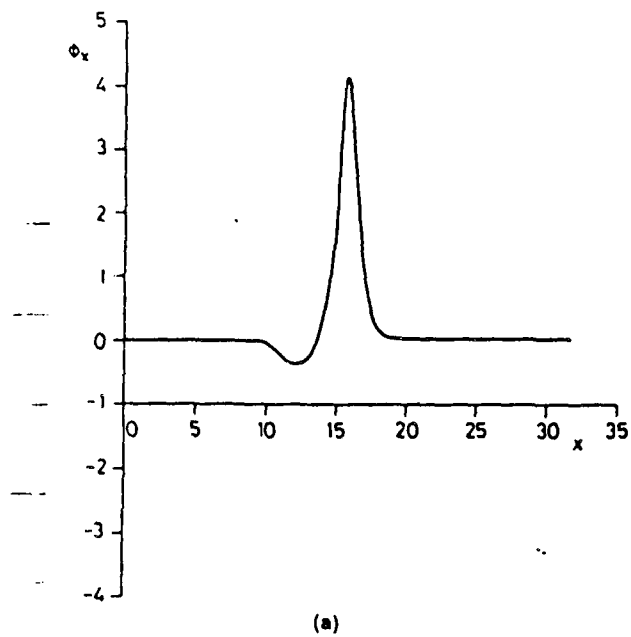
FIG. 3. Stabilization of the fluxon after a bias change illustrated by the first four mode speeds as in Fig. 1.  $\alpha = 0.18$ ,  $\beta = 0.1$ ,  $\gamma = 0.83$ , and  $l = 16$ .

$$\gamma = \frac{4u_0}{\pi} \frac{(1-\gamma^2)^{1/4}}{(1-u_0^2)^{1/2}} \left[ \alpha + \frac{\beta}{3} \frac{(1-\gamma^2)^{1/2}}{1-u_0^2} \right]. \quad (13)$$

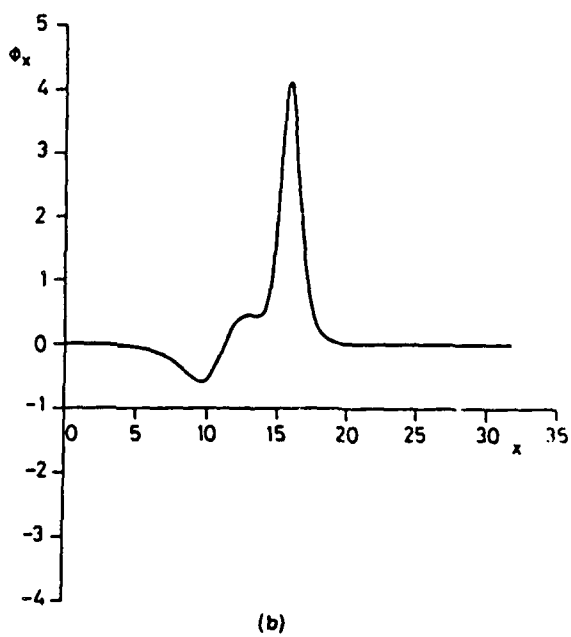
In the limit  $\gamma \rightarrow 0$ ,  $u_0$  assumes the value found by McLaughlin and Scott.<sup>13</sup> After some time the solution relaxes toward a fixed profile traveling with a constant speed  $u$ . The value of  $u$  is determined either by a measurement of the mode phase velocities, or by a direct measurement of the fluxon position, depending on the

particular numerical code used.

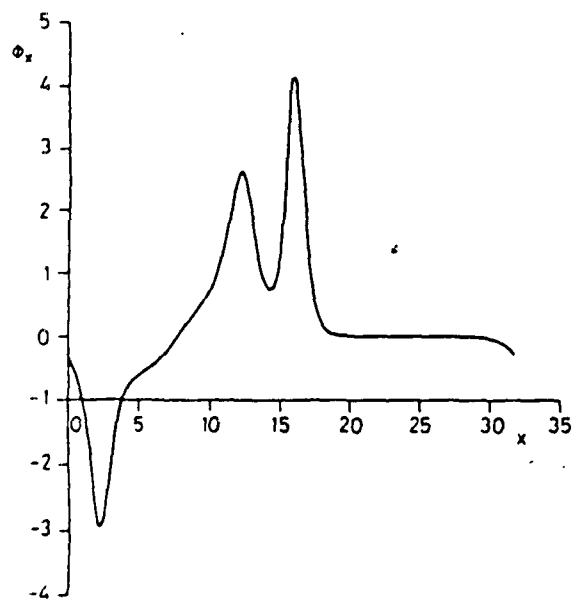
When the  $\beta$  losses are absent,<sup>13</sup> a constant speed  $u$  is found for all values of  $\gamma$  less than one. If a small  $\beta$  loss is present, i.e.,  $\beta \ll \alpha$ , a constant speed  $u$  is not found for  $\gamma$  values very close to one. For  $\gamma > 1$  there are no more static solutions of Eq. (1), therefore, a solution of fluxon structure is not possible. This leads to the first kind of switching mechanism. It can be described as the disappearing of the stable equilibrium solutions of Eq. (1), which form the asymptotic state of any fluxonlike solu-



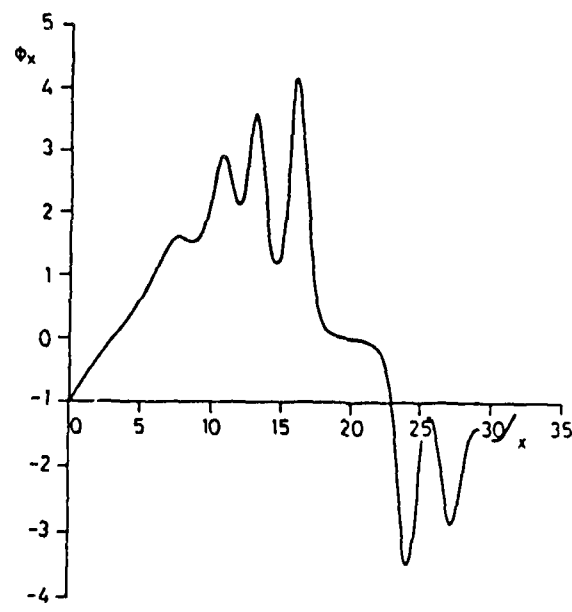
(a)



(b)

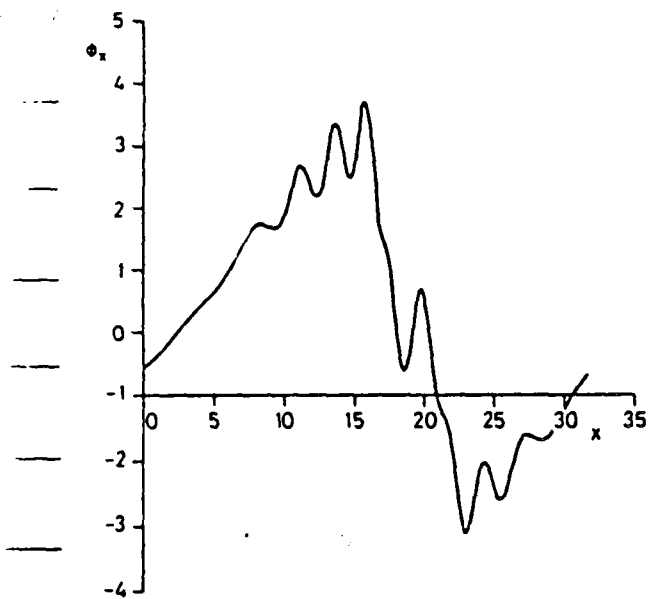


(c)

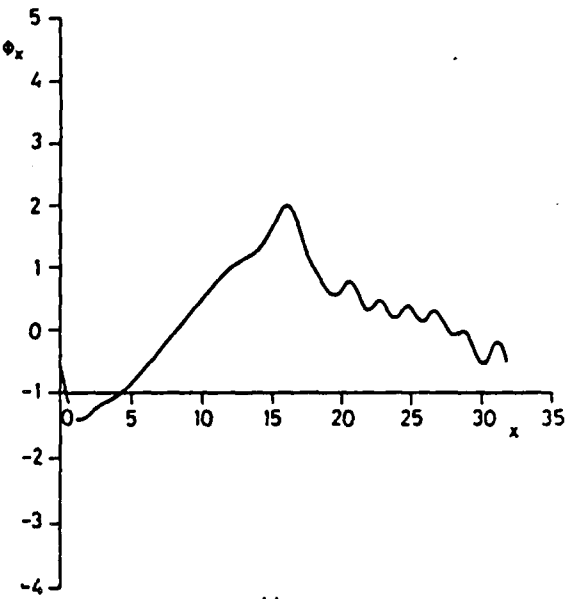


(d)

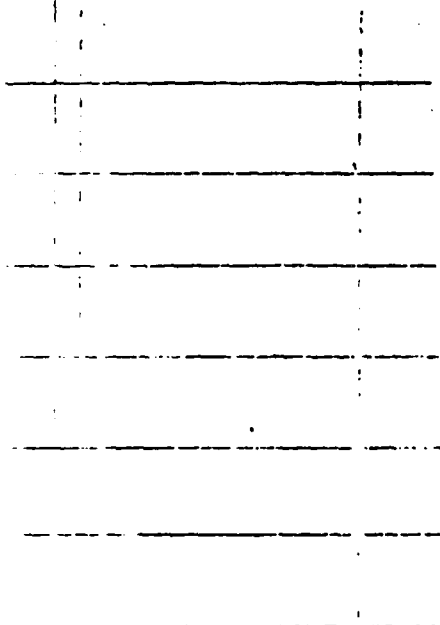
FIG. 4. Time sequence of the switching. (a)  $t = 25$ ; (b)  $t = 50$ ; (c)  $t = 55$ ; (d)  $t = 60$ ; (e)  $t = 65$ ; (f)  $t = 70$ ; (g)  $t = 75$ .



(e)



(f)



(g)

FIG. 4. (Continued).]

tion. In terms of the chain of pendula analog, this correspond to the starting of a uniform rotation of all the pendula. If Ref. 14, Burkov *et al.* have made a detailed stability analysis of Eq. (1) with  $\beta=0$  and with periodic boundary conditions corresponding to an annular geometry junction. Their results also reveal stability of the fluxon when  $\gamma < 1$ . The same result is found in Refs. 15 and 16 for a fluxon in an interval extending from  $-\infty$  to  $+\infty$ . However, the stability analyses in Refs. 14 and 17 are valid only when the  $\beta$  losses are absent. We shall show in the following that the effect of the  $\beta$  losses is to decrease the critical value of  $\gamma$  for which a stable fluxon motion can occur.

The presence of the perturbative terms in Eq. (1) introduces a modification of the fluxon line shape from the sine-Gordon one.<sup>4</sup> The modification becomes more pronounced for increasing bias values. In Fig. 2 the numerical results for the  $x$  derivative of the fluxon line shape are shown. The parameters are:  $\alpha=0.05$ ,  $\beta=0.02$ ,  $l=8$ ,  $\gamma=0.75$  (solid curve), and  $\gamma=0.8$  (dashed curve). The main difference from the sine-Gordon form of the fluxon line shape in Fig. 2 is the presence of an overshoot at the trailing edge of the fluxon. The overshoot is present when the surface impedance term  $\beta$  is not negligible and is more pronounced at high bias. In the following we will show that it is just the presence of the  $\beta$  term in Eq. (1)

that limits the maximum bias current that sustains the fluxon motion in annular junctions.

In order to determine the critical current values for the switching, the following numerical procedure has been followed. At the beginning, Eq. (12) is used as initial condition with a value of  $\gamma$  relatively small (in order to be in a stable region). After some time of integration,  $\gamma$  is increased slowly (with a time derivative  $< 10^{-3}$ ) to a new value. Then Eq. (1) is integrated for time (typically 50 units) at constant  $\gamma$  to allow a stabilization of the solution. The whole procedure is repeated again until a switching is observed. The measure of the mode phase velocities is used to check that the fluxon has assumed a stable profile. In Fig. 3 is shown the stabilization process in terms of the time evolution of the speed of the first four modes. As is clearly shown, all the modes tend rapidly to have the same speed, indicating that the fluxon has assumed a constant profile. When the critical value  $\gamma_{cr}$  is reached, the stabilization of the modes speed does not take place and a switching is observed.

In Figs. 4(a)-4(g) a detailed time sequence of the switching is shown. The parameters are, in this case,  $\alpha=0.18$ ,  $\beta=0.1$ ,  $l=32$ , and  $0.89 \leq \gamma \leq 0.9$ . All the plots are referred to a reference frame moving with the fluxon. The switching can be described in the following way: First the overshoot at the trailing edge of the fluxon starts to grow in size and decreases its speed [Figs. 4(a)-4(b)]; when the overshoot is large enough, it breaks in a fluxon-antifluxon pair, Fig. 4(b) (in this plot a fluxon is represented by a positive pulse and an antifluxon by a negative one); the new fluxon starts to move forward and bunches with the original one, while the new antifluxon starts to move backward, driven by the current bias [Fig. 4(c)]; the process of nucleation of fluxon-antifluxon pairs continues adding new fluxons and antifluxons [Fig. 4(d)]; when the group of fluxons meets the group of antifluxons which has traveled all the way around the junction, a multiple collision occurs [Figs. 4(e) and 4(f)]. These finding were briefly reported in Ref. 17. As a result a net energy loss occurs in each fluxon (or antifluxon) to such an extent that they are not able to survive the next collision and form breatherlike structures; these structures do not gain energy from the bias and relax down to the flat configuration:  $\phi_x = 2\pi/l$ ,  $\phi_y \gg 1$  [Fig. 4(g)]. The final state obtained (a uniform phase twist increasing quickly in time) corresponds to the McCumber curve for the annular junction.

The mechanism for the switching just described suggests that the presence of the overshoot in the fluxon line shape plays a vital role for the triggering of the switching. The qualitative behavior of the overshoot can be understood by studying the traveling wave reduction of Eq. (1). With the following change of variables

$$\xi = x + ut, \quad (14)$$

Eq. (1) reduces to

$$(1-u^2)\phi_{xx} - \sin\phi = au\phi_x - \beta u\phi_{x\bar{x}} - \gamma. \quad (15)$$

This ODE has a three-dimensional phase space with fixed points

$$\phi_x = \sin^{-1}\gamma \pm 2j\pi, \quad \phi_{\bar{x}}, \phi_{x\bar{x}} = 0, \quad (16a)$$

$$\phi_x = \pi - \sin^{-1}\gamma \pm 2k\pi, \quad \phi_{\bar{x}}, \phi_{x\bar{x}} = 0, \quad (16b)$$

The single fluxon solution of Eq. (1) corresponds to a curve connecting the points  $\phi_x$  and  $\phi_{x+1}$ , as is shown in Fig. 5. Since the overshoot occurs near the  $\phi_x$  point, a linearization of Eq. (15) around this fixed point can provide useful information on the character of the oscillations forming the overshoot. Linearizing Eq. (15) around  $\phi_x$  gives

$$(1-u^2)y_{xx} - (1-\gamma^2)^{1/2}y = auy_x - \beta uy_{x\bar{x}}, \quad (17)$$

where  $\|y\| \ll 1$ . This equation has a general solution of the form

$$y = Ae^{\lambda_1 x} + Be^{\lambda_2 x} + Ce^{\lambda_3 x}, \quad (18)$$

where  $A$ ,  $B$ , and  $C$  are integration constants and  $\lambda_1$ ,  $\lambda_2$ , and  $\lambda_3$  are the roots of the characteristic polynomial:

$$P(\lambda) = -\lambda^3 - \frac{1-u^2}{\beta u}\lambda^2 + \frac{\alpha}{\beta}\lambda + \frac{(1-\gamma^2)^{1/2}}{\beta u}. \quad (19)$$

Because of its structure,  $P(\lambda)$  has always a positive real root and can have either two negative real roots or two complex conjugate roots with negative real part. This implies that the fixed points are either saddle points or saddle foci, as described by Hayashi.<sup>18</sup> Eq. (19) can be solved by standard methods, obtaining a fairly complicated expression for  $\lambda_1$ ,  $\lambda_2$ , and  $\lambda_3$ . It should be noted, however, that the solution of Eq. (19) has the speed  $u$  as an independent parameter, while  $u$  is in reality a function of the other parameters  $\alpha$ ,  $\beta$ , and  $\gamma$ . Since the exact relation for  $u$  is not known, only approximate results can be then obtained by this linear analysis. Assuming, for high bias,  $u = 1$ , it is easy to compute that in order to have complex roots, the bias must satisfy the following condition:

$$\gamma < \left[ 1 - \frac{4}{27} \frac{\alpha^3}{\beta} \right]^{1/2}. \quad (20)$$

Since, for reasonable values of  $\alpha$  and  $\beta$ , the right-hand side of Eq. (20) is always very close to one, this condition states that the oscillating overshoot, associated with the complex roots of Eq. (19), is always present. In the same

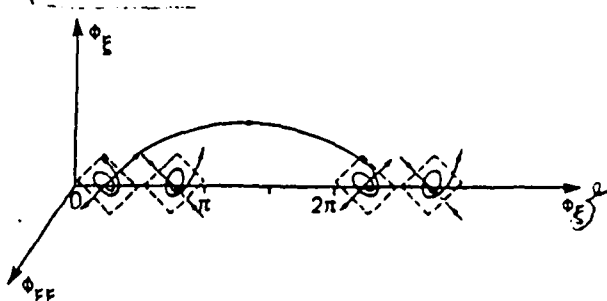


FIG. 5. Sketch of the phase space for Eq. (15). The fluxon solution connecting  $\phi_x$  to  $\phi_{x+1}$  is shown.

way it is possible to compute the period  $T$  and the decay rate  $\mu$  of the overshoot oscillations as<sup>4</sup>

$$T = \frac{\pi}{\sqrt{3}} \frac{\beta^{1/3}}{(1-\gamma^2)^{1/6}}, \quad (21)$$

$$\mu = -\frac{(1-\gamma^2)^{1/6}}{\beta^{1/3}}, \quad (22)$$

where terms of the order of  $\alpha/\beta$  have been neglected. The result from Eqs. (21) and (22) has been checked with the numerical results, finding good agreement. However, because of the limitation mentioned above, this phase-space analysis cannot predict the critical bias current value at which the fluxon solution becomes unstable. A qualitative explanation of the switching is nevertheless possible. Perhaps a careful global analysis of the ODE, Eq. (15), may lead to a quantitative description of the onset of the switching.

#### IV. OVERLAP GEOMETRY

In this section a study of the mechanism for the switching in junctions of overlap geometry is presented. Overlap geometry Josephson junctions with normalized lengths  $l \gg 1$  and without external magnetic field applied, i.e.,  $\eta = 0$ , are considered. In Fig. 6 an experimental current-voltage characteristic is shown, with six ZFS's. The first zero-field step (ZFS1) results from the oscillation of one fluxon; the next step (ZFS2) corresponds to two oscillating fluxons, etc. For all steps, at sufficiently high bias current, the fluxon oscillations become unstable and a switch to the McCumber curve occurs. The switching is indicated by the arrows in Fig. 6. Figure 7 depicts the phase  $\phi(x, t)$  of one fluxon performing a stable oscillation back and forth at  $\gamma = 0.5$ , as obtained from Eq. (1) solved numerically. The parameter values used are  $\alpha = 0.05$ ,  $\beta = 0.02$ , and  $l = 8$ . An overshoot behind the fluxon is clearly visible. Increasing  $\gamma$  to 0.7 the fluxon becomes unstable and a fast spatially uniform rotation emerges after a short transient. In Fig. 8 this transient motion is shown in more detail for a junction of length  $l = 12$  and with  $\gamma = 0.74$  using otherwise the same parameter values as in Fig. 7. Figure 8 displays

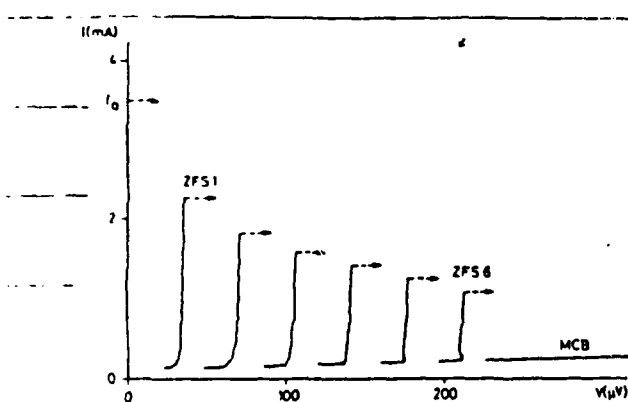


FIG. 6. Experimental  $I$ - $V$  characteristics of a long Josephson junction of overlap geometry. Six ZFS's are shown.

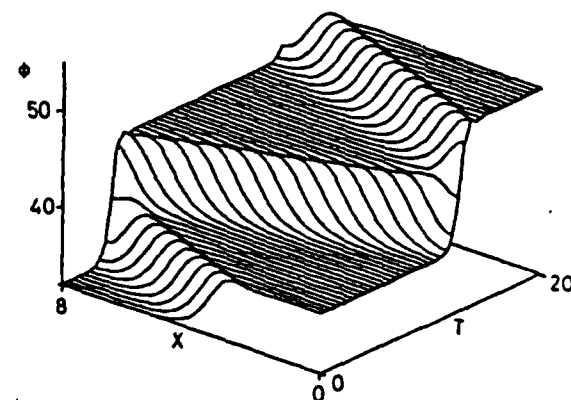


FIG. 7. Stable fluxon oscillations corresponding to ZFS1 in an overlap junction.

the phase at successive times  $t$  during the switching starting at the arbitrarily chosen reference time  $t=0$ . At  $\gamma=0.73$  the fluxon oscillation is stable. Increasing  $\gamma$  to the value 0.74 the fluxon becomes unstable and after a couple of oscillations the fluxon hits the right-hand boundary ( $t=12$ ) at time  $t \sim 6$  and during this reflection it becomes unstable. Immediately after the reflection the phase has increased by  $4\pi$  but is now unstable and it continues increasing after the time  $t \sim 14$  leading to the formation of additional fluxons which travel from the right-

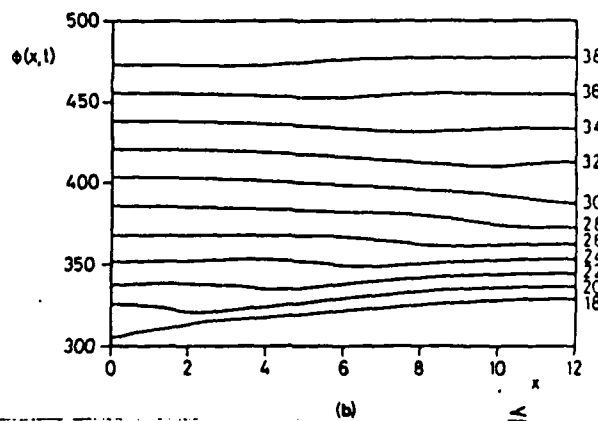
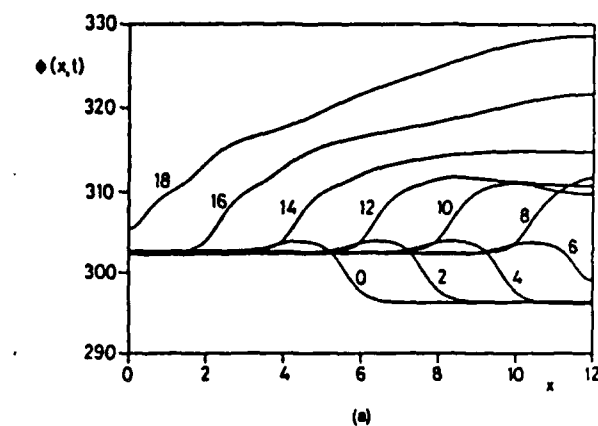


FIG. 8. Time sequence of the switching. (a) 0  $\leq$   $t$   $\leq$  18. (b) 18  $\leq$   $t$   $\leq$  38.

hand boundary towards the left-hand boundary. At time  $t=18$  these fluxons are reflected from the left-hand boundary and annihilate the incoming ones. Eventually the phase develops into the spatially uniform rotating solution as can be seen from Fig. 8(b). From Fig. 8 it is evident that the fluxon is destabilized at one of the boundaries during a reflection and thereby triggers the formation of successive fluxons which unwind during the next reflection at the opposite boundary. The same finding has been reported by Cirillo *et al.*<sup>19</sup> from a study of the mechanical analog of the long Josephson junction.

The switching can be illustrated also in terms of energy. The sine-Gordon energy<sup>3</sup> of the junction is

$$H_T = \int_0^l [\frac{1}{2}(\phi_x)^2 + \frac{1}{2}(\phi_t)^2 + 1 - \cos\phi] dx . \quad (23)$$

In terms of the pendula model, the first term in Eq. (23) is the elastic energy arising from the elastic coupling between the pendula, the second term is the kinetic energy, and finally the term in  $(1 - \cos\phi)$  is the potential energy measured from the static downward equilibrium state. In the case where the dissipation and the external bias are absent, Eq. (1) reduces to the pure sine-Gordon equation which can be written as a Hamiltonian system with the Hamiltonian given by Eq. (23). When the perturbative terms are present,  $H_T$  is merely the total energy of the system. By differentiating Eq. (23) with respect to the

time  $t$  and using Eq. (1) together with the boundary conditions, Eq. (5), it is easy to obtain

$$\frac{dH_T}{dt} = P_y + P_\alpha + P_\beta + \eta[\phi_x(l,t) - \phi_x(0,t)] , \quad (24)$$

where the power input and output have been defined according to

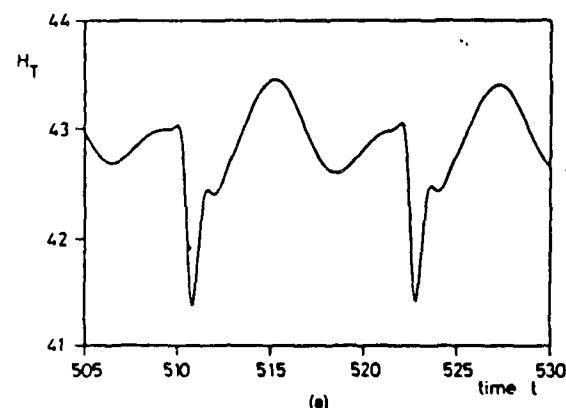
$$P_y = + \int_0^l \gamma \phi_t dx , \quad (25a)$$

$$P_\alpha = - \int_0^l \alpha(\phi_x)^2 dx , \quad (25b)$$

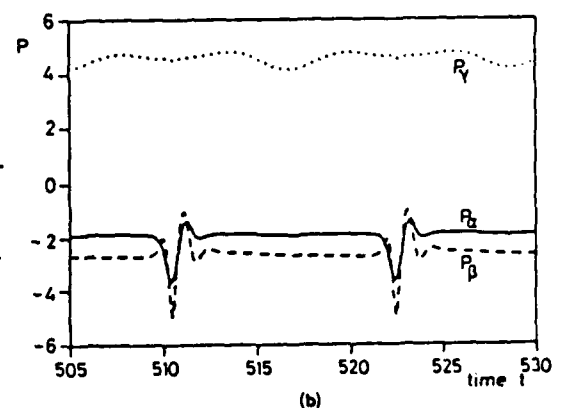
$$P_\beta = - \int_0^l \beta(\phi_{xt})^2 dx . \quad (25c)$$

Note that the terms  $P_\alpha$  and  $P_\beta$  extract energy from fluxons or antifluxons whereas the term  $P_y$  is an energy-injection term which accelerates fluxons and antifluxons in opposite directions.

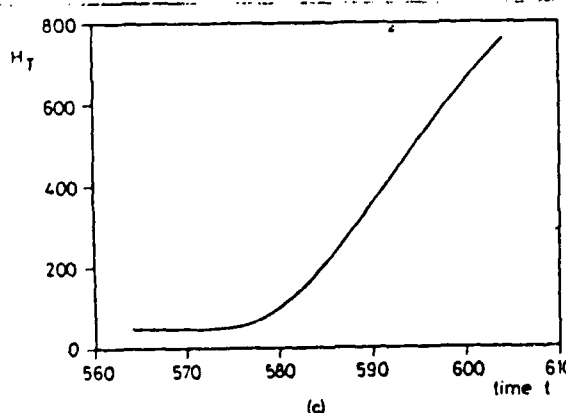
Figure 9 shows the time evolution of the total energy and the power input and output terms in Eq. (25). Using the parameter values  $\alpha = 0.05$ ,  $\beta = 0.02$ , and  $l = 12$ , Figs. 9(a) and 9(b) depict the total energy and powers in the case of a stable fluxon oscillation at  $\gamma = 0.73$  just below the critical bias current  $\gamma_{sw}$ . Over one period of oscillation the total energy remains constant and the power input balances the power output. During a reflection at one of the boundaries a fast  $4\pi$  change occurs in the phase  $\phi$



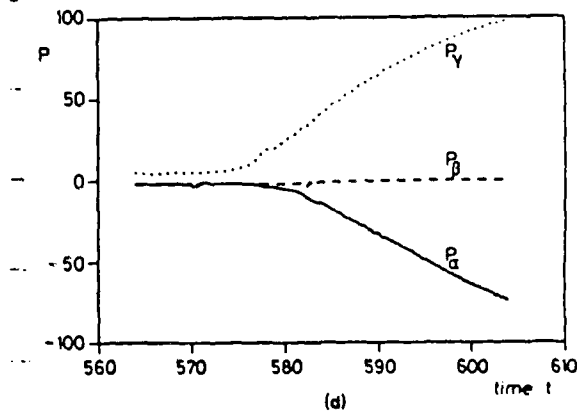
(a)



(b)



(c)



(d)

FIG. 9. Time evolution of (a) the total energy  $H_T$ , and (b) the powers  $P_y$ ,  $P_\alpha$ , and  $P_\beta$  during the stable motion on ZFS1. Time evolution of (c) the total energy  $H_T$ , and (d) the powers  $P_y$ ,  $P_\alpha$ , and  $P_\beta$  during the switching from ZFS1.

and the dissipation from both terms in  $\alpha$  and  $\beta$  increases. This results in a pronounced dip in the total energy during a reflection. It is important to note that this energy loss at the boundaries is purely dissipative and is not a result of radiation from the junction end. Such radiation is not accounted for in this model. In Figs. 9(c) and 9(d)  $\gamma$  has been increased to the value 0.74 where switching occurs (see also Fig. 8). During the switching the total energy significantly increases, as does the loss due to the  $\alpha$  term. Eventually the system approaches the spatially uniform McCumber state and accordingly the loss due to the  $\beta$  term vanishes. When equilibrium has been reached on the McCumber solution the averaged total energy will again be constant and over one period of oscillation  $P_y$  will balance  $P_a$ . This equilibrium state is not shown in Figs. 9(c) and 9(d).

## V. STABILITY ANALYSIS BY BOUNDARY MODEL

In this section a boundary-based model is introduced to explain the switching from the ZFS's to the McCumber curve in the overlap geometry Josephson junctions. The phenomenon of the switching in overlap junctions appears to be related to some instability that takes place at the junction boundary. This was first pointed out by Cirillo *et al.*<sup>19,20</sup> from observations on the mechanical analog of a Josephson junction. The same idea can be deduced by a careful analysis of Figs. 7 and 8. In fact in Fig. 8(a) it can be seen that the reflection of the fluxon that occurs at  $t \sim 6$  does not leave the boundary in a static phase configuration ( $\phi = \sin^{-1}\gamma + 2m\pi$ ) as occurs when stable fluxon oscillations are observed (Fig. 7). A way to analyze this phenomenon can be to study the dynamics of the phase at the junction boundary (say at  $x=0$ ). In terms of the chain of pendula analog of the PSGE this corresponds to studying the dynamics of a single pendulum, namely the last of the chain, under the fluxon-antifluxon collision that describes the process of reflection of a fluxon at the junction boundary. Following this idea one can rewrite Eq. (1) as

$$\phi_{xx} + \alpha\phi_{xx} + \sin\phi = \gamma + \phi_{xx} + \beta\phi_{xx}. \quad (26)$$

This equation can be viewed as the equation of a single pendulum [the left-hand side of Eq. (26)] driven by an effective force [the right-hand side of Eq. (26)]. This effective force is made of the external bias  $\gamma$  and the coupling to other pendula of the chain ( $\phi_{xx} + \beta\phi_{xx}$ ). The problem here is that the effective force is not known, being dependent on the solution  $\phi$  of the same equation. A reasonable approximation may, however, be given by the analytic expression for the fluxon-antifluxon collision solution of the sine-Gordon equation, which can be rewritten in a form that takes into account the perturbative terms in Eq. (26)<sup>4</sup> as

$$\phi^0 = \sin^{-1}\gamma + 4 \tan^{-1} \left[ \frac{1}{u} \sinh \left( \frac{ut}{\Gamma} \right) \operatorname{sech} \left( \frac{x}{\Gamma} \right) \right], \quad (27)$$

where  $\Gamma$  is the corrected Lorentz factor introduced in Eq. (12) as

$$\Gamma = \frac{(1-u^2)^{1/2}}{(1-\gamma^2)^{1/4}} \quad (28)$$

and the velocity  $u$  may be determined by the single fluxon power-balance expression of Eq. (13). Thus Eq. (26) becomes

$$\phi_{xx} + \alpha\phi_{xx} + \sin\phi = \gamma + \phi_{xx}^0(x=0) + \beta\phi_{xx}^0(x=0), \quad (29)$$

where

$$\phi_{xx}^0(x=0, t) = \frac{-4u\Gamma^{-1}\sinh(u\Gamma^{-1}t)}{u^2 + \sinh^2(u\Gamma^{-1}t)} \quad (30)$$

and

$$\begin{aligned} \phi_{xx}^0(x=0, t) \\ = \frac{-4u^2\Gamma^{-3}\cosh(u\Gamma^{-1}t)[u^2\sinh^2(u\Gamma^{-1}t)]}{[u^2 + \sinh^2(u\Gamma^{-1}t)]^2} \end{aligned} \quad (31)$$

Equation (29) has a static solution  $\phi = \sin^{-1}\gamma$  as  $t \rightarrow \infty$  corresponding to the configuration of the  $x=0$  pendulum in the mechanical model when the fluxon is still far away. When the incoming fluxon reaches the  $x=0$  point ( $t \rightarrow 0$ ) the right-hand side of Eq. (29) changes very fast leading to a  $4\pi$  increase of the phase. After the fluxon is reflected ( $t \rightarrow +\infty$ ), the phase can either relax to the new equilibrium state  $\phi = \sin^{-1}\gamma + 4\pi$  or go to the rotating state corresponding to the McCumber solution of the simple pendulum. The first case will correspond to a "normal" reflection and to the stable dynamical state of the ZFS's, while the second case will correspond to the switching to the McCumber branch is shown in Figs. 8 and 9. The value of the bias  $\gamma$  that corresponds to the transition from the first case to the second one will then be the one that determines the switching from the ZFS's to the McCumber branch. In Fig. 10 the time evolution is shown of  $\phi$  and of  $\phi_x$  for different  $\gamma$  values (curves 1-5) obtained by a numerical integration of Eq. (29). It can

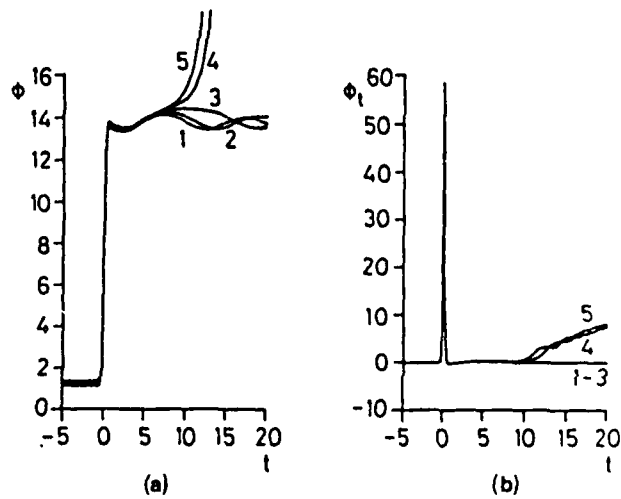


FIG. 10. Time evolution of  $\phi$  (left) and  $\phi_x$  (right) for the boundary model. The curves labeled 1-5 correspond to bias values from 0.90 to 0.98 in steps of 0.02. The switching occurs at  $\gamma = 0.95 \pm 0.01$ ,  $\alpha = 0.05$ ,  $\beta = 0.02$ , and  $l = \infty$ .

clearly be seen that curve 3 (corresponding to  $\gamma=0.94$ ) is the last stable state and a further increase of  $\gamma$  leads to the switching.

## VI. RESULTS AND DISCUSSIONS

Our results are summarized in Fig. 11. Figure 11(a), curve *a*, shows the length dependence of the critical switching value of  $\gamma$  for overlap junctions with  $\alpha=0.05$  and  $\beta=0.02$ . Curve *b* is the  $l \rightarrow \infty$  limit for the switching value in annular junctions having the same loss parameters. As can be seen, the critical  $\gamma$  for overlap junctions tends asymptotically to a value lower than that for annular junctions. In passing, we note that curve *a* is quite similar in form to, but slightly higher in current than, the curve shown in Fig. 2 of Ref. 7 (nominally the same problem). In this connection, we comment that the value of  $\gamma_{sw}$  obtained depends rather sensitively on how  $\gamma$  is increased during the computations: the more "adiabatic" the increase, the more accurate the value of  $\gamma_{sw}$ .

Figure 11(b) shows the  $\alpha$  dependence, for  $\beta=0.02$  and  $l=12$ , for overlap junctions (curve *a*), annular junctions (curve *b*), and for the boundary model (curve *c*). Once again, it is apparent that overlap junctions switch at lower current values than do annular junctions. And

once again, our curve *a* is quite similar to that shown in Fig. 4 of Ref. 7.

Figure 11(c) shows the  $\beta$  dependence, for  $\alpha=0.05$  and  $l=12$ , of  $\gamma_{sw}$  for the same three cases as before. As before, curve *a* lies below curve *b*. Comparing our curve *a*, however, with the curve shown in Fig. 5 of Ref. 7, a significant difference is apparent: our result indicates that  $\gamma_{sw}$  tends smoothly to 1 as  $\beta \rightarrow 0$ , whereas Zhang and Wu's curve bends over and terminates near  $\gamma \approx 0.7$ . In this connection, we comment that the implicit finite difference routine of Ref. 12, used also by Zhang and Wu, was developed specifically to integrate Eq. (1) with  $\beta \neq 0$ . In fact, for  $\beta=0$ , Eq. (1) is a second- rather than third-order equation, and much more efficient explicit algorithms are available.<sup>21</sup> Our experience indicates that for  $\beta \rightarrow 0$  this implicit algorithm must be used with great care. Even though condition (10) is satisfied, unless very small spatial and temporal increments,  $\Delta x$  and  $\Delta t$ , are used, the algorithm tends to generate spurious oscillations which can completely falsify results.

As is apparent from Figs. 11(b) and 11(c), the boundary model, curve *c*, gives a good qualitative description of the  $\alpha$  and  $\beta$  dependences of the computed  $\gamma_{sw}$  values, curves *a*. The essential difference is an almost constant shift of about 0.15 in  $\gamma$ . This remarkable result strengthens the

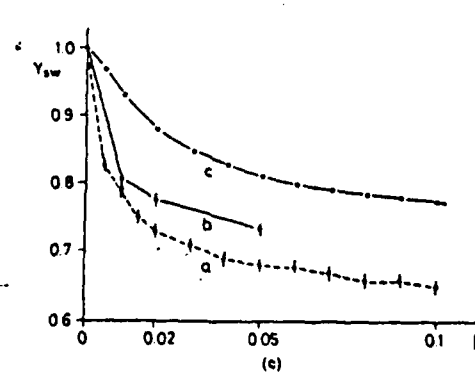
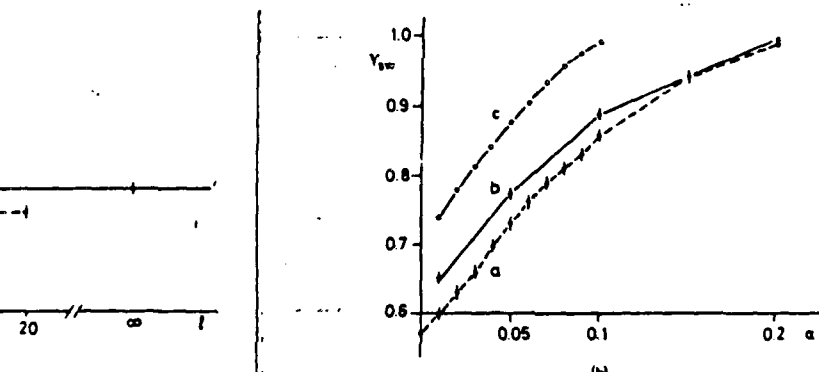
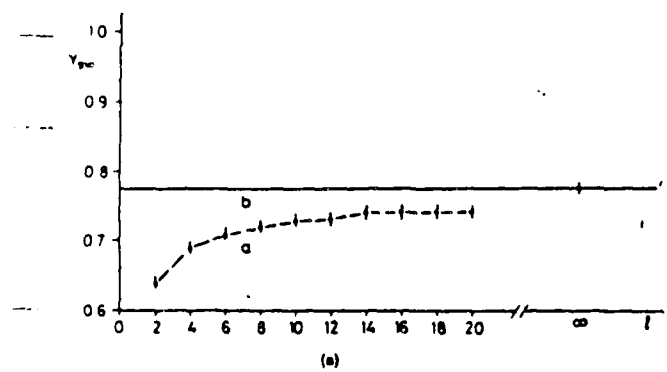


FIG. 11. (a) Dependence of the critical bias on the junction length. *a* overlap geometry. *b* annular geometry ( $l \rightarrow \infty$ ).  $\alpha=0.05$  and  $\beta=0.02$ . (b) Dependence of the critical bias on  $\alpha$ . *a* overlap geometry. *b* annular geometry. *c* boundary model.  $\beta=0.02$  and  $l=12$ . (c) Dependence of the critical bias on  $\beta$ . *a* overlap geometry ( $l=12$ ). *b* annular geometry. *c* boundary model.  $\alpha=0.05$  and  $l=12$ .

idea suggested by the numerical simulations that in long junctions of overlap geometry the switching phenomenon is connected to an instability that is generated at the boundaries after the fluxon-antifluxon reflection. The almost constant shift between the results of the simple model Eq. (29) and the ones from the complete model Eq. (26) is fully due to the choice (27) for  $\phi^0$ . In fact, as has been shown in the preceding sections, the sine-Gordon solutions are not anymore a good approximation to the solution of Eq. (26) at high bias values. Indeed, using in Eq. (29) a numerical solution of Eq. (26) for  $\phi$  computed in a stable state close to the switching ( $\alpha=0.05$ ,  $\beta=0.02$ ,  $\gamma=0.7$ ,  $l=12$ ) the correct switching value for  $\gamma$  is computed ( $\gamma_{sw}=0.72$ ).

## VII. CONCLUSIONS

In this paper we have addressed the problem of the stability of the fluxon motion at high bias values. Two different geometrical configurations have been considered. For the junctions of annular geometry the instability in the fluxon motion arises from the disappearance of the asymptotic static states for  $\gamma \approx 1$ , in the case  $\beta \ll l$ , or, for  $\beta$  that are not small, from the nucleation of fluxon-antifluxon pairs. In the latter case the critical bias value is smaller than one and tends to decrease with increasing  $\beta$  [Fig. 11(c)].

An analysis of the third-order ordinary differential equation (ODE) governing the traveling fluxons in the junction is able to describe qualitatively the deformation of the fluxon profile due to  $\beta$  losses that are not small, but it cannot predict the critical bias value at which the

fluxon solution becomes unstable.

In the overlap geometry junction the disappearing of the fluxon oscillations is due to an instability that is originated at the junction boundaries after a fluxon-antifluxon reflection. This instability causes a switching to the McCumber curve for bias values lower than the ones required in the annular geometry case. However, the dependence of  $\gamma_{sw}$  on the parameters  $\alpha$  and  $\beta$  is similar for the two geometries. The dependence of  $\gamma_{sw}$  on the junction length shows a saturation for  $l \geq 10$ , to a value smaller than the corresponding one in the annular junction case [Fig. 11(a)].

A simple model, based on the simulation of a fluxon-antifluxon reflection, is able to reproduce qualitatively the numerical results. An analysis based on the Floquet theory supports the idea that the switching is due to a parametric excitation of the Fourier components of the phase.<sup>22</sup> However, since all the components are involved in the process, it is not possible to obtain analytical expressions for the critical bias values.

## ACKNOWLEDGMENTS

We thank M. Salerno for helpful discussions about the boundary model analysis. The financial support from the European Economic Community through Contract No St-2-0267-J-C(A), from the European Research Office of the United States Army through Contract No. DAJA-45-85-C-0042, the Thomas B. Thriges Fond (Denmark), and the Gruppo Nazionale di Struttura della Materia, Consiglio Nazionale delle Ricerche Centro Interuniversitario di Struttura della Materia, Ministero della Pubblica Istruzione (Italy) is gratefully acknowledged.

<sup>11</sup>Permanent address: Istituto di Cibernetica del Consiglio Nazionale delle Ricerche, via Toiano 6, I-80072 Arco Felice, Italy.

<sup>12</sup>Permanent address: Dipartimento di Fisica, Università degli Studi di Salerno, I-84100 Salerno, Italy.

<sup>13</sup>A. Barone and G. Paternó, *Physics and Applications of the Josephson Effect* (Wiley, New York, 1982).

<sup>14</sup>T. A. Fulton and R. C. Dynes, Solid State Commun. **12**, 57 (1973).

<sup>15</sup>D. W. McLaughlin and A. C. Scott, Phys. Rev. A **18**, 1652 (1978).

<sup>16</sup>S. Pagano, N. F. Pedersen, S. Sakai, and A. Davidson, IEEE Trans. Magn. **Magn.** **23**, 1114 (1987).

<sup>17</sup>A. Ferrigno and S. Pace, Phys. Lett. **112A**, 77 (1985).

<sup>18</sup>A. Davidson, B. Dueholm, B. Kryger, and N. F. Pedersen, Phys. Rev. Lett. **55**, 2059 (1985).

<sup>19</sup>Y. M. Zhang and P. H. Wu, *Extended Abstracts of the 1987 International Superconductivity Electronics Conference*, Tokyo, Japan, 1987 (unpublished), p. 115.

<sup>20</sup>V. M. Vinokur, J. Phys. (Paris) **47**, 1425 (1987).

<sup>21</sup>S. Pagano, M. P. Soerensen, R. D. Parmentier, P. L. Christiansen, O. Skovgaard, J. Mygind, N. F. Pedersen, and M. R. Samuelsen, Phys. Rev. B **33**, 174 (1986).

<sup>22</sup>DGEAR routine, IMSL Inc., International Mathematical and Statistical Library (ed. 5), Houston, Texas, 1982.

<sup>11</sup>FFT2C routine, IMSL Inc., International Mathematical and Statistical Library (ed. 9), Houston, Texas, 1982.

<sup>12</sup>P. S. Lomdahl, O. H. Soerensen, and P. L. Christiansen, Phys. Rev. B **25**, 5737 (1982); see also, P. S. Lomdahl, Ph.D. thesis, DCAMM, Denmark, 1982 (unpublished). A

<sup>13</sup>M. Büttiker and H. Thomas, Phys. Lett. **77A**, 372 (1980); Phys. Rev. A **37**, 235 (1988).

<sup>14</sup>S. E. Burkov and A. E. Lifsch, Wave Motion **5**, 197 (1983).

<sup>15</sup>M. Büttiker and R. Landauer, Phys. Rev. A **23**, 1397 (1981).

<sup>16</sup>K. K. Likarev, *Dynamics of Josephson Junctions and Circuits* (Gordon and Breach, New York, 1986).

<sup>17</sup>A. Davidson, N. F. Pedersen, and S. Pagano, Appl. Phys. Lett. **48**, 1306 (1986).

<sup>18</sup>C. Hayashi, *Nonlinear Oscillations in Physical Systems* (McGraw-Hill, New York, 1964), p. 45.

<sup>19</sup>M. Cirillo, S. Pace, and B. Savo, in *Proceedings of the 17th International Conference on Low Temperature Physics*, (LT-17), edited by U. Eckern, A. Schmid, W. Weber, and H. Wühl (Elsevier, Amsterdam, 1984), Vol. I, p. 703.

<sup>20</sup>M. Cirillo, R. D. Parmentier, and B. Savo, Physica **3D**, 565 (1981).

<sup>21</sup>R. K. Dodd, J. C. Eilbeck, J. D. Gibbon, and H. C. Morris, *Solitons and Nonlinear Wave Equations* (Academic, London, 1982), Chap. 10.

<sup>22</sup>M. P. Soerensen (unpublished). ←

RC 13744 (#61576) 5/13/88  
Physics 24 pages

# Research Report

## Crises in a Driven Josephson Junction Studied by Cell Mapping

M. P. Soerensen

Laboratory of Applied Mathematical Physics  
The Technical University of Denmark  
DK 2800 Lyngby, Denmark

A. Davidson

IBM Research Division  
T. J. Watson Research Center  
Yorktown Heights, N.Y. 10598

N. F. Pedersen

Physics Laboratory I  
The Technical University of Denmark  
DK 2800 Lyngby, Denmark

S. Pagano

Laboratory of Applied Mathematical Physics  
The Technical University of Denmark  
DK 2800 Lyngby, Denmark

**LIMITED DISTRIBUTION NOTICE:** This report has been submitted for publication outside of IBM and will probably be copyrighted if accepted for publication. It has been issued as a Research Report for early dissemination of its contents and will be distributed outside of IBM up to one year after the IBM publication date. In view of the transfer of copyright to the outside publisher, its distribution outside of IBM prior to publication should be limited to peer communications and specific requests. After outside publication, requests should be filled only by reprints or legally obtained copies of the article (e.g., payment of royalties).

**IBM** Research Division  
Almaden • Yorktown • Zurich

# Crises in a Driven Josephson Junction Studied by Cell Mapping

M.P. Sørensen<sup>a</sup>, A. Davidson<sup>b</sup>, N.F. Pedersen<sup>c</sup>, and S. Pagano<sup>a</sup>

<sup>a</sup> Laboratory of Applied Mathematical Physics  
The Technical University of Denmark  
DK 2800 Lyngby, Denmark

<sup>b</sup> IBM Research Division  
T.J. Watson Research Center  
Yorktown Heights, NY 10598, U.S.A.

<sup>c</sup> Physics Laboratory I  
The Technical University of Denmark  
DK 2800 Lyngby, Denmark

## Abstract

We use the method of cell-to-cell mapping to locate attractors, basins, and saddle nodes in the phase plane of a driven Josephson junction. The cell mapping method is discussed in some detail, emphasizing its ability to provide a global view of the phase plane. Our computations confirm the existence of a previously reported interior crisis. In addition we observe a boundary crisis for a small shift in one parameter. The cell mapping method allows us to show both crises explicitly in the phase plane, at low computational cost.

## 1. Introduction.

Strange attractors of a periodically driven Josephson Junction are studied numerically by means of simple cell mapping<sup>1</sup>. We focus here on the sudden changes of strange attractors, which may occur when some parameter values are altered. These changes are called crises<sup>2-5</sup>. Two different types of crises are discussed, namely the boundary crisis and the interior crisis.

Following the notation of Grebogi<sup>2,3</sup> et al. we call the collision of a stable chaotic attractor with an unstable periodic orbit at a basin boundary, a boundary crisis. Boundary crises result in the sudden annihilation of the chaotic attractor. In contrast, an interior crisis arises from a similar collision of attractors from within a single basin. In this case the chaotic attractor has a sudden expansion in phase space.

We have chosen to study the driven Josephson junction for a range of parameters already studied by Kautz<sup>5,6</sup>. Kautz has found two crises, one at each end of the parameter range, and he has identified one as an interior crises. We confirm this result, and show that the other crisis is a boundary crisis.

To study numerically the global behavior of the Josephson junction it is advantageous to use cell mapping methods<sup>1,7-10</sup>. We shall use only the simple cell mapping algorithm where the 2-dimensional phase space is divided into rectangles or cells and the governing dynamical equation defines a way to map each cell onto another in the phase plane. A more elaborate cell mapping method is the generalized cell mapping procedure<sup>8</sup>. Here it is allowed for a mapping of a cell to have multiple image cells with appropriate individual mapping probabilities. In Ref. 9 the two above cell mapping methods are combined into "compatible simple" and "generalized" cell mapping.

The organization of this paper is as follows. Section II briefly introduces the dynamical equation of the system under study, including parameter values. Then the concepts of the

cell mapping method are developed, and some of its limitations are pointed out. Section III presents the computed current-voltage (I-V) curve for the parameters of interest, along with a 1 dimensional Poincare map. These were the tools used by Kautz in his investigation, and we repeat them here both as confirmation of his work, and to provide benchmarks for our cell mapping study. Section IV uses cell mapping and Poincare sections to identify parameters for which a boundary crisis occurs, and to locate in phase space the relevant attractors. Section V extends cell mapping to compute basins of attraction, and manifold crossings. Both the new boundary crisis identified in Section IV and Kautz's interior crises are studied.

## II. Model Equation and Numerical Method.

The equation describing the dynamics of a driven Josephson junction is given by<sup>11</sup>

$$\ddot{\phi} + \alpha\dot{\phi} + \sin\phi = \eta + A \sin(\omega t) . \quad (1)$$

Here overdots denote derivatives with respect to time  $t$ .  $\phi = \phi(t)$  is the phase difference across the junction,  $\alpha$  is the quasi particle damping term, given by  $\alpha = 1/\sqrt{\beta}$ , where  $\beta$  is the McCumber parameter<sup>11</sup>, and  $\eta$  is the constant dc bias current.  $A$  and  $\omega$  denote the amplitude and frequency of the external driving force, respectively. Only the  $\eta$ -term has been varied and the other parameters have been fixed at the values:  $\alpha = 0.2$ ,  $A = 10.198039$  (for comparison with ref. 5), and  $\omega = 1.0$ . The dynamical equation (1) is solved numerically using a fourth-order Runge-Kutta algorithm. The solution may be displayed in the phase plane as a Poincare section where points  $(\phi(t), \dot{\phi}(t))$  are plotted after every period  $T = 2\pi/\omega$  of the drive cycle. Here  $\phi(t)$  is treated modulo  $2\pi$ , from  $-\pi$  to  $\pi$ . The Poincare map gives a good geometrical view of the dynamics by which we can identify the different attractors. To study the global behavior of the system, the basins of attraction of the different attractors must be found. To do this by solving Eq.1 numerically with initial conditions distributed uniformly

over a finite subset of the phase plane is a very time consuming procedure. A more efficient way of getting the basins of attraction is to use the cell mapping method<sup>1,7-10</sup>.

In the cell mapping method we divide an interesting subset of the phase plane into cells. Let us for simplicity introduce the notation  $\phi = x_1$  and  $\dot{\phi} = x_2$ . A finite rectangular subset of the 2-dimensional phase space of Eq. 1 is then divided into  $N$  rectangular cells. We shall use uniform cells of width  $b_1$  and height  $b_2$ . If  $N_1$  denotes the number of cells in the  $x_1$ -direction, and  $L_1$  denotes the length of the subset in the  $x_1$ -direction, then  $b_1 = L_1/N_1$ . Similarly, we have for the  $x_2$  direction that  $b_2 = L_2/N_2$ . The cells are counted sequentially beginning, for example, at the cell in lowest row to the left, counting along the lowest row, and ending with the cell No.  $N = N_1 N_2$  in the uppermost row to the right. The  $i$ 'th cell  $Z^i = (z_1^i, z_2^i)$ ,  $i = 1, 2, \dots, N$ , is now defined to contain all points  $(x_1, x_2)$  which satisfy

$$z_j^i - \frac{1}{2} b_j \leq x_j < z_j^i + \frac{1}{2} b_j \quad j = 1, 2. \quad (2)$$

$z_j^i$ ,  $j = 1, 2$ , are the coordinates of the center point of the  $i$ 'th cell. To get a cell to cell mapping we integrate Eq. 1 over one period  $T$  of the external driving force using the center point  $Z^i$  of the  $i$ 'th cell as initial condition. This is done for each cell  $i$ . The final state point after the integration will lie either inside an existing cell which can be identified according to Eq. 2 or outside the subset of interest. In the later case we shall introduce a sink cell, denoted  $Z^0$ , which then absorbs points escaping outside the region of interest.

By definition the sink cell is mapped into itself. To each cell including the sink cell we have now assigned an image cell and the mapping so defined is denoted  $C$ . Let  $Z(1)$  be an arbitrary initial cell. After  $n$  applications of  $C$ ,  $Z(1)$  is mapped into  $Z(n)$  and we write  $Z(n+1) = C(Z(n))$ . The evolution of the system can be periodic in the sense that a cell  $Z^i$  is mapped into itself after  $K$  applications of  $C$ . Such a motion is called  $K$  periodic or a P-K

motion. The K different cells traversed in a P-K motion form a periodic group and the cells belonging to this group are called P-K cells. The cells which eventually are mapped into this group through repeated application of C belong to the basin of attraction of this P-K group.

The evolution of the system from a given initial cell can lead to only three different outcomes. 1) The initial cell is itself a periodic cell, 2) the initial cell belongs to the basin of attraction of a P-K group, or 3) the initial cell is mapped into the sink cell. This elementary analysis forms the basis for a very efficient unravelling numerical algorithm designed by C.S. Hsu et. al. in Ref. 1. This algorithm has been used here to determine all regions of attraction and their basins of attraction for Eq. 1. in a given subset of phase space. After having made the discretization into cells and determined the cell to cell map the system dynamics have been reduced to simple sorting of integers which requires only a minimum amount of computer resources. However, the simple cell mapping procedure has to be used cautiously. The reason is that the discretization introduces errors which result in qualitative differences from the original system. The cell map may find periodic groups which correspond to unstable attractors in the continuous problem. Some periodic groups with a high period may correspond to a chaotic attractor, or several groups may represent different parts of the same attractor in the original system. These errors can be ameliorated by using finer grids or by using the refined cell mapping procedures described in Refs. (8-9), but they are inherent in the discretization of phase space used in cell mapping.

### III. Interpretation of the I-V characteristic in terms of crises.

Before applying the cell mapping procedure, we shall give an interpretation in terms of crises of the part of the I-V characteristic shown in Fig. 1. This I-V curve was obtained by numerically solving Eq. 1 and plotting the bias current  $\eta$  versus the time average  $\langle \phi \rangle$ , which is proportional to the voltage across the junction. The same I-V curve (with the same

parameters) has been published by Kautz<sup>5,6</sup> in another connection, hence a direct comparison is possible.

In Fig. 1  $\eta$  was varied from  $\eta = 1.78$  to  $\eta = 1.90$ , and the other parameters were fixed at the values stated in the previous section. We focus on the vertical line segment in Fig. 1 at the value 10 on the voltage axis. It can be shown that along this line  $\phi$  is phase-locked to the oscillatory driving force. The question we address (and addressed by Kautz<sup>5</sup>) is, how is the phase lock destroyed at either end of this constant voltage step? Kautz was able to show that the gradual departure at the top of the step is due to an interior crisis, but he left the lower end unresolved. Note that the lower end involves a hysteresis loop, where the voltage jumps back and forth between the step and some noisy curve as the current is changed very slightly between  $\eta = 1.802$  and  $\eta = 1.822$ . The hysteresis loop implies that two attractors coexist in phase space, and suggests that a boundary crisis between these two attractors could be involved.

This is shown more clearly in Fig. 2, where we have plotted  $\dot{\phi}(nT)$  from the Poincaré section at corresponding  $\eta$ -values, where  $T = \frac{2\pi}{\omega}$  denotes the period of the external driving frequency. From Fig. 2 it is evident that a chaotic dynamic state exists in the  $\eta$ -interval  $1.78 < \eta < 1.822$  and this chaotic state causes the erratic form of the I-V characteristic.

Coexistent with the chaotic dynamic state there is a simple period one solution in the  $\eta$ -interval  $1.802 < \eta < 1.822$ . The associated piece of the I-V curve is phase locked and the voltage  $V = \langle \dot{\phi} \rangle = 10$  is strictly constant. The phase locked state is characterized by the relation  $\phi(t + nT) = \phi(t) + 2m\pi$  and accordingly the voltage across the junction becomes  $V = \langle \dot{\phi} \rangle = \frac{m}{n} \times \frac{2\pi}{T}$ . In the case of Fig. 1  $m=10$  and  $n=1$ , i.e. the junction is locked on the step No.  $\frac{m}{n} = 10$ . When  $\eta$  is increased beyond 1.822 the chaotic attractor disappears and only the period one or phase locked state remains. The reason for this behavior is apparent from Fig. 2. Together with the stable period one state there exists an unstable period

one hyperbolic point shown as a dashed curve and marked U-1. The unstable periodic points shown in this figure and in the Figs. 4-7 have been located with the Newton-Raphson algorithm described in Ref. 12. When the chaotic attractor collides with this unstable periodic solution, a boundary crisis occurs and the chaotic attractor disappears. After the occurrence of this boundary crisis only the phase locked part of the I-V curve remains, as may be seen in Fig. 1.

The interior crisis at the top of the voltage step in Fig. 1 can also be discerned in Fig. 2. Here we see a Feigenbaum sequence with period doubling bifurcations when increasing  $\eta$  from 1.822 up to 1.888. At the first period doubling bifurcation we have  $m=20$  and  $n=2$ , at the next we have  $m=40$  and  $n=4$ , and so on. This means that the junction remains on the phase locked step number  $\frac{m}{n} = 10$ , and even in the chaotic region, which follows the period doubling bifurcations, the voltage across the junction remains constant. As the voltage is determined as a mean value  $\langle \phi \rangle$ , we cannot see from the I-V curve alone that the above period doubling bifurcation followed by a chaotic window has occurred. However, at  $\eta = 1.888$  a change in the I-V curve is again observed. The voltage  $V$  decreases and becomes irregular. From the Poincare section we notice that an unstable period three orbit marked U-3 and created at  $\eta = 1.851$ , has collided with the chaotic region mentioned above. This collision results in an interior crisis and accordingly the chaotic region expands suddenly, filling out a larger subset of phase space. When this expansion occurs the junction is no longer phase locked on step number 10.

#### IV. Cell to cell mapping and boundary crisis.

We shall now apply the cell to cell mapping to show in more detail the collision between the unstable periodic orbit and the chaotic attractor in the  $\eta$ -interval [ 1.80 ; 1.825 ]. Figs. 3a-c are phase plane plots approaching the crisis, and in Fig. 3d, the crisis has occurred. All

of these plots show the conventionally generated Poincare maps as a multitude of tiny dots, one dot for each cycle of the periodic driving force. The larger symbols represent various periodic groups as found by the cell mapping method. The small open circle labelled U-1 is a saddle point as calculated by the Newton Raphson technique<sup>12</sup>. No basins of attraction are shown. The extended chaotic attractor made visible by the Poincare maps in Figs. 3a-c disappears in Fig. 3d because of the crisis.

The general trend to follow in these figures, is that as  $\eta$  rises and we move from Fig. 3a to Fig. 3b to Fig. 3c, a finger of the chaotic attractor moves toward the unstable saddle point. When the finger touches the saddle point the crisis occurs, and the chaotic attractor disappears, as in Fig. 3d. The beauty of the cell-mapping method is first, that it can find unstable attractors, and second that it gives us a measure of confidence that we are following all the relevant attractors in phase space.

In the cell to cell mapping we have divided the subset  $[-\pi \leq x_1 \leq \pi] \times [-2\pi \leq x_2 \leq 2\pi]$  into  $NX \times NY = 50 \times 100$  cells. In Fig. 3a  $\eta$  equals 1.80 and only one chaotic attractor exists at this  $\eta$ -value. However, in the cell to cell map we found 5 periodic groups. For each of these groups the average voltage was calculated for the associated periodic motion and the attractors were then sorted according to their voltages. In the original system the voltage corresponding to a given attractor is an integer if biased on a phase locked state. To each phase locked state there exists only one attractor. Therefore, when using cell mapping, we regard two or more attractors which are formally distinct as identical provided their periodic motion give rise to the same integer voltage. In regions of chaos the chaotic attractor will result in voltages which are non-integers.

The identification of chaotic attractors with periodic groups is a little more subtle. Due to the finite number of cells we can only get periodic orbits when using cell mapping. However, we may identify a chaotic attractor with a periodic group if the group period is large

and the corresponding voltage is non-integer. As in the phase locked case, formally distinct cell map groups will be considered to belong to the chaotic attractor, provided the voltage is non-integer. (This will be the case even if the voltages are not identical.) The only requirement is that the voltages are non-integer and that the Poincare map reveals only one chaotic attractor for the parameter values under consideration.

As mentioned above we found 5 groups in the cell to cell map at  $\eta=1.80$  (see Fig. 3a). Two of these are a P-16 group with voltage  $V=8.750$  and a P-6 group with voltage  $V=8.501$ . As the voltages are non-integer and as we know from the Figs. 1-2 that only one chaotic attractor exists at  $\eta=1.80$  the two periodic groups are artificially distinct and we shall regard both of them as belonging to the chaotic attractor. In Fig. 3a these two groups together are marked by crosses, and we observe that they fit well to the real attractor obtained from the Poincare section. This means that the cell to cell map provides a fairly accurate picture of the chaotic attractor even with such a crude discretization grid as  $50 \times 100$ . Furthermore, the cell map reveals a P-2 group, marked by downward pointing triangles, with voltage  $V=8.000$ , (step 8), a P-1 group marked by a solid square with  $V=9.008$ , (step 9), and finally a P-1 group marked by an upward pointing triangle with  $V=10.003$ , (step 10). These periodic cell map groups have been found artificially, and they are not stable in the original model equation (1). However, the above three steps or attractors are stable for  $\eta$ -values nearby. We believe that there are periodic transients or 'shadows' of the above periods which the cell map procedure picks up. This fact is useful when searching for attractors in a given parameter region.

In Fig. 3b  $\eta$  is raised from 1.80 to 1.81 and from Figs. 1-2 two coexistent attractors are present, a chaotic one and a periodic one with  $V=10$ . Six periodic groups have been found by cell mapping. There is a P-12 group with  $V=8.498$ , marked by crosses, which is clearly associated with the chaotic attractor. Three other groups, marked in common with

down pointing triangles are associated with a shadow of a nearby  $V=8$  attractor. Finally cell mapping produced two  $V=10$  attractors, in the form of a P-1 group and a P-2 group marked by up pointing triangles in Fig. 3b. The two circled triangles are the P-2 group.

Clearly, these last two groups correspond to step No. 10 in the continuous problem, and are not shadows. The P-1 group coincides with the period one orbit (marked by a diamond on Fig. 3c) obtained from direct numerical simulations of Eq.1. The P-2 group is the unstable periodic orbit created at the saddle-node bifurcation at  $\eta=1.802$ . It is easy to understand why the cell map is able to pick up this unstable saddle point. If the saddle point is approached along one of its two stable manifolds it will take very long time to reach the saddle point. Therefore a cell around the saddle or very close to it may be mapped into itself. In this case two cells close to the saddle have been mapped into themselves and their positions indicate with good accuracy the position of the saddle point. This has been verified by the Newton-Raphson iteration procedure for finding fixed points<sup>12</sup>. The exact position of the unstable saddle point is shown by the small open circle in Fig. 3b.

In Fig. 3c  $\eta$  is raised to the value 1.82. The cell map procedure gives three periodic groups on step No. 10, namely two P-1 groups and one P-2 group. One of the P-1 groups is positioned at the unstable orbit and in Fig. 3c its position is marked by the lettering U-1. We observe that the chaotic attractor (small dots) nearly touches the saddle point U-1, so that we are close to the boundary crisis which occurs at  $\eta=1.822$ . The stable periodic orbit determined directly from Eq.1 is marked by a diamond, and agrees well with the cell map result. Similarly the Newton-Raphson algorithm finds the unstable saddle point to be located very close to the unstable point found by cell mapping. In Fig. 3c the exact position is shown by a circle. Furthermore, the cell to cell map shows a P-22 group with  $V=8.634$  and again this large group fits well with the chaotic attractor obtained from the Poincare section.

In Fig. 3d  $\eta$  has been increased to the value 1.825 which is above the the value of  $\eta = 1.822$  where the boundary crisis occurs. The chaotic attractor has vanished and only the period one stable solution marked by a diamond is present. However, the cell map procedure has found 6 periodic groups. Two of them, marked with up triangles, correspond to step No. 10, and the one closest to the diamond mark is the stable period one solution, and the other one is the unstable saddle point, still labeled U-1, which has just collided with the chaotic attractor. The position of the unstable point found from the Newton-Raphson iteration procedure is marked by a circle and again the cell map result shows excellent agreement with the Newton-Raphson algorithm. The other groups that the cell to cell map has picked are again shaows, the results of transients of real attractors which appear close to the  $\eta$ -value of 1.825. These artificial groups are: one P-5 group with voltage  $V=9.000$ , a P-6 and a P-2 group with voltages  $V=8.004$  and  $V=7.996$ , respectively, and finally a 'chaotic' P-7 group with  $V=8.433$ . This P-7 group is the result of the chaotic transient due to the chaotic attractor which existed before the boundary crisis.

Fig. 3 clearly shows that a crisis occurs as the strange attractor touches the saddle point, but why should such an event be termed a boundary crisis? The reason is, as shown in the next section, that the saddle point lies directly on a basin boundary.

##### V. Basin boundaries and heteroclinic manifold crossings.

In this section we shall use the cell to cell mapping to illustrate heteroclinic tangencies and crossings of the stable and unstable manifolds of saddle orbits on basin boundaries<sup>2,3,13</sup>. Both the boundary crisis and the interior crisis will be treated. We will use cell mapping to compute basins of attraction, and illustrate that the saddle points lie on basin boundaries. We consider the subset  $[-\pi \leq x_1 \leq \pi] \times [0 \leq x_2 \leq 1]$  which is divided into  $NX \times NY = 100 \times 100$  cells. Note that the division into cells is finer in this case than pre-

viously, therefore the cell to cell map will give considerably more precise results. We start with the boundary crisis. Fig. 4 shows the basin of attraction (marked by dots) of the stable period one solution on step No. 10, just at the  $\eta$ -value 1.822 where the boundary crisis occurs. Note that the chaotic attractor just touches the border of the basin of attraction for the No. 10 step. This "touching" is a tangency, as discussed below.

The attracting point is marked by the up triangle. The white region consists of cells which disappear from the subset of interest and they are mapped into the sink cell. (Considering all of the phase plane, points in the white region actually belong to the basin of attraction of the chaotic attractor.) The period one saddle point (U-1) is marked by a circle in Fig. 4 and lies on the borderline of the basin of attraction of the stable period one attractor. This borderline is also the stable manifold of the saddle point (U-1). That is, points on the basin boundary are attracted to (U-1). One branch of the unstable manifold (along which points are repelled from (U-1)) is directed along the chaotic attractor. The other unstable branch extends toward the up triangle. We see from Fig. 4 that part of the unstable manifold, namely the strange attractor, actually touches the stable manifold, the basin boundary, in several places at the same time. Hence if the system begins in a state of chaos on the strange attractor, it will eventually touch the stable manifold of (U-1) and be sent to the stable fixed point attractor with  $V=10$  represented by the up triangle in Fig. 4, and this is the most complete illustration of the boundary crisis.

From Fig. 4 this tangency of the strange attractor at (U-1) would be called a homoclinic tangency, since only one saddle point is shown. However, since the mapping was computed modulo  $2\pi$ , we actually have infinitely many saddle points. In accordance with ref. 2, we believe that the unstable manifold of a given saddle accumulates on the stable manifold of the previous saddle point, and accordingly Fig. 4 shows heteroclinic tangencies when the boundary crisis occurs.

In Fig. 5,  $\eta$  has been increased to the value 1.823 which is above the value where the boundary crisis occurred. The basin of attraction of the period one attractor, shown as dots, has been obtained using the cell to cell mapping procedure. The crosses denote periodic groups that lie on the transient chaotic attractor which is a remnant of the stable chaotic attractor for  $\eta$  less than 1.822. This transient indicates heteroclinic crossings of stable and unstable manifolds. Points on the transient chaotic attractor will eventually come close to the saddle point, marked by the circle in Fig. 5, passing it along the unstable orbit which lies in the basin of attraction of the stable period one attractor. Thereby, the chaotic attractor from Fig. 4 is destroyed. (That is, the attractor for the No. 10 step, marked by the up triangle, is now the only stable attractor.)

Now we consider the interior crisis. Fig. 6 depicts the phase locked chaotic attractor (solid line) as obtained from direct numerical simulation of Eq. 1 at  $\eta=1.886$ . This chaotic attractor appears after the Feigenbaum sequence seen in Fig. 2. The cell to cell map found a P-17 group with  $V=10.000$ , a P-1 group with  $V=9.996$ , and finally a P-2 group with  $V=10.001$ . These three cell map groups all belong to step No. 10. The associated basin of attraction for these three attractors is shown as dots. The cell map groups are marked by up triangles, and they all lie, except for the P-1 group, exactly on the phase locked chaotic attractor (solid line). From the Newton-Raphson algorithm we have identified the P-1 group as the period one saddle point shown in Fig. 2 and marked by a circle in Fig. 6. The interior crisis occurs between  $\eta=1.886$  and  $\gamma=1.887$  and what happens is that the chaotic attractor collides with the unstable period three saddle<sup>5</sup> shown as circles and labelled (U-3) in Fig. 6. The period three saddle has been obtained by using the Newton-Raphson algorithm. Its trajectories are shown as dashed curves in Fig. 2 (marked again by the lettering U-3) which also indicates the collision between the chaotic attractor and the period three saddle. The chaotic attractor is again a subset of the unstable manifolds of the period three saddles. The stable

manifolds lie on the basin boundaries. From Fig. 6 we observe that the unstable manifolds become tangent to the stable manifolds at the  $\eta$  value where the interior crisis happens. For  $\eta$  above this value the unstable and stable manifolds intersect each other resulting in an expansion of the chaotic attractor. This intersection is apparent from Fig. 7 where  $\eta$  has been increased to 1.883.

#### VI. Conclusions.

We have used cell to cell mapping to study and explicitly display a boundary crisis and an interior crisis in a driven Josephson Junction. Using a coarse cell division the cell mapping procedure will pick up remnant periodic and remnant chaotic transients in addition to the original existing attractors. With finer cell division we obtained very precise pictures of the tangencies and crossings of unstable and stable manifolds during both a boundary crisis and an interior crisis. This has been confirmed by calculating fixed points from the Newton-Raphson algorithm and from Poincare sections.

When exploring the global behavior of the Josephson junction the cell mapping procedure provides a fairly accurate picture of the dynamics. Stable and unstable fixed points and associated basins of attractions can be found efficiently and at a low computational cost. The same applies to the strange attractors and their basins of attraction. When more detailed and accurate results are needed one can use the information gained from the cell mapping in applying the more precise tools, such as the Poincare map and the Newton-Raphson iteration procedure. This is particularly valuable in the latter case where a good initial guess for the position of an unstable fixed point is necessary.

#### Acknowledgements

We gratefully acknowledge financial support from the European Research Office of the United States Army through Contract No. DAJA-37-82-C-0057, from IBM Denmark, and from the European Economic Community through contract St 2-0267-J-C (A). We should also like to thank Henrik Svensmark for illuminating discussions.

## References

- [ 1 ] C.S. Hsu and R.S. Guttalu, Journal of Applied Mechanics, 47, 940, (1980).
- [ 2 ] C. Grebogi, E. Ott, and J.A. Yorke, Phys. Rev. Lett. 48, 1507, (1982).
- [ 3 ] C. Grebogi, E. Ott, and J.A. Yorke, Physica 7D, 181, (1983).
- [ 4 ] Yao Huang Kao, Jeun Chyuan Huang, and Yih Shun Gou, Phys. Rev. A. 34, 1628, (1986).
- [ 5 ] R.L. Kautz, "Global Stability of the Chaotic State Near an Interior Crisis," to be published in the proceedings of the MIDIT workshop 1986.
- [ 6 ] R.L. Kautz, J. Appl. Phys. 52, 6241 (1981).
- [ 7 ] C.S. Hsu, Journal of Applied Mechanics, 47, 931, (1980).
- [ 8 ] C.S. Hsu, Journal of Applied Mechanics, 48, 634, (1981).
- [ 9 ] C.S. Hsu and H.M. Chiu, Journal of Applied Mechanics. Preprint.
- [ 10 ] A. Davidson and N.F. Pedersen, Pys. Rev A36, 2455 (1987).

- [ 11 ] A. Barone and G. Paterno, "Physics and Applications of the Josephson Effect," (Wiley-Interscience, New York, 1982).
- [ 12 ] T.S. Parker and L.O. Chua, "Proceedings of the IEEE special issue on chaotic systems", ed. L.O. Chua, 1982, August 1987.
- [ 13 ] C. Grebogi, E. Ott, and J.A. York, Physica 24D, 243, (1987).

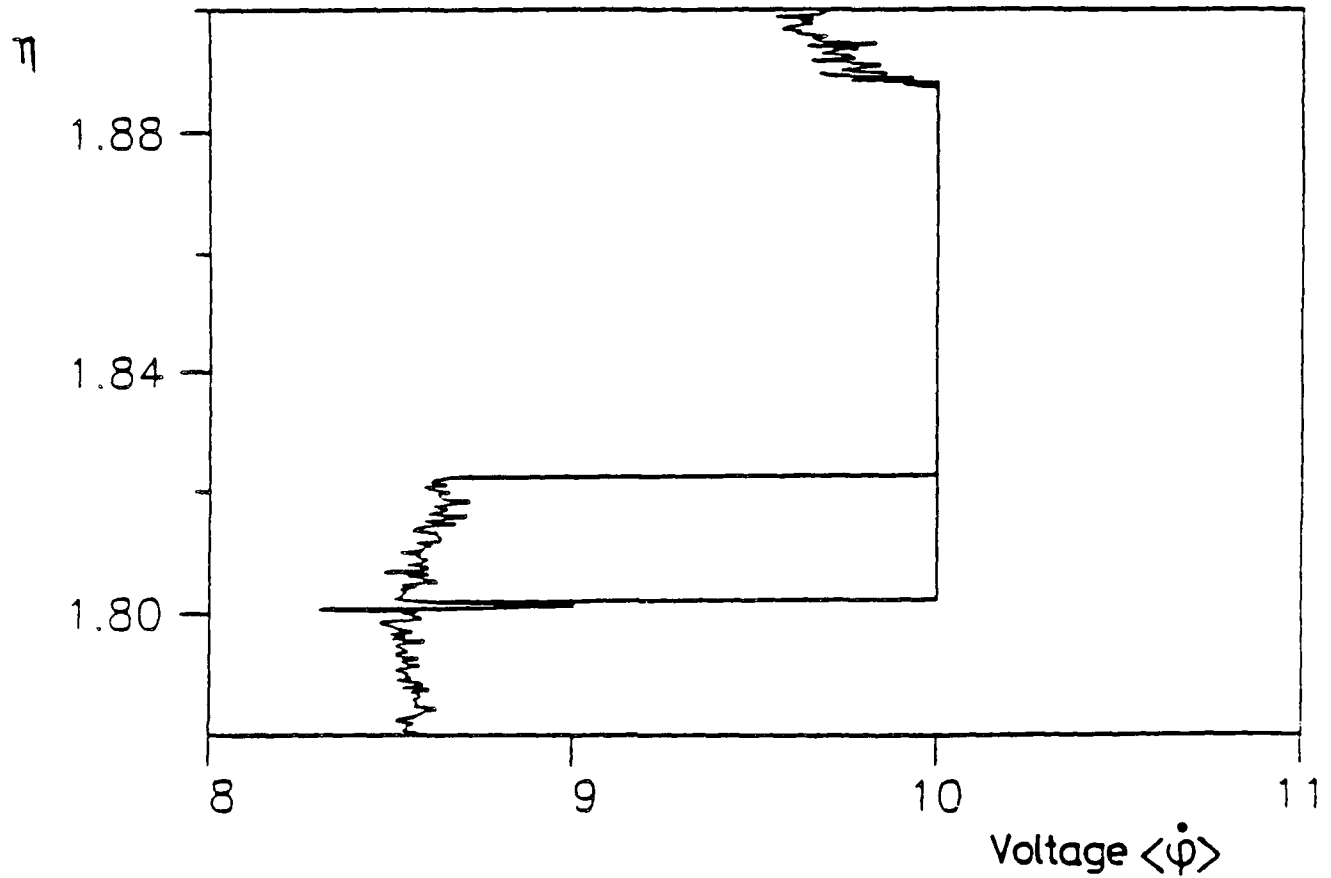
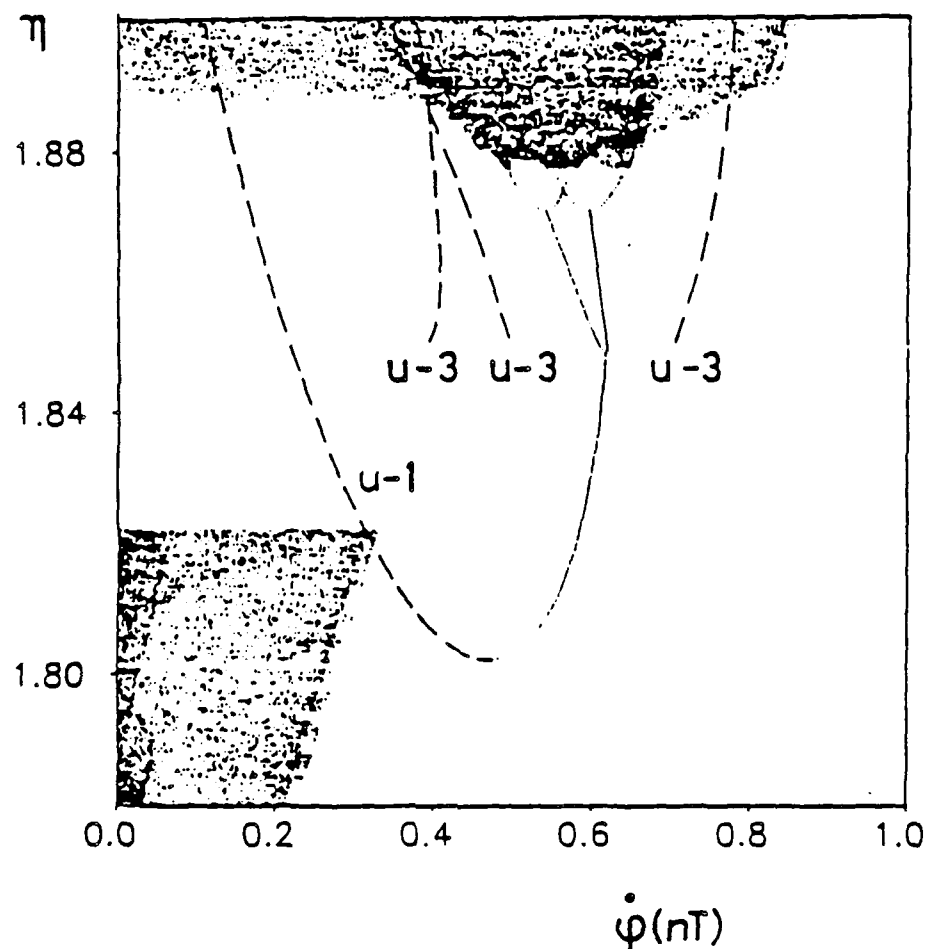


Fig. 1 I-V characteristic for the parameter values  $\alpha = 0.2$ ,  $A = 10.198039027$ , and  $\omega = 1.0$ .



**Fig. 2** Bifurcation diagram showing a boundary crisis and an interior crisis. The parameter values used are as in Fig. 1. The unstable period one and period three saddles are shown as dashed curves marked U-1 and U-3, respectively.

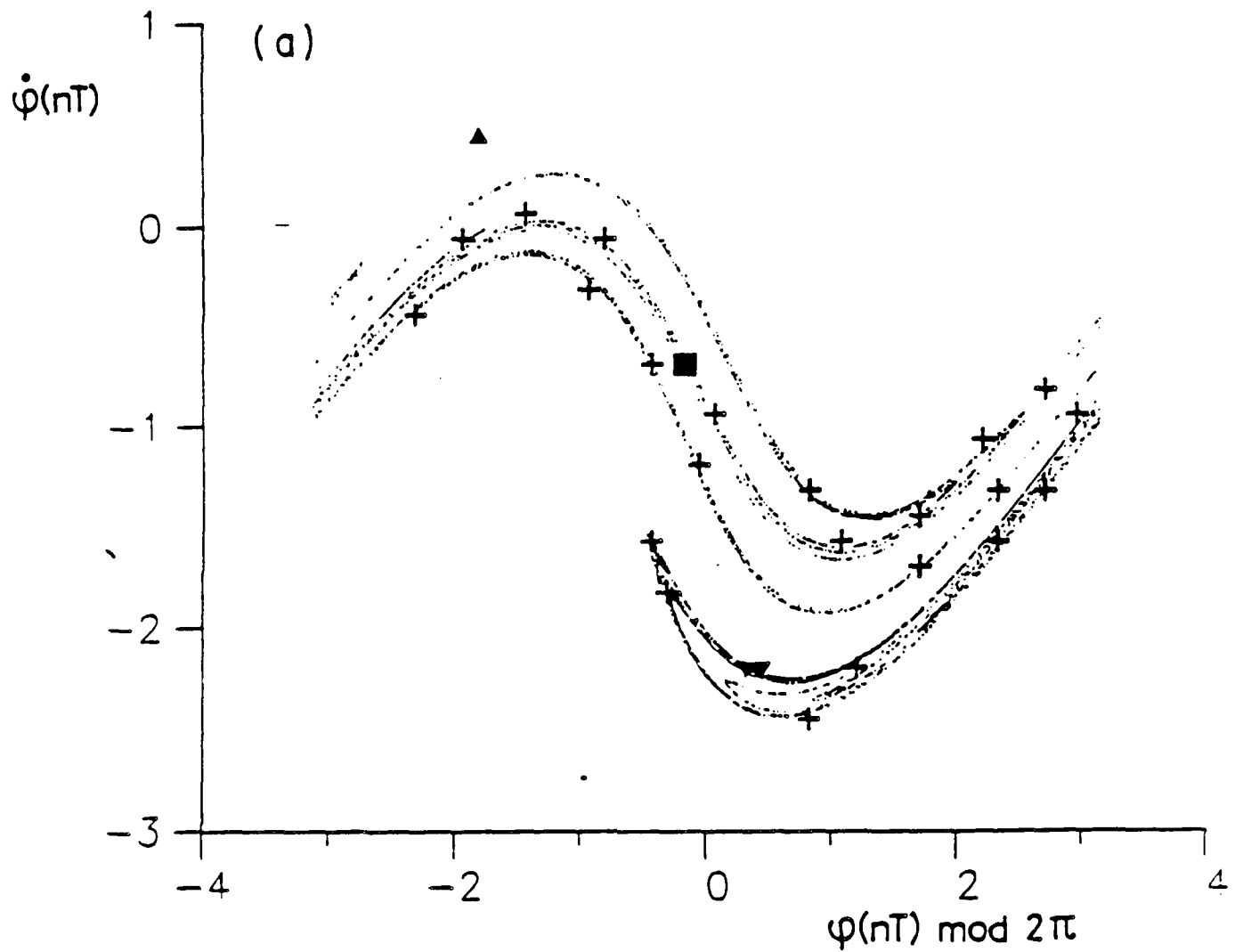


Fig. 3 Poincaré section of the chaotic attractor for Eq. I at parameter values  $\alpha = 0.2$ ,  $A = 10.198039027$ , and  $\omega = 1.0$ . Periodic attractors obtained from the cell mapping procedure are also shown using the subset  $[-\pi \leq x_1 \leq \pi] \times [-2\pi \leq x_2 \leq 2\pi]$  which have been divided into  $50 \times 100$  cells. The average voltage of the periodic groups marked by down pointing triangles, squares, and up pointing triangles, are 8, 9, and 10, respectively, corresponding to step Nos. 8, 9 and 10. The crosses denote periodic groups with non-integer voltage. Stable periodic orbits determined directly from the Poincaré section are marked with a diamond and circles show period one saddles determined from the Newton-Raphson algorithm. (a)  $\eta = 1.80$ , (b)  $\eta = 1.81$ , (c)  $\eta = 1.82$ , (d)  $\eta = 1.825$ .

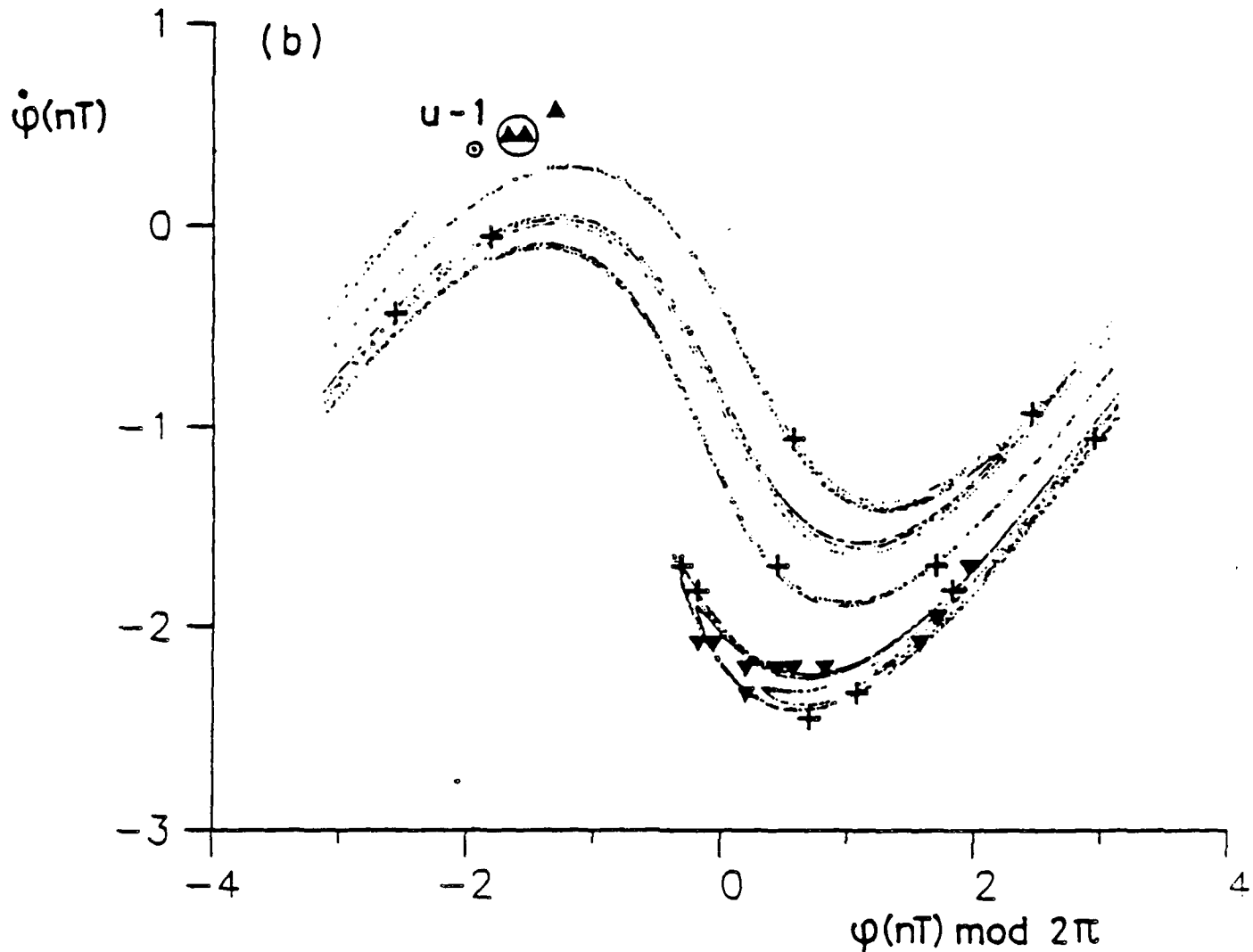


Fig. 3 Poincaré section of the chaotic attractor for Eq. 1 at parameter values  $\alpha = 0.2$ ,  $A = 10.198039027$ , and  $\omega = 1.0$ . Periodic attractors obtained from the cell mapping procedure are also shown using the subset  $[-\pi \leq x_1 \leq \pi] \times [-2\pi \leq x_2 \leq 2\pi]$  which have been divided into  $50 \times 100$  cells. The average voltage of the periodic groups marked by down pointing triangles, squares, and up pointing triangles, are 8, 9, and 10, respectively, corresponding to step Nos. 8, 9 and 10. The crosses denote periodic groups with non-integer voltage. Stable periodic orbits determined directly from the Poincaré section are marked with a diamond and circles show period one saddles determined from the Newton-Raphson algorithm. (a)  $\eta = 1.80$ , (b)  $\eta = 1.81$  (c)  $\eta = 1.82$ , (d)  $\eta = 1.825$ .

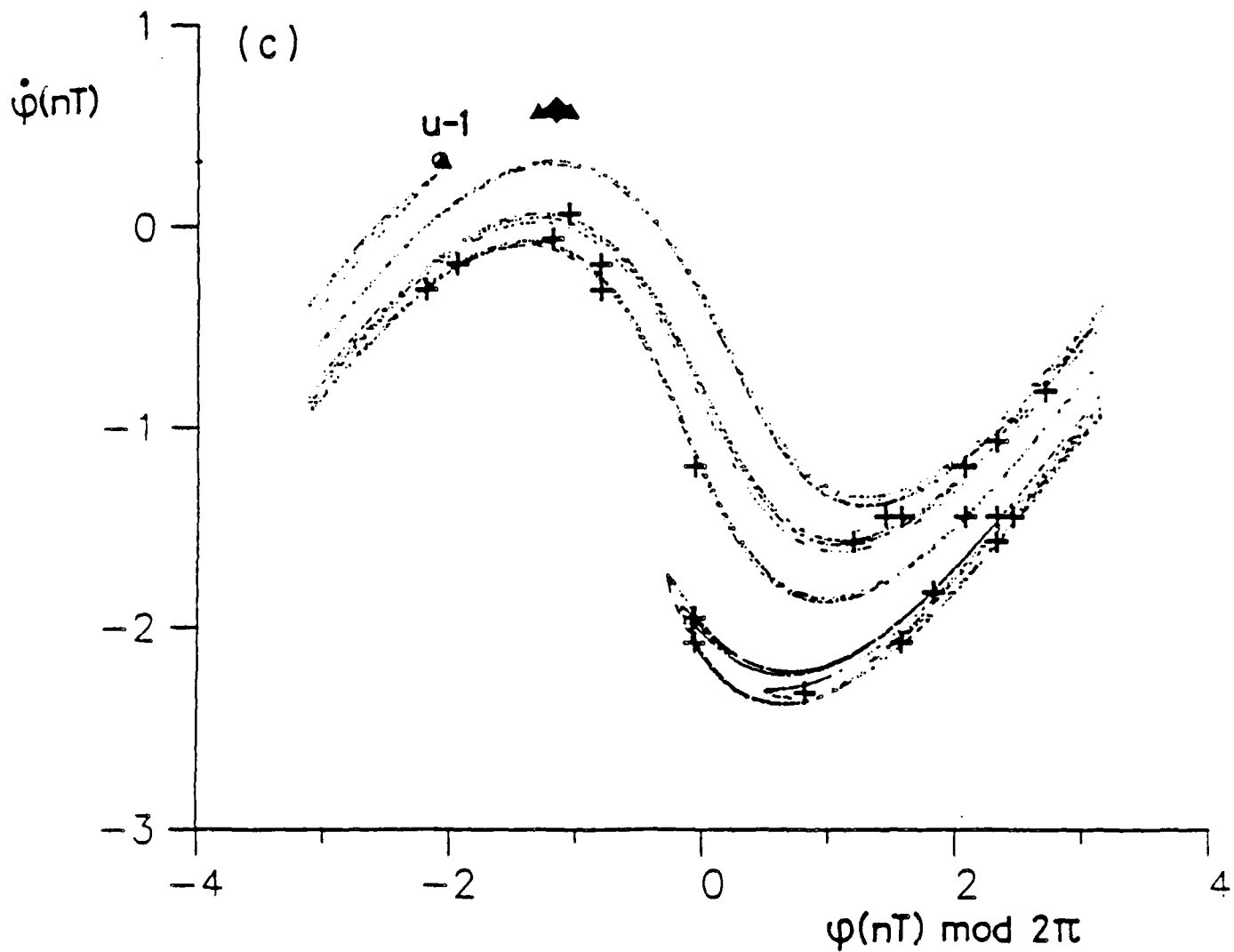


Fig. 3 Poincaré section of the chaotic attractor for Eq. 1 at parameter values  $\alpha = 0.2$ ,  $A = 10.198039027$ , and  $\omega = 1.0$ . Periodic attractors obtained from the cell mapping procedure are also shown using the subset  $[-\pi \leq x_1 \leq \pi] \times [-2\pi \leq x_2 \leq 2\pi]$  which have been divided into  $50 \times 100$  cells. The average voltage of the periodic groups marked by down pointing triangles, squares, and up pointing triangles, are 8, 9, and 10, respectively, corresponding to step Nos. 8, 9 and 10. The crosses denote periodic groups with non-integer voltage. Stable periodic orbits determined directly from the Poincaré section are marked with a diamond and circles show period one saddles determined from the Newton-Raphson algorithm. (a)  $\eta = 1.80$ , (b)  $\eta = 1.81$ , (c)  $\eta = 1.82$ , (d)  $\eta = 1.825$ .

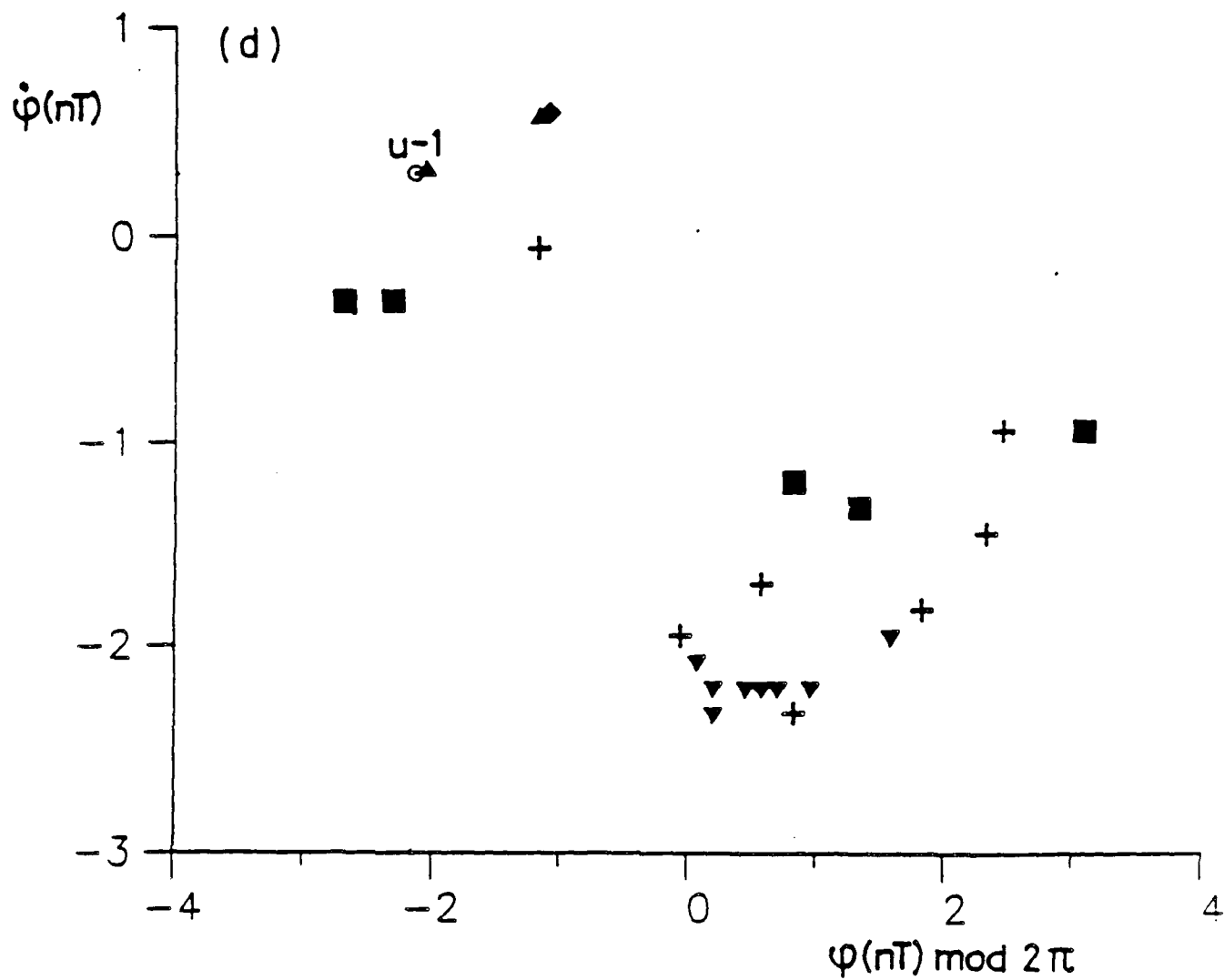
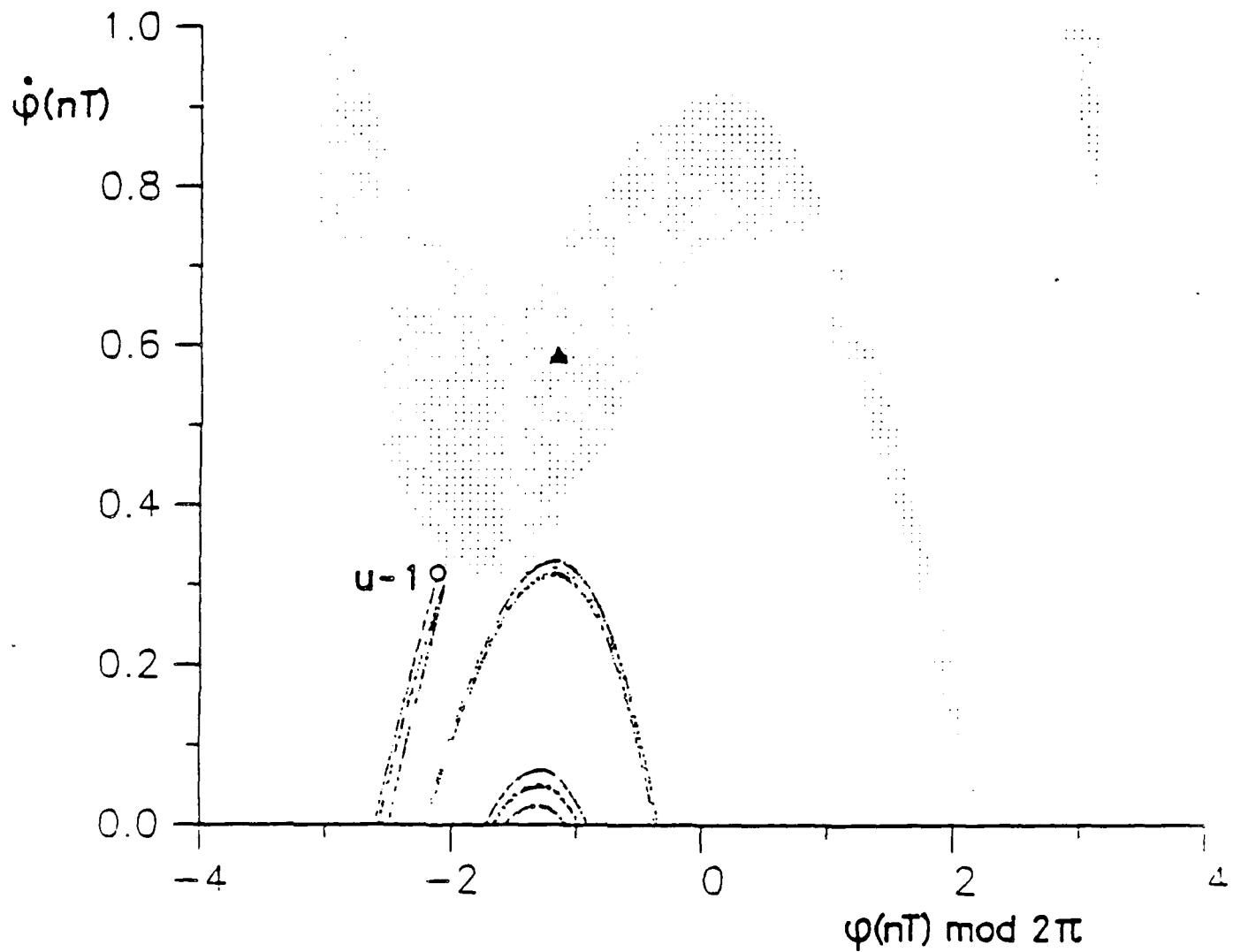


Fig. 3 Poincaré section of the chaotic attractor for Eq. 1 at parameter values  $\alpha = 0.2$ ,

$A = 10.198039027$ , and  $\omega = 1.0$ . Periodic attractors obtained from the cell mapping procedure are also shown using the subset  $[-\pi \leq x_1 \leq \pi] \times [-2\pi \leq x_2 \leq 2\pi]$  which have been divided into  $50 \times 100$  cells. The average voltage of the periodic groups marked by down pointing triangles, squares, and up pointing triangles, are 8, 9, and 10, respectively, corresponding to step Nos. 8, 9 and 10. The crosses denote periodic groups with non-integer voltage. Stable periodic orbits determined directly from the Poincaré section are marked with a diamond and circles show period one saddles determined from the Newton-Raphson algorithm. (a)  $\eta = 1.80$ , (b)  $\eta = 1.81$ , (c)  $\eta = 1.82$ , (d)  $\eta = 1.825$ .



**Fig. 4** Heteroclinic tangencies at the boundary crisis.  $\eta = 1.822$ , and the other parameter values used are as in Fig. 1. The basin of attraction for the period one solution (marked by up pointing triangle) is shown as small dots. The circle shows the position of the unstable period one saddle point (U-1).

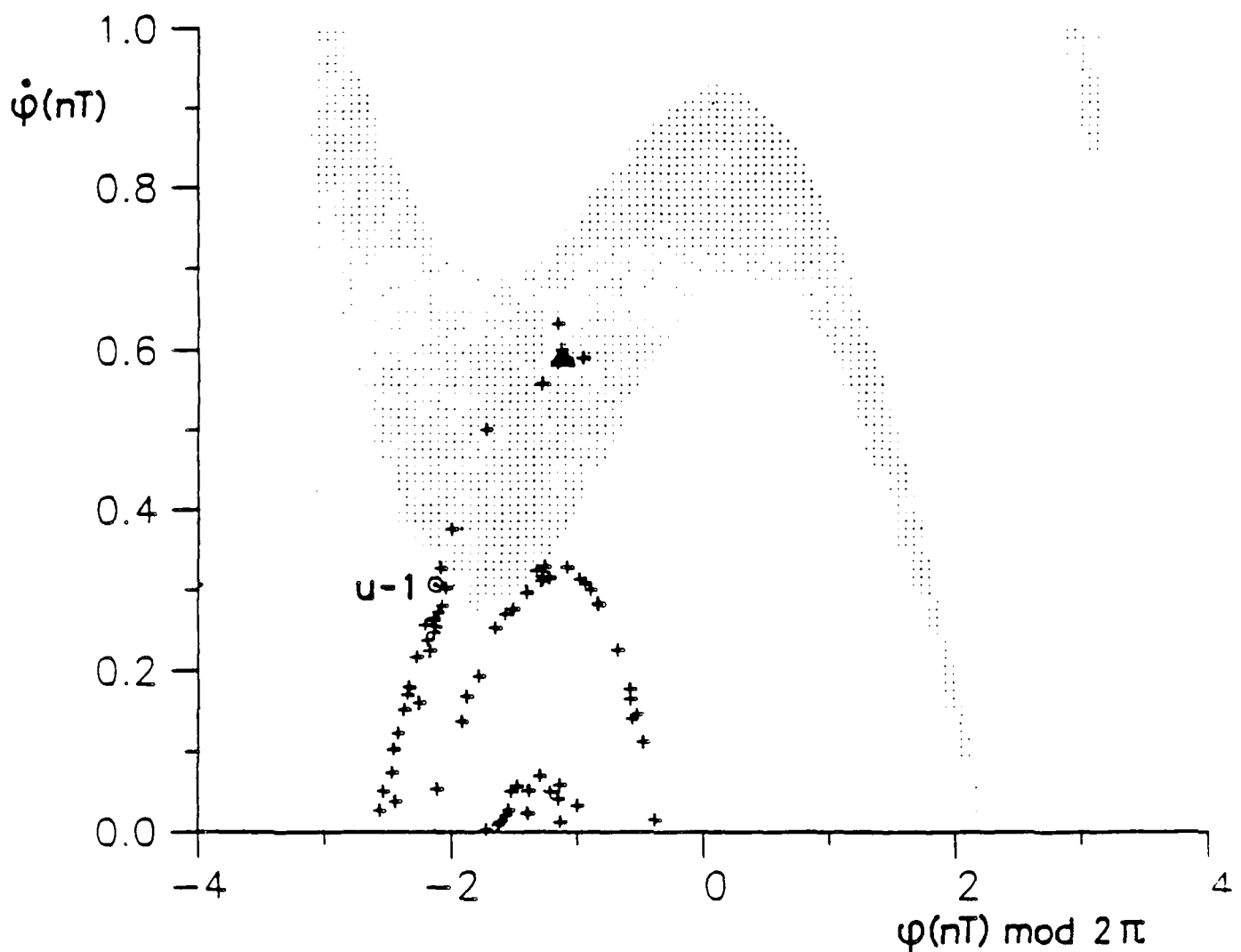


Fig. 5 Heteroclinic crossings after the boundary crisis.  $\eta=1.823$ , and the other parameter values used are as in Fig. 1. Notation as in Fig. 4.

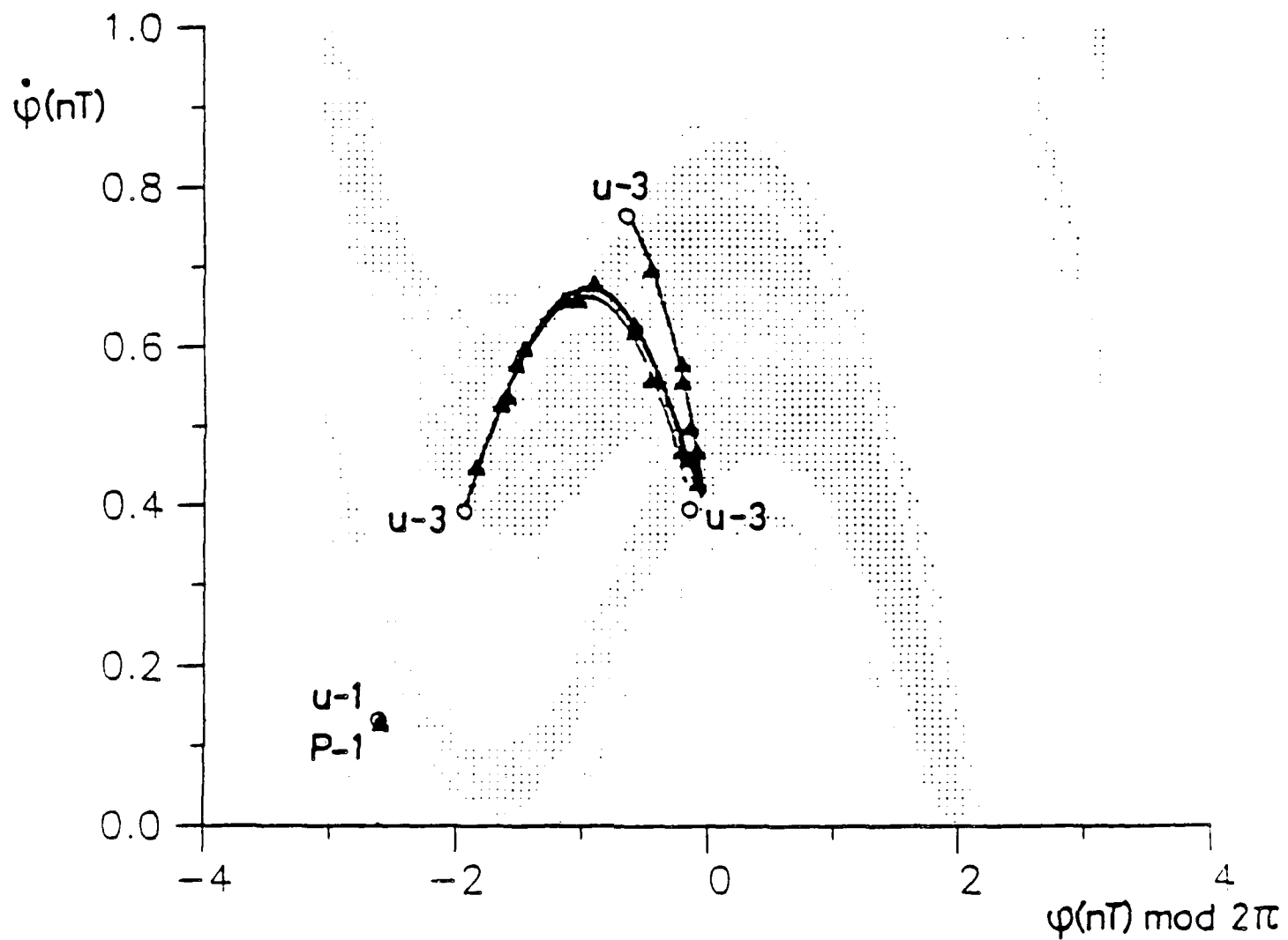


Fig. 6 Heteroclinic tangencies at the interior crisis.  $\eta = 1.886$ , and the other parameter values used are as in Fig. 1. Notation as in Fig. 4.

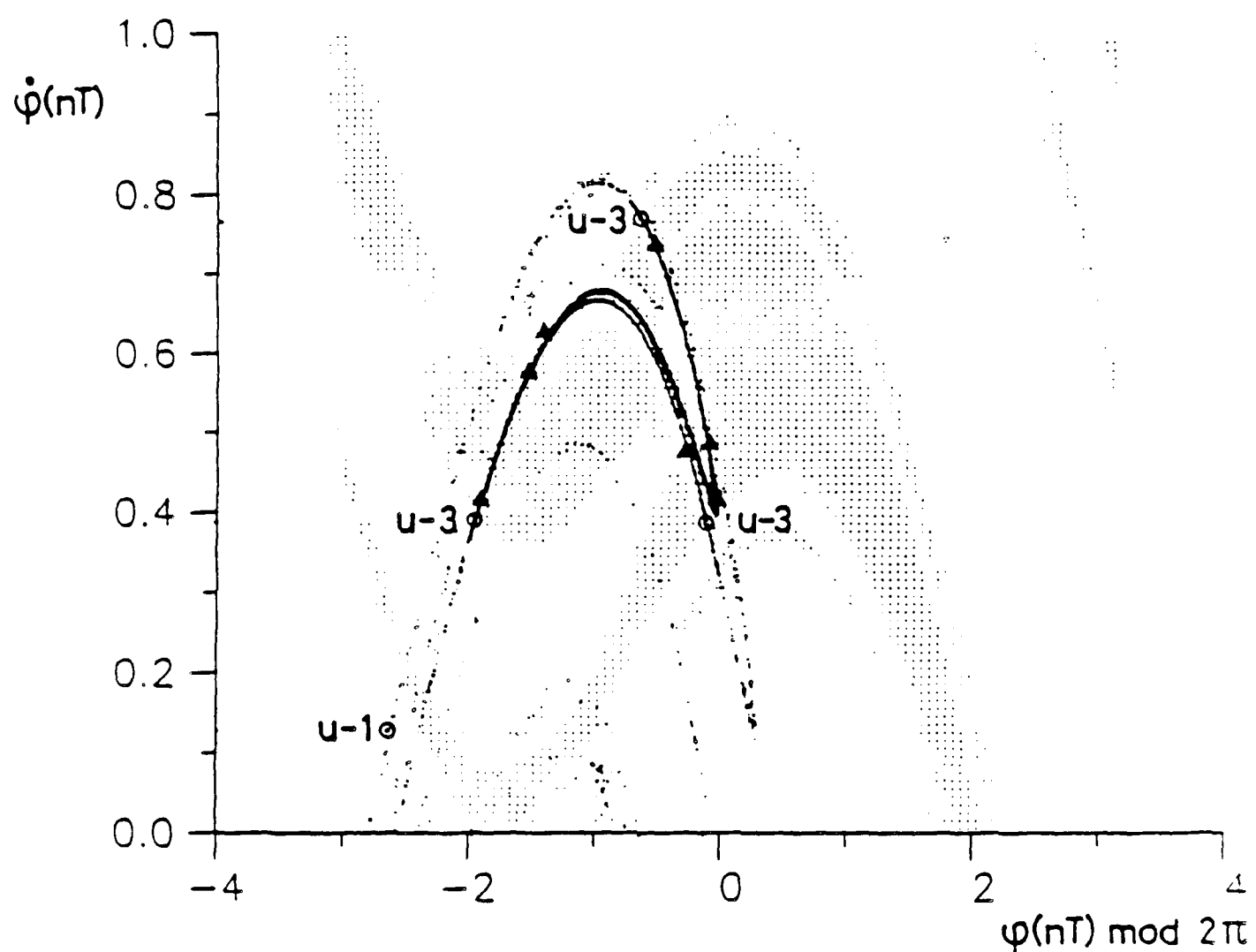


Fig. 7 Heteroclinic crossings after the interior crisis.  $\eta = 1.888$ , and the other parameter values used are as in Fig. 1. Notation as in Fig. 4.

# Numerical Evidence for Global Bifurcations Leading to Switching Phenomena in Long Josephson Junctions

M.G. Forest\*, S. Pagano\*\*, R.D. Parmentier\*\*\*,  
P.L. Christiansen, M.P. Soerensen, and S.-P. Sheu\*

Laboratory of Applied Mathematical Physics  
The Technical University of Denmark  
DK-2800 Lyngby  
Denmark

## Abstract

Fluxons in long Josephson junctions are physical manifestations of travelling waves that connect rest states of the model partial differential equation (p.d.e.), which is a perturbed sine-Gordon equation. In the reduced travelling wave ordinary differential equation (o.d.e.), fluxons correspond to heteroclinic connections between fixed points. In the absence of surface impedance effects, fluxons persist in parameter regimes until the fixed points disappear, after which the system "switches" to another configuration. It is known that the presence of surface impedance produces a singular perturbation of the model equation, together with a new phenomenon: the fluxons switch in parameter regimes before the fixed points are lost. Why this occurs is unknown, and is the focus of this paper. Two disjoint possibilities are: 1) instability: fluxons still exist, but they become unstable in the p.d.e. due to surface impedance effects; 2) nonexistence: the fluxons fail to exist, even though the fixed points remain. Here, we provide compelling numerical evidence for the second scenario, characterized by a global bifurcation in the travelling wave phase space: a breakdown of heteroclinic orbits, undetected at the local linearized level. Moreover, this global o.d.e. bifurcation occurs at parameter values consistent with the p.d.e. switching phenomenon.

## I. Introduction

The propagation of magnetic flux quanta (fluxons) in long Josephson tunnel junctions has attracted research interest, both theoretically, in connection with the intrinsic nonlinear dynamics involved, and practically, in view of potential applications in high-performance electronic systems [1]. Fluxons in Josephson junctions correspond to quasi-soliton solutions of the underlying model equation, which is a sine-Gordon (sG) equation modified by the addition of dissipative and energy-input terms [2]. Such terms destroy the perfect integrability of the pure sG system and thus pose questions regarding the existence and stability of fluxon solutions in various regions of the parameter space of the model equation.

The most direct experimental signature of fluxon propagation in long junctions is provided by the so-called zero-field steps (ZFS's) in the current-voltage (I-V) characteristics of such devices. These are a set of rather brusque, approximately constant-voltage spikes in the I-V characteristic; a typical experimental tracing is shown in Fig. 1. Extensive analytic, numerical, and experimental investigations have established the following basic facts about ZFS's:

- a) The ZFS order number corresponds to the number of fluxons participating in the associated dynamic state, i.e., ZFS1 is due to one fluxon, ZFS2 to two, etc.
- b) The voltage on a ZFS is strictly proportional to the average fluxon propagation velocity.
- c) The formation of a fluxon state, and hence of a ZFS, at low current values is due to a parametrically excited instability of the so-called McCumber state, which is the uniform background state that, in Fig. 1, corresponds to the curve labelled MCB and to its extrapolation to lower voltages.
- d) For a given junction at a given temperature each ZFS terminates abruptly at a well-defined current value that is typically 0.3 - 0.8 times the maximum zero-voltage current (labelled  $I_0$  in Fig. 1); at this current value the junction switches to a higher-voltage state (indicated by arrows in Fig. 1).

Fact a) accounts, for example, for the approximately equal voltage spacing between adjacent ZFS's. Fact b) implies that raising the bias current drives the fluxons toward an asymptotic limiting velocity. Fact c) explains the structure near the "feet" of ZFS's. Fact d) is the focus of the present paper.

To understand the mechanism that determines the height of ZFS's is of considerable importance to the experimentalist, and several theoretical approaches have been proposed in the literature. All are based on analysis of the perturbed sG equation, which, in normalized form, is [2]

$$\phi_{xx} - \phi_{tt} - \sin \phi = \alpha \phi_t - \beta \phi_{xxt} - \gamma . \quad (1)$$

Here,  $\phi(x, t)$  is the usual Josephson phase variable [1],  $x$  is distance along the junction normalized to the Josephson penetration length,  $t$  is time normalized to the inverse of the Josephson plasma angular frequency, and subscripts denote partial derivatives. It is assumed that the junction geometry is long and narrow, so that a 1 + 1 dimensional model is appropriate.

The perturbation on the pure sG structure is characterized by the parameters  $\alpha$ ,  $\beta$  and  $\gamma$ . The term in  $\alpha$  represents shunt loss due to quasiparticle tunneling (here assumed ohmic), the term in  $\beta$  represents dissipation due to the surface resistance of the superconducting films comprising the junction electrodes, and  $\gamma$  is the spatially uniform bias current normalized to the maximum zero-voltage Josephson current. It is worthwhile noting that the term in  $\beta$  constitutes a singular perturbation of Eq. (1). The necessity of including this term in the model was first suggested by Scott [3], and accumulated experience has amply demonstrated that even though its inclusion represents a mathematical complication, its presence is essential for the description of real, physical junctions.

It is necessary also to prescribe appropriate boundary conditions in order to specify completely the problem. Physically reasonable boundary conditions emerge from considerations on the junction geometry. Two commonly studied configurations are the so-called overlap geometry and the annular geometry [1,4]. For the overlap geometry appropriate boundary conditions are

$$\phi_x(0, t) = \phi_x(L, t) = \eta , \quad (2)$$

where  $L$  is the normalized length of the junction and  $\eta$  is normalized measure of the external magnetic field applied in the plane of the junction perpendicular to its long dimension [2]. For the annular geometry the appropriate boundary condition is one of periodicity:

$$\phi(x + L, t) = \phi(x, t) + 2\pi n , \quad (3)$$

where  $n$  is the difference between the number of fluxons and antifluxons present in the junction (since the junction is a closed loop  $n$  is a conserved quantity). Overlap-geometry junctions have undoubtedly received more experimental attention since the fabrication of experimental samples is somewhat simpler for such devices. From the theoretical point of view, on the other hand, the annular geometry offers the advantage of a simpler dynamics due to the absence of the

fluxon-antifluxon reflection effects that occur at the finite ends of overlap junctions. Fluxon propagation on an annular junction may be described by a travelling wave reduction of Eq. (1). Specifically, assuming a travelling wave solution of the form

$$\phi(x,t) = \Phi(x - ut) \equiv \Phi(\xi) \quad (4)$$

in which  $u$  is an arbitrary, constant propagation velocity ( $u \geq 0$ ), we can reduce Eq. (1) to the o.d.e.

$$(1 - u^2) \ddot{\Phi} - \sin \Phi = -\alpha u \dot{\Phi} + \beta u \ddot{\Phi} - \gamma \quad (5)$$

where overdots denote derivatives with respect to  $\xi$ . Moreover, if the normalized circumferential length,  $L$ , of the annular junction is large compared with unity, the situation may be well-approximated by the infinite-length limit. In this case, fluxons correspond to heteroclinic connections between fixed points of Eq. (5). Our present study of the mechanism that determines the height of ZFS's is based on a detailed numerical analysis of just this case.

To put our work into a proper perspective, we note that various approaches to this problem have been reported in the literature. Solutions of Eq. (5), with  $\beta = 0$ ,  $\alpha = \text{constant}$ ,  $(1 - u^2) > 0$ , and  $n = 1$ , were studied many years ago in other contexts [5,6]. The salient features that emerge from these studies are: For given  $\alpha$ ,  $\gamma$ , and  $u$ , there exists at most one periodic solution of Eq. (5). For  $\gamma > 1$ , a periodic solution always exists. For  $\gamma < 1$ , a periodic solution exists provided that  $\alpha < \alpha_c$ , where  $\alpha_c u / \sqrt{1 - u^2} \simeq 1.2$ . Moreover, these periodic solutions are stable (in the context of the o.d.e.).

The earliest (to our knowledge) application of Eq. (5), with  $\beta \neq 0$  and  $n \geq 1$ , to the problem of fluxon propagation in long Josephson junctions was reported in 1968 by Johnson [7], who integrated Eq. (5) using a hybrid computer. Johnson employed a two-valued, piecewise-constant, voltage-dependent  $\alpha$ , and he used physically reasonable estimates for the parameters  $\alpha_1$ ,  $\alpha_2$  and  $\beta$ . He found values for  $\gamma_{\max}$  in the range 0.3 - 0.6, with  $\gamma_{\max}$  a decreasing function of the order number,  $n$ , of the ZFS's, as is normally observed experimentally (see Fig. 1). Johnson's work, unfortunately, was never widely publicized, perhaps because at that time ZFS's had not yet been observed experimentally.

Parmentier and Costabile [8] showed that Eq. (5) can be integrated analytically for  $\beta = 0$  and  $\alpha = \Gamma |\phi|$ , i.e., a dissipation coefficient proportional to the absolute value of the voltage, leading to a quadratic, rather than ohmic, dissipation.

pation. Their analysis gives  $\gamma_{\max} \approx 1$ , but with  $\gamma_{\max}$  an increasing function of  $n$ . A qualitatively very similar result was found by Marcus and Imry [9] by integrating Eq. (5) numerically with  $\beta = 0$  and  $\alpha = \text{constant}$ . A significant difference between the results of Refs. 8 and 9 and those of Johnson [7] is that the former considered  $n$ -periodic solutions of Eq. (5) for a finite-length annular junction, whereas Johnson considered  $n$ -bunches of fluxons for an (effectively) infinite-length junction. Elementary topological considerations, in fact, show that  $n$ -bunch solutions ( $n > 1$ ) of Eq. (5) in the infinite-length limit cannot exist if  $\beta = 0$ .

An approach used by several authors is a Fourier-Galerkin multi-mode decomposition of Eq. (1), with the boundary condition of Eq. (2), together with a solution of the resulting multi-mode equations by means of the resonant Krylov-Bogoliubov approximation. The pioneering work in this direction was that of Takanaka [10], who considered a single-mode approximation with  $\beta = 0$  and  $\alpha = \text{constant}$ , in the absence of applied magnetic field ( $\eta = 0$ ). Chang et al. [11] extended this to a two-mode approximation, also with  $\beta = 0$  and  $\eta = 0$ . Finally, Enpuku et al. [12] presented the general N-mode approximation, with  $\alpha, \beta$  and  $\eta$  all different from zero. In all cases, this approach gives  $\gamma_{\max} \leq 1$  for ZFS1 (the only case considered), and, as might be expected, the results improve as the number of modes used increases.

Linear stability analyses of travelling wave solutions of Eq. (1), i.e., solutions of Eq. (5), with the boundary condition of Eq. (3), for  $\beta = 0$  and  $\alpha = \text{constant}$ , were given by Burkov and Lifsic [13] and by Büttiker et al. [14]. Burkov and Lifsic considered junctions of arbitrary length with  $n \geq 1$ , whereas Büttiker et al. focused on the infinite-length limit with  $n = 1$ . Burkov and Lifsic conclude that periodic fluxon solutions of Eq. (5) are stable (in the context of the p.d.e.) for  $n < 1$ . Büttiker et al. show that the  $n = 1$  fluxon solutions on the infinite-length junction are stable for  $0 \leq \gamma < 1$ . Since, as pointed out by Marcus and Imry [9], (for  $\beta = 0$ )  $\gamma \rightarrow \gamma_{\max}$  for  $u \rightarrow 1$ , and

$$\overline{\gamma_{\max}} \approx \sqrt{1 + (2\pi\alpha n/L)^2} \quad (6)$$

the two results are consistent.

An approximation that permits analytic solution of Eq. (5) is to replace the nonlinear term,  $\sin \Phi$ , with a piecewise-linear sawtooth function. Sakai and Tateno [15] used this approach to calculate periodic solutions of Eq. (5) with  $\beta = 0$ ,  $\alpha = \text{constant}$ , and  $n \geq 1$ . Their analysis gives

$$\gamma_{\max} = \coth(L/2\pi\alpha n), \quad (7)$$

which, although quantitatively different, is qualitatively quite similar to Eq. (6); in particular,  $\gamma_{\max} \rightarrow 1$  in the infinite-length limit. The piecewise-linear approach was extended by Sakai and Pedersen [16] to the  $\beta = \text{constant}$ ,  $\alpha = \text{constant}$ ,  $n = 1$  case in the infinite-length limit. Their work showed that, for  $\beta$  larger than a certain threshold value,  $\gamma_{\max}$  decreases with increasing  $\beta$ . Sakai [17] further extended this approach to obtain 2-bunch solutions of Eq. (5) in the infinite-length limit. The results in this case are quite reminiscent of those obtained by Johnson [7].

Perturbative methods have been employed to calculate the  $\gamma - u$  relation for  $n = 1$  solutions of Eq. (5) in the infinite-length limit [4,18,19]. The procedure, in all cases, involves selecting a solution ansatz from a related, but simpler, problem and imposing a balance between the average power lost to dissipation and that furnished by the bias current. McLaughlin and Scott [4] used an unperturbed sG kink as a solution ansatz. This ansatz gives reliable results for  $\gamma \ll 1$ , but it breaks down at high bias, giving  $\gamma \rightarrow \infty$  for  $u \rightarrow 1$ . Ferrigno and Pace [18] improved this result by incorporating into their ansatz the shift of the sG ground state due to non-zero  $\gamma$  and the limited (i.e., non-Lorentz) contraction of fluxons due to a  $\beta = 0$  and  $\alpha = \text{constant}$  dissipation. Their result reduces to that of McLaughlin and Scott for  $\gamma \ll 1$ , but it gives  $\gamma \rightarrow 1$  for  $u \rightarrow 1$ . A related approach, with similar results, was reported by Pagano et al. [19], who also clearly pin-pointed the fact that the failure of the perturbative approach to capture accurate values for  $\gamma_{\max}$  in the presence of a non-zero  $\beta$ -loss term is attributable to the fact that this loss term causes a significant distortion of the fluxon waveform that is not well-described by the ansätze employed.

A frequently used approach is the direct numerical integration of Eq. (1), with boundary conditions given either by Eq. (2) or Eq. (3). One of the earliest efforts in this direction was that of Nakajima et al. [20], who integrated Eq. (1), with  $\eta = 0$  in Eq. (2), for various values of  $\alpha$  and  $\beta$ , and initial conditions corresponding to various values of  $n$ , using a finite-difference scheme. Further results were reported by Marcus and Imry [9], Erné and Parmentier [21], and Lomidahl et al. [2]. An important contribution was that of Davidson et al. [22], who focused their attention on the  $\beta$ -loss term, thus providing a stimulus for a number of successive works. Perhaps the most detailed work to date is that of Pagano et al. [23], who considered the dependence of  $\gamma_{\max}$  on  $\alpha$ ,  $\beta$  and  $L$  for both the

overlap and the annular geometries. A careful reading of the various works employing the direct numerical integration approach reveals a number of quantitative discrepancies in the determination of  $\gamma_{\max}$ . These may be attributed to the following two causes: 1) Discretization errors: excessively coarse spatio-temporal grids used with finite-difference algorithms tend to give values for  $\gamma_{\max}$  that are lower than the true values; 2) "Non-adiabatic" parameter variations: increments in the bias current,  $\gamma$ , applied as temporal step functions and/or initial conditions chosen "too far" from the final fluxon waveforms also tend to cause premature switching, i.e. depressed values for  $\gamma_{\max}$ .

The body of existing literature on the subject, reviewed briefly above, allows the formulation of the following working hypothesis: In the absence of a  $\beta$ -loss term,  $\gamma_{\max} = 1$  for  $n = 1$ , both for infinite-length annular-geometry junctions and for finite-length overlap-geometry junctions. For finite-length annular-geometry junctions, the  $n$ -dependence of  $\gamma_{\max}$  is given approximately by Eq. (6) or by Eq. (7). In the presence of a  $\beta$ -loss term,  $\gamma_{\max}$  in all cases is reduced to lower values. We propose herein to examine the mechanism responsible for this reduction for the case of  $n = 1$  in the infinite-length limit. Specifically, we develop refined numerical procedures that: 1) reliably determine a fluxon solution (heteroclinic connection) when it exists, in the form of a numerical continuity proof; 2) determine an apparent numerical breakdown of the heteroclinic connection as parameters in the equation are varied, corresponding to a qualitative change in the numerical continuity diagnostic; 3) rule out the breakdown of the connection due to local phenomena (such as behavior of the linearized eigenspaces at the fixed points); and 4) thus lead us to conjecture a global bifurcation phenomenon for fluxon switching in the presence of surface impedance effects. The precise mathematical nature of this global bifurcation is an open problem. Moreover, this paper represents a step toward the development of general purpose codes to reliably detect existence and breakdown of orbits homoclinic or heteroclinic to hyperbolic fixed points, in particular when oscillations are present.

## II. Reduction to the travelling wave o.d.e. and phase space discussion

The justification for using the reduced travelling wave ode, Eq. (5), to determine  $\gamma_{\max}$  for annular-geometry junctions derives from information obtained via the numerical integration of Eq. (1), with the boundary condition of Eq. (3). Typically, fluxon solutions of Eq. (1) are easily found numerically, with a fairly

large computational domain of attraction (except when  $\gamma \rightarrow \gamma_{\max}$ ). If we decompose Eq. (1) into Fourier spatial modes, we can define a mode phase velocity as

$$u_m = -F_m(\phi_t)/F_m(\phi_x), \quad (8)$$

where  $F_m(Y)$  is the m'th component of the spatial Fourier transform of Y. During steady propagation it is observed [23] that all of the  $u_m$  tend rapidly to a common asymptotic value, which is just the velocity  $u$  of Eq. (5).

We may note that Eq. (5) is invariant under the transformation

$$\Phi' = -\Phi, \quad \gamma' = -\gamma \quad (9)$$

Consequently, no loss of generality is incurred by imposing  $\gamma \geq 0$ .

For  $\gamma < 1$ , Eq. (5) has two classes of fixed points:

$$\Phi_{2j+1} = \arcsin(\gamma) + 2j\pi, \quad \dot{\Phi}_{2j+1} = 0, \quad \ddot{\Phi}_{2j+1} = 0 \quad (10a)$$

and

$$\Phi_{2j} = \pi - \arcsin(\gamma) + 2j\pi, \quad \dot{\Phi}_{2j} = 0, \quad \ddot{\Phi}_{2j} = 0 \quad (10b)$$

where  $j = 0, \pm 1, \pm 2, \dots$ , and  $0 \leq \arcsin(\gamma) < \pi/2$ . For  $\gamma > 1$  no such fixed points exist. The linear stability of the fixed points of Eqs. (10a,b) is determined by the zeroes of the polynomial

$$P_{\pm}(\lambda) = -\beta u \lambda^3 + (1 - u^2) \lambda^2 + \alpha u \lambda \pm \sqrt{1 - \gamma^2} \quad (11)$$

where the plus sign before the last term holds for the fixed points of Eq. (10b) and the minus sign for those of Eq. (10a). Elementary analysis shows that  $P_+(\lambda)$  has one positive real zero and either two negative real zeroes or two complex conjugate zeroes with negative real part, whereas  $P_-(\lambda)$  has one negative real zero and either two positive real zeroes or two complex conjugate zeroes with positive real part. The fixed points of Eqs. (10a,b) correspond to time-stationary, space-independent solutions of Eq. (1); equivalently, they correspond to the equilibrium solutions of a plane pendulum subjected to a constant torque. From this analogy, it is clear that the fixed points of Eq. (10a) correspond to stable static solutions and those of Eq. (10b) to unstable ones (in the context of the p.d.e.). Consequently, stable fluxon solutions of Eq. (1) correspond to heteroclinic connections between the fixed points of Eq. (10a). Heteroclinic connections between the fixed points of Eq. (10b) also exist; however, these do not correspond to stable fluxons in the p.d.e.

In the limit  $\gamma \rightarrow 1$ ,  $P_+(\lambda)$  and  $P_-(\lambda)$  coalesce. In this case zeroes are  $\lambda = 0$  plus one positive and one negative value.

The numerical results presented in the following section show that for each  $\gamma \leq \gamma_{\max}$  there is a unique  $u(\gamma)$  such that there exists a connection from  $\Phi_1$  to  $\Phi_1$ . This connection corresponds [23] to a stable single-fluxon solution of Eq. (1). Likewise, there is a unique, but different,  $u(\gamma)$  for the existence of a  $\Phi_0$  to  $\Phi_2$  connection. Two examples of such connections are shown in Figs. 2 and 3. Moreover, there exist still other heteroclinic connections, corresponding, for example, to bunched multi-fluxon solutions of the p.d.e., but these are not investigated further herein.

To be specific, we now fix the particular values

$$\sigma = 0.18, \text{ and } \beta = 0.10 \quad (12)$$

(as will be seen in the following section, this choice is less restrictive than at first might appear). With these values, all linearized eigenvalues are real for  $0 < \gamma \lesssim 0.4$ , which yields non-oscillatory heteroclinic orbits. For  $0.4 \lesssim \gamma < \gamma_{\max}$  there are two complex conjugate eigenvalues, which yields in the corresponding solution an oscillatory overshoot phenomenon in the asymptotic approach to the fixed point.

### III. Numerical Global Connection Curves.

In the previous section we have studied the fixed points of Eq.(5), which describes the travelling wave solutions of Eq. (1). From the study of the linearization near the fixed points we have deduced the behavior of the flow near the equilibrium points. This information, though important in determining the rôle of the perturbative parameters  $\alpha, \beta$  and  $\gamma$ , does not determine the existence of global connections between the fixed points.

In this section we first analyze the symmetry and invariance properties of Eq. (5) in order to obtain useful information on the existence of the global connections. Then the numerical methods and results are presented.

There are two obvious transformations which leave Eq. (5) invariant: One, Eqs. (9), has already been indicated in the previous section. The other transformation is:

$$u' = -u, \quad \xi' = -\xi \quad (13)$$

which provides a numerical advantage, by exploiting "time" reversal, in computing the global connection curves. For example the orbit which leaves the fixed point  $\Phi_1$  along the two-dimensional unstable manifold,  $W_u^s(\Phi_1)$ , and connects to  $\Phi_3$  along the one-dimensional stable one,  $W_s^s(\Phi_3)$ , is intractable numerically in forward time. One would need to search over all directions leaving  $W_u^s(\Phi_1)$ . However, by reversing time via Eqs. (13), one shoots numerically along the unique direction,  $W_s^s(\Phi_3)$ .

Another invariance of Eq. (5) is given by a generalized Lorentz transformation

$$\xi' = f(u)\xi \quad (14a)$$

$$u' = [1 - (1 - u^2)f^2(u)]^{\frac{1}{2}} \quad (14b)$$

$$\alpha' = \frac{u}{u'} f(u) \alpha \quad (14c)$$

$$\beta' = -\frac{u}{u'} f^3(u) \beta , \quad (14d)$$

where  $f(u)$  is any real function satisfying  $0 < f^2(u) \leq (1 - u^2)^{-1}$  for  $u^2 < 1$  and  $0 < f(u)$  for  $u^2 > 1$ . This transformation gives a scaling law in the parameters  $\alpha$  and  $\beta$  which can be used to extend the results contained here for fixed  $\alpha, \beta$ .

An important invariant transformation is

$$\xi' = f(u) \xi \quad (15a)$$

$$\Phi' = \pi - \Phi \quad (15b)$$

$$u' = [1 + (1 - u^2)f^2(u)]^{\frac{1}{2}} \quad (15c)$$

$$\alpha' = -\frac{u}{u'} f(u) \alpha \quad (15d)$$

$$\beta' = -\frac{u}{u'} f^3(u) \beta \quad (15e)$$

with  $f(u)$  real,  $f(u) \neq 0$  for  $u^2 < 1$ , and  $0 < f^2(u) < (u^2 - 1)^{-1}$  for  $u^2 > 1$ . In the special case  $f(u) \equiv -1$  and  $u = 1$  we find the transformation

$$\xi' = -\xi \quad (16a)$$

$$\Phi' = \pi - \Phi \quad (16b)$$

$$u' = 1 \quad (16c)$$

$$\alpha' = \alpha \quad (16d)$$

$$\beta' = \beta . \quad (16e)$$

This invariance property implies that, for  $u = 1$ , either both connections  $\Phi_1$  to  $\Phi_3$  and  $\Phi_0$  to  $\Phi_2$  exist simultaneously or else neither exists. As suggested in Fig. 2 and indicated more clearly in Fig. 4 this fact corresponds to the intersection, at  $u = 1$ , of existence curves of  $\Phi_1$  to  $\Phi_3$  connections and of  $\Phi_0$  to  $\Phi_2$  connections, at values of  $\gamma$  less than unity. This is in contrast with the  $\beta = 0$  case: in that case,  $u = 1$  only for  $\gamma = 1$ , and the fixed points themselves coalesce.

We proceed now to discuss the numerical determination of these global connections. The details are deferred to the appendix, but we will describe the main features. We employ a shooting method as follows : For fixed  $\alpha$ ,  $\beta$  as in Eq. (12) we first choose a value of  $\gamma \in [0, 1]$ , beginning near 0. In order to seek a connection from  $\Phi_1$  to  $\Phi_3$  we exploit the "time" reversal symmetry (13). That is, rather than vary over all directions emanating from  $W_2^s(\Phi_1)$ , we shoot from  $\Phi_3$  along the unique direction  $W_1^s(\Phi_3)$  approximated by the stable eigenvector at  $\Phi_3$ . The numerical code iterates trying to minimize over  $u$  the distance function  $d(u)$

$$d_{\Phi_1}(u) \equiv \min_{0 \leq \xi \leq \Xi} \sqrt{(\Phi - \Phi_1)^2 + \Phi_\xi^2 + \Phi_{\xi\xi}^2} . \quad (17)$$

$\Xi$  having a large enough value. The absolute minimum,  $d_{\Phi_1}(\hat{u})$ , if sufficiently close to 0, gives a candidate for the velocity value associated to the  $\Phi_1$  to  $\Phi_3$  connection. We then refine the iteration steps on this  $\hat{u}$  in order to exhibit that  $d_{\Phi_1}(\hat{u})$  can be brought arbitrarily close to zero.

At this point we implement an additional numerical algorithm to reinforce that a fixed point connection has been found. Shooting methods for connections to stable fixed points are highly stable numerically, whereas connections into unstable fixed points are numerically unstable. The final algorithm we use is a numerical continuity argument which is applicable for shooting into a one-dimensionally unstable fixed point. We construct a sphere of radius  $R$  around the fixed point  $\Phi_1$ . The value of  $R$  is chosen small enough ( $R \leq 0.1$ ) that a linearization of the flow inside the sphere is appropriate. When the orbit approaching  $\Phi_1$  intersects the sphere, we identify the intersection point  $\vec{\Phi}' = (\Phi', \dot{\Phi}', \ddot{\Phi}')$  as the initial condition for the evolution in the linearized space. The approach into the sphere about  $\Phi_1$  is

always nearly tangent to the stable manifold, which defines an equatorial plane for the sphere. The departure will necessarily be transverse to this plane, along the unstable manifold, and will either be out the top (the "northern hemisphere") or bottom (the "southern hemisphere") of the sphere. We can then solve analytically the linearized o.d.e. :

$$(1 - u^2) \ddot{\Phi} - \sin(\Phi_j) - \cos(\Phi_j) \Phi = -\alpha u \dot{\Phi} + \beta u \ddot{\Phi} - \gamma \quad (18)$$

obtaining

$$\Phi(\xi) = A e^{\lambda_1 \xi} + B e^{\lambda_2 \xi} + C e^{\lambda_3 \xi} + \Phi_j \quad (19)$$

where  $\lambda_1, \lambda_2$ , and  $\lambda_3$  are the roots of  $P_{\pm}(\lambda)$  (Eq. (11)) and A,B, and C are determined by the initial conditions :  $\dot{\Phi}(0) = \dot{\Phi}'$ . In our case, i.e. the oscillatory heteroclinic orbit and  $j = 1$ , we have  $\lambda_1 = k > 0, \lambda_2 = \bar{\lambda}_3 = \mu + i\omega$ , where  $\mu < 0$  (note that, by using the transformation of Eqs. (13), the sign of the real eigenvalue can always be taken positive). The local behavior of the solution will then depend on the value of A, which can be expressed simply as :

$$A = \frac{\ddot{\Phi}' - 2k\dot{\Phi}' + (\Phi' - \Phi_j)(k^2 + \omega^2)}{(\mu - k)^2 + \omega^2} \quad (20)$$

If  $A = 0$  the solution  $\Phi$  will tend toward  $\Phi_j$ , while for  $A \neq 0$  it will diverge through the "top" of the sphere for  $A > 0$  or through the "bottom" of the sphere for  $A < 0$ . We iterate  $u$ , in a neighborhood of  $\hat{u}$ , to show that for  $u^+ > \hat{u}$  the solution diverges in one direction, while for  $u^- < \hat{u}$  it diverges in the other direction. This provides a numerical continuity diagnostic. When the continuity argument and the shooting method both imply a connection we accept this as numerical proof. By iterating on  $\gamma$  this process yields the  $\Phi_1$  to  $\Phi_3$  and the  $\Phi_0$  to  $\Phi_2$  connection curves of Fig. 4. We remark that the connection curves intersect at  $u = 1$  as discussed earlier. Moreover, as can be seen in Fig. 4b, these curves persist past  $u = 1$  contrary to the  $\beta = 0$  case. (This result was also found by Sakai and Pedersen [16] for a related system where the sine-term is replaced by a piecewise linear approximation). The existence of a stable fluxon solution propagating at a velocity  $u > 1$  might at first seem surprising, but it is simply a consequence of the fact that, with a non-zero  $\beta$ -term, Eq. (1) is no longer hyperbolic. Fig. 5 shows such a stable fluxon solution, obtained by a full simulation of Eq. (1) with  $\alpha = 0.18, \beta = 0.10$ , and  $\gamma = 0.888$ . The velocity here, measured as described in the discussion surrounding Eq. (8), is

$\mu = 1.0018$ . In the  $\beta = 0$  case  $\mu$  approaches 1 as  $\gamma$  approaches 1 corresponding to the coalescence of  $\Phi_1$  and  $\Phi_0$ . Beyond this point the fixed points disappear, so that the termination of the global connections coincides with this local degeneracy.

The fundamental result of this paper is the simultaneous termination of the fixed point connection curves of Fig. 4 at the critical value  $\gamma^* \simeq 0.8877$  (for the chosen values of  $\alpha$ , and  $\beta$ ). For  $\gamma > \gamma^*$  the numerical code cannot reduce the distance function,  $d_{\Phi_j}(\mu)$ , arbitrarily close to 0: in fact  $d_{\Phi_j}(\mu)$  reaches a minimum bounded well away from zero. Fig. 6 shows the dramatic jump observed in this minimum distance function at  $\gamma = \gamma^*$ . We emphasize that this phenomenon occurs simultaneously for both connection curves, which are computed independently. We also emphasize that this critical  $\gamma^*$  where the fixed point connections fail to exist numerically does not correspond to any local bifurcation. Fig. 7 shows that there is no signature of a bifurcation in the linearized eigenspace at  $\Phi_j$ .

We therefore conclude that the termination of these connections corresponds to a global bifurcation in this o.d.e. phase space. It remains to be determined how this breakdown of heteroclinic orbits is reflected topologically.

We recall also that the critical value  $\gamma^*$  is consistent with the numerical studies of the full p.d.e. (Eq.(1)) reported in [23]. In this study the global bifurcation was shown to result in the switching from the fluxon state to the running mode state.

## Discussions and Conclusion

For Josephson junctions with surface impedance effects, we have provided compelling numerical evidence that the fluxon switching phenomenon is a nonexistence phenomenon, as opposed to an instability mechanism. Mathematically, this scenario is described by a global bifurcation in the phase space of the reduced travelling wave o.d.e.

The phenomenon which we numerically document here is the breakdown of heteroclinic orbits in a three dimensional dynamical system, undetected in the linearized eigenvalues of the associated fixed points. Mathematical methods have been developed for detecting such global phenomena (see, for example, the text by Guckenheimer and Holmes [24]), but for dynamical systems which do not include our example. Similar phenomena have been studied extensively in models of nerve propagation [25 – 27], reaction-diffusion equations [28 – 30], and population growth [31]. The analytical success in these works rests mainly with proving ex-

istence of global connections between fixed points with purely real linearized eigenvalues. In our example, the heteroclinic connections persist well into the oscillatory regime. Moreover, these rigorous proofs referenced above do not shed light on the breakdown of heteroclinic connections. Our paper provides a model mathematical example for this global bifurcation phenomenon, and poses a challenging problem to prove the scenario we indicate here.

Additional problems are suggested in this study, related to the specific example and to general computational algorithms. Higher order connections between fixed points separated by integer multiples of  $2\pi$  are known to exist and also exhibit switching. We have not investigated these states, but surmise that they also switch due to global bifurcations.

Another area touched upon here and that needs development is the construction of optimal numerical algorithms that establish when a global connection exists, accurately compute it, and then detect global bifurcations as we have illustrated for our example. Global connection algorithms are available for connection from unstable to stable fixed points [32], but the problem is considerably more delicate when orbits connect between unstable fixed points.

## Acknowledgements

We thank Prof. A.C. Scott, Prof. D.W. McLaughlin, and Prof. D. Terman for helpful discussions. The financial support from the European Economic Community through Contract No. St-2-0267-J-C(A), from the European Research Office of the United States Army through Contract No. DAJA-45-85-C-0042, the Thomas B. Thriges Fond (Denmark), and the Gruppo Nazionale di Struttura della Materia, Consiglio Nazionale delle Ricerche - Centro Interuniversitario di Struttura della Materia, Ministero della Pubblica Istruzione (Italy) is gratefully acknowledged.

## Appendix

We take as initial condition for the integration of the  $\Phi_1$  to  $\Phi_3$  connection of Eq. (5) the vector  $\tilde{\Phi} = \tilde{\Phi}_3 + \varepsilon \tilde{\Phi}_u$ , where  $\tilde{\Phi}_u$  is a unit eigenvector associated to  $W'(\Phi_3)$ , (which, under the transformation of Eqs. (13), becomes one-dimensionally unstable), and  $\varepsilon \leq 0.01$ . As emphasized by Miura [27], it is essential to guarantee that  $\varepsilon$  is small enough that the results of the integration do not depend on its value. For all of the calculations reported we have checked this by reducing  $\varepsilon$  until no changes resulted in the computed solution ( $\varepsilon$  down to  $10^{-5}$ ).

Once the initial condition is chosen, the orbit is computed by integrating Eq. (5) using a sixth-order, variable step-size, Runge-Kutta method [33]. This routine has a control over the global error; for all of our computations the global error has been kept sufficiently low that it did not affect the results (typical values of the maximum global error range from  $10^{-5}$  to  $10^{-9}$ ). At each "time" step in the integration the distance  $d(u)$  is computed. The integration is carried on until the orbit, after a first approach to  $\Phi_1$ , diverges away from it. The minimum distance of approach,  $d_{\Phi_1}(u)$ , together with information on "overshooting" or "undershooting" of the solution, is then used to determine the next trial value of  $u$ . The shooting algorithm is repeated several times, each time reducing the interval of  $u$ -values scanned over, until the value  $\hat{u}$  is found to nine significant digits. This procedure is illustrated in Fig. 8, which shows  $d(u)$  vs.  $\Delta u$  on three different scales, where  $\Delta u$  is the variation of  $u$  about  $\hat{u}$ , for the parameter values  $\alpha = 0.05$ ,  $\beta = 0.02$ ,  $\gamma = 0.7$ .

Since  $d_{\Phi_1}(\hat{u})$  will never be exactly zero because of the finite precision of the integration, this procedure, by itself, does not constitute a proof of the existence of a connection. For this reason, we next pass to the continuity diagnostic described in Section III: The velocity  $u$  is varied around  $\hat{u}$  (nine significant digits), and the corresponding value of  $A$  is computed. If  $A$  changes sign crossing  $\hat{u}$ , this strongly implies that there exists a value of  $u$  for which  $A = 0$ , thus demonstrating the existence of an orbit that connects to  $\Phi_1$ .

Analogously to the discussion regarding the choice of the parameter  $\varepsilon$  in the initial condition, we note that a similar consideration applies to the radius,  $R$ , of the sphere constructed around  $\Phi_1$ . As was done for  $\varepsilon$ , we have reduced  $R$  until no changes resulted in the computed solution.

A similar procedure is used to locate the  $\Phi_0$  to  $\Phi_2$  connection, shooting out of  $\Phi_0$ . The procedure could, presumably, also be used to find higher-order connections ( $\Phi_1$  to  $\Phi_5$ , etc.) but we have not yet attempted to do so.

An indication of the overall accuracy of our numerical scheme is suggested in Fig. 2: the theoretical discussion presented in Section III (Eqs. (16) et seq.) shows that simultaneous  $\Phi_0$  to  $\Phi_2$  and  $\Phi_1$  to  $\Phi_3$  connections should exist for  $u = 1$ ; numerically, we find these simultaneous connections for  $u = 0.999999872$ .

## References

- \* Permanent address: Dept. of Mathematics, Ohio State University, Columbus, Ohio 43210, U.S.A.
- \*\* Permanent address: Istituto di Cibernetica del Consiglio Nazionale delle Ricerche, via Toiano 6, I-80072 Arco Felice, Italy.
- \*\*\* Permanent address: Dipartimento di Fisica, Universita degli Studi di Salerno, I-84100 Salerno, Italy.
- 1. A. Barone and G. Paterno, *Physics and Applications of the Josephson Effect*, Wiley, New York, (1982).
- 2. P.S. Lomdahl, O.H. Soerensen, and P.L. Christiansen, "Soliton excitations in Josephson tunnel junctions", *Phys. Rev. B* 25, 5737-5748, (1982).
- 3. A.C. Scott, "Distributed device applications of the superconducting tunnel junction", *Solid-State Electronics* 7, 137-146 (1964).
- 4. D.W. McLaughlin and A.C. Scott, "Perturbation analysis of fluxon dynamics", *Phys. Rev. A* 18, 1652-1680 (1978).
- 5. F. Tricomi, "Integrazione di una equazione differenziale presentatasi in elettrotecnica", *Ann. Scuola Norm. Sup. Pisa* 2, 1-20 (1933).
- 6. M. Urabe, "The least upper bound of a damping coefficient ensuring the existence of a periodic motion of a pendulum under constant torque", *J. Sci. Hiroshima Univ., Ser. A*, 18, 379- (1955).
- 7. W.J. Johnson, "Nonlinear wave propagation on superconducting tunneling junctions", Ph.D. Thesis, University of Wisconsin, Madison (1968).
- 8. R.D. Parmentier and G. Costabile, "Fluxon propagation and d.c. current singularities in long Josephson junctions", *Rocky Mountain J. Math.* 8, 117-124 (1978).

9. P.M. Marcus and Y. Imry, "Steady oscillatory states of a finite Josephson junction", *Solid State Commun.* 33, 345-349 (1980).
10. K. Takanaka, "Zero field steps in Josephson junctions", *Solid State Commun.* 29, 443-445 (1979).
11. J.-J. Chang, J.T. Chen, and M.R. Scheuermann, "Simultaneous excitation of low-frequency cavity modes in short Josephson tunnel junctions", *Phys. Rev. B* 25, 151-156 (1982).
12. K. Enpuku, K. Yoshida, and F. Irie, "Self-resonant current steps of Josephson tunnel junctions in the presence of multimode oscillation", *J. Appl. Phys.* 52, 344-351 (1981).
13. S.E. Burkov and A.E. Lifsic, "Stability of moving soliton lattices", *Wave Motion* 5, 197-213 (1983).
14. M. Büttiker and H. Thomas, "Propagation and stability of kinks in driven and damped nonlinear Klein-Gordon chains", *Phys. Rev. A* 37, 235-246 (1988) + references therein.
15. S. Sakai and H. Tateno, "Analytical solutions of traveling fluxon waves on a Josephson transmission line with shunt conductance and uniform bias current", *Jpn. J. Appl. Phys.* 22, 1374-1381 (1983).
16. S. Sakai and N.F. Pedersen, "Analytic solution for fluxons in a long Josephson junction with surface losses", *Phys. Rev. B* 34, 3506-3509 (1986).
17. S. Sakai, "Bunching of solitons in long Josephson junctions", *Jpn. J. Appl. Phys.* 26, Supplement 26-3, 1579-1580 (1987).
18. A. Ferrigno and S. Pace, "An approximate analysis of the I-V characteristic of zero-field singularities in long Josephson junctions", *Phys. Lett.* 112A, 77-80 (1985).
19. S. Pagano, N.F. Pedersen, S. Sakai, and A. Davidson, "Analytical and numerical results for a long Josephson junction with surface losses", *IEEE Trans. Magnetics MAG-23*, 1114-1117 (1987).

20. K. Nakajima, Y. Onodera, T. Nakamura, and R. Sato, "Numerical analysis of vortex motion on Josephson structures", *J. Appl. Phys.* 45, 4095-4099 (1974).
21. S.N. Erné and R.D. Parmentier, "Microwave oscillators based on the resonant propagation of fluxons in long Josephson junctions", *J. Appl. Phys.* 51, 5025-5029 (1980).
22. A. Davidson, N.F. Pedersen, and S. Pagano, ""Effect of surface losses on soliton propagation in Josephson junctions", *Appl. Phys. Lett.* 48, 1306-1308 (1986).
23. S. Pagano, M.P. Soerensen, P.L Christiansen, and R.D. Parmentier, "Stability of fluxon motion in long Josephson junction at high bias", *Phys. Rev. B* 38, (in press).
24. J. Guckenheimer and P. Holmes, *Nonlinear Oscillations, Dynamical Systems and Bifurcations of Vector Fields*, Springer, Berlin (1983).
25. S.P. Hastings, "On the existence of homoclinic and periodic orbits for the FitzHugh-Nagumo equations", *Quarterly J. Math. Oxford*, Ser. 27, 23-24 (1976).
26. A.C. Scott, *Neurophysics*, Wiley, New York (1977).
27. R.M. Miura, "Accurate computation of the stable solitary wave for the FitzHugh-Nagumo equations", *J. Math. Biology* 13, 247-269 (1982).
28. W.C. Troy, "The existence of travelling wave front solutions of a model of the Belousov-Zhabotinsky chemical reaction", *J. Differential Equations* 36, 89-98, (1980).
29. C. Conley and R. Gardner, "An application of the generalized Morse index to travelling wave solutions of a competitive reaction-diffusion model", *Indiana University Math. J.* 33, 319-343, (1984).
30. D. Terman, "Connection problems arising for nonlinear diffusion problems", *Proc. Microprogram on Nonlinear Diffusion Equations and their Equilibrium States*, (J. Severin et. al. eds.) Berkeley, California (1986).

31. S. Dunbar, "Travelling wave solutions of the diffusive Lotka-Volterra equations: A heteroclinic connection in competitive reaction-diffusion model in  $\mathbb{R}^4$ ", *Trans. of the AMS* 286, 557-594, (1984).
32. AUTO Numerical Package developed by E. Doedel.
33. Subroutine DVERK in IMSL, Inc. (Houston, Texas), International Mathematical and Statistical Library (Edition 9), 1982.

## Figure captions

- Fig. 1** Experimental I-V characteristic of a long Josephson junction with overlap geometry. The critical current  $I_0$  and six ZFS's are shown. Arrows indicate the direction of the voltage change during the switching.
- Fig. 2a**  $\Phi_1 - \Phi_3$  connection (full curve) and  $\Phi_0 - \Phi_2$  connection (dashed curve) projected into the  $(\phi, \phi_t)$  plane as obtained from numerical integration of Eq. (5).  $\alpha = 0.18, \beta = 0.1, \gamma = 0.883442, u = 0.999999872$ .
- Fig. 2b** Same connections as in Fig. 2a but projected into the  $(\phi, \phi_{tt})$  plane.
- Fig. 3a** Phase space projections into the  $(\phi, \phi_t)$  plane of the orbits leaving  $\Phi_0$  and  $\Phi_3$ .  $\alpha = 0.18, \beta = 0.1, \gamma = 0.88, u = 0.998733778$ . For these parameter values only the  $\Phi_1 - \Phi_3$  connection exists.
- Fig. 3b** Same as Fig. 3a but projected into the  $(\phi, \phi_{tt})$  plane.
- Fig. 4a** Locus of the  $\Phi_1 - \Phi_3$  (a), and of the  $\Phi_0 - \Phi_2$  (b) connections in the  $\gamma - u$  plane near  $u = 1$ .  $\gamma^* \approx 0.888$  is the switching bias value.  $\alpha = 0.18, \beta = 0.1$ .
- Fig. 4b** Detail of curves of Fig. 4a.
- Fig. 5** 3-D picture of the numerical solution of the p.d.e. Eq. (1) showing a stable fluxon moving with a speed larger than unity.  $\alpha = 0.18, \beta = 0.1, \gamma = 0.888, u = 1.0018$ .
- Fig. 6** Locus of the  $\Phi_1 - \Phi_3$  (full line) and the  $\Phi_0 - \Phi_2$  (dash-dotted line) connections in the  $\gamma - u$  plane near  $u = 1$ . Also shown are  $d_{\Phi_1}$  (dotted line) and  $d_{\Phi_2}$  (dashed line) vs  $\gamma$ .
- Fig. 7** Roots of  $P_+(\lambda)$  (a,b) and  $P_-(\lambda)$  (c,d) along the locus of the  $\Phi_1 - \Phi_3$  (a,c) and the  $\Phi_0 - \Phi_2$  (b,d) connections. The real root (dash-dotted line) and the complex conjugate roots (full line = real part, dashed line = imaginary part) are shown vs  $\gamma$ .  $\alpha = 0.18, \beta = 0.1$  and  $\gamma^* \sim 0.8877$  is the switching bias value

**Fig. 8**  $d_{\Phi_1}$  vs  $\Delta u$  at various scales.  $\alpha = 0.05$ ,  $\beta = 0.02$ ,  $\gamma = 0.7$ ,  $u = \hat{u} + \Delta u$ ,  $\hat{u} = 0.9956555358$  is the velocity value at which the  $\Phi_1 - \Phi_3$  connection exists. (a) shows a false local minimum at  $\Delta u \approx 0.00015$ , (b) shows another false local minimum at  $\Delta u \approx -2 \times 10^{-7}$ , (c) shows the true minimum ( $\Delta u = 0$ ).

Fig. 1  
Forest e

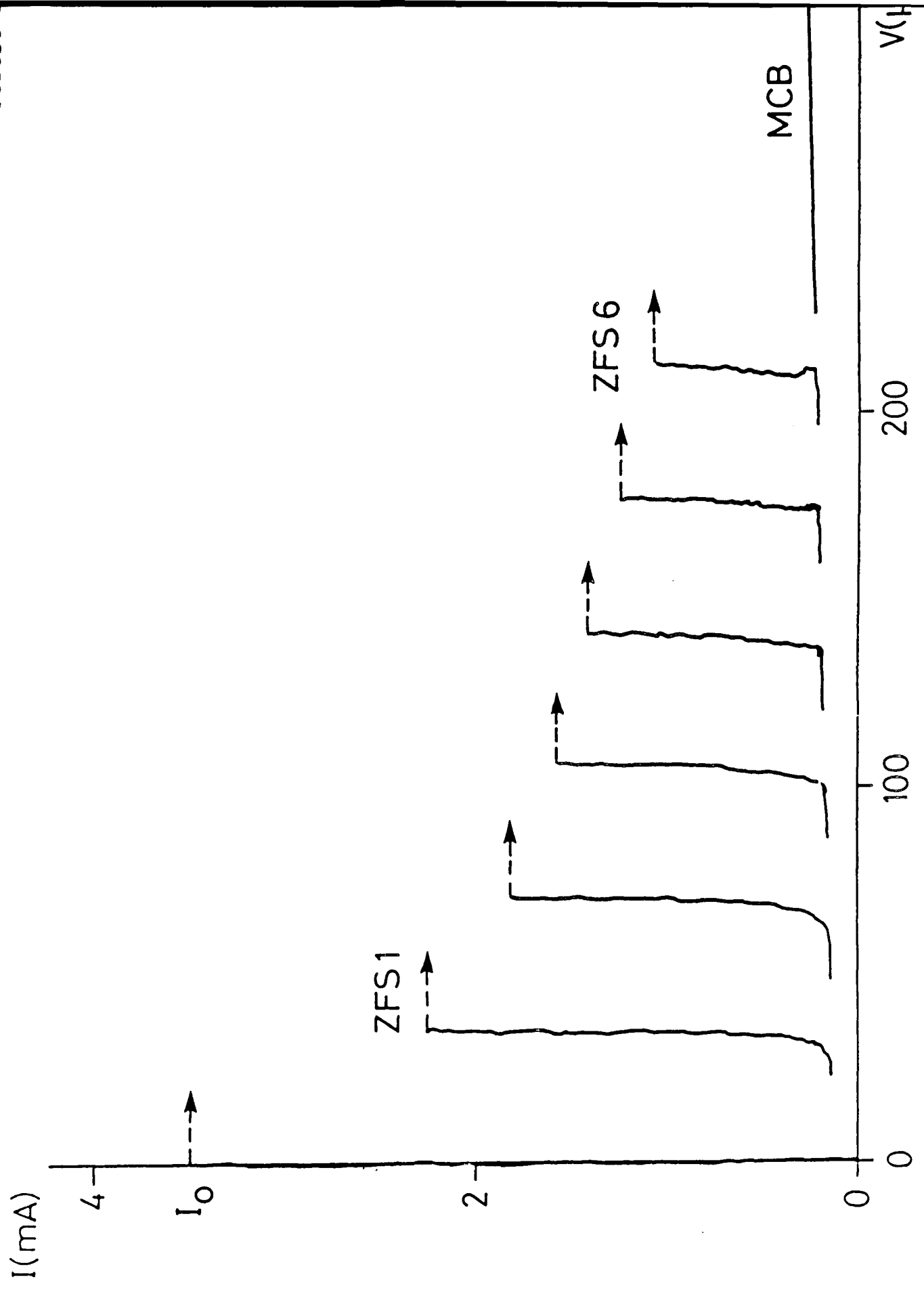


Fig. 2a  
Forest &

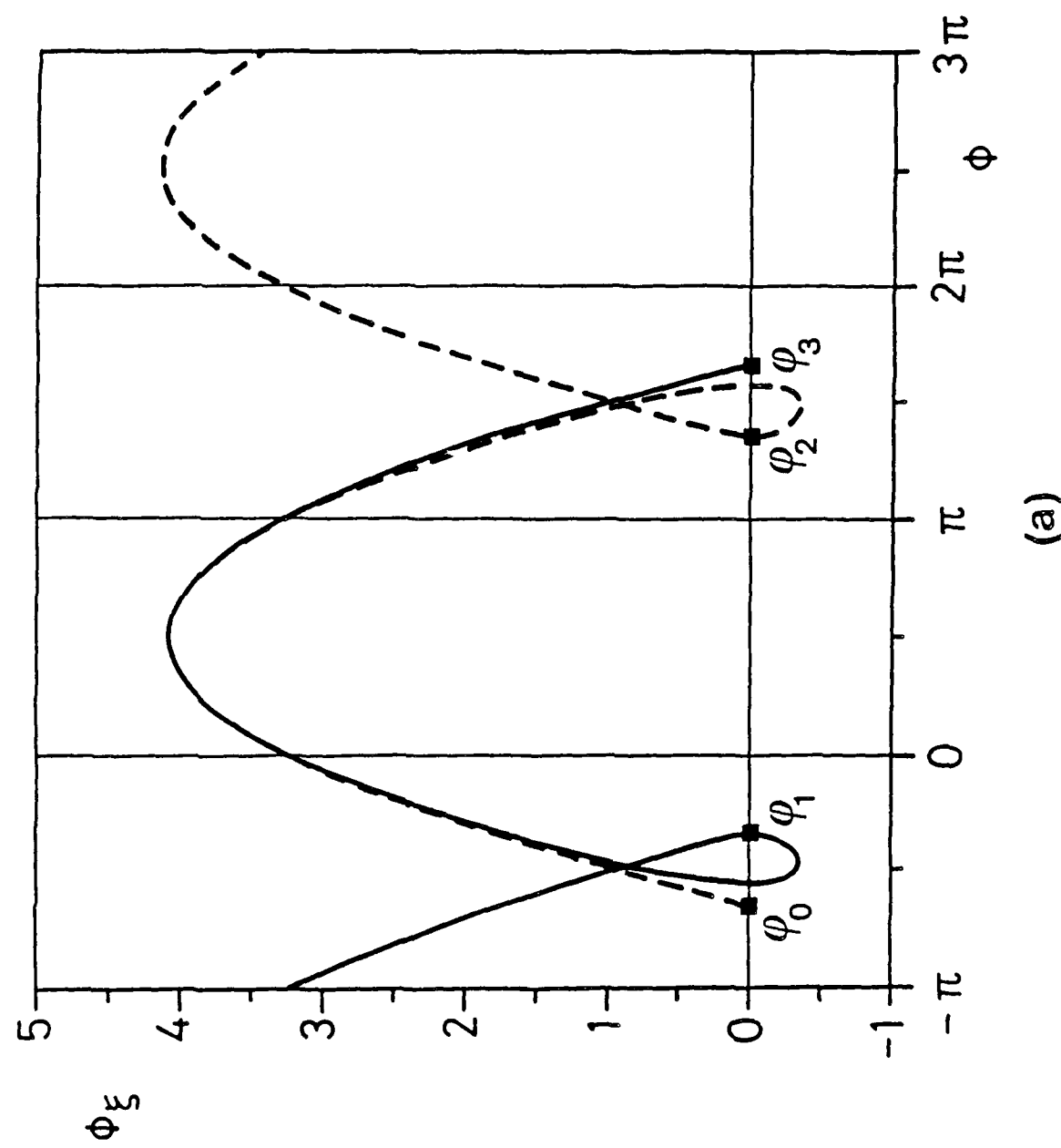


Fig. 2b  
Forest e

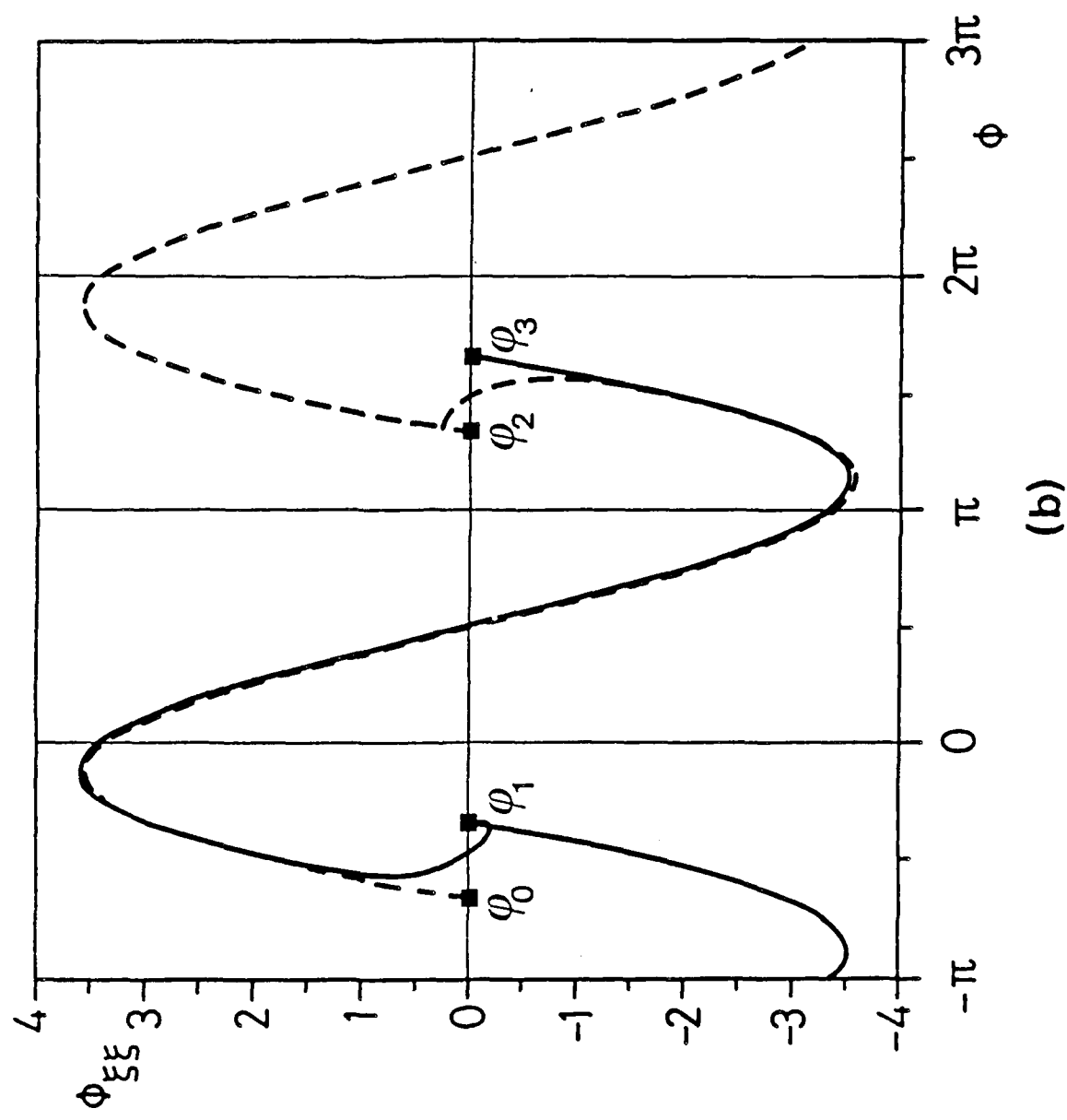


FIG. 3a  
Forest e

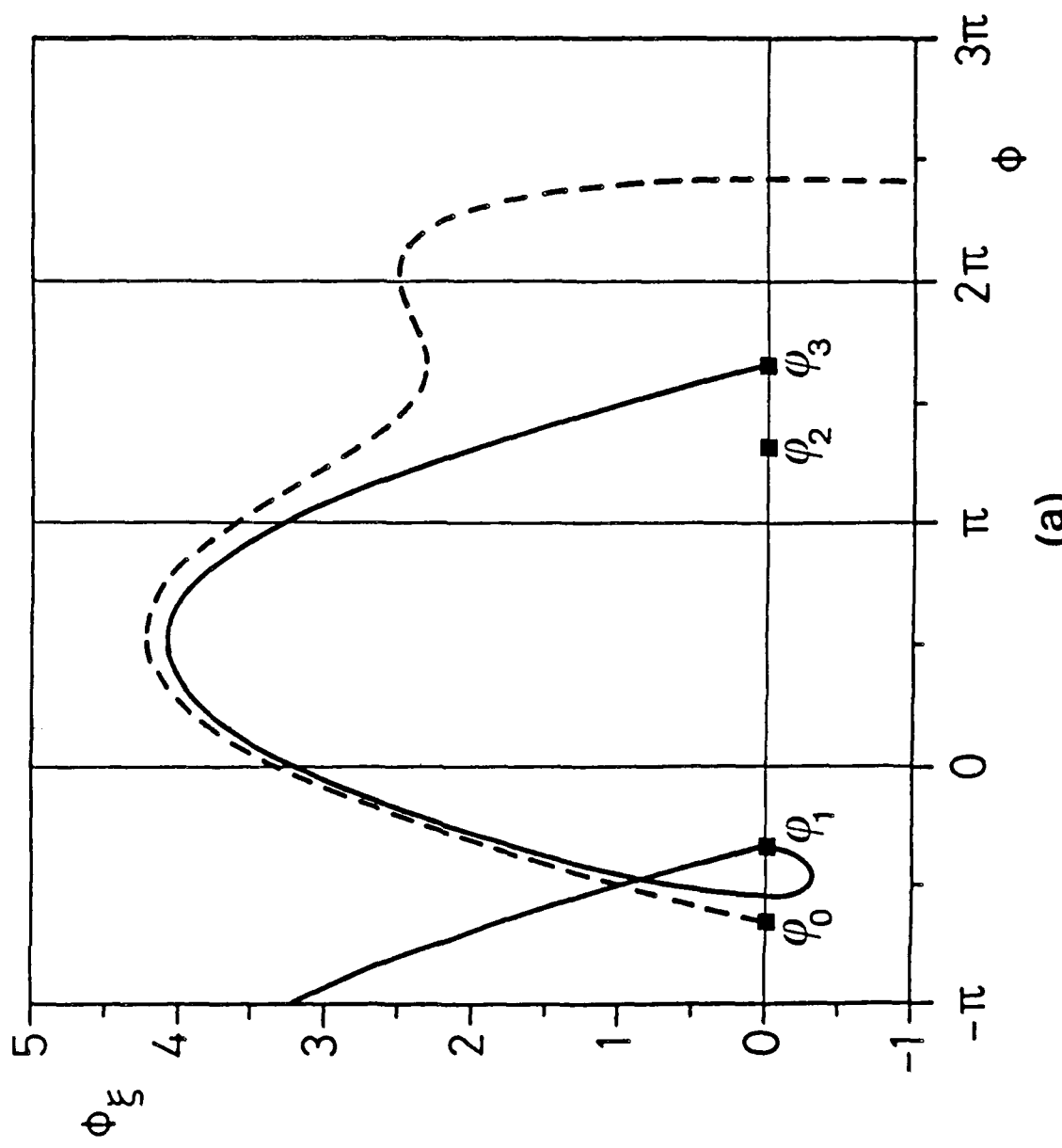


Fig. 3b  
Forest e

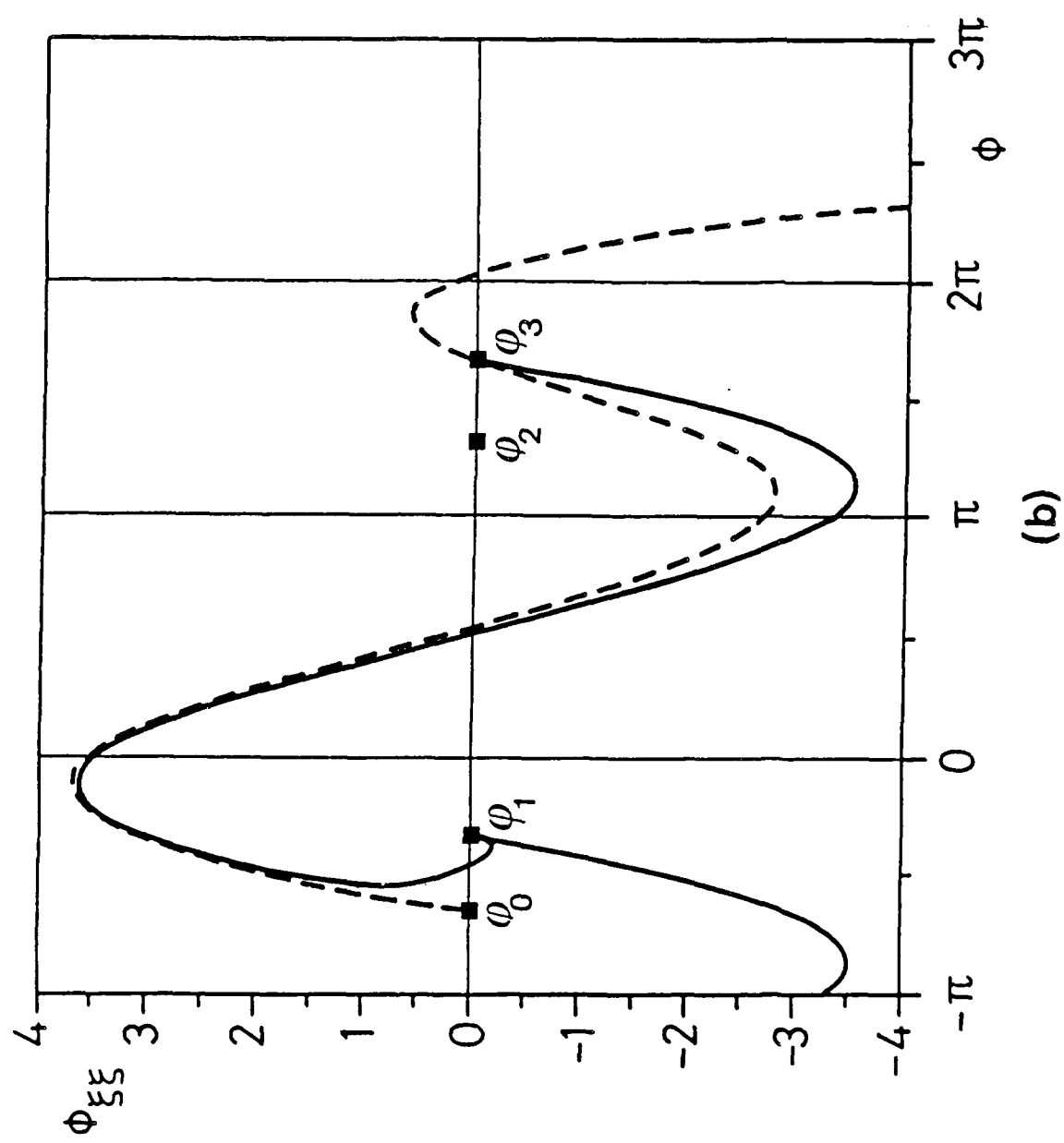


Fig. 4a  
Forest  $\epsilon$

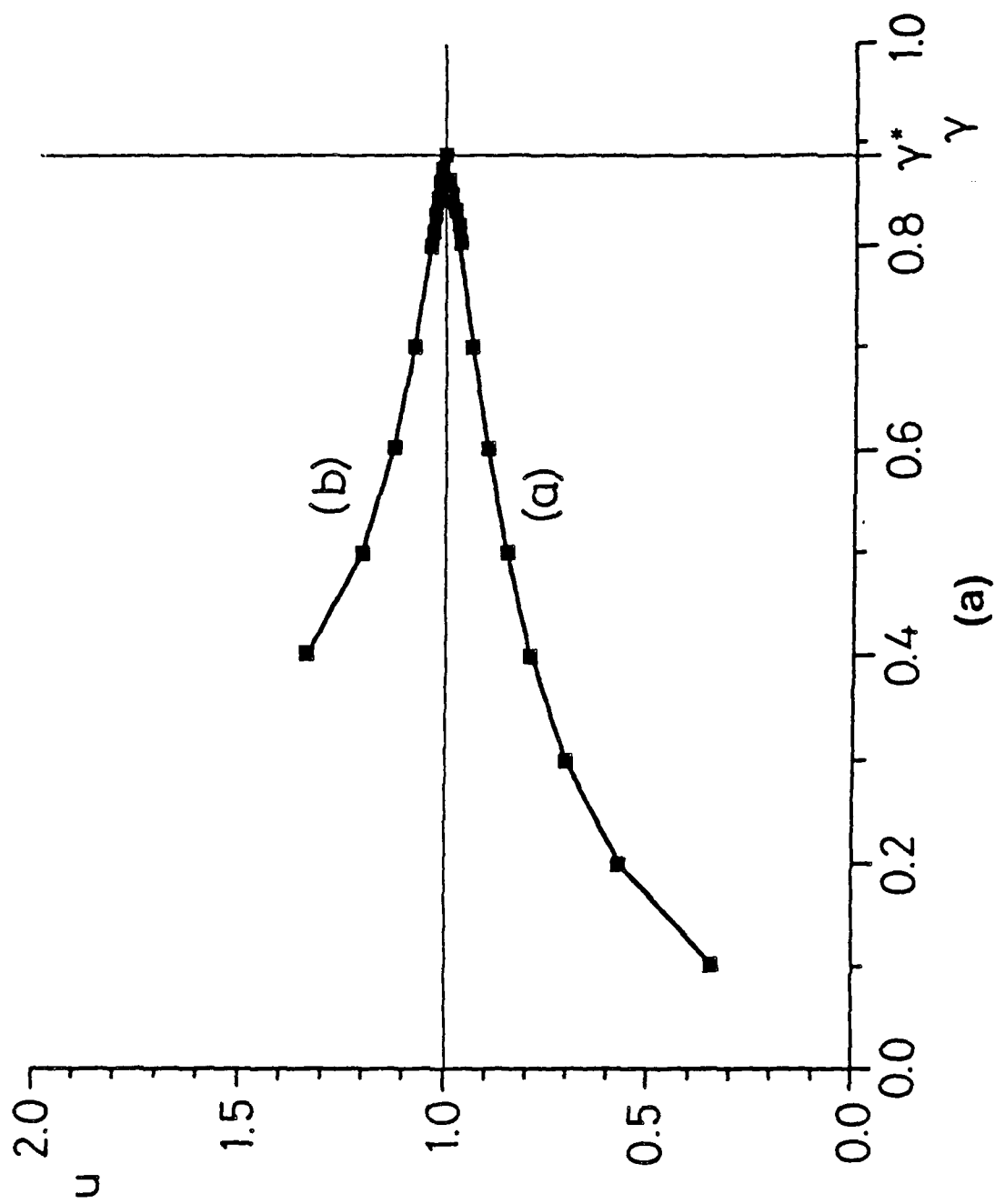


Fig. 4b  
Forest e

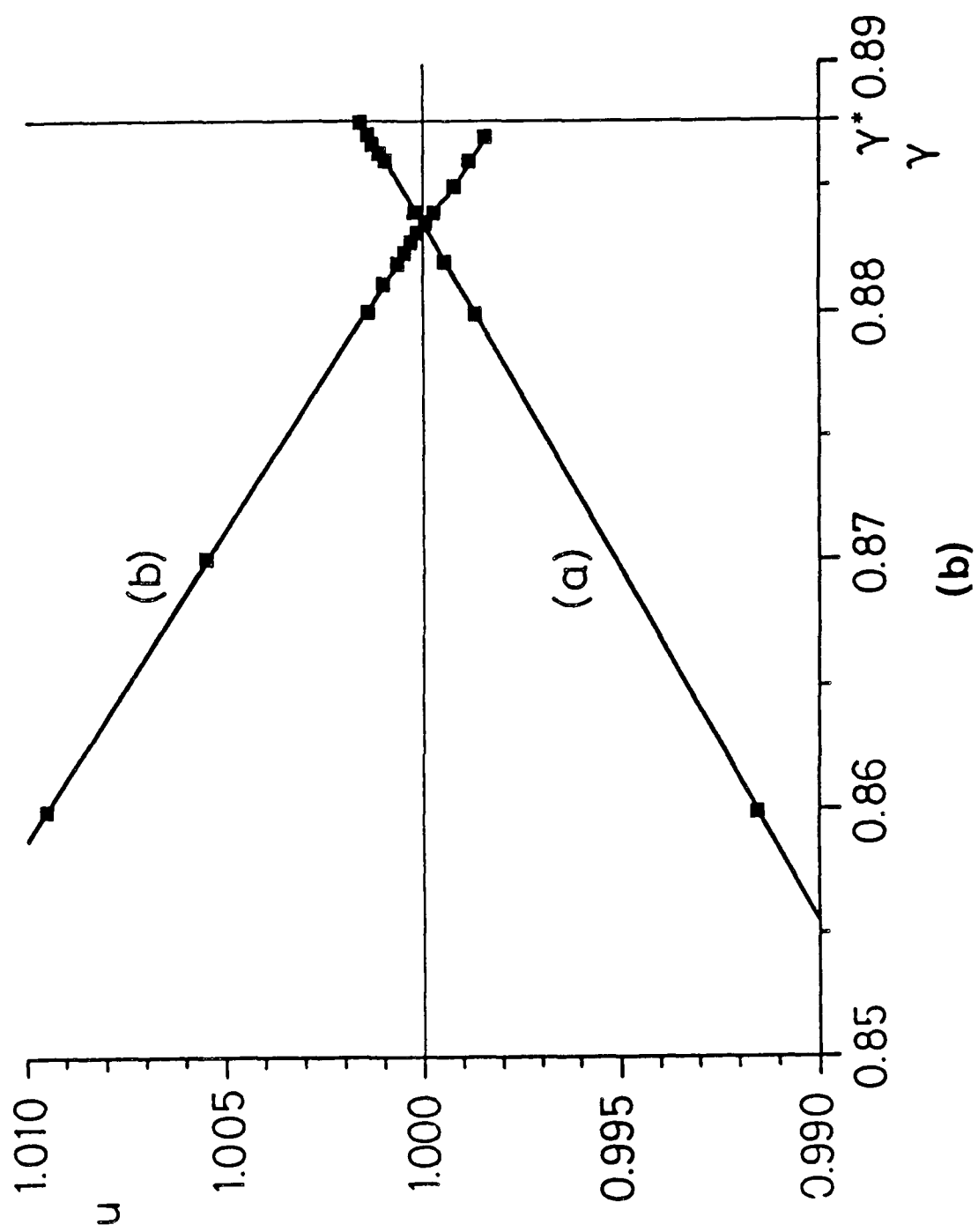
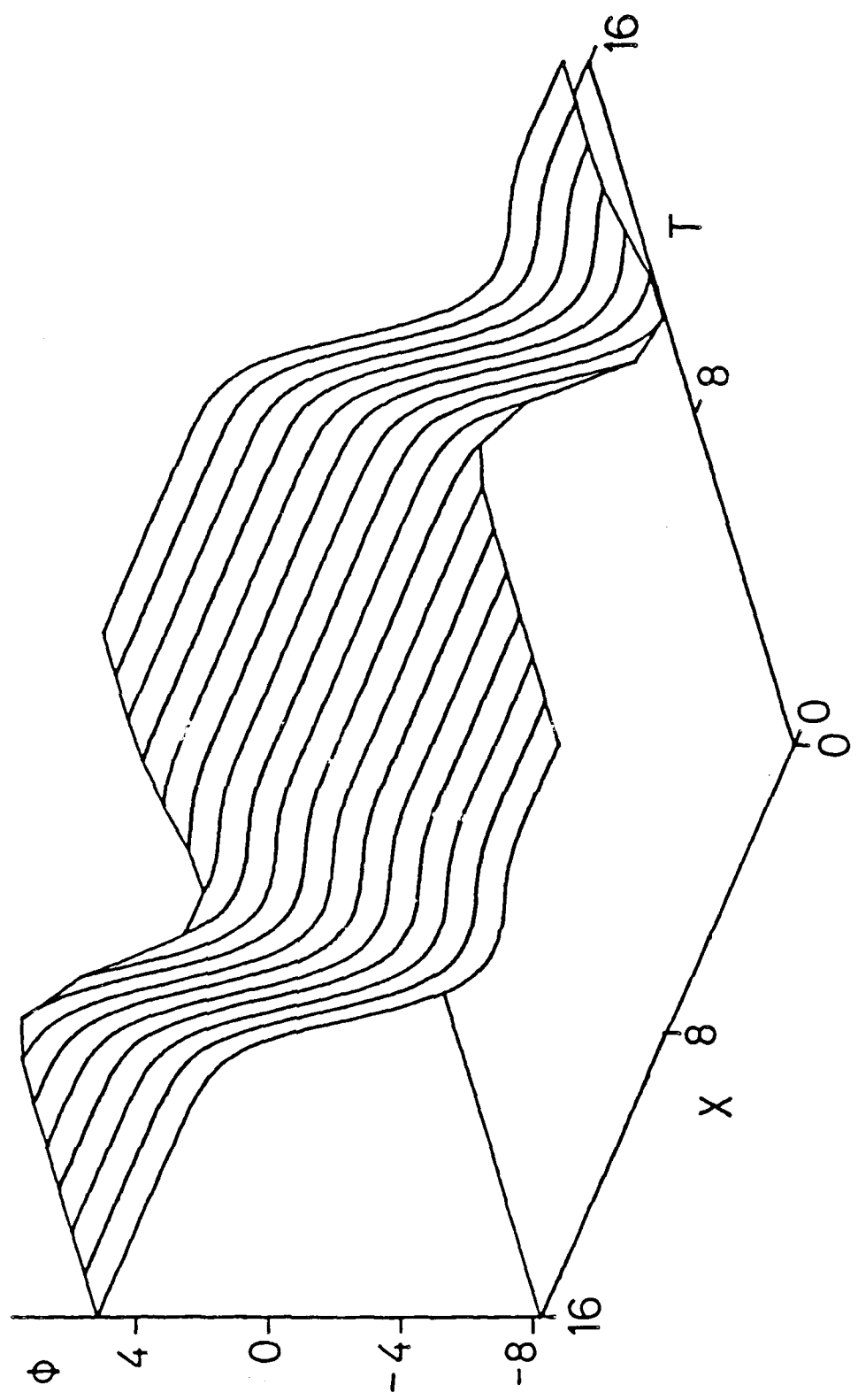
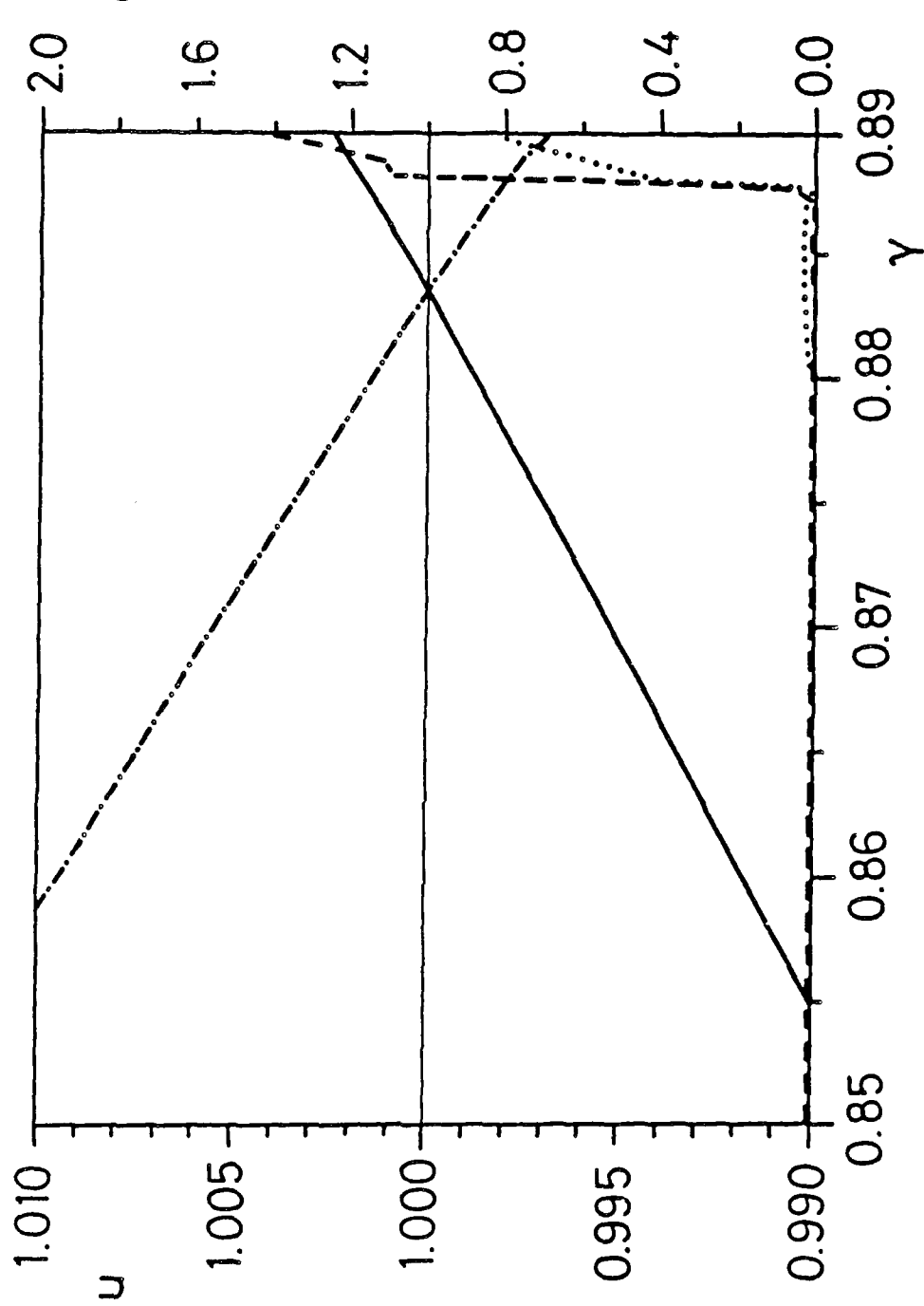


Fig. 5  
Forecast of





Forrest e

F29. 6 .

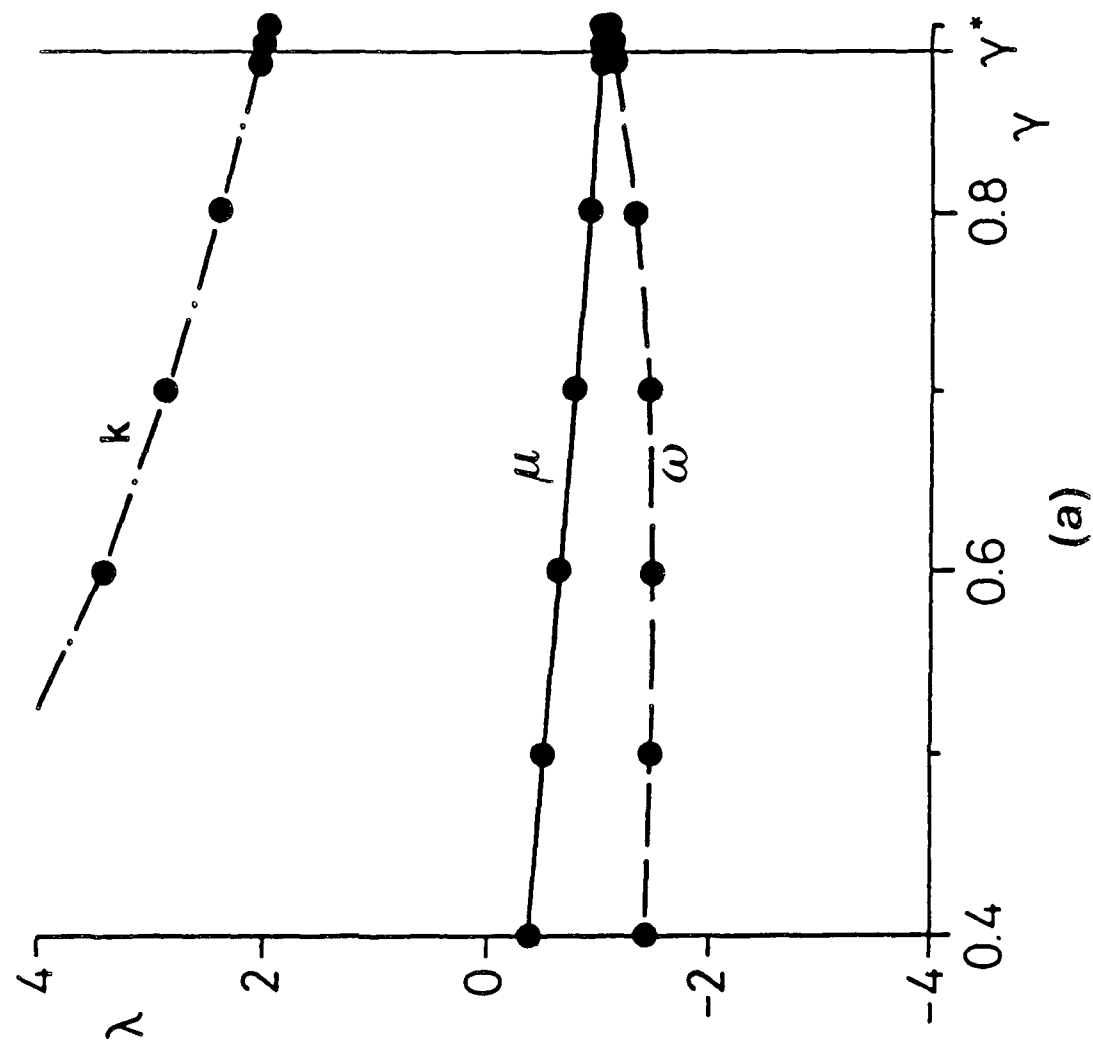


Fig. 7b  
Forest et

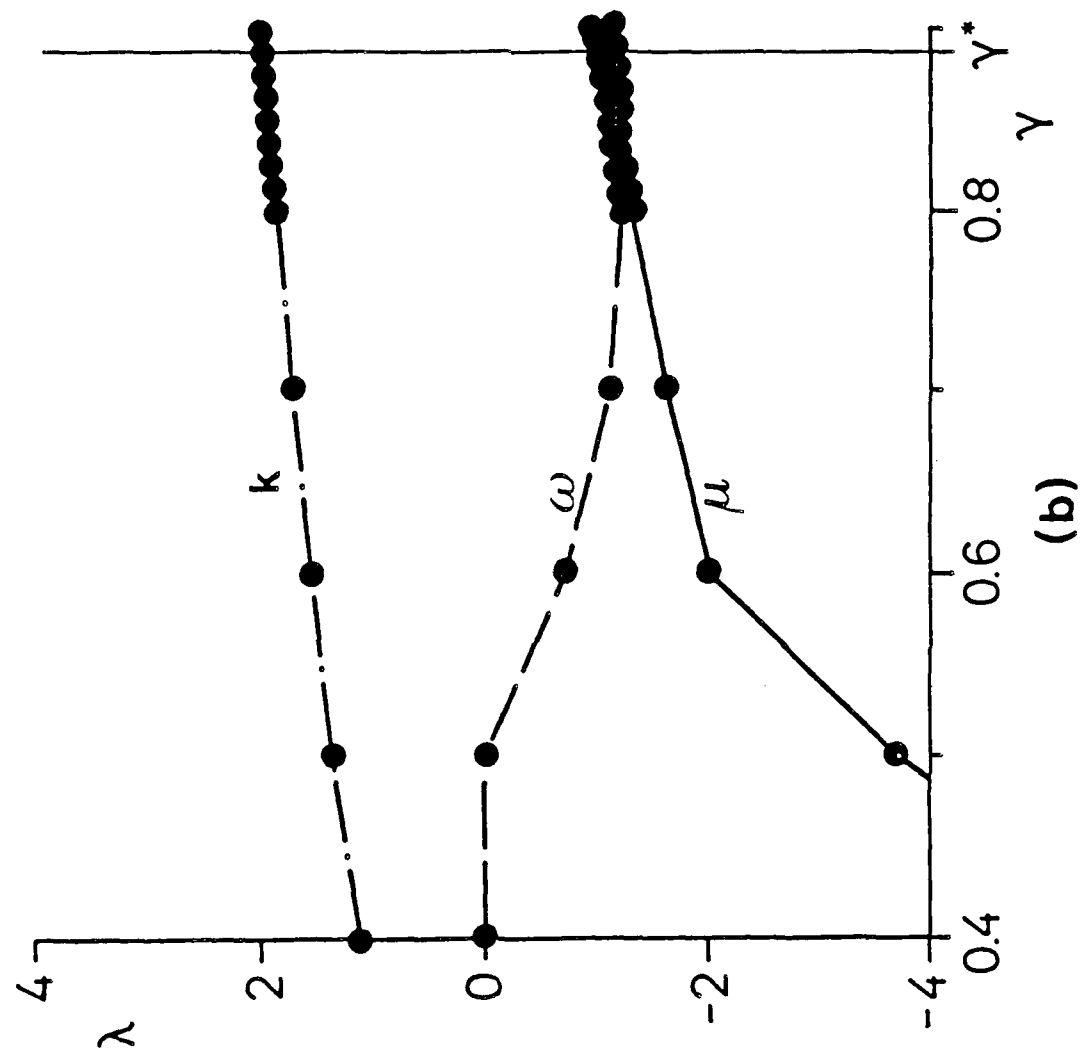


FIG. 7C  
Forest e

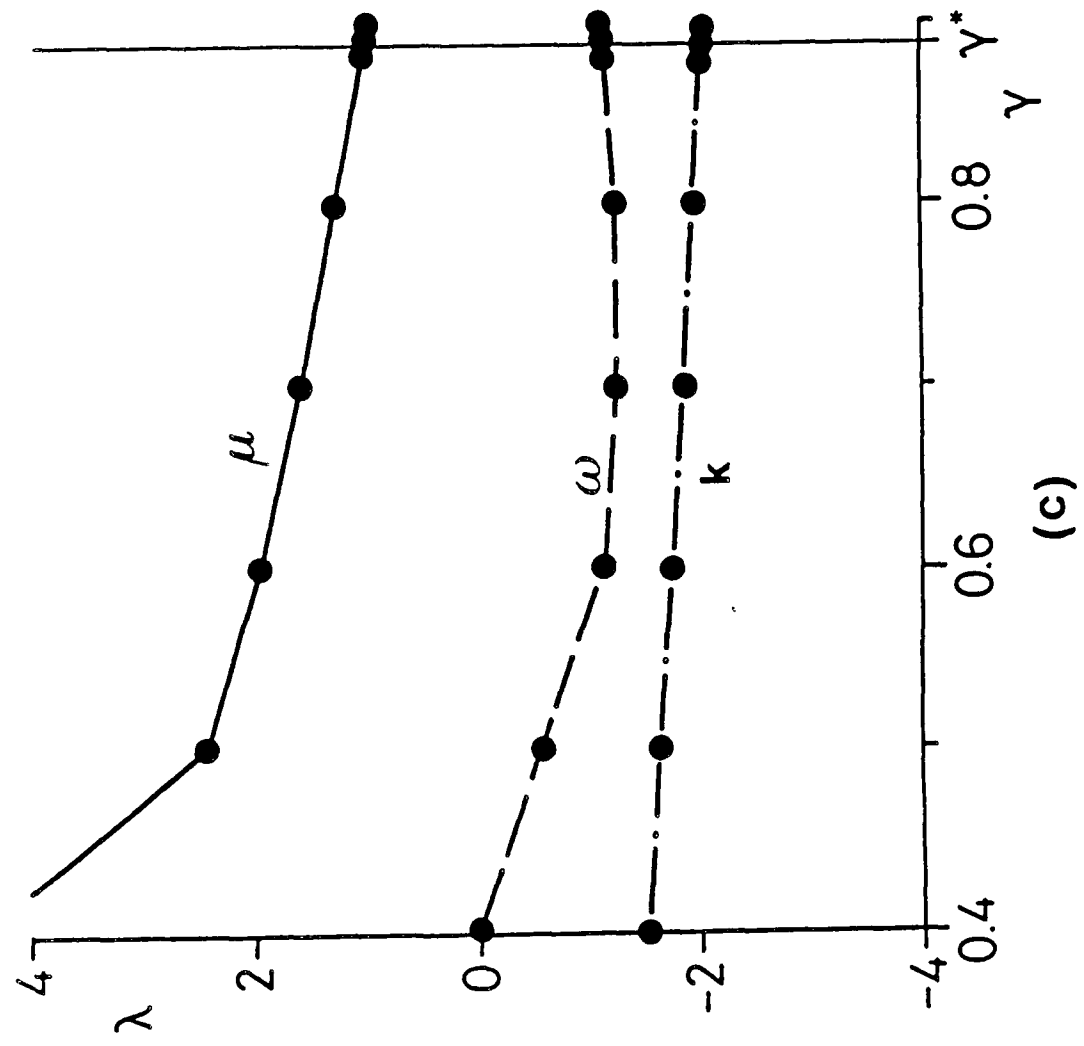


Fig. 7d  
Forest e

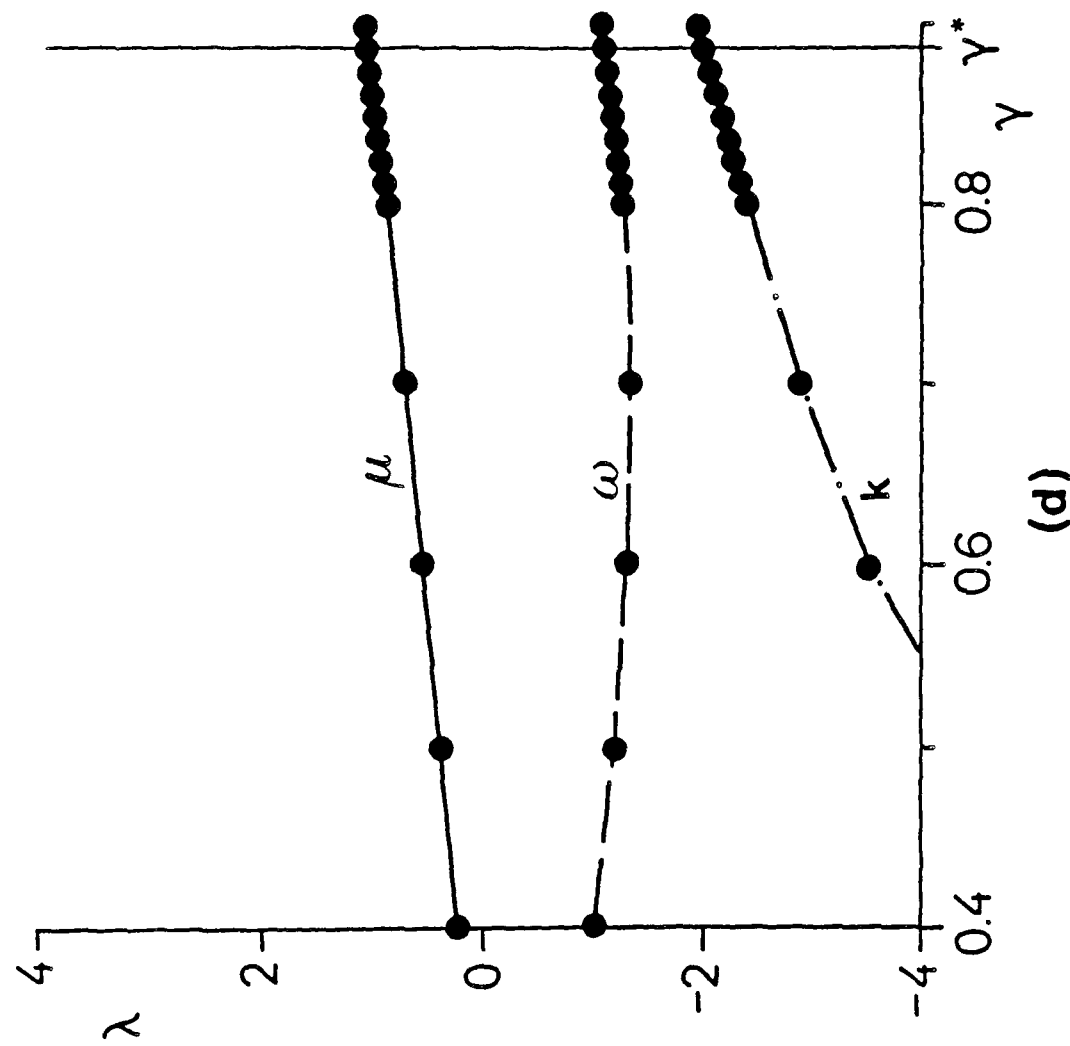
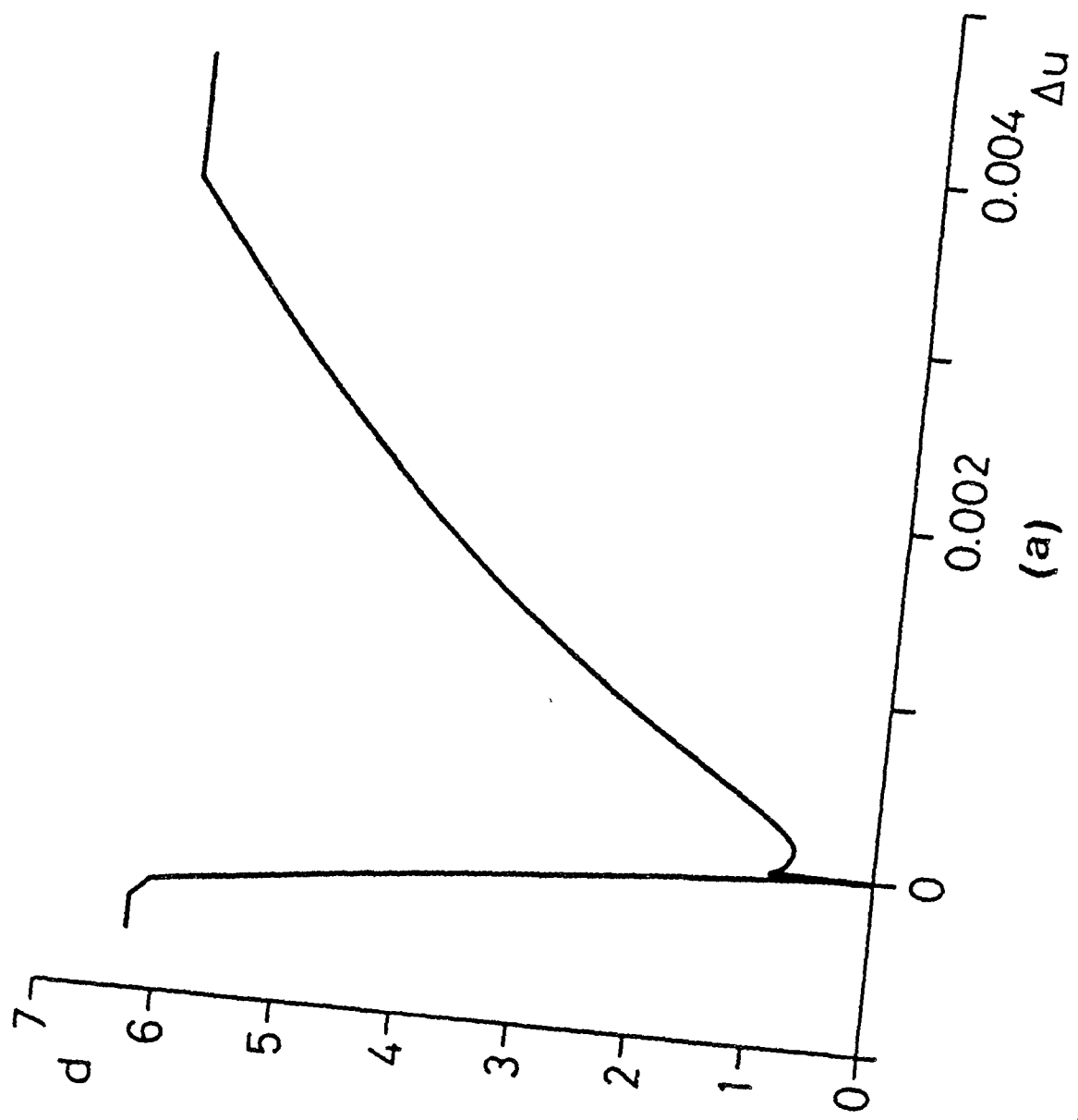


Fig. 8a  
Forest e<sub>1</sub>



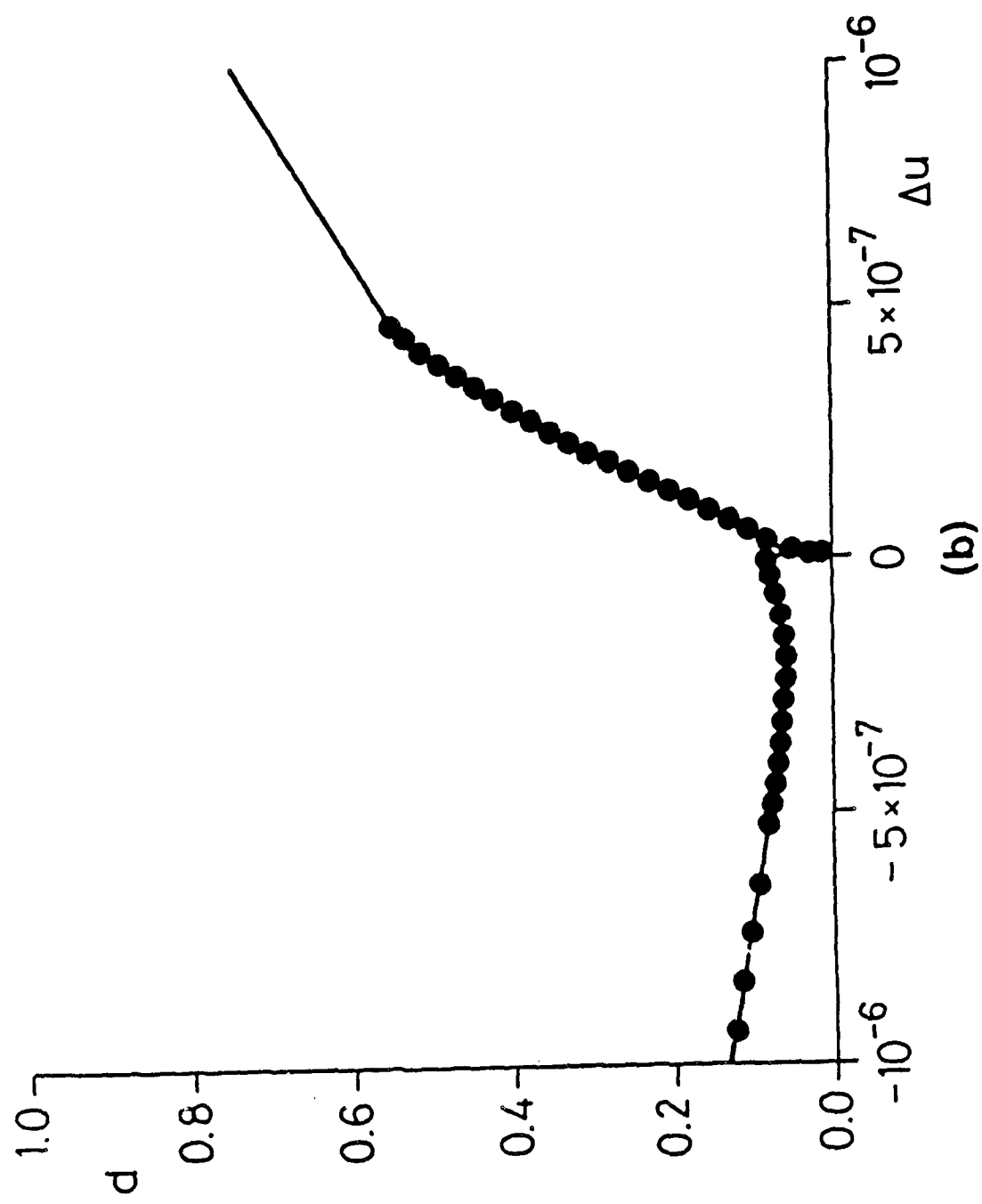
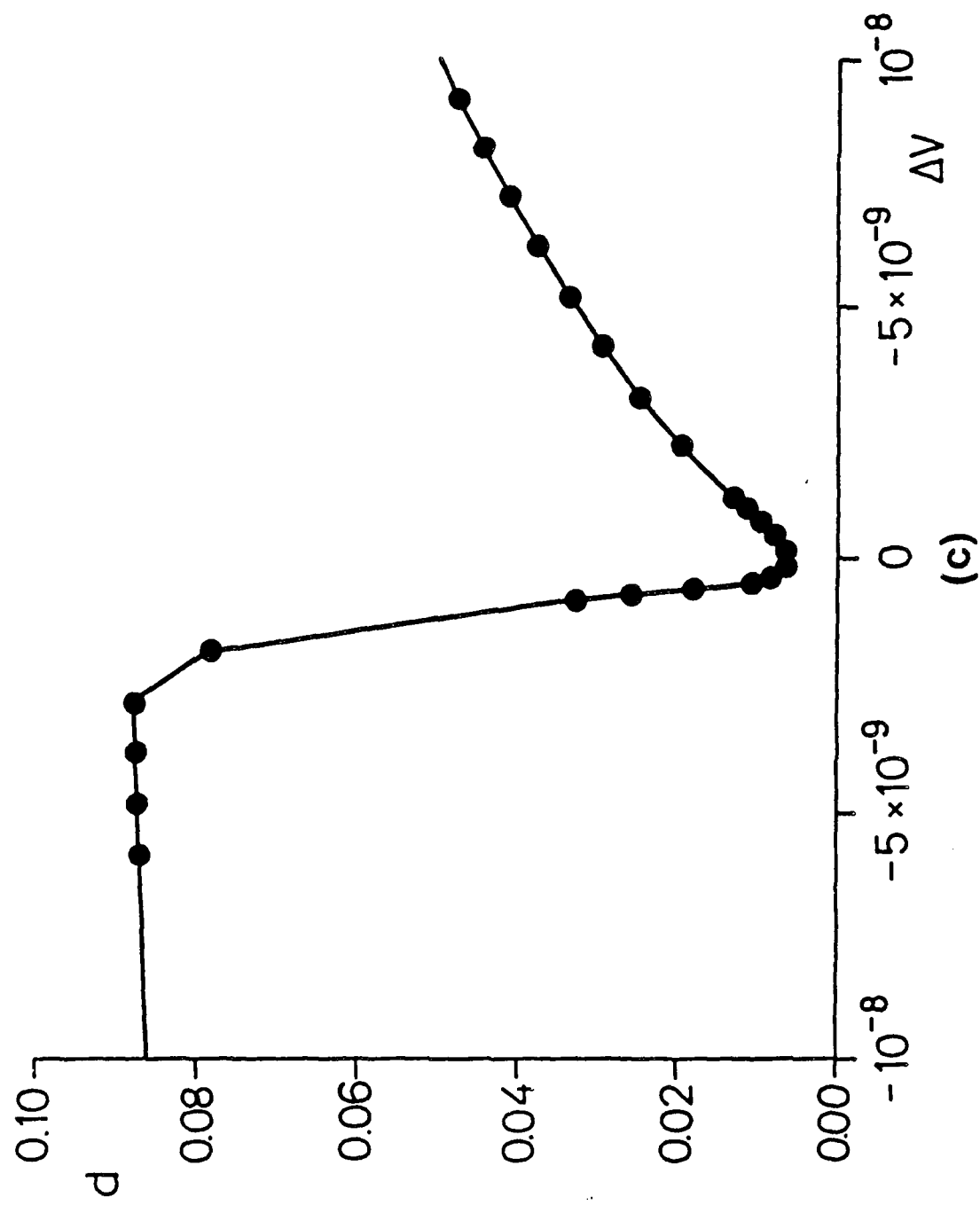


Fig. 8c  
Forecast e



internal oscillation frequencies and anharmonic effects for  
the double sine-Gordon kink

by

M. Salerno\*, M. R. Samuelsen\*\*

MIDIT, The Technical University of Denmark  
DK-2800 Lyngby, Denmark.

submitted to  
Phys Rev B

\*) also Laboratory of Applied Mathematical Physics,  
The Technical University of Denmark, DK-2800 Lyngby  
(permanent address: Dipartimento di Fisica Teorica dell'  
Universita', I-84100 Salerno, Italy)

\*\*) also Physics Laboratory I, The Technical University of  
Denmark, DK-2800 Lyngby, Denmark.

Abstract

A simple derivation of the small oscillation frequency around  $4\pi$ -kink solutions of the double sine-Gordon equation is presented. Small corrections to these frequencies due to anharmonic effects are also numerically and analytically investigated. The analysis is based on energetic considerations and on the mechanical interpretation of a  $2\pi$ -kink as two point particles connected by a spring.

## I. Introduction

The double sine-Gordon equation (DSG)

$$\Phi_{xx} - \Phi_{yy} + \lambda_1 \sin\Phi + \lambda_2/2 \sin(\Phi/2) = 0 \quad (1)$$

has received much attention during the past years because of its connection with several physical phenomena such as spin dynamics of superfluid  $^3\text{He}$  [1], commensurate-incommensurate phase transitions [2], magnetic chains [3], domain walls [4], etc. In both limits  $\lambda_1 = 0$  and  $\lambda_2 = 0$  equation (1) reduces to the well-known sine-Gordon equation (SG) with exact soliton solutions. For  $\lambda_1 \neq 0$  and  $\lambda_2 \neq 0$  equation (1) has different classes of solitary wave solutions which undergo weakly inelastic scattering [5]. Among these solutions there is a subclass (4 $\pi$ -kink) which can be expressed as linear superposition of two sine-Gordon solitons [6]

$$\Phi(x, R_c) = 4\tan^{-1}[\exp(-x+R_c)] + 4\tan^{-1}[\exp(x+R_c)] + 2\pi \quad (2)$$

with  $2R_c$  a constant representing the distance between the two sine-Gordon solitons, and  $R_c$  is related to  $\lambda_1$  and  $\lambda_2$  in (1) by

$$\lambda_1 = \tanh^2 R_c, \quad \lambda_2 = -4 \operatorname{sech}^2 R_c. \quad (3)$$

From numerical studies on the small oscillation problem around solution (2) it is well known that besides a zero mode

frequency (related to translational invariance) there is an additional bound state corresponding to internal oscillations of the two sine-Gordon solitons around the center of mass of solution (2). Slightly different analytical expressions for the frequency of such oscillation have been derived [7,8]. The aim of the present paper is to present a simple derivation of the small oscillation frequencies around 4n-kink solutions and to study corrections to these frequencies due to anharmonic effects. The analysis will be based on energetic considerations and on a mechanical analog of solution (2) as two point particles connected by a nonlinear spring [9,10]. The frequency of the oscillations is then computed in terms of the mass of the particle and of the spring constant of the 4n-kink oscillator. A numerical investigation of the anharmonic effects of the 4n-kink oscillations is also performed and compared with results obtained by a perturbation analysis. As a result we find the same analytical expression for the small oscillation frequency reported in Ref. [7], while the corrections to these frequencies due to anharmonicity appear to be very small.

The organization of the paper is as follows. In section II we present the derivation of the small oscillation frequency expression while in section III we study both numerically and analytically the corrections to this frequency due to anharmonic effects.

Finally, section IV contains the summary and the conclusions of the paper.

#### II. DERIVATION

We start by introducing the hamiltonian for eq. (1)

$$H = \int_{-\infty}^{+\infty} [1/2(\phi_+^2 + \phi_-^2) + \lambda_1(a_+ - \cos\phi) + \lambda_2(a_- - \cos(\phi/2))] dx \quad (4)$$

where  $a_+$ ,  $a_-$  are suitable normalization constants.

Equation (2) is an exact solution of equation (1) when  $R_+$  is a constant and  $\lambda_1$ ,  $\lambda_2$  are given by equation (3). In this case the hamiltonian (4) aquires the form

$$H = \int_{-\infty}^{+\infty} [1/2(\phi_+^2 + \phi_-^2) + (1 - \operatorname{sech}^2 R_0)(1 - \cos\phi) + 4\operatorname{sech}^2 R_0(1 + \cos(\phi/2))] dx \quad (5)$$

where the normalization constants  $a_+$ ,  $a_-$  have been chosen to give zero energy at  $\phi = \pm 2\pi$ . In order to characterize small oscillations around solution (2), we observe that for a "wobbler" (i.e. an oscillating  $4\pi$ -kink) the distance between the two sine-Gordon solitons oscillates around their static separation  $2R_+$ . It is therefore natural to assume for such a solution an analytical expression given by equation (2) but with  $R_+$  replaced by a time dependent function  $R(t)$  according to

$$\phi = \phi(x, R(t)) = 4\tan^{-1}[\operatorname{sinh}x\operatorname{sech} R(t)] \quad (6)$$

By substituting (6) in (5) and performing the corresponding integral one obtains after some computations

$$H(R, R_t) = E[1 - (2R/\operatorname{sinh}2R)]R^2 + V(R, R_t) \quad (7)$$

where

$$E = (1/4)\tanh^2(R)[1 - (2R/\operatorname{sinh}2R)] + \\ (R/\operatorname{sinh}2R)[1 + \operatorname{cosech}(2R/\operatorname{sinh}2R)](R/\operatorname{tanh}(2R-1)).$$

AD-A205 469

COHERENCE AND CHAOS PHENOMENA IN JOSEPHSON OSCILLATORS  
FOR SUPERCONDUCTIN

373

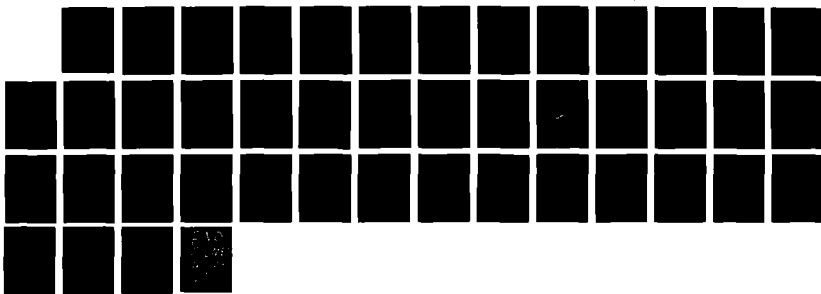
(U) TECHNICAL UNIV OF DENMARK

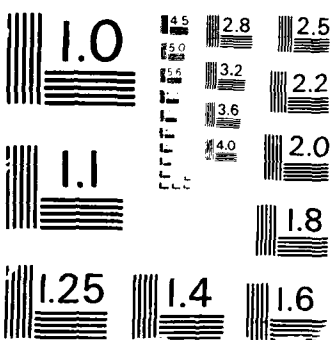
LYNGBY LAB OF APPLIED MATHEMATICAL P

UNCLASSIFIED P L CHRISTIANSEN ET AL 25 JAN 89

F/G 9/1

NL





Equation (7) simply represents the total energy of the waveform (6) expressed as the sum of a kinetic part and a potential one (note the analogy with particles). We also note that in deriving eq. (7) the only approximation made was the ansatz (6) for the oscillating 4n-kink. When  $2R$  is equal to the static separation  $2R_0$  of the two subsolitons equation (7) simply reduces to the rest mass energy of solution (2)

$$M_0 = 16[1 - R_0/(S_0 C_0)]. \quad (9)$$

where  $S_0 \equiv \sinh R_0$  and  $C_0 \equiv \cosh R_0$ .

Introducing the instantaneous mass

$$M(t) = 16[1 - 2R(t)/\sinh(2R(t))] \quad (10)$$

equation (7) acquires the form

$$H(R, R_{\dot{}}) = 1/2 M(t) \dot{R}^2 + V(R, R_{\dot{}}). \quad (11)$$

To study small oscillations around  $2R_0$ , we let  $|R-R_0| \ll 1$ . In this case we can expand the potential energy around  $R_0$  as:

$$V(R, R_{\dot{}}) \approx V_{,0} + V_{,0}'(R-R_0)' + 1/2 V_{,0}''(R-R_0)^2 + \dots \quad (12)$$

(here primes denote derivatives with respect to  $R$  while the subscript zero means evaluation at  $R = R_0$ ).

From eq. (8) the first derivative of  $V$  is easily calculated as

$$V''(R, R_e) = \frac{8[(\cosh^2 R / \cosh^2 R_e) - 1][2\cosh^2 R \sinh^2 R + \sinh^2 R \cosh^2 R - R(4\sinh^2 R + 2)]}{(\sinh^2 R \cosh^2 R)} \quad (13)$$

from which one see that

$$V_{ee}'' = 0 \quad (14)$$

i.e.,  $R_e$  is an extremum for the potential  $V(R, R_e)$ .

In Fig. 1  $V(R, R_e)$  is plotted versus  $R$  for different values of  $R_e$ , from which one see that  $R_e$  is actually a minimum for  $V$ . (Note also that the potential has a finite value at  $R=0$ ).

By inserting equation (14) in (12) we get

$$V(R, R_e) \approx V_{ee} + (1/2)V_{ee}''(R-R_e)^2 \quad (15)$$

and Eq. (11) becomes

$$H \approx 1/2 M_e \ddot{R}^2 + 1/2 V_{ee}''(R-R_e)^2 + V_{ee} \quad (16)$$

where we have approximated  $M(t)$  with its equilibrium value  $M_e$  and neglected higher order terms in  $R-R_e$ .

Equation (16) is just the energy of a harmonic oscillator in the presence of an external constant potential. The frequency is then evaluated as

$$\omega^2 = 3/S_e^2 - 2(S_e C_e + R_e)/[2(C_e S_e^2(S_e C_e - R_e))] \quad (17)$$

which is exactly the same expression as in given in Ref. [7].

### III. Anharmonic effects

In this section we study the corrections to the small oscillation frequency (17) due to anharmonic effects.

To this end we must take into account the fact that the mass of the oscillator is a function of time (see Eq. (10)). By differentiating Eq. (11) with respect to time and expanding the resulting equation in powers of  $\xi = R(t) - R_0$  up to third order one get

$$M_0 \ddot{\xi} + \omega_0^2 \xi + 1/2 V_0''' \xi^2 + 1/2 M_0' (\dot{\xi}^2 + 2\ddot{\xi}\dot{\xi}) + 1/2 M_0'' (\dot{\xi}^2 + \xi\ddot{\xi}) \xi + 1/6 V_0'''' \xi^3 = 0 \quad (18)$$

introducing the transformation  $\tau = \omega t$  and expanding  $\xi$  and  $\omega$  in Eq. (18) in power of  $\epsilon$  according to

$$\xi = \epsilon \xi_1 + \epsilon^2 \xi_2 + \dots \quad (19)$$

$$\omega = \omega_0 + \epsilon \omega_1 + \epsilon^2 \omega_2 + \dots$$

one derives from (18) a set of equations (after equating equal powers of  $\epsilon$ ) which can be then solved recursively. After a lengthy but standard computation (see for example Ref. [1]) one finally get for the frequency the following expression:

$$(\omega_+^2 - \omega_-^2)/2\omega_+^2 \epsilon^2 = -1/16 (V_{++}''' / V_{++}'' + 1/8 M_{++}'' / M_{++} - 1/16 (M_{++} / M_{++})^2$$

$$+ 5/48 (V_{++}''' / V_{++}'' )^2 - 1/8 (V_{++}''' / V_{++}'' ) (M_{++}' / M_{++}) )$$
 (20)

where

$$V_{++}''' = -16[21 + 28S_{++}^2 + 4S_{++}^4]/((C_{++}^2 S_{++}^2) + 16R_{++}[21 + 42S_{++}^2 + 24S_{++}^4]/(C_{++}^2 S_{++}^2),$$
 (21)

$$V_{++}'''' = 16[144 + 288S_{++}^2 + 164S_{++}^4 + 8S_{++}^6]/((C_{++}^2 S_{++}^2) - 16R_{++}[144 + 384S_{++}^2 + 340S_{++}^4 + 112S_{++}^6]/((C_{++}^2 S_{++}^2))$$
 (22)

In Fig. 2 Eq. (20) is plotted versus  $R_{++}$ .

To close this section we like to compare this result with a numerical experiment on the anharmonic motion of an oscillating  $4\pi$ -kink. To this end we have numerically integrated the DSG equation with  $\lambda_1, \lambda_2$  in (1) given by Eq.(3) for different values of  $R_{++}$ . The oscillatory motion of a  $4\pi$ -kink was started by taking as initial condition expression (6) with  $R(t=0) = R_0 > R_{++}$ . The frequency of the resulting oscillation was then computed by following in time the motion of a point on the  $4\pi$ -kink profile. (This was checked to be an accurate way to measure the frequency since no radiation (or very little) was generated in the system).

In Figs. 3 and 4 a plot of the resulting frequency versus the amplitude of the oscillation is reported for the values of  $R_0$  respectively of 2 and 3. The stars in these figures correspond to numerical results while the solid curves represent the theoretical values predicted by equation

(20). We note that the agreement between perturbation theory and experiments is quite good for small values of  $R_1$ - $R_2$ . From Figs. 3-4 it is also clear that the anharmonicity in this system start to be relevant only at large oscillation amplitudes.

### V. Conclusion

In the present paper we have given a simple derivation of the small oscillation frequency around  $4\pi$ -kink solutions of the double sine-Gordon system. The analysis was based on the assumption (6) for the wave form of such oscillating solution.

Finally, a numerically experiment on anharmonic oscillations of  $4\pi$ -kink solutions was performed and compared with the predictions of a perturbation treatment. As a result we find a good agreement between the perturbative analysis and the numerical results for small oscillation amplitudes.

### Acknowledgements

One of us (MS) acknowledges financial support from the European Economic Communities through contract St 2-0267-J-C(4), from the European Research Office of the United States Army through contract n. DAJA-45-85-C-0042, the Thomas B. Thriges Fond (Denmark) and the Gruppo Nazionale di Struttura della Materia, Centro Interuniversitario di Struttura della Materia.

### References

- [1] K. Maki, P. Kumar, Phys.Rev. B14, 118 (1976);  
3290 (1976)
- [2] O. Hudák, J.Phys.Chem. 16, 2641 (1982); 2659 (1983)
- [3] K.M. Leung, Phys.Rev. B27, 2877 (1982)
- [4] E. Nagyari, Phys.Rev. B29, 7082 (1984)
- [5] R.K. Bullough and P.J. Caudrey, in: "Nonlinear evolution equations solvable by the spectral transform".  
ed. F. Calogero (Pitman, London, 1978) pp. 180-224.
- [6] T. Uchiyama, Phys.Rev. D14, 3520 (1976)
- [7] D.K. Campbell, M. Peirard, P. Sodano, Physica D19, 165  
(1986)
- [8] C.R. Willis, M. El-Batanouny, S. Burdick, R. Boesh,  
F. Sodano. Phys.Rev.B35, 3496 (1987)
- [9] M. Salerno, Physica D17 227 (1985)
- [10] M. Salerno, M.R. Samuelsen, Phys.Lett. A126, 424 (1987)
- [11] A.H. Nayfeh "Perturbation methods", John Wiley & Sons,  
New York, 1973.

Figure captions

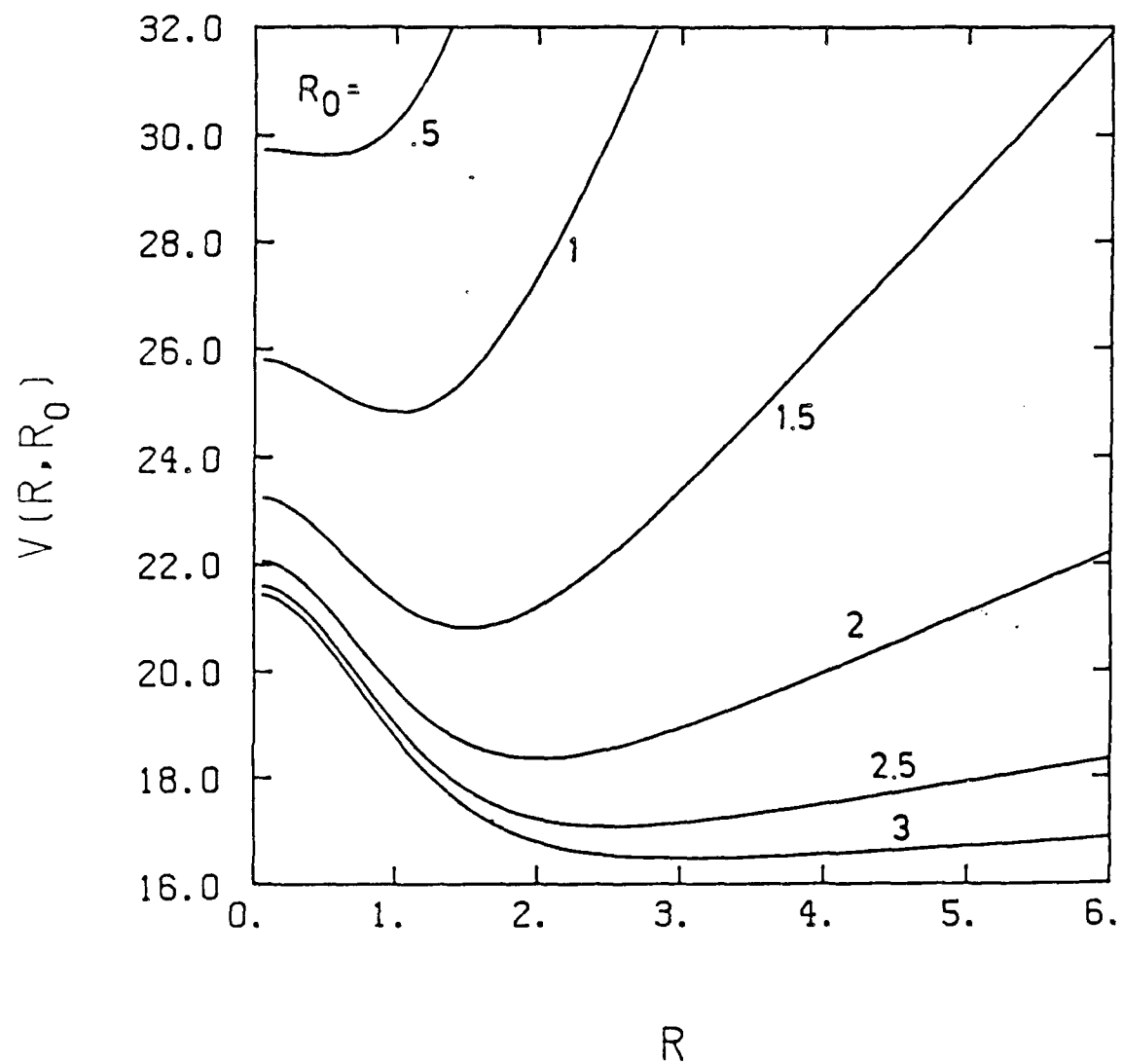
Fig. 1 Different curves of  $V(R, R_c)$  versus  $R$  for different values of  $R_c$ .

Fig. 2 Oscillatory frequency given by Eq. (20) plotted versus  $R_c$ .

Fig. 3 Oscillatory frequency of a 4n-“wobber” versus  $(R_c - R_{c_0}) = \epsilon R_c$  for the value  $R_c = 2$ .  
The stars are experimental points while the solid curve correspond to theoretical values derived from Eq. ~~(22)~~<sup>20</sup>.

Fig. 4 The same as in Fig. 3 but for  $R_c = 3$ .

Fig 1  
Sauer



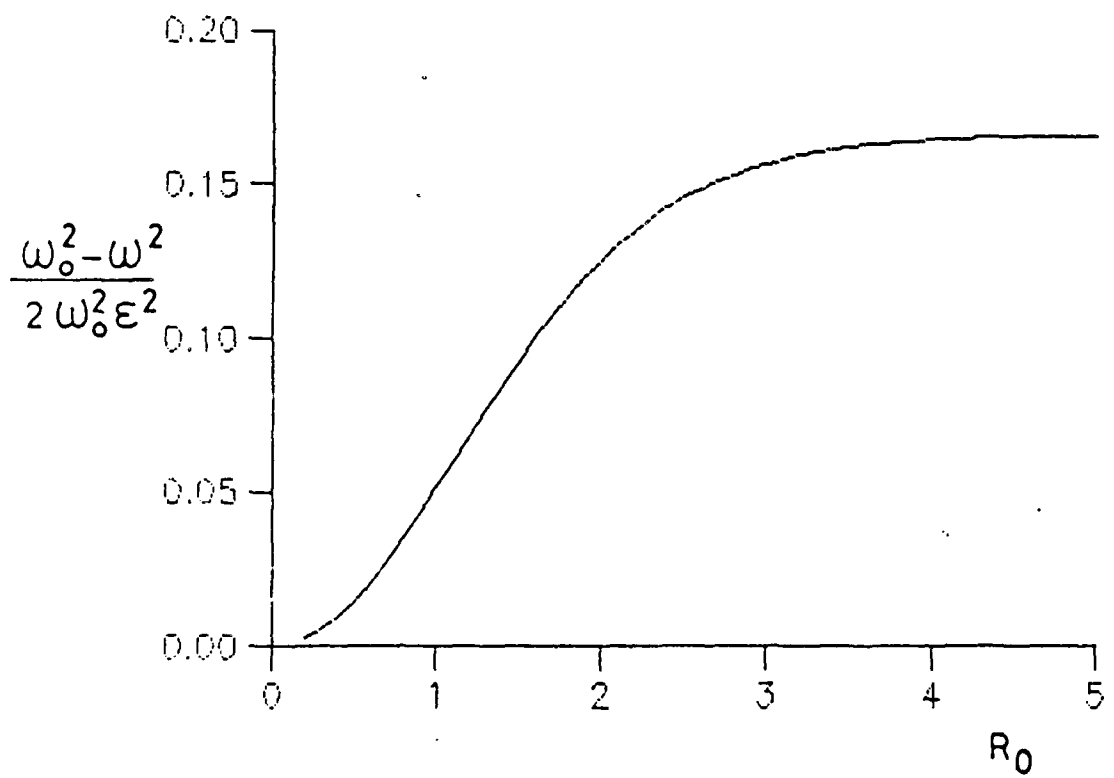
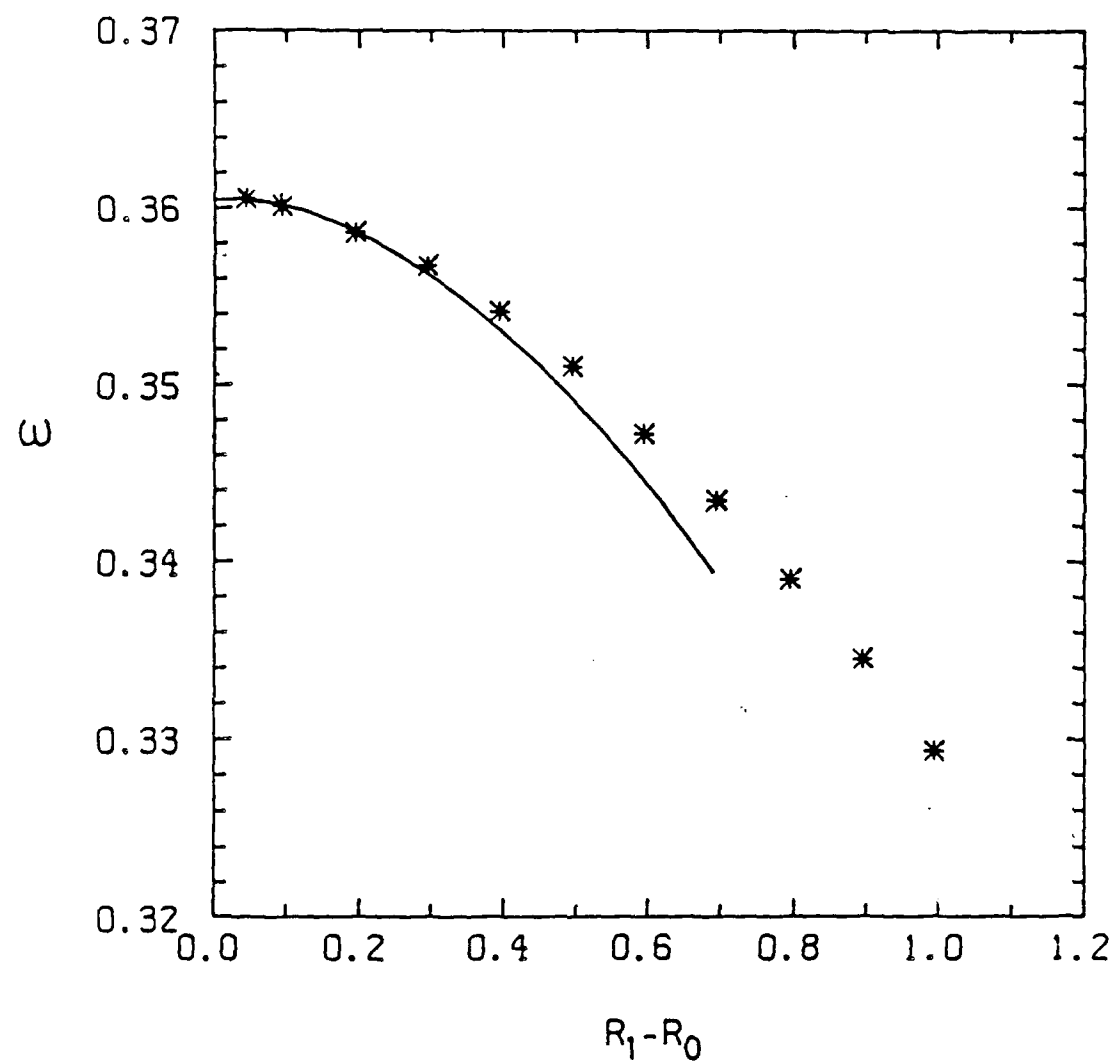
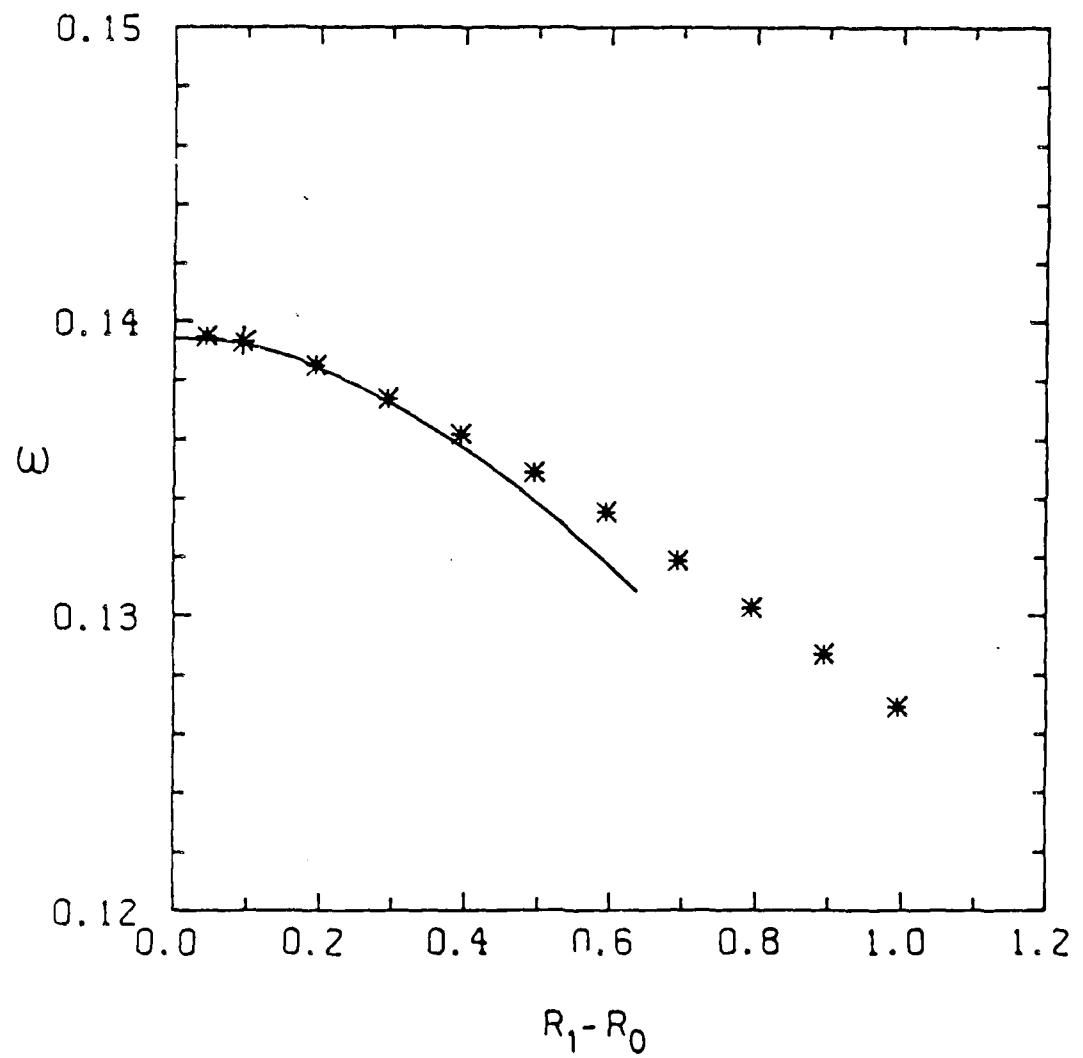


Fig 3



$\zeta = 2$



## A SIMPLE MAP DESCRIBING PHASE-LOCKING OF FLUXON OSCILLATIONS IN LONG JOSEPHSON TUNNEL JUNCTIONS

M. Salerno<sup>a</sup>, M. R. Samuelsen<sup>b</sup>, G. Filatrella<sup>c</sup>, S. Pagano<sup>d</sup>, and R. D. Parmentier<sup>c</sup>

MIDIT Center,  
The Technical University of Denmark,  
DK-2800 Lyngby, Denmark.

### Abstract

Application of soliton perturbation theory to a Josephson junction fluxon subjected to a microwave field reduces the problem of phase-locking of the fluxon oscillation to the study of a two-dimensional functional map. Phase-locked states correspond to fixed points of the map. The approach captures much of the experimental phenomenology.

Interest in the phenomenon of phase-locking of fluxon oscillations in long Josephson tunnel junctions has recently been stimulated by the possibility of employing arrays of such long junctions as local oscillators in integrated superconductive microwave or millimeter-wave receivers for radioastronomy and space communications [1]. A complete mathematical model of an array of fluxon oscillators would be a system of nonlinear coupled partial differential equations. A detailed study of such a system would, *a priori*, present notable difficulties (also because the exact nature of the coupling between the individual oscillators of such an array has not yet been well-characterized). A simpler, but related, problem is to study the interaction of a single oscillator with a fixed, external microwave field [2].

Our theoretical approach to the study of this simpler problem is based on the perturbation analysis of fluxon dynamics pioneered by McLaughlin and Scott [3]. This perturbation analysis was applied to the very same problem by Chang [4], whose work clearly suggested the power of the method. As will be shown below, our approach reduces the problem to the study of a discrete, two-dimensional functional map, in which, for example, a stable phase-locked fluxon oscillation corresponds to one (or more) stable fixed point(s) in the map. Obviously this approach reduces enormously the computational effort required to study the problem. In spite of this drastic simplification, however, the approach succeeds remarkably in capturing, at least qualitatively, much of the experimentally observed phenomenology.

The mathematical model used to describe the dynamics of fluxon oscillations in long Josephson junctions is a sine-Gordon equation, modified by the addition of energy input and dissipation terms [5]. For an overlap-geometry junction an appropriate model equation is, in normalized form

$$\varphi_{xx} - \varphi_{tt} - \sin\varphi = \alpha\varphi_t - \gamma . \quad (1a)$$

with the boundary conditions

$$\varphi_x(0,t) = \varphi_x(L,t) = \eta . \quad (1b)$$

Details of the normalizations may be found in Ref. 5

Our theoretical approach to the study of phase-locking in long junctions is based on two fundamental hypotheses:

- i) The influence of an external microwave field on a long-junction oscillator is felt only through the boundary conditions, Eq. (1b), not through the p.d.e., Eq. (1a), i.e., we assume the experimental conditions to be such that the microwave field does not penetrate significantly the interior of the junction.

ii) The dynamics of fluxons in the interior of a junction is adequately described by the perturbation analysis of McLaughlin and Scott [3].

Furthermore, purely for computational convenience, we make the following simplifying assumptions:

- The junction length  $L$  is large compared with unity so that we can employ as a solution ansatz a form appropriate to the infinite-length limit.
- Only dynamic states involving a single fluxon (or antifluxon) are considered.

We follow herein the procedure first reported by McLaughlin and Scott [3] and further elaborated by Christiansen and Olsen [6] and by Levring et al. [7]. In the infinite-length limit, a fluxon solution of Eq. (1a) is well-characterized by its momentum  $P_f$ , defined as

$$P_f = - \int_{-\infty}^{+\infty} \varphi_x \varphi_t dx . \quad (2)$$

From Eqs. (1a) and (2), the equation of motion for a single fluxon is

$$\frac{dP_f}{dt} = - \alpha P_f + 2\pi\gamma . \quad (3)$$

For the pure sine-Gordon equation ( $\alpha = \gamma = 0$ ) in the infinite-length limit, the momentum of the single fluxon solution may be calculated explicitly as

$$P_{f0} = 8u/(1 - u^2)^{1/2} , \quad (4)$$

in which  $u$  is the propagation velocity.

The first essential ingredient of the perturbation analysis is to assume that if  $\alpha$  and  $\gamma$  in Eq. (1a) are sufficiently small, we may substitute  $P_f$  in Eq. (3) by  $P_{f0}$  from Eq. (4). In this case the fluxon position  $X(t)$  is given by

$$X(t) = x_0 + \int_0^t u(\tau) d\tau , \quad (5)$$

where  $x_0$  is the initial position. One simple, well-known result of this procedure is that, for given  $\alpha$  and  $\gamma$ , there exists an equilibrium velocity, called  $u_\infty$ , for which energy input and dissipation are exactly balanced. This velocity is found from the stationary solution of Eq. (3). The result is

$$u_\infty = (1 + (4\alpha/\pi\gamma)^2)^{-1/2} . \quad (6)$$

Eq. (3) may be integrated conveniently in terms of the quantity  $z(t)$ , defined as

The result of the integration is

$$z(t) = z_\infty + (z_0 - z_\infty) \exp(-\alpha t), \quad (8)$$

in which  $z_0$  is the initial value of  $z$ , and  $z_\infty$  corresponds to  $u_\infty$  in Eq. (6). The fluxon trajectory may then be found by combining Eqs. (5), (7) and (8). The result is

$$\begin{aligned} X(t) = & x_0 + u_\infty t - \frac{1}{\alpha} \log \left[ \frac{z + (z^2 + 1)^{1/2}}{z_0 + (z_0^2 + 1)^{1/2}} \right] \\ & - \frac{u_\infty}{\alpha} \log \left[ \frac{1 + z_\infty \cdot z_0 + (z_\infty^2 + 1)^{1/2} \cdot (z_0^2 + 1)^{1/2}}{1 + z \cdot z_\infty + (z^2 + 1)^{1/2} \cdot (z_\infty^2 + 1)^{1/2}} \right]. \end{aligned} \quad (9)$$

The second essential ingredient of the perturbation analysis is the treatment of the boundary condition, Eq. (1b). Following Levring et al. [7], we observe that during a reflection from a boundary, due to Eq. (1b) a fluxon undergoes an energy variation  $\Delta H_f$ , given by

$$\Delta H_f = \pm 4\pi\eta. \quad (10)$$

For constant  $\eta$ , this variation is positive at (say) the left-hand boundary and negative at (say) the right-hand boundary. To relate this energy variation to the fluxon trajectory  $X(t)$ , we recall that the energy of a pure sine-Gordon fluxon may be calculated explicitly as

$$H_{f0} = 8/(1 - u^2)^{1/2} = P_{f0}/u. \quad (11)$$

Thus, an energy variation given by Eq. (10) may be related to a velocity variation through Eq. (11), whereupon the calculation of  $X(t)$  proceeds as before. An additional approximation introduced here is that we can neglect the effects of phase-shift and dissipation during reflections [8] and that the energy variation of Eq. (10) occurs instantaneously.

We take for the term  $\eta$  in Eq. (1b) the form

$$\eta = \eta_0 \sin(\omega_{rf} t + \vartheta) \quad (12)$$

as a model of the microwave field acting upon the junction. We define the fundamental period  $T$  of a fluxon oscillation to be the time employed by the fluxon to complete one back and forth round trip along the junction. Thus, the condition for phase-locking at the fundamental frequency is, with an obvious notation

$$T_{k,k+2} = T_{k,k+1} + T_{k+1,k+2} = \frac{2\pi}{\omega_{rf}}. \quad (13)$$

In addition, we may *a priori* expect to observe both harmonic and subharmonic phase-lock-

$$T_{k,k+2} = \frac{m}{n} \frac{2\pi}{\omega_{rf}} . \quad (14)$$

where  $m$  and  $n$  are integers.

Phase-locking of a fluxon oscillation to an external field is manifested experimentally by the appearance of a constant-voltage step in the current-voltage characteristic. In terms of our model, the height in current of such a step will be determined by how much we can vary the parameter  $\gamma$  without breaking the locking condition of Eq. (14).

We can now proceed to calculate the fluxon dynamics. Having specified the parameters  $\alpha$ ,  $\gamma$ ,  $L$ ,  $\eta_0$ ,  $\omega_{rf}$  and  $\vartheta$ , we choose an arbitrary initial value,  $z_0^{(0)}$ , of  $z$  at  $x = 0$ ,  $t = 0$  (setting  $x_0$  in Eq. (9) to zero). By inverting (numerically) Eq. (9), i.e., by imposing  $X(T_{0,1}) = L$ , we calculate the time of flight,  $T_{0,1}$ , from  $x = 0$  to  $x = L$ . Inserting  $T_{0,1}$  into Eq. (8), we calculate the final value,  $z_f^{(1)}$ , of  $z$  at  $x = L$ , i.e.,  $z_f^{(1)} = z(T_{0,1})$ . At this point, from the energy variation,  $\Delta H_f$  of Eq. (10), we calculate a  $z$ -variation,  $\Delta z^{(1)}$ , which, when added to  $z_f^{(1)}$ , defines a new initial value,  $z_0^{(1)}$ , of  $z$  at  $x = L$ ,  $t = T_{0,1}$ . Explicitly, we find

$$z_0^{(1)} = \left[ \left\{ \left( z_f^{(1)} \right)^2 + 1 \right\}^{1/2} + (-1)^k \frac{\pi \eta_0}{2} \sin(\omega_{rf} t + \vartheta) \right]^2 - 1 \right]^{1/2} . \quad (15)$$

where, in this case,  $k = 1$  and  $t = T_{0,1}$ . We then iterate this procedure as desired for successive spatial intervals of length  $L$ , substituting for  $t$  the sum of the preceding times of flight. In this way, Eqs. (8), (9) and (15), generalized to arbitrary  $k$ , constitute a discrete functional map for the quantities  $T_{k,k+1}$  and  $z_0^{(k+1)}$ . Fixed points of this map correspond to phase-locked states of the fluxon dynamics.

Figs. 1 - 3 show some preliminary numerical results obtained using this approach. Fig. 1 shows a portion of the current-voltage (I-V) characteristic of a junction characterized by  $\alpha = 0.05$ ,  $L = 12$ , subjected to a microwave field of frequency  $\omega_{rf} = 0.24$ , for different values of the field amplitude,  $\eta_0$ , in the condition of phase-locking at the fundamental frequency, given by Eq. (13). The smooth curve (a) is the I-V characteristic in the absence of a microwave field. This is essentially a plot of Eq. (6), inasmuch as the bias current is proportional to  $\gamma$ , and the voltage, in this case, is proportional to  $u_\infty$ . The two discontinuous curves, (b) and (c), show, respectively, the response of the junction for  $\eta_0 = 0.3$  and  $\eta_0 = 0.6$ . Here we use the general expression for the voltage,  $4\pi/T_{k,k+2}$ .

Fig. 2 shows the height in current of the step of Fig. 1, measured from the center of the step to the peak, as a function of the field amplitude,  $\eta_0$ . The evident linear de-

step height on the square root of microwave power normally observed experimentally [9].

Fig. 3 indicates in more detail the dynamics of the phase-locking process. In this figure, the fluxon frequency is defined as  $2\pi/T_{k,k+2}$ , and the drive frequency is just  $\omega_{rf}$ . The power spectrum is calculated by representing the time sequence  $T_{k,k+2}$  as a sequence of unit delta functions and by taking the Fourier transform of this sequence. Clearly evident in Fig. 3 is the fact that as the drive frequency approaches the unlocked fluxon frequency, mixing products (the small peaks near the edges of the figure) begin to appear. At a certain point, the fluxon frequency is pulled into synchronism with the driver, where it remains locked for a certain interval (the central region of the figure). Beyond this region the fluxon frequency unlocks, and mixing products are once again seen. This behavior should be compared with Fig. 3 of Cirillo and Lloyd [2] and Fig. 3 of Monaco *et al.* [1], which depict experimental recordings of the same scenario.

Our approach to the study of phase-locking of fluxon oscillations can clearly be extended in several directions. The effects of phase-shift and energy loss during the reflections of the fluxon from the junction boundaries [8], which become progressively more important for shorter junctions, can be incorporated into the analysis in a straightforward manner. The procedure can also be applied to junctions of in-line geometry [5]; in fact, for the in-line geometry the phase-locking map can be expressed explicitly, rather than implicitly, thus permitting an analytic study of the existence and stability of fixed points. Furthermore, the analysis can be extended, numerically if not analytically, to the general condition for phase-locking, Eq. (14), as opposed to the condition for locking at the fundamental frequency, Eq. (13). These extensions are presently under study and will be reported in the near future.

We are pleased to acknowledge fruitful discussions regarding the experimental aspects of phase-locking with M. Cirillo, G. Costabile and R. Monaco. We are grateful for the financial support received from the European Economic Community through contract no. St-2-0267-J-C(A) and through the ERASMUS program, from the European Research Office of the U.S. Army through contract no. DAJA-45-85-C-0042, and from the Ministero della Pubblica Istruzione (Italy).

**Notes and References**

- a** Permanent address: Department of Theoretical Physics, University of Salerno, I-84100 Salerno, Italy.
- b** Permanent address: Physics Laboratory I, The Technical University of Denmark, DK-2800 Lyngby, Denmark.
- c** Permanent address: Department of Physics, University of Salerno, I-84100 Salerno, Italy.
- d** Permanent address: Institute of Cybernetics of the CNR, I-80072 Arco Felice (NA), Italy.

- [1] R. Monaco, S. Pagano, G. Costabile, Phys. Lett. **131A** (1988) 122.
- [2] M. Cirillo, F. L. Lloyd, J. Appl. Phys. **61** (1987) 2581.
- [3] D. W. McLaughlin, A. C. Scott, Phys. Rev. **A18** (1978) 1652.
- [4] J.-J. Chang, Phys. Rev. **B34** (1986) 6137.
- [5] A. Barone, G. Paternò, **Physics and Applications of the Josephson Effect** (Wiley, New York, 1982).
- [6] P. L. Christiansen, O. H. Olsen, Wave Motion **2** (1980) 185.
- [7] O. A. Levring, N. F. Pedersen, M. R. Samuelsen, J. Appl. Phys. **54** (1983) 987.
- [8] O. H. Olsen, N. F. Pedersen, M. R. Samuelsen, H. Svensmark, D. Weiner, Phys. Rev. **B33** (1986) 168.
- [9] G. Costabile, R. Monaco, S. Pagano, "Experimental observation of phase-locking of fluxon oscillations in long Josephson tunnel junctions", Preprint submitted to Physics Letters A.

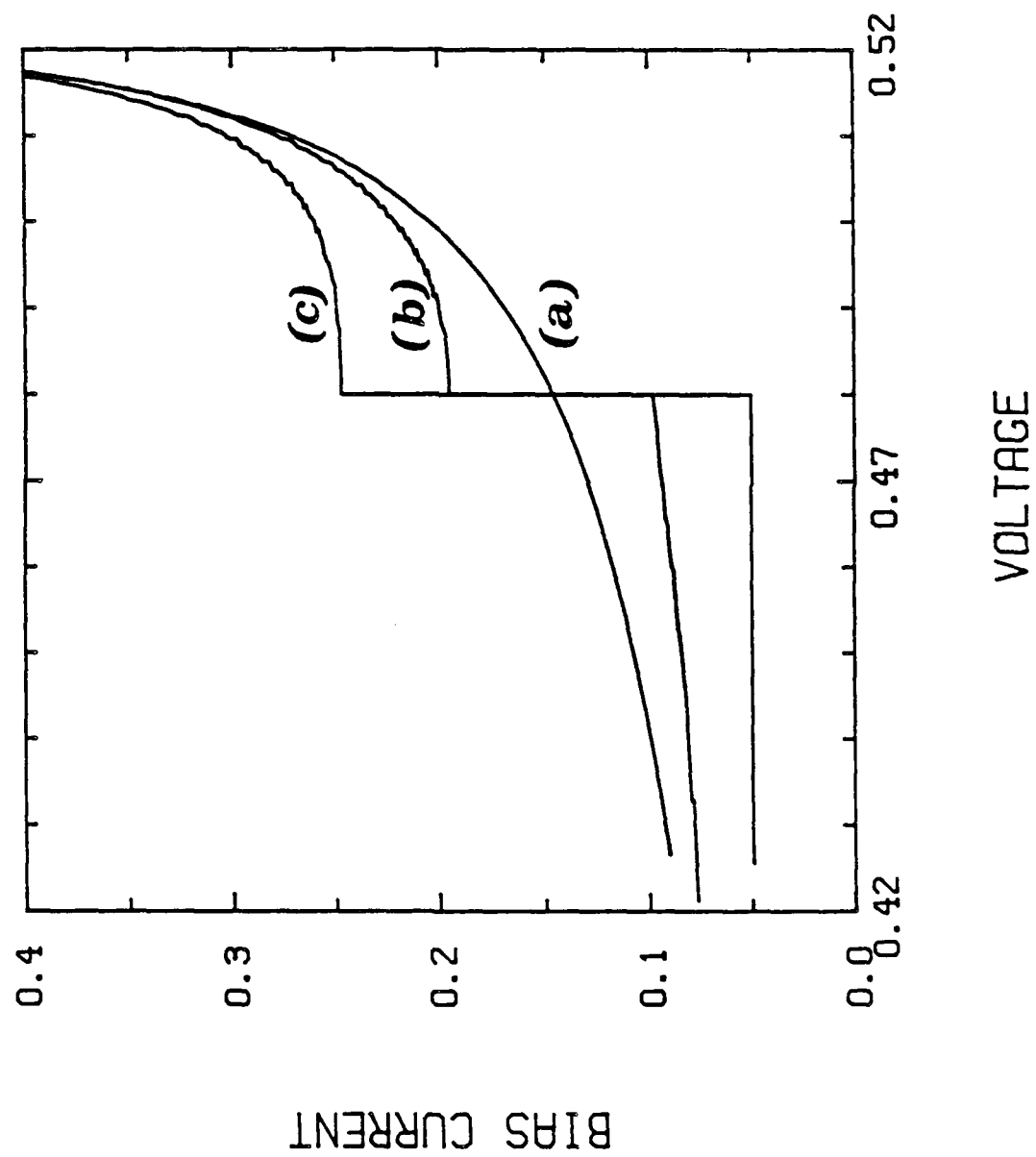
**Figure Captions**

Fig. 1. Portion of the I-V characteristic of a junction having  $\alpha = 0.05$ ,  $L = 12$ , irradiated by a microwave field of frequency  $\omega_{rf} = 0.24$ . Smooth curve (a): no field. Vertical steps, curves (b) and (c): fundamental phase-locking for  $\eta_0 = 0.3$  and  $\eta_0 = 0.6$ , respectively.

Fig. 2. Dependence of the height in current of the step of Fig. 1 on field amplitude,  $\eta_0$ . Parameters:  $\alpha = 0.05$ ,  $L = 12$ ,  $\omega_{rf} = 0.24$ .

Fig. 3. Dynamics of phase-locking. See text for details.

Fig. 1  
*Filatrella*  
et al.



FIELD AMPLITUDE

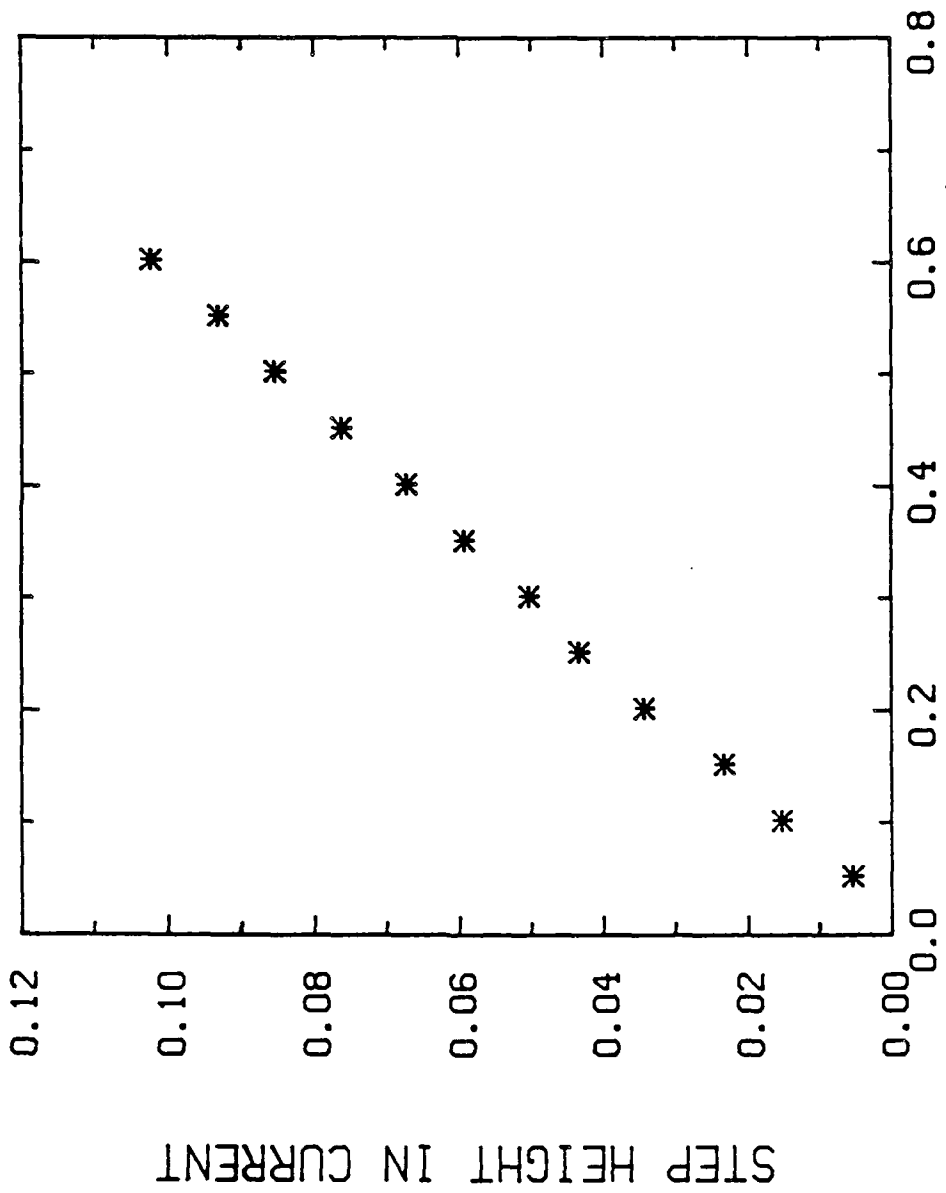


Fig. 2  
Filatrella  
et al.

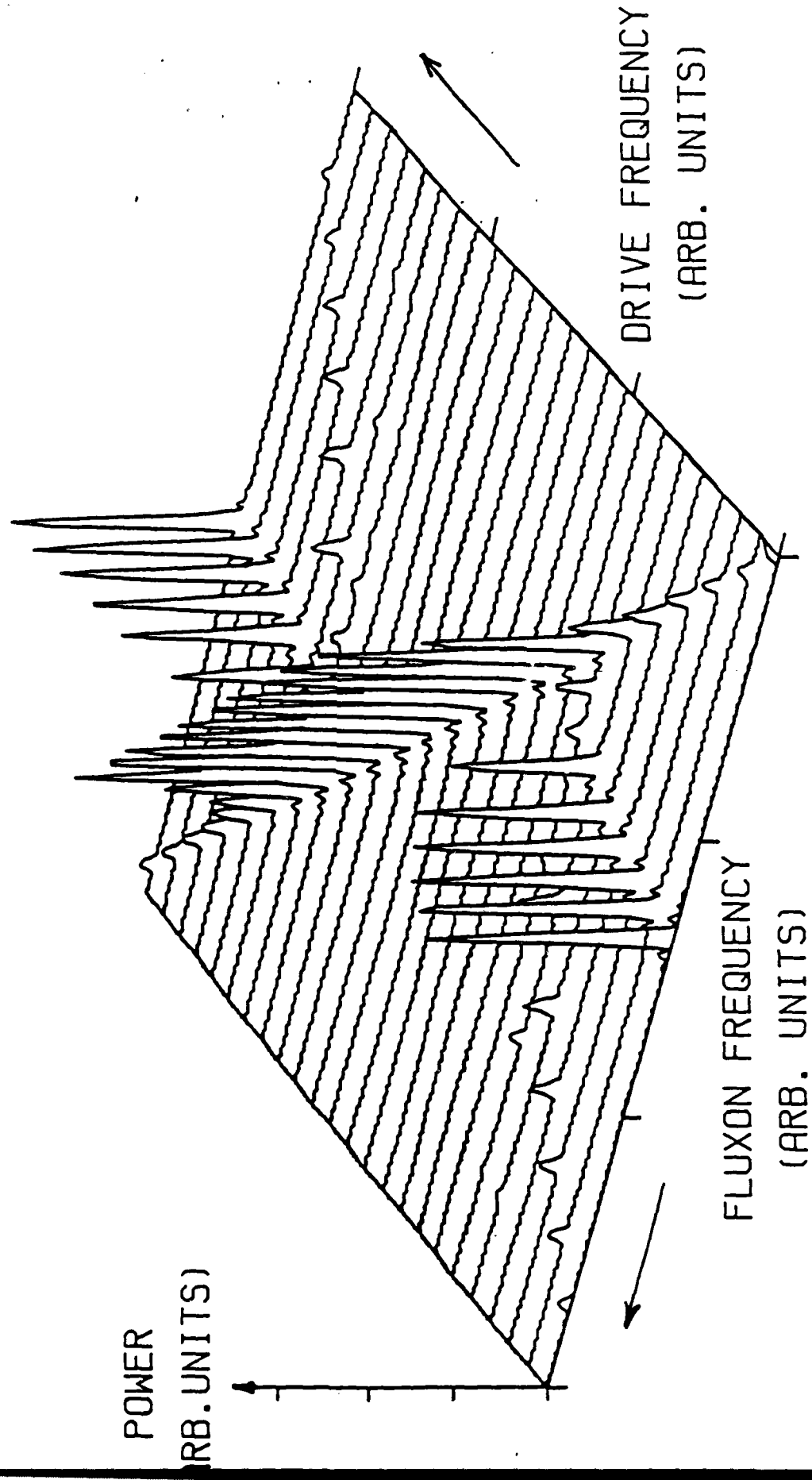


Fig. 3  
*Filatrella*  
et al.

Correlations Between Chaos in the Perturbed Sine-Gordon  
Equation and Finite Modal Equations

M. Gregory Forest

Laboratory for Applied Mathematical Physics  
The Technical University of Denmark  
DK-2800 Lyngby, Denmark

and

Department of Mathematics  
Ohio State University  
Columbus, OH 43210, USA.

ABSTRACT

This paper summarizes numerical and analytical work on a specific bifurcation route to chaos in the damped, periodically driven sine-Gordon equation. The emphasis here is on the modelling of this bifurcation sequence and the coordinatization of the chaotic attractors by truncated modal equations. The underlying structure which we establish and focus upon in both the p.d.e and truncated o.d.e. systems is the existence of homoclinic orbits in an integrable, unperturbed phase space. Thus, under weak perturbations, there exists a natural mechanism for generating chaotic dynamics. We proceed to numerically test whether these homoclinic structures are observed in the chaotic dynamics. The upshot is a four-dimensional truncated system of modal equations which correlates remarkably well with the chaotic dynamics of the full p.d.e. This paper is a condensed version of [8], based on joint work with A.R. Bishop, R. Flesch, D.W. McLaughlin, and E.A. Overman.

Outline:

1. Bifurcations to Chaos in the Weakly Perturbed Sine-Gordon Equation.
2. A Truncated Finite Mode Ansatz in the Nonlinear Schrödinger Limit.
3. Properties of the Unperturbed Modal Equations.
4. Bifurcations to Chaos in the Perturbed Modal Equations.
5. Correlations Between the Infinite-Dimensional and Reduced Systems.

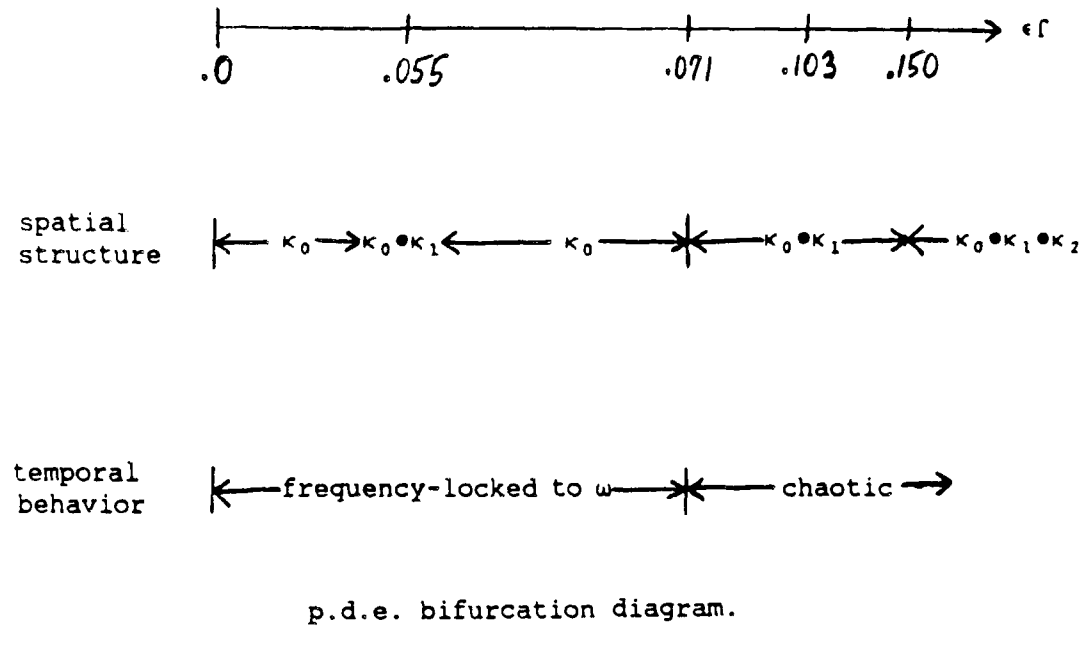
1. BIFURCATIONS TO CHAOS IN THE WEAKLY PERTURBED SINE-GORDON EQUATION

We begin with one finely tuned numerical experiment on the weakly damped, periodically forced, sine-Gordon equation,

$$u_{tt} - u_{xx} + \sin u = \epsilon [-\alpha u_t + \Gamma \cos(\omega t)], \quad (1)$$

with even spatial symmetry, and periodic boundary conditions of length  $L = 12$ . The linear damping coefficient is fixed,  $\alpha = .04$ , the initial condition is always chosen as a singlehump sine-Gordon breather localized within the period, and the driving frequency is fixed at  $\omega = .87$ . Thus, we focus on the large time ( $t \gg 1$ ) attractors of this system as a function of the single bifurcation parameter,  $\epsilon\Gamma$ , which is the amplitude of the external driver. (Refer to [1, 2] for more extensive numerical studies.)

In this controlled experiment, we observe the following bifurcation sequence in these long-time "attractors", which are specified here by their spatial structure and temporal behavior.



p.d.e. bifurcation diagram.

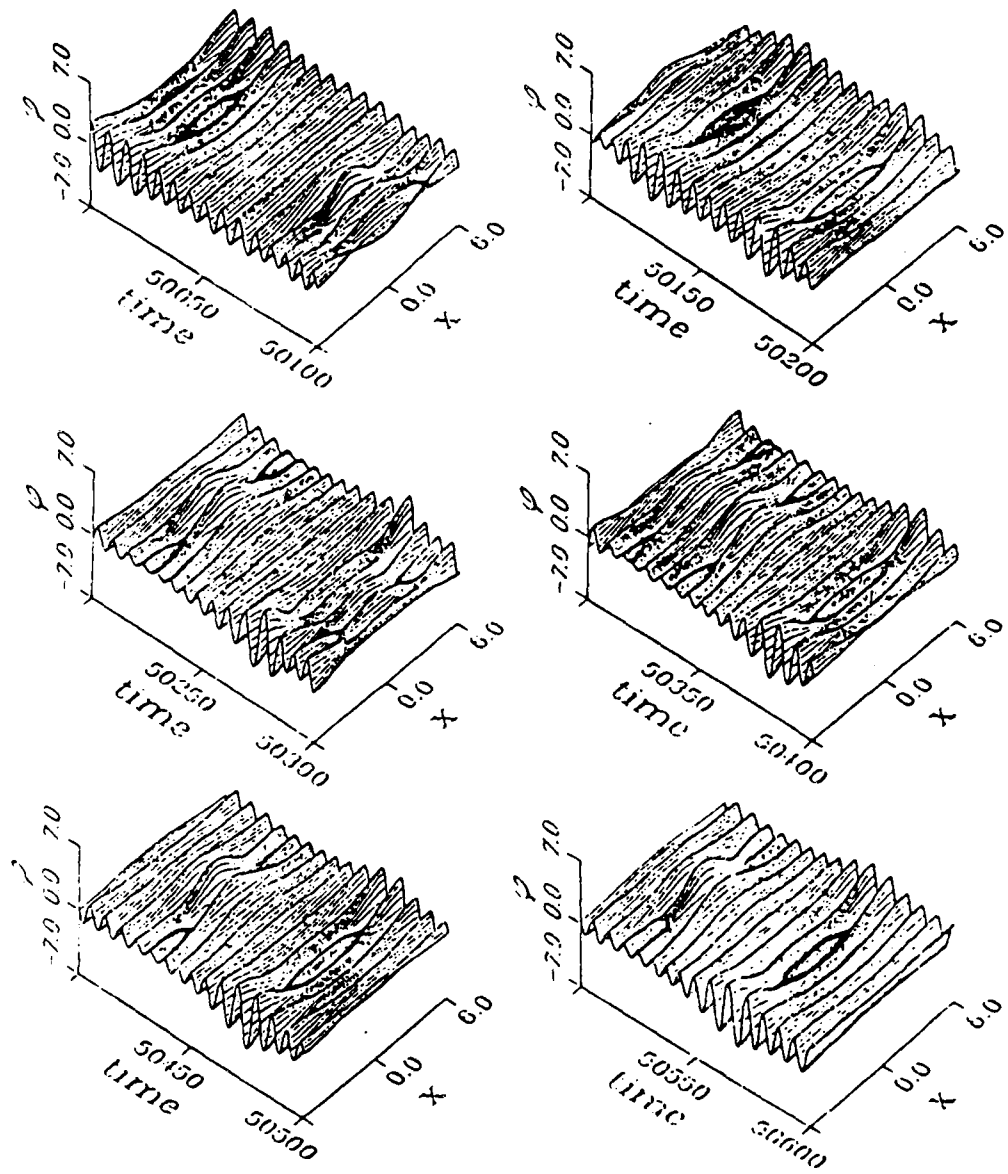
FIGURE 1.

Here  $\kappa_0$  denotes a spatially flat, zero wavenumber component,  $\kappa_1$  denotes a period  $L$  component of wavenumber  $\kappa_1 = 2\pi/L$ ,  $\kappa_0 * \kappa_1$  denotes the nonlinear superposition of these two modes, etc. The time flow is periodic with the same frequency  $\omega$  of the driver, and then chaotic, which implies a broadband frequency spectrum. (We often observe quasiper-

odicity in  $t$  before chaos [1, 2], but not in this specific parameter regime. Apparently, the quasiperiodic states exist in this diagram, but are either unstable or these initial conditions are not in the basin of attraction of stable quasiperiodic states. As we see below, our modal equations suggest the former alternative.)

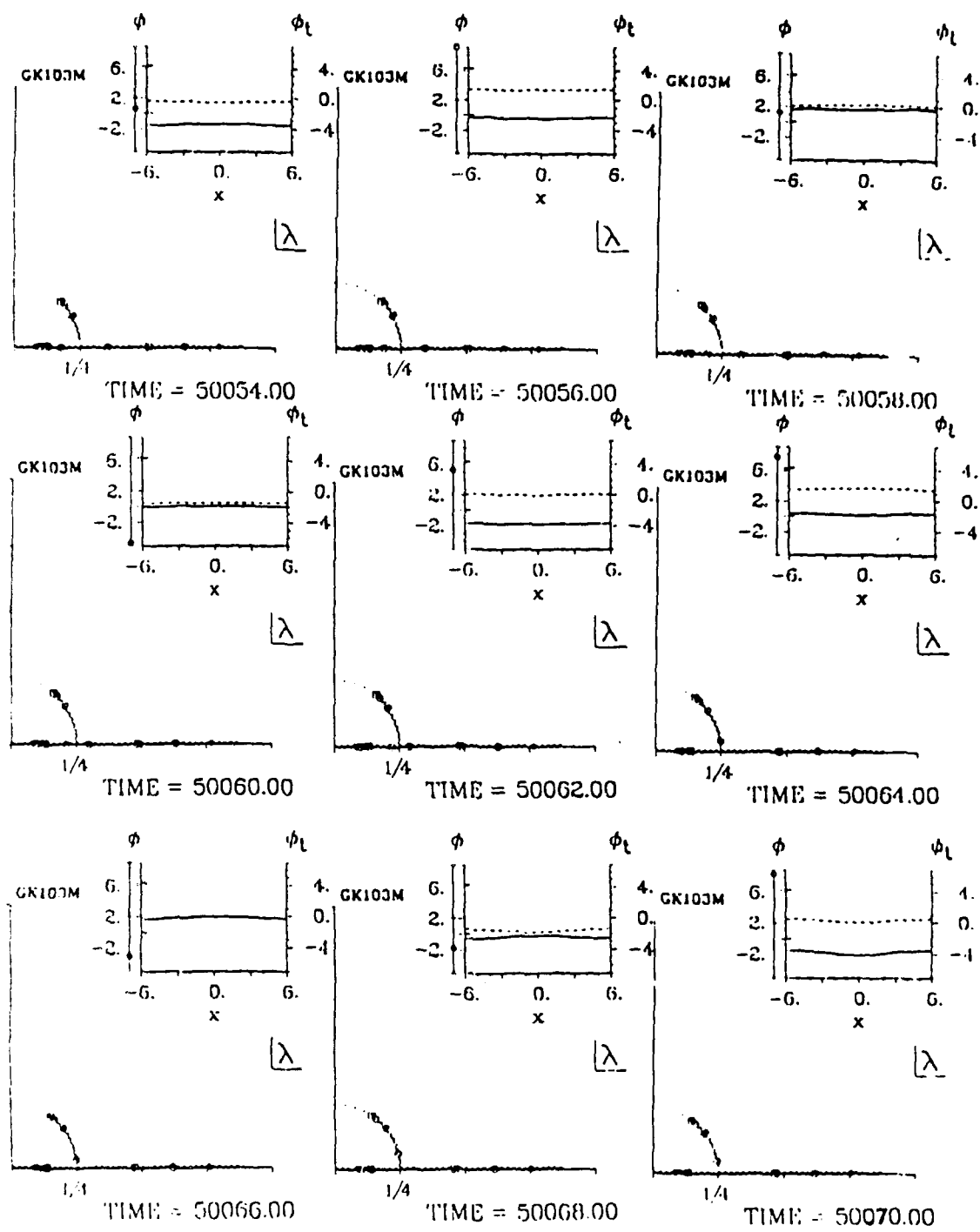
The chaos here is intermittent chaos. The next figure is for  $\epsilon\Gamma = .103$ , displaying the 3-D plot of the numerically integrated solution to Eq. (1). At each time step, there is spatial coherence: either a breather in the center of the interval superimposed on a flat background, a breather localized at the ends of the interval on top of the  $\kappa_0$  component, or the intermediate flat  $\kappa_0$  state. The "laminar" regions are where the system chooses one configuration, say the breather in the middle. The "chaotic bursts" are associated to the passage out of the laminar state (presumably due to the buildup of a weak instability), through the intermediate  $\kappa_0$  configuration, and then into either of the two breather states. This chaotic attractor consists of the set of spatial states observed in Figure 2, and the chaos is this intermittent jumping between the breathers localized in the center or the wings, through an intermediate spatially flat configuration.

Next we quantify this spatial mode measurement ( $\kappa_0$ ,  $\kappa_0 \cdot \kappa_1$ , etc.) by taking  $u^\epsilon(x, t_n)$  at each time step  $t_n$  from the integration of Eq. (1), and using a sine-Gordon spectral code to measure the exact nonlinear sine-Gordon mode content in the field  $u^\epsilon(x, t_n)$ . These are given in Figure 3, from the same time series as Figure 2.



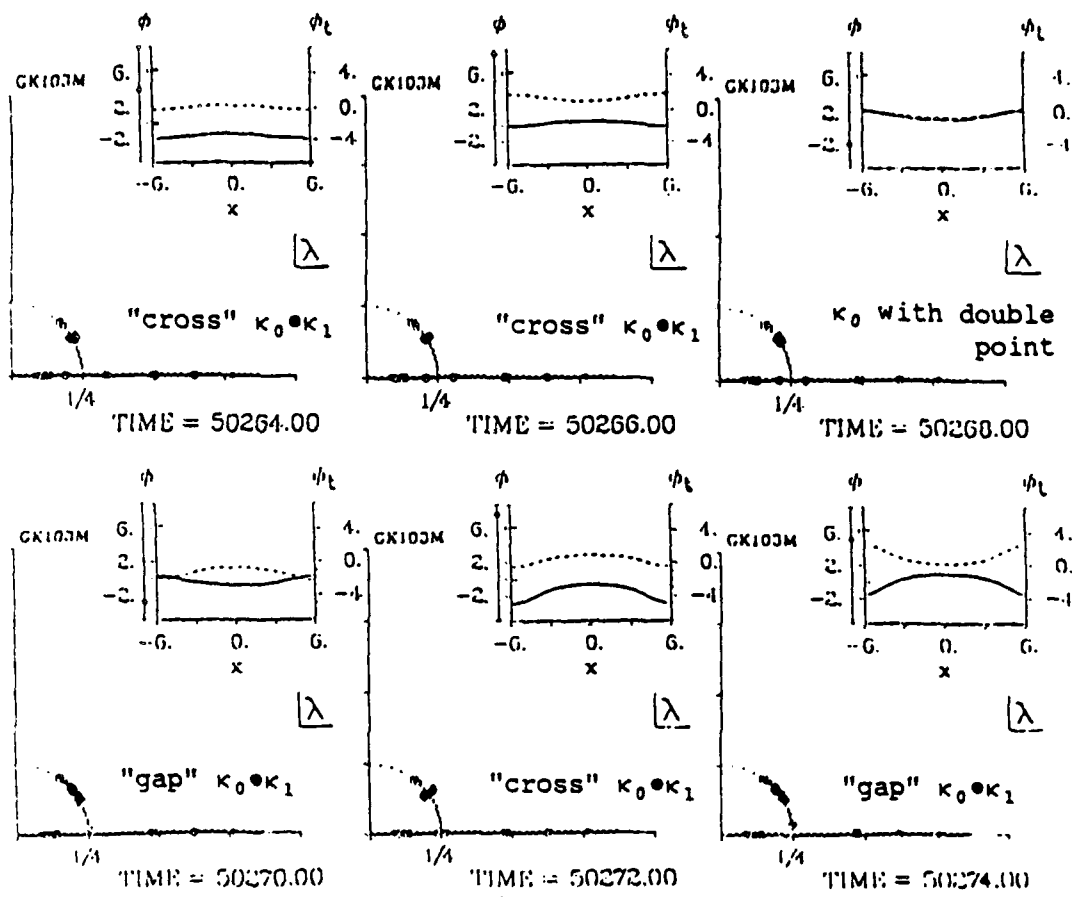
Numerically computed solution  $\phi = u^\epsilon(x,t)$  of Eq. (1).  
 $\epsilon \Gamma = .103, \quad 50,000 \leq t \leq 60,000.$

FIGURE 2.



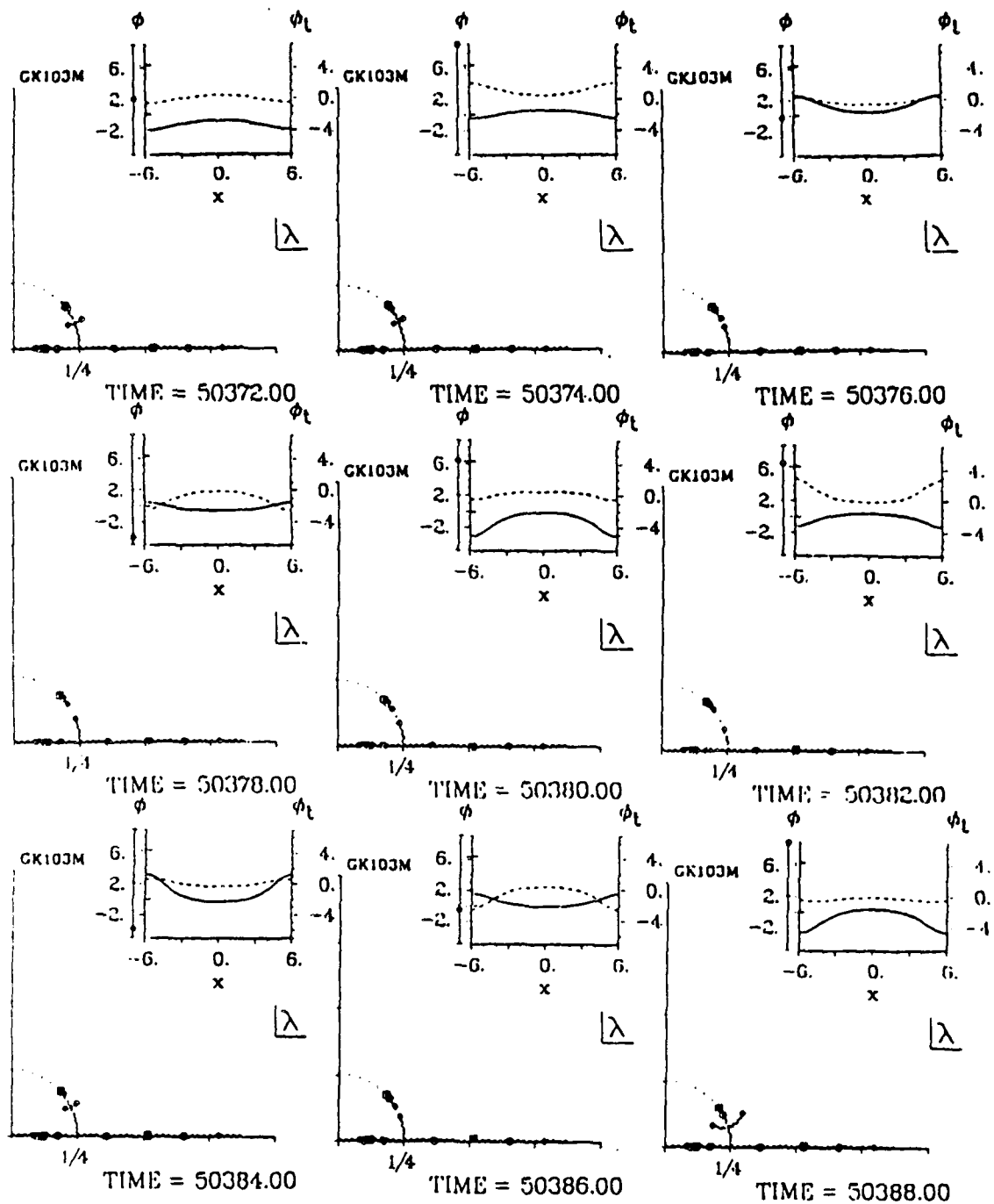
Sine-Gordon mode measurement while  $u^\epsilon(x,t)$ , Figure 2,  
hovers at the frequency-locked, flat  $\kappa_0$  state.

FIGURE 3a.



Sine-Gordon spectral sequence depicting a flutter between the "gap" and "cross"  $\kappa_0 \otimes \kappa_1$  spectral states, all tightly bunched around the double point, limiting state in the upper right frame. The waveform  $\phi$  need not be flat in this apparent  $\kappa_0$  spectral configuration: in fact, this  $\kappa_1$  component is precisely the homoclinic component associated to the complex double point. Notice from Figure 2 during this time sequence the corresponding p.d.e. waveform flutters between the breather states localized in the center or ends of the interval.

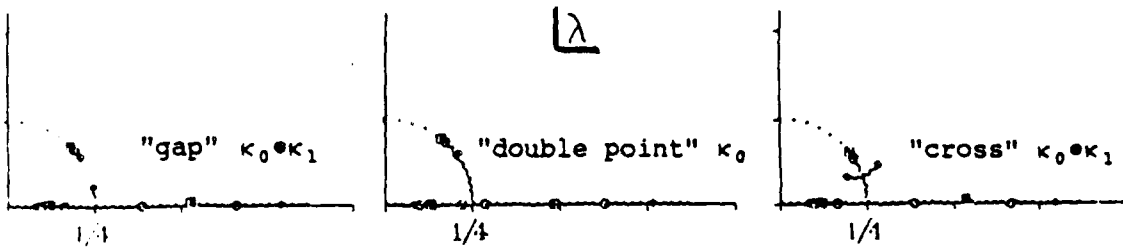
FIGURE 3b.



Spectral measurement of  $u^\epsilon(x, t_n)$  depicting a time sequence where the "cross"  $\kappa_0 \bullet \kappa_1$  state begins to settle into the "gap"  $\kappa_0 \bullet \kappa_1$  state, then flutters back and forth, finally settling back into the "cross" configuration from 50,388 until 50,420.

FIGURE 3c.

The predominant nonlinear modes are (Figure 4):



The three dominant spectral configurations corresponding to the three dominant spatial states observed in Figure 2.

FIGURE 4.

Here we have truncated to the two pure  $\kappa_0 * \kappa_1$  states (4a, 4c), and the intermediate configuration (4b), and the dynamics is viewed as a flow through the spatial states associated to these spectral configurations. (We surmise the other small amplitude modes are "slaved" to this dynamics).

The upshot of all these preliminaries is that the low-dimensional configurations in Figure 4 are rich enough to produce chaos under perturbations. Specifically, in [3, 4, 5] we establish the following facts about the unperturbed, integrable sine-Gordon equation with periodic boundary conditions.

Fact 1 The exact  $\kappa_0 * \kappa_1$ , breather plus nonzero mean, solutions of sine-Gordon, with spectrum as indicated in Figures 4a,c, are linearly, neutrally stable.

Fact 2 The intermediate  $\kappa_0$  state, corresponding to a purely oscillatory pendulum solution, with spectrum as in Figure 4b, is linearly exponentially unstable, with order 1 growth rate. There is precisely one unstable mode, the  $\kappa_1$  mode, labelled by the complex "double point" (the shaded square) in Figure 4b. This local linearized instability is related to a global homoclinic orbit in the sine-Gordon periodic phase space. In other words, there is an exact sine-Gordon solution which asymptotically relaxes to this flat pendulum state as  $|t| \rightarrow \infty$ , but which is a  $\kappa_1$  mode in  $x$ . (See [5] for exact formulas.)

Thus, our thesis is: (i) these low-dimensional homoclinic structures provide a mechanism for chaos, (ii) the spectral measurement of

the perturbed flow in the chaotic regime indicates an irregular passage through these homoclinic configurations, and (iii) thus, we may be able to coordinatize the chaotic attractors with a low-dimensional truncation. Our first attempt at this program is the remainder of this paper.

## 2. A TRUNCATED FINITE MODE ANSATZ IN THE NONLINEAR SCHRÖDINGER LIMIT

At frequencies  $\omega$  near but less than one, the sine-Gordon flow (Eq. (1)) resonates with breather-like modes. Thus, one is naturally led to the derivation of a nonlinear Schrödinger envelope equation, with the benefit that we explicitly factor out the driver frequency  $\omega$ , while at the same time retaining integrability at the unperturbed level.

Let  $\omega = .87 = 1 - \epsilon\bar{\omega}$ . Seek a solution  $u^\epsilon$  of Eq. (1) in the form (with  $X = \sqrt{2\epsilon\bar{\omega}} x$ ,  $T = \epsilon\bar{\omega}t$ )

$$u^\epsilon = 2\sqrt{\epsilon\bar{\omega}} [B(X, T) e^{i\omega T} + \text{complex conjugate}] + O(\epsilon\bar{\omega}) . \quad (2)$$

Then one easily finds the envelope  $B(X, T)$  satisfies:

$$-iB_T + B_{XX} + (|B|^2 - 1)B = i(\tilde{\alpha}B + \tilde{\Gamma}) , \quad (3a)$$

where the new scaled parameters are

$$\tilde{\alpha} = .155 , \quad L_X = 12\sqrt{2\epsilon\bar{\omega}} , \quad k^2 = \left(\frac{2\pi}{L_X}\right)^2 = 1.05 , \quad (3b)$$

and the scaled bifurcation parameter  $\tilde{\Gamma}$  is

$$\tilde{\Gamma} \approx 2.66 \epsilon\bar{\omega} . \quad (3c)$$

By factoring out the driver frequency, we reduce to a simpler perturbation (fixed damping, constant driver) of the integrable nonlinear Schrödinger equation (Eq. (3a) with  $\tilde{\alpha} = \tilde{\Gamma} = 0$ ). Thus, steady solutions of Eq. (3) correspond to locked periodic solutions  $u^\epsilon$  of Eq. (1), T-periodic solutions of Eq. (3) correspond to quasiperiodic behavior of perturbed sine-Gordon, and chaos is chaos.

The truncation on fully nonlinear modes of Eqs. (1) or (3) is under development [6], and codes are being constructed to handle the inherent complexities ([7], such as Riemann surface periods, associated theta

functions, and appropriate derivatives and averages of these functions). In the meantime, we follow the numerical indications of the full p.d.e. and attempt to capture the qualitative dynamical features of Eq. (1) with a truncation on the Fourier  $\kappa_0$  and  $\kappa_1$  modes. We seek

$$B(X,T) = c(T) + b(T) \cos(kX), \quad k = \frac{2\pi}{L_X} \quad (4)$$

insert this ansatz into the perturbed NLS equation, Eq. (3), and find the following complex amplitude equations:

$$\begin{cases} -ic_T + (|c|^2 + \frac{1}{2}|b|^2 - 1)c + \frac{1}{2}(cb^* + c^*b)b = i\bar{a}c + i\tilde{r} \\ ib_T + (|c|^2 + \frac{1}{2}|b|^2 - (1+k^2))b + (cb^* + c^*b)c = i\bar{a}b, \end{cases} \quad (5)$$

$$\tilde{a} \approx .155.$$

Before detailing the predictions of this two-mode truncation, we remark on one salient feature of these equations, and the reflected structure in the perturbed sine-Gordon solution  $u^\epsilon$  corresponding to this approximation:

$$u^\epsilon \sim 2\sqrt{\epsilon\bar{\omega}} [(c(T) + b(T) \cos(kX))e^{i\omega t} + c.c.] + O(\epsilon\bar{\omega}). \quad (6)$$

The perturbed o.d.e.'s (Eq. (5)) admit the symmetry  $(c, b) \rightarrow (c, -b)$ , which corresponds for  $u^\epsilon$  to a translation in  $x$  by  $L/2$ . Thus, for each fixed point  $(c, b)$  of the modal equations, corresponding to a small amplitude breather plus nonzero mean, there also exists another fixed point  $(c, -b)$ , reflecting the half-period translate of the breather. If we recall Figure 2 and the surrounding discussion, the chaotic p.d.e. dynamics is qualitatively a competition between two such states. Also, this symmetry implies  $b = 0$  is an invariant subspace, and for  $u^\epsilon$  this is the  $\kappa_0$  intermediate state.

Another important feature of this approximation (Eq. (6)) regards Figure 4. Namely, by varying  $c(T)$ ,  $b(T)$  we are able to produce all three spectral configurations: the gap spectrum with  $\kappa_0 \cdot \kappa_1$ , the cross spectrum with  $\kappa_0 \cdot \kappa_1$ , and the  $\kappa_0$  homoclinic configuration. The flow through these configurations will appear in the last section.

So far, the individual qualitative features of the perturbed sine-Gordon dynamics (Figure 2) exist in this truncated NLS approximation, and now we focus on the associated dynamics and deeper parallels between the full and reduced systems.

### 3. PROPERTIES OF THE UNPERTURBED MODAL EQUATIONS

Consistent with our interpretation of the perturbed flow (Eq. (1)) in terms of the integrable sine-Gordon phase space, we develop the unperturbed modal structure relevant for this paper. (See [8] for details.) The unperturbed ( $\tilde{a} = 0$ ,  $\tilde{\Gamma} = 0$ ) modal equations are:

$$\begin{cases} -ic_T + (|c|^2 + \frac{1}{2}|b|^2 - 1)c + \frac{1}{2}(cb^* + c^*b)b = 0, \\ -ib_T + (|c|^2 + \frac{1}{2}|b|^2 - (1+k^2))b + (cb^* + c^*b)c = 0. \end{cases} \quad (7)$$

Property 1 The system (Eq. (7)) is an integrable, Hamiltonian system, with two real independent integrals,

$$\begin{cases} I = |c|^2 + \frac{1}{2}|b|^2 \\ H = \frac{1}{2}|c|^4 + |b|^2|c|^2 + \frac{3}{16}|b|^4 - \frac{1}{2}(1+k^2)|b|^2 - |c|^2 + \frac{1}{2}(b^2c^{*2} + b^{*2}c^2). \end{cases} \quad (8)$$

Property 2 Symmetry considerations produce three rings of fixed points:

$$\text{Ring 1 } (c, b) = (e^{i\phi}, 0), \quad \phi \in [0, 2\pi],$$

$$\text{Ring 2 } (c, b) = \left( 0, e^{i\phi} \sqrt{\frac{4}{3}(1+k^2)} \right), \quad \phi \in [0, 2\pi], \quad (9)$$

$$\text{Ring 3 } (c, b) = \left( e^{i\phi} \sqrt{\frac{1+2k^2}{5}}, e^{i\phi} 2 \sqrt{\frac{2-k^2}{15}} \right), \quad \phi \in [0, 2\pi].$$

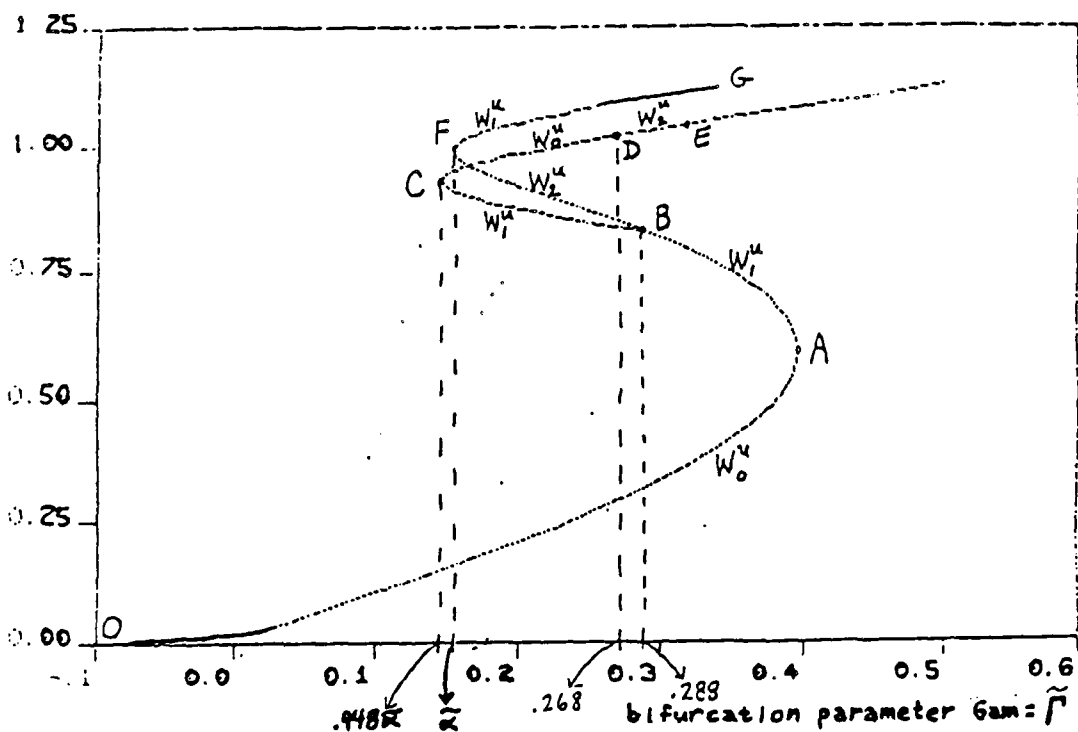
Property 3 Fixed point Ring 1 has a one-dimensional stable and unstable eigenspace, with eigenvalues  $\pm k\sqrt{2-k^2}$ , and two zero eigenvalues. Fixed point Rings 2, 3 have a four-dimensional center manifold.

Property 4 In Ring 1,  $H \equiv -\frac{1}{2}$ ,  $I \equiv 1$ , there are heteroclinic orbits on this energy surface which approach Ring 1 as  $|T| \rightarrow \infty$ . Thus, as in the unperturbed p.d.e., the  $\kappa_0$  solutions ( $b \equiv 0$ ) are exponentially unstable, with order 1 growth rate, and have homoclinic orbits on their energy surfaces.

#### 4. BIFURCATIONS OF THE PERTURBED MODAL EQUATIONS

The behavior of the unperturbed properties under the perturbation (Eq. (5)), with  $\bar{\alpha} \equiv .155$ , as  $\tilde{\Gamma}$  varies, is the crux of this paper. By simple perturbation arguments, the perturbation "phase locks" to discrete points on the Rings 1, 2, 3, for example. We will not discuss these aspects, but rather produce the numerically generated global bifurcation curves (due to M. Jolly and Y. Kevrekides), along with the stability of each branch (due to J.M. Hyman).

L-2 norm of the solution



Bifurcation diagram,  $a = 0.155 = \bar{\alpha}$ .

$W_j^u$  denotes a  $j$ -dimensional unstable eigenspace.

FIGURE 5.

Property 1 The curve OABFG consists of pure  $\kappa_0$  states ( $b \equiv 0$ ). The upper  $\kappa_0$  branch FG is the phase-locked continuation of Ring 1, which maintains the one-dimensional unstable manifold, and thus is the perturbed o.d.e. signature of the homoclinic p.d.e. structures in Figures 2 and 3.

Property 2 The curve BCDE is a double curve of  $\kappa_0 \cdot \kappa_1$  fixed points,  $(c, b)$  and  $(c, -b)$ ,  $b \neq 0$ . The double  $\kappa_0 \cdot \kappa_1$  branch CD is the stable phase-locked continuation of Ring 3, consisting of stable breather plus mean states, related by half-period translation.

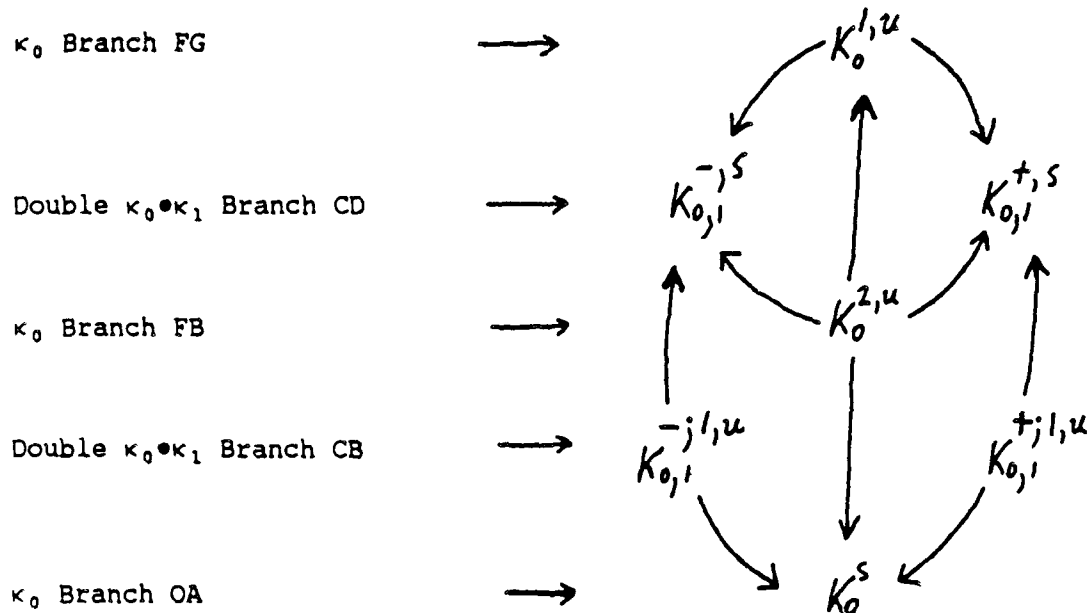
Property 3 The lower hysteresis curves CB and FB pick up an additional unstable eigenvalue due to the perturbation.

Property 4 The key feature in this diagram is point D on the  $\kappa_0 \cdot \kappa_1$  branch, at  $\tilde{\Gamma} \approx .268$ , which corresponds to a subcritical Hopf bifurcation. The previously stable  $\kappa_0 \cdot \kappa_1$  fixed points become two-dimensionally weakly unstable owing to the perturbation. For  $\tilde{\Gamma} > .268$ , the system (Eq. (5)) develops chaotic dynamics, as we describe below.

(We note this model predicts that when there is a second frequency generated in  $u'$  by Hopf bifurcation, it is unstable, explaining why quasi-periodicity was not observed in the p.d.e. bifurcation diagram of Figure 1.)

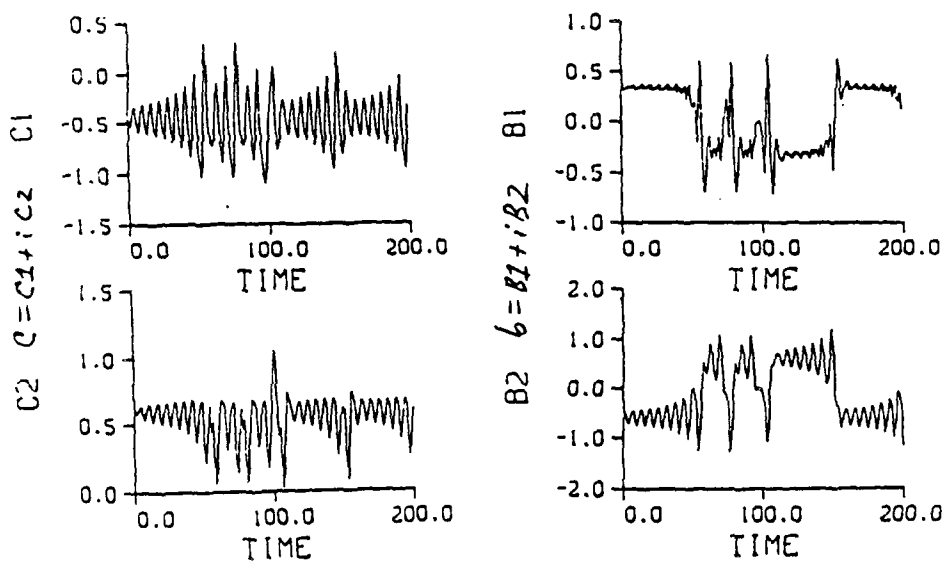
Property 5 The following global fixed point connections are observed just before Hopf bifurcation (Figure 6).

Property 6 After the Hopf bifurcation,  $\tilde{\Gamma} \geq .268$ , the previously stable  $\kappa_{0,1}^\pm$  fixed points become two-dimensionally, weakly unstable. This coincides with the onset of intermittent chaos in the dynamics of the o.d.e's, as depicted below in Figure 7 for  $\tilde{\Gamma} = .275$ , which corresponds to the p.d.e., Figures 2 and 3, with  $\epsilon\Gamma = .103$ .



Global fixed point connections,  $.155 < \bar{\Gamma} < .268$ .

FIGURE 6.

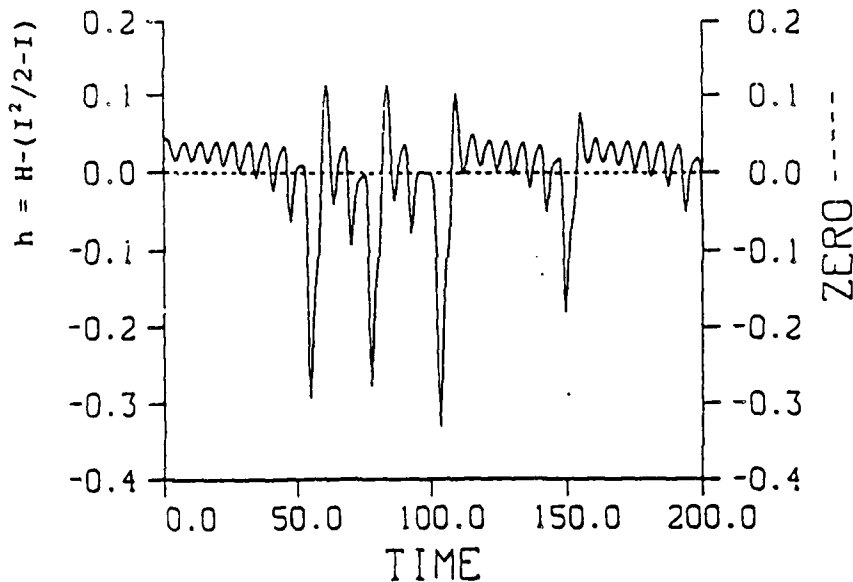


$\Gamma_L = 0.275$	$a_{L0} = -7.000$	$c_{10} = -0.1611$
$a_L = 0.155$	$r_{L0} = -7.000$	$c_{20} = 0.6103$
$\epsilon_{p1} = -0.010$	$\epsilon_{p3} = 0.000$	$b_{10} = 0.3083$
$\epsilon_{p2} = 0.050$	$\epsilon_{p1} = 0.000$	$b_{20} = -0.5206$

FIGURE 7.

Property 7 The chaotic o.d.e. "attractor" contains the two weakly unstable breather plus mean states, related by a half-period translation, and then the intermittent chaotic bursts in and out of these metastable states. In order to correlate with the p.d.e. scenario, Figures 2 and 3, the intermediate states must include a passage near the  $\kappa_0$  homoclinic structure. We measure this next.

Property 8 During the flow in the chaotic attractor, we measure passage near the homoclinic structure in two ways. First, we graph  $h = H - ((I^2/2) - I)$ , which is zero on the homoclinic Ring 1, and check for zero crossings of  $h$  during the intermittent bursts (Figure 8). Also, we compute distances to each fixed point in Figure 6 during the flow, and determine which fixed points are being visited at each phase in the dynamics (Figure 9).



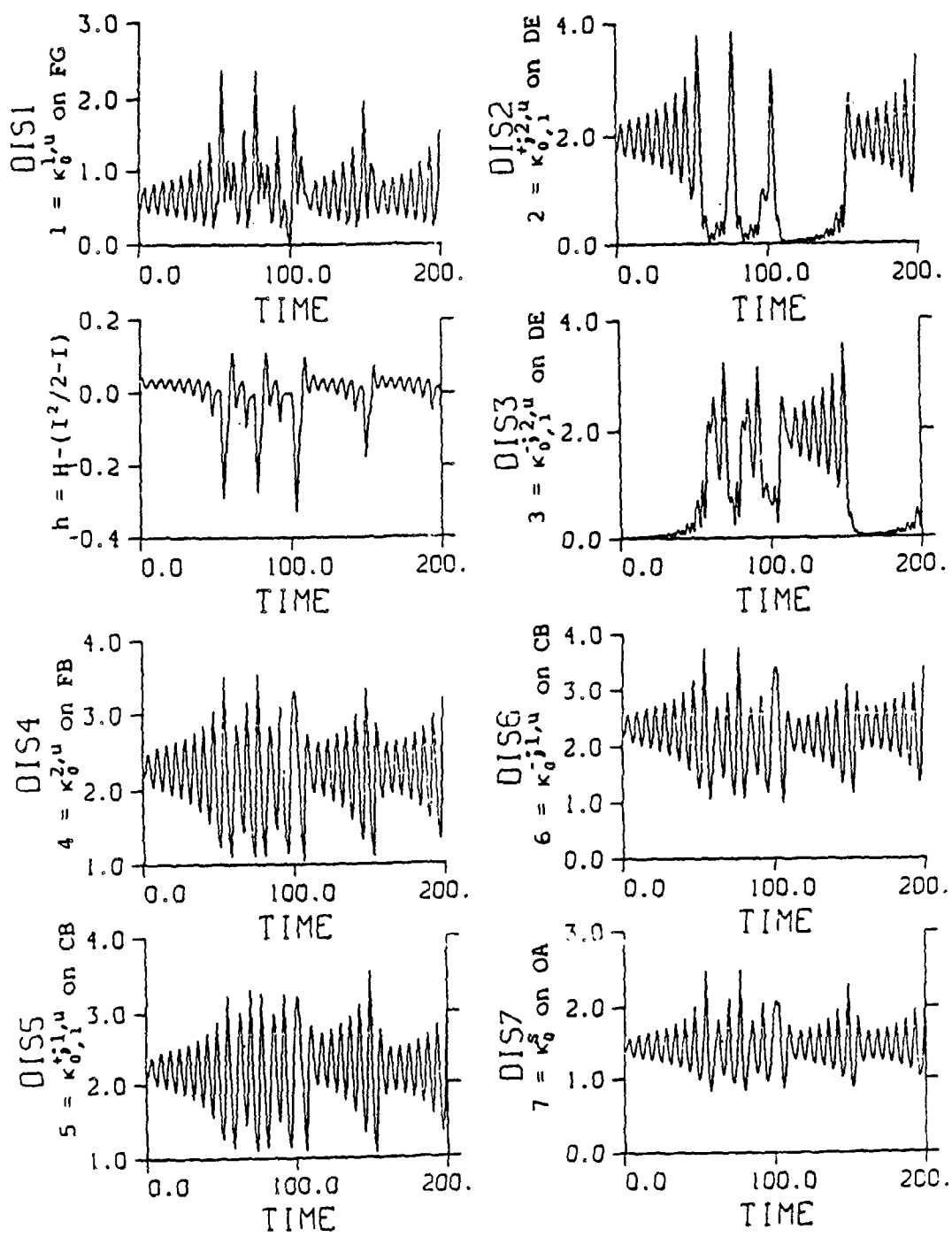
```

rt = 0.275 otol--7.000 c10- -0.4641
at = 0.155 rtol--7.000 c20- 0.6103
eps1--0.010 eps3- 0.000 b10- 0.3883
eps2- 0.050 eps4- 0.000 b20- -0.5206

```

Time series of  $h = H - (I^2/2 - I)$ .

FIGURE 8.



$r_L = 0.275$     $a_{tot} = -7.000$     $c_{10} = -0.4641$   
 $\Delta L = 0.155$     $r_{tot} = -7.000$     $c_{20} = 0.6103$   
 $\epsilon_{ps1} = -0.010$     $\epsilon_{ps3} = 0.000$     $b_{10} = 0.3883$   
 $\epsilon_{ps2} = 0.050$     $\epsilon_{ps4} = 0.000$     $b_{20} = -0.5206$

DISJ = distance from  $(c(T), b(T))$  to fixed point J.

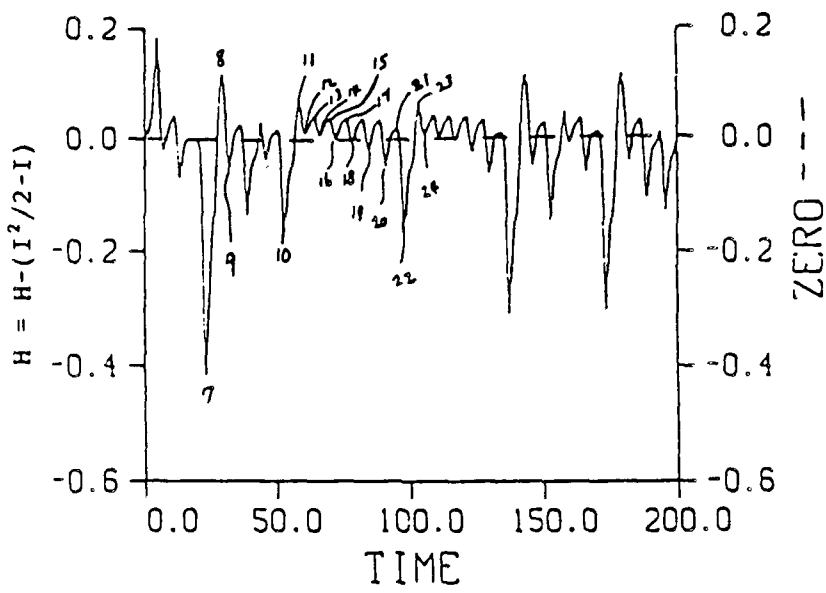
FIGURE 9.

The upshot of this analysis is that  $h$  does have zero crossings in the intermittent chaotic bursts, whereas  $h$  oscillates near the nonzero value corresponding to the  $\kappa_0 \cdot k_1$  fixed points during the laminar phases. Moreover, in these bursts out of laminar regions, the phase-locked fixed point  $\kappa_0^{1,u}$  from the homoclinic ring is approached, sometimes getting very close to it, whereas the flow never comes within unit distance of the other four fixed points.

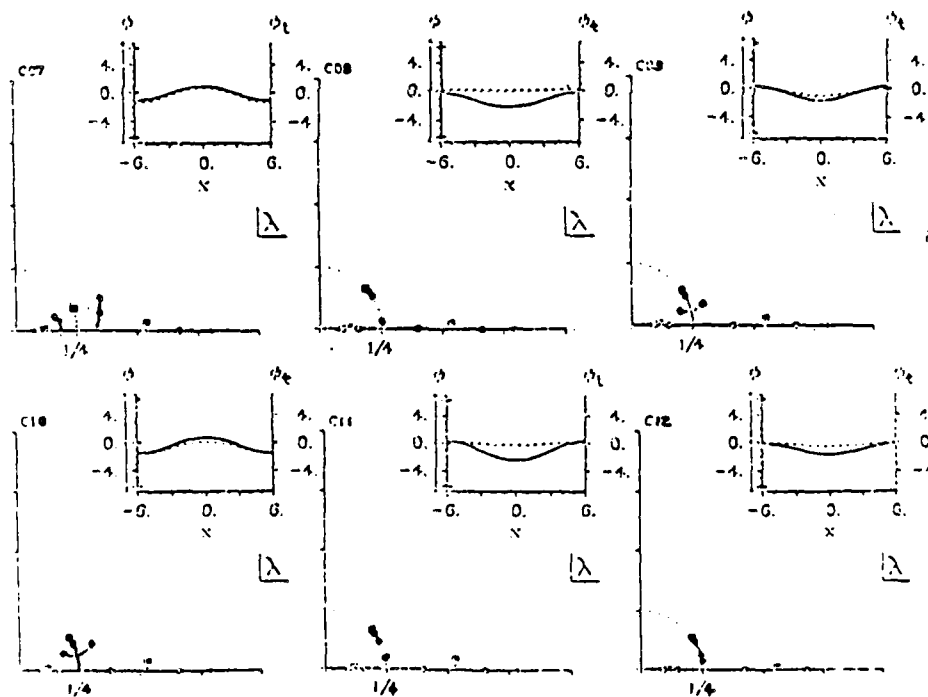
Thus, the chaotic o.d.e. scenario truly reflects the qualitative p.d.e. scenario quite well. We close with one final test of this interpretation.

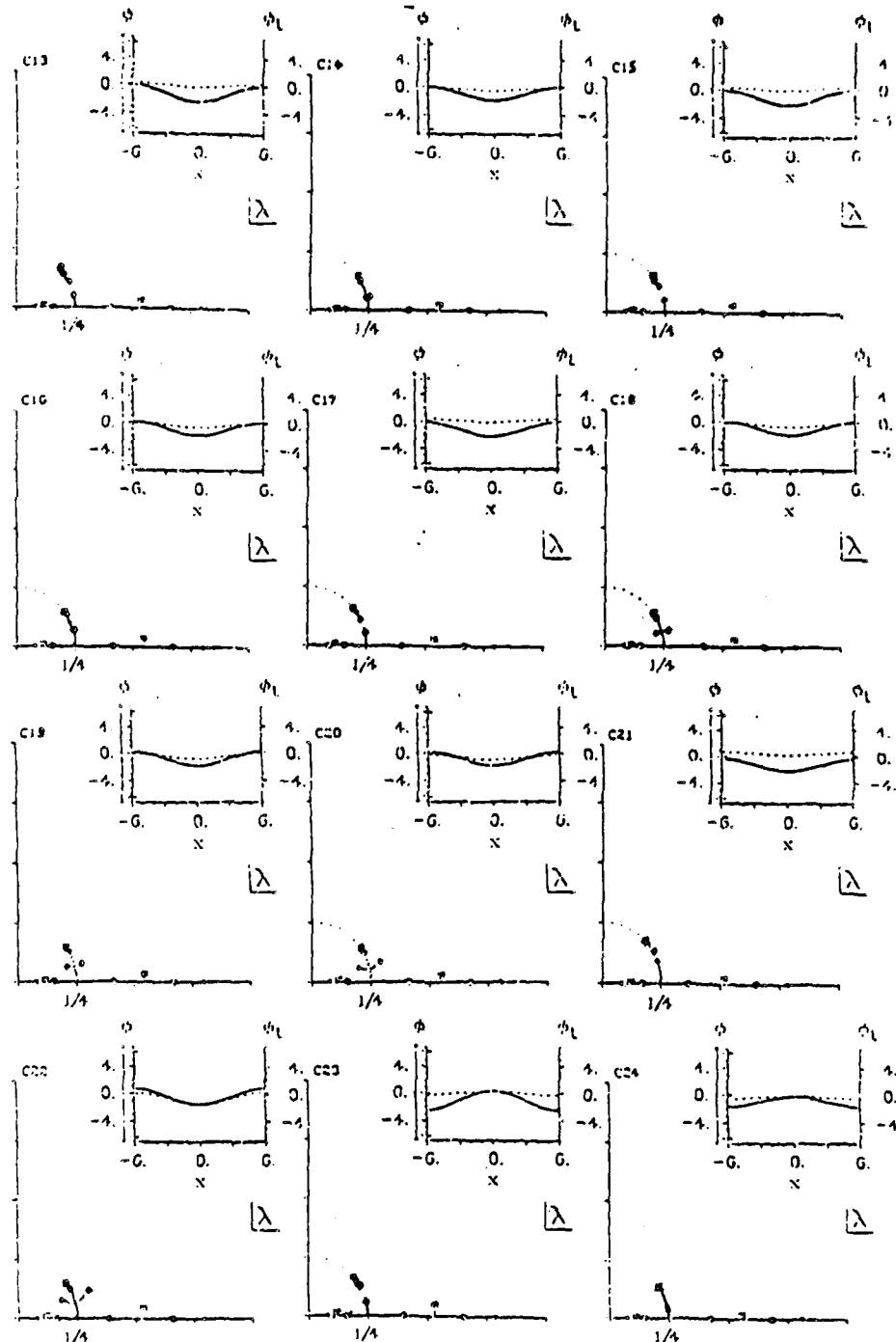
## 5. CORRELATIONS BETWEEN THE INFINITE-DIMENSIONAL AND REDUCED SYSTEMS

So far, we have measured homoclinic crossing in two distinct ways: in the perturbed p.d.e. by graphing the exact sine-Gordon spectrum of  $u^\epsilon$  at each time step, and in the o.d.e. by graphing  $h = H - (\frac{1}{2}I^2 - I)$  and checking for zero crossings. As a final test of this homoclinic phenomenon, we combine the two measurements. We take  $c(T_n)$ ,  $b(T_n)$  during the flow that generates  $h$ , reconstruct the perturbed sine-Gordon solution  $u^\epsilon$  by the approximation (Eq. (6)), and then compute the sine-Gordon spectral measurement of  $u^\epsilon$ . When  $h$  goes through a zero crossing, does the perturbed sine-Gordon field  $u^\epsilon$  pass through a homoclinic spectral configuration? The results appear in Figure 10.



$r_t = 0.275$     $atol = -6.000$     $c10 = -0.4500$   
 $al = 0.155$     $rtol = -6.000$     $c20 = -0.8000$   
 $b10 = -0.1000$     $b20 = -0.1000$





Time series of  $h = H - (I^2/2 - I)$  with labelled time sequence 7-24, followed by the spectral sequence of the reconstructed perturbed sine-Gordon solution  $u^\epsilon$  from the corresponding values of  $c, b$  at times 7-24.

FIGURE 10.

The correlation is surprisingly good, with errors arising only very near to the homoclinic state. This is to be expected owing to the linear vs. nonlinear truncation. (We expect more precision when we model the nonlinear mode truncation.)

The mathematical analysis to support the arguments developed in this paper and [8] will be presented elsewhere [6, 9, 10].

#### REFERENCES

- [1] Bishop, A.R., Forest, M.G., McLaughlin, D.W., and Overman II, E.A., *Physica* 23D, 293-328 (1986), and references therein.
- [2] Overman, E.A., Bishop, A.R., and McLaughlin, D.W., "Coherence and Chaos in the Driven, Damped Sine-Gordon Equation: Measurement of the Soliton Spectrum", *Physica* 19D, 1-41 (1986).
- [3] Ercolani, N.M., Forest, M.G., and McLaughlin, D.W., "Geometry of the Modulational Instability: Local Results", preprint 1986, to be submitted to *Comm. Pure Appl. Math.*
- [4] Ercolani, N.M., Forest, M.G., and McLaughlin, D.W., "Geometry of the Modulational Instability: Global Results", preprint 1986, to be submitted to *Comm. Pure Appl. Math.*
- [5] Ercolani, N.M., Forest, M.G., and McLaughlin, D.W., "Homoclinic Orbits in the Periodic Sine-Gordon Equation", submitted to *Physica D*.
- [6] Ercolani, N.M., Forest, M.G., and McLaughlin, D.W., "Finite Amplitude Modal Equations for Nearly Integrable P.D.E.'s", in progress.
- [7] Flesch, R. and Forest, M.G., "Numerical Implementation of the Inverse Spectral Transform, with Applications to Theta Function Solutions, Linearized Growth Rates, and Averaged Modulation Equations", in progress.
- [8] Bishop, A.R., Flesch, R., Forest, M.G., McLaughlin, D.W., and Overman II, E.A., "Correlations Between the Perturbed Sine-Gordon Equation and a Novel Truncated Modal System", submitted to *Physica D*.

- [9] Initial discussions with S. Wiggins suggest a Melnikov-type theorem may be formulated, proved, and applied to this four-dimensional system.
- [10] Melnikov-type arguments are also being pursued by Ercolani, Forest, and McLaughlin on this problem and the finite-amplitude, nonlinear truncated modal equations in [6].

ACKNOWLEDGEMENTS. The author acknowledges the hospitality of the Technical University of Denmark and the financial support from the European Research Office of the United States Army through Contract No. DAJA-45-85-C-0042.

END  
FILMED  
4 - 89  
DTIC